

# A FIRST PRINCIPLES STUDY OF COMPLEX OXIDES

THESIS SUBMITTED FOR THE DEGREE OF  
DOCTOR OF PHILOSOPHY (SCIENCE)

IN  
PHYSICS (THEORETICAL)

BY

HENA DAS

DEPARTMENT OF PHYSICS  
UNIVERSITY OF CALCUTTA  
FEBRUARY, 2011

**To my family**

**.....for being a great support always.**

# Acknowledgments

During my Ph.D period, I have been supported and accomplished by many people.

I want to owe my deepest gratitude to my supervisor for the invaluable guidance, whole-hearted support. My supervisor gave me the opportunity to involve in different types of projects and collaborations, that helped to increase the periphery of my experience and knowledge. I learned two powerful *ab initio* methods: LMTO and NMTO from my supervisor. I always encouraged not only to discuss academic related problems but also my personal problems and got help from my supervisor to overcome the situation. In these years my supervisor criticized my work a lot, which seemed to unfair initially, but with time and experience I realized that "Criticism is a way to make a person more perfect". Most importantly I would like to thank my supervisor for believing in me.

I am deeply grateful for the opportunities that I got to pursue collaborative work with many distinguished scientists: Prof. D. D. Sarma, Prof. U. V. Waghmare, Prof. C. Gros, Prof. R. Valentí , Prof. N. A. Spaldin and Prof. K. Held. I express my gratitude and regards to all of them. The discussions that I had with them and often with their group members, helped me to understand the subject and to develop my own way to express my understanding of the subject. A bulk amount of work that I carried out in these years was done in collaboration with Prof. U. V. Waghmare. I would like to thank him for inviting me to JNCASR, Bangalore to pursue a part of the collaborative project. He introduced me into the *ab initio* code "PWscf" and helped to learn "Barry phase calculations", I deeply grateful for that. I wish to thank Prof. C. Gros and R. Valentí , for inviting me to visit their group in Frankfurt and giving me the opportunity to learn a new theoretical method, "Stochastic Series expansion (SSE) method". A special thank to the distinguished scientist Prof. D. D. Sarma for giving his invaluable time for discussion and the wonderful ideas that he shared with us. I am grateful to Prof. N. A. Spaldin for giving me the chance to interact with her dynamic group. This collaboration introduced me to the field of "Superlattices". I found her always open for discussion and her friendly behavior encouraged me to ask any question without hesitation. Finally, I would like to thank Prof. K. Held for inviting me in Vienna and interact with his group. I really enjoyed my stay there and learned a lot from the discussions with him and with his group members. I am mostly amazed by their group activity and the work culture.

I would like to give a special thank to Prof. O. K. Andersen for the useful discussion during the visit to MPI, Stuttgart. I would also like to thank Prof. G. P. Das for giving me the first lesson on "Density functional theory".

I like to convey my thanks and best regards to my senior and collaborators Dr. Molly De Raychaudhury and Dr. Prabuddha Sanyal. Whenever I got stuck into a problem they helped me to come out of it. The magneto optical calculations that have been presented in this thesis I learned from Molly di. The working experience with Prabuddha was great and helpful. His deep understanding about the subject helped me to enrich my understanding too.

I record my acknowledgement to S.N. Bose National Centre for Basic Sciences (SNBNCBS) for giving me the opportunity to pursue research and providing me the fellowship. I thank all the faculty members of the Materials Science Department for encouragement. Also I want to thank all the office staff members of the department and institute for their help in all organizational matters and the all present and former members of our computer service group for their help.

I have really enjoyed working in the "Computational material science group". I thank all the present and former members of the group for their support and help. I extend my thanks to all the students of SNBNCBS for their help and the friendly atmosphere. Special thank to Raka and Swastika for being very comfortable company and the memorable moments that we spent together. A special mention has to be made for the person who always helped me to face all the difficulties that came in my way during these years, my friend Rudra. Being in the same field of research he helped me to learn many theoretical tools and a lot on Linux operating system. Thank you Rudra.

Being a very lucky person, I was born in a most supportive and cultural family. Though my father is no more with me, but his words of appreciation still encourage me to go ahead. Before he died he told me and my sisters that "Nothing can stop your life, you have to keep your journey on and on". This line always supplied the power to fight with any bad situation. My higher study would not be possible without the great support and encouragement of my mother. I went through many ups and downs in my life, but I always followed my mother's words: "Be steady and let the good moments to come". From the very childhood I always followed my elder sister, Ajanta Das. I am thankful to my "di" for setting up a perfect line to follow. From my very childhood time I was accompanied by two of the most wonderful and energetic persons, my lovely sisters Kamal and Anu. They filled my life with full of vivacity and wiped out all stress. I want convey my love to the junior most member of my family, my nephew Swastik. He has filled up my life with full of joy and happiness. I would like thank my mother-in-law and father-in-law for their support.

This acknowledgment is incomplete if I do not mention the name of the person who

introduced me into the field of "Computational material science", my husband Saurabh. Being in the same field of research he helped me to learn many computational tools and gave me the space to discuss with him about the subject. I appreciate his constant patience, understanding and love.

# Preface

Complex oxides represent a class of materials with a plethora of fascinating physical properties. The intriguing interplay of charge, spin, and orbital ordering in these systems coupled with lattice effects opens up a scientifically rewarding playground for both fundamental and application-oriented research. In particular transition metal oxides (TMO) continue to attract a great deal of attention both experimentally and theoretically spanning over many decades, due to their several interesting properties, e.g. Mott transition, High- $T_c$  superconductivity, ferromagnetism, antiferromagnetism, low-spin/high-spin transition, ferroelectricity, antiferroelectricity, colossal magnetoresistance, charge ordering *etc.*

These systems have been theoretically investigated using Density functional theory based tools as well as using model Hamiltonians. The first principles density functional based calculations, which take into account all the structural and chemical aspects correctly, fail to predict the ground state properties of such materials since the presence of strongly electron-electron interaction has a crucial role to play. On the other hand, model Hamiltonian-based calculations have the obvious limitation that the parameters of the model Hamiltonian are vastly unknown and therefore fails to capture the material specific complexity of the oxide materials. In recent years there has been a significant effort to combine these two approaches in terms of building up a first principles derived model Hamiltonian, followed by the solution of the model Hamiltonian by means of many body techniques. Since often the electronic structure of these oxide materials involve only few active degrees of freedom (e.g Cu  $d_{x^2-y^2}$  as in case of High- $T_c$  cuprates ), a crucial step in the model Hamiltonian building involves filtering out the informations provided by a full first-principles calculation to arrive to a few-orbital, low energy description starting from a full first principles calculation. This has been achieved in recent years in terms of N-th order muffin tin orbital (NMTO) based downfolding method, that has been vastly employed in the present thesis to derive low energy, few orbital model Hamiltonian. The present thesis contain a investigation of properties of few chosen transition metal oxides based on Density functional theory (DFT) as well as first principles derived model Hamiltonian approach. In cases, the first principles derived model Hamiltonians have been solved with many body tools like, quantum Monte Carlo (QMC), dynamical mean field theory (DMFT) and exact diagonalization (ED). The theoretical methods that we used in the present study are described in **Chapter-2**. Hereafter, the result of our studies is presented.

**Chapter-3** describes the study of electronic and magnetic structure of a spin-gapped system  $\text{CuTe}_2\text{O}_5$ . Recent experimental results for this system revealed that the structural dimer of this system does not coincide with the magnetic dimers. Even the detection of the magnetic structure based on previous theoretical studies were not unambiguous. There-

fore we derived the low-energy spin model for  $\text{CuTe}_2\text{O}_5$  using first-principles electronic structure calculations based on the NMTO-downfolding technique to explain the underlying magnetic structure of the system. We checked the validity of our model by computing the magnetic susceptibility with quantum Monte Carlo technique and comparing it with available experimental data.

In **Chapter-4**, we present the investigation of the correlated electronic structure of  $\text{La}_2\text{CuO}_4$  in the so-called T and T' crystal structures which serve as the parent compounds for the hole-doped and electron-doped high  $T_c$  superconducting compounds, using NMTO-based downfolding technique in combination with dynamical mean field theory (DMFT).  $\text{La}_2\text{CuO}_4$ , which naturally forms in T structure, was reported to made to form in T' structure by means of special thin-film synthesis technique of replacing La by isovalent rare earth (RE) (RE = Y, Lu, Sm, Gd. . .) ions (A. Tsukada *et al.*, Solid State Commun. **133**, 427 (2005)). The experimental studies on T'-structured  $\text{La}_2\text{CuO}_4$  revealed contrasting properties to that in T structure, which we examined by means of electronic structure calculations.

In **Chapter-5**, we present an investigation of the kinetic energy driven antiferromagnetic phases in electron doped double perovskite system  $\text{Sr}_2\text{FeMoO}_6$  using first-principles density-functional calculations, together with exact diagonalization of Fe-Mo Hamiltonian constructed in a first-principles Wannier-function basis. We used  $\text{La}^{3+}$  ion to dope the system which cause a net electron doping into the system. We considered the whole concentration range from  $x=0.0$  (*i.e.*  $\text{Sr}_2\text{FeMoO}_6$ ) to  $x=2.0$  (*i.e.*  $\text{La}_2\text{FeMoO}_6$ ) and studied the relative stability of the various magnetic phases as one increases the carrier concentration through the increased doping of La.

In **Chapter-6**, we explore the origin of the ferromagnetic  $T_c$  trend in Cr-based double perovskite series,  $\text{Sr}_2\text{CrB}'\text{O}_6$  ( $\text{B}'=\text{W}/\text{Re}/\text{Os}$ ) with increasing number of valence electron count. We compared the situation with La-doped  $\text{Sr}_2\text{FeMoO}_6$  double perovskite series which show very different magnetic behavior as a function of increasing number of valence electrons. In addition, we explore the possibility of large magneto-optic signals in these materials, which may be important for device application.

**Chapter-7**, contains a study of the electronic and magnetic properties of the ferromagnetic semiconducting double perovskite compound  $\text{La}_2\text{NiMnO}_6$ , which show a magnetic transition close to room temperature and additionally exhibit an interesting magnetic field sensitive dielectric anomaly as a function of temperature. We used an extended Kugel-Khomskii model to explain the ferromagnetism in the system. We investigated the second order coupling between spin and phonon using density functional perturbation

theory (DFPT), which is given by the change in  $\Gamma$ -point IR active phonon frequencies with the change in magnetic ordering between magnetic sites, to explain the experimentally observed dielectric anomaly. Additionally we calculated Born effective charges  $Z^*$  for  $\text{La}_2\text{NiMnO}_6$  using DFPT.

Finally conclusion of the entire study has been given in **Chapter-8**.

# Publications

1. Piezoelectrics by Design: A route through choice of chemical components in short-period superlattices.  
**Hena Das**, Umesh V. Waghmare, T. Saha-Dasgupta, accepted in J. Appl. Phys. (2011).
2. Origin of magnetism and trend in  $T_c$  in Cr based double perovskites: Interplay of two driving mechanisms.  
**Hena Das**, Prabuddha Sanyal, T. Saha-Dasgupta, D.D. Sarma, accepted in Phys. Rev. B (2011).
3. Chemical control of polar behavior in bicomponent short-period superlattices.  
**Hena Das**, Nicola A. Spaldin, Umesh V. Waghmare and T. Saha-Dasgupta, Phys. Rev. B **81**, 235112 (2010).
4. Evidence of kinetic-energy-driven antiferromagnetism in double perovskites: A first-principles study of La-doped  $\text{Sr}_2\text{FeMoO}_6$ .  
Prabuddha Sanyal, **Hena Das** and T. Saha-Dasgupta, Phys. Rev. B **80**, 224412 (2009).
5. Effects of chemical pressure on the Fermi surface and band dispersion of the electron-doped high- $T_c$  superconductors.  
M. Ikeda, T. Yoshida, A. Fujimori, M. Kubota, K. Ono, **Hena Das**, T. Saha-Dasgupta, K. Unozawa, Y. Kaga, T. Sasagawa, and H. Takagi, Phys. Rev. B **80**, 014510 (2009).
6. Electronic Structure of  $\text{La}_2\text{CuO}_4$  in T and T' structure: A NMTO+DMFT study.  
**Hena Das** and T. Saha-Dasgupta, Phys. Rev. B **79**, 134522 (2009).
7. Theoretical evidence and chemical origin of the magnetism-dependent electrostructural coupling in  $\text{La}_2\text{NiMnO}_6$ .  
**Hena Das**, Umesh V Waghmare, T. Saha-Dasgupta and D. D. Sarma, Phys. Rev. B **79**, 144403 (2009).
8. Moderate to large magneto-optical signals in high  $T_c$  double perovskites.  
**Hena Das**, Molly De-Raychaudhury, T. Saha-Dasgupta, Appl.Phys.Lett. **92**, 201912 (2008).
9. Proposed low energy model Hamiltonian for spin-gapped system  $\text{CuTe}_2\text{O}_5$ .  
**Hena Das**, T. Saha-Dasgupta, C. Gross and R. Valenti, Phys. Rev. B, **77**, 224437 (2008) (*Editor's suggestion*).

10. Electronic structure, phonons and dielectric anomaly in ferromagnetic insulating double perovskite  $\text{La}_2\text{NiMnO}_6$ .

**Hena Das**, Umesh V Waghmare, Tanusri Saha-Dasgupta and D. D. Sarma, Phys. Rev. Lett. **100**, 186402 (2008).

# Contents

<b>1</b>	<b>Introduction</b>	<b>1</b>
1.1	General introduction about Oxides . . . . .	1
1.2	Theoretical methods to study oxides . . . . .	7
1.3	Systems under study . . . . .	9
<b>2</b>	<b>Theoretical methods</b>	<b>23</b>
2.1	Introduction . . . . .	23
2.2	Density Functional theory (DFT) . . . . .	24
2.2.1	Exchange correlation functional . . . . .	27
2.2.2	Different DFT based first principles methods . . . . .	31
2.3	$N^{th}$ Order Muffin Tin Orbital (NMTO) - a downfolding method . . . . .	39
2.4	Many body techniques . . . . .	42
2.4.1	Stochastic series expansion of quantum Monte Carlo method . . . . .	42
2.4.2	Dynamical Mean Field Theory (DMFT) . . . . .	43
2.4.3	Exact diagonalization method . . . . .	45
2.5	Outline of the present study . . . . .	46
<b>3</b>	<b>Proposed low-energy model Hamiltonian for the spin-gapped system <math>\text{CuTe}_2\text{O}_5</math></b>	<b>51</b>
3.1	Introduction . . . . .	51
3.2	Crystal structure . . . . .	54
3.3	Electronic structure . . . . .	55
3.4	Derivation of Low-energy model Hamiltonian . . . . .	57
3.5	Susceptibility, magnetization and specific heat . . . . .	63
3.6	Summary and outlook . . . . .	66
<b>4</b>	<b>Electronic structure of <math>\text{La}_2\text{CuO}_4</math> in the T and T' crystal structures.</b>	<b>69</b>
4.1	Introduction . . . . .	69
4.2	Structural details . . . . .	70
4.3	One-particle electronic structure . . . . .	71
4.4	LDA+DMFT results and discussion . . . . .	74

4.5	Summary and outlook . . . . .	76
<b>5</b>	<b>Evidence of kinetic-energy-driven antiferromagnetism in double perovskites.</b>	<b>80</b>
5.1	Introduction . . . . .	80
5.2	Computational Details . . . . .	82
5.3	Result and discussions . . . . .	83
5.3.1	Structural details . . . . .	83
5.3.2	Total energy, electronic structure, and relative stability of magnetic phases . . . . .	84
5.3.3	Determination of low-energy, few-orbital Hamiltonian . . . . .	90
5.3.4	Calculations of magnetic phase diagram and magnetic transition temperatures in terms of low-energy Hamiltonian . . . . .	94
5.4	Summary and outlook . . . . .	96
<b>6</b>	<b>Study of magnetism and magneto-optic effect in Cr-based double perovskites</b>	<b>100</b>
6.1	Introduction . . . . .	100
6.2	Computational details . . . . .	101
6.3	Investigation of the increasing trend in $T_c$ . . . . .	102
6.3.1	Examination of basic electronic structure . . . . .	102
6.3.2	NMTO-downfolding calculations . . . . .	103
6.3.3	Total energy calculations . . . . .	105
6.3.4	Exact diagonalization study of model Hamiltonian . . . . .	106
6.4	Investigation of magneto optical properties . . . . .	108
6.4.1	Microscopic theory of magneto optical effect . . . . .	108
6.4.2	Results and discussion . . . . .	110
6.5	Summary and outlook . . . . .	113
<b>7</b>	<b>Electronic Structure, phonons and dielectric anomaly and chemical origin of the Magneto-electro-structural coupling in ferromagnetic insulating double-perovskite <math>\text{La}_2\text{NiMnO}_6</math> (LNMO)</b>	<b>116</b>
7.1	Introduction . . . . .	116
7.2	Structural details . . . . .	118
7.3	Computational details . . . . .	119
7.4	Basic electronic structure . . . . .	120
7.5	Ferromagnetism - The extended Kugel-Khomskii model . . . . .	121
7.6	Spin-phonon coupling-Origin of dielectric anomaly . . . . .	124
7.7	Born effective charges in LNMO . . . . .	126
7.7.1	Electronic origin . . . . .	128

7.7.2	Comparison with other compounds . . . . .	131
7.8	Summary and outlook . . . . .	132
<b>8</b>	<b>Conclusion</b>	<b>135</b>

# List of Figures

1.1	Symmetry and corresponding Crystal field splitting of $d$ levels for some known regular TM-O polyhedra: (b) Octahedra, (d) Square pyramid, (e) Square planar, (f) Tetrahedra. Panels (a) and (c) show the additional splitting in the $d$ levels due to tensile and compressive JT distortions in octahedral symmetry respectively. . . . .	2
1.2	The two Jahn-Teller modes $Q_2$ and $Q_3$ . . . . .	3
1.3	Examples of configurations for transition-metal $d$ orbitals which are bridged by ligand $p$ orbitals (Taken from Ref.[2]). . . . .	4
1.4	Schematic diagram showing the coexistence of at least two ferroic forms of ordering leads to additional interactions. From Ref:[4]. . . . .	6
1.5	Schematic diagram of the combined approach. . . . .	9
1.6	The simplest ladder model consists of two spin chains. $J_C$ and $J_R$ represents the exchange coupling along the spin chain and along the rung of the ladder respectively. . . . .	12
1.7	Phase diagram of electron and hole doped superconductors, showing superconductivity (SC), antiferromagnetic (AF), pseudogap, and normal-metal regions. Taken from Ref-[55]. . . . .	13
1.8	Crystal structure of T (left panel) and T' (right panel) structures. The rare-earth, Cu, and O atoms are represented by the large, mediums and small sized balls, respectively. The in-plane and out-of-plane oxygen atoms are represented by dark and light shades, respectively. . . . .	14
1.9	A rock-salt ordered double perovskite structure ( $A_2BB'O_6$ ). . . . .	15
1.10	Structure, tolerance factor ( $f$ ), and magnetic properties of various double perovskites. Taken from Ref:[59]. . . . .	17
2.1	DFT self consistent cycle. . . . .	27
2.2	The construction of Muffin-Tin potential . . . . .	34
2.3	Constituents of Kink partial wave (KPW), $\phi$ , $\phi_0$ and $\varphi$ . . . . .	41
2.4	The Nth order approximation to the energy dependence of a partial wave for a discrete (Lagrange) mesh. . . . .	41

2.5	The DFMT replaces a the full lattice of a correlated electron system with a single impurity site coupled to a self consistent bath (Taken from Ref.[45]). . . . .	44
2.6	Flowchart of the DMFT self consistent cycle. . . . .	45
3.1	(a)Temperature dependences of the ESR intensity and the dc susceptibility. (b)Temperature dependences of the spin susceptibility (circles) in $\text{CuTe}_2\text{O}_5$ . The lines are best fits obtained by the models : (1)A pure dimer model (black dashed line), (2)An alternating spin chain model (blue solid line), (3)Interacting dimer model (red solid line). Taken from Ref.[16]. . . . .	52
3.2	An antiferromagnetic dimer system with intra dimer interaction strength $J$ . . . . .	52
3.3	An alternating antiferromagnetic spin chain with alternating exchange constants $J_1$ and $J_2$ . . . . .	53
3.4	Building units of $\text{CuTe}_2\text{O}_5$ . (a) $\text{CuO}_6$ -distorted octahedron. (b) $\text{Cu}_2\text{O}_{10}$ -structural dimer unit. (c) $\text{TeO}_4$ -tetrahedra. (d) Crystal structure of $\text{CuTe}_2\text{O}_5$ . The largest balls represent Te1 and Te2. Te1 and Te2 are shown in gray and black colors, respectively. Cu atoms are represented by medium sized balls, situated at the center of the distorted octahedra. The smallest balls denote the oxygen atoms. . . . .	54
3.5	Partial density of states of Cu $d$ (in black full lines), O $p$ (in red dashed lines), and Te $p$ (in cyan or gray full lines) orbitals for $\text{CuTe}_2\text{O}_5$ . The inset shows the density of states for O $p$ and Te $p$ in the energy range close to $E_F$ , dominated by Cu $d_{x^2-y^2}$ character. . . . .	55
3.6	LDA band structure of $\text{CuTe}_2\text{O}_5$ plotted along various symmetry directions of the monoclinic lattice. The zero of the energy has been set up at the LDA Fermi energy. The dominant orbital contributions in various energy ranges are shown in boxes on the right-hand side. The various Cu $d$ characters are shown in the local reference frame as described in the text. . . . .	56
3.7	Bands obtained with downfolded Cu $d_{x^2-y^2}$ basis (solid lines) compared to full LDA band structure (dashed lines). $E_0$ , $E_1$ and $E_2$ mark the energy points used in NMTO calculation. . . . .	57
3.8	Effective Cu $d_{x^2-y^2}$ orbital with lobes of opposite signs colored as black and white. The $d_{x^2-y^2}$ orbital is defined with the choice of local reference frame as described in the text. . . . .	57
3.9	Cu-Cu interaction paths $t_n$ . The color convention is the same as Fig. 3.4.	59

3.10	Effective orbital corresponding to the downfolded NMTOs, placed at two Cu sites situated at two different structural dimer units corresponding to the $t_4$ interaction. Lobes of orbitals placed at different Cu sites are colored differently. Lobe colored black (white) at one Cu site represents the same sign as that colored magenta (cyan) at other Cu site. . . . .	60
3.11	Effective orbital corresponding to the downfolded NMTOs, placed at two Cu sites situated at two different structural dimer units corresponding to the $t_6$ hopping term. Color convention is the same as in Fig. 3.10 . . .	60
3.12	Cu $d_{x^2-y^2}$ downfolded NMTOs, placed at two Cu sites situated within the same structural dimer. The O2 sites with long Cu-O2 bond lengths have been removed for better view. Color convention is the same as in Fig. 3.10. . . . .	61
3.13	The 2D coupled dimer model shown on a $8 \times 4$ (32 site) lattice. Periodic boundary conditions have been applied on both directions. The thick, thin and dashed lines represent the strongest $J_4$ , the next strong $J_6$ and the weak structural intradimer interaction $J_1$ , respectively. The site index $k$ is given by $k=N_1(l + m)$ , where $m$ runs over number of rows in the square lattice ( $m=0,1, . . . ,N_1$ ) and $l$ runs over the number of columns in the square lattice ( $l=0,1, . . . ,N_2$ ). . . . .	62
3.14	Temperature dependence of magnetic susceptibility for $\text{CuTe}_2\text{O}_5$ . The circles correspond to experimental data (Ref.[16]) and the solid line corresponds to calculated susceptibility based on a 2D-coupled dimer model.	63
3.15	Magnetization plotted as a function of temperature for the 2D-coupled dimer model of $\text{CuTe}_2\text{O}_5$ in an applied magnetic field of strengths $h/J=0.2, 0.5, 1.0$ (bottom to top) which correspond to $H=12.7, 31.7, 63.4$ T. The inset shows the magnetization versus $H$ upto the saturation magnetic field at $T=10$ K. . . . .	65
3.16	Magnetization plotted as a function of temperature for the 2D-coupled dimer model of $\text{CuTe}_2\text{O}_5$ and the alternating chain model of Ref.[16] for two values of the magnetic field $H=12.7$ T and $H=31.7$ T. . . . .	65
3.17	Specific heat plotted as a function of temperature for $\text{CuTe}_2\text{O}_5$ for the 2D-coupled dimer model (solid line) and the model of Ref.[16] (dashed line). . . . .	66
4.1	Comparison of resistivity of $\text{La}_2\text{CuO}_{4\pm y}$ thin films with the T- and T'-structure for $y \sim 0$ (taken from Ref.[5]). The vary high resistivity in the T' phase below 150 K was not measurable with their experimental set up.	70

4.2	Crystal structure of T (left panel) and T' (right panel) structures. The rear-earth, Cu, and O atoms are represented by the large, mediums and small sized balls, respectively. The in-plane and out-of-plane oxygen atoms are represented by dark and light shades, respectively. . . . .	71
4.3	Band structure of $\text{La}_2\text{CuO}_4$ in T (left panel) and T' (right panel) structures plotted along the high symmetry points of the body centered tetragonal BZ. The fatness associated with each band is proportional to the orbital character of Cu $d_{x^2-y^2}$ . The single band shown as thick line is the effective one band obtained by NMTO downfolding technique. The inset shows the corresponding Fermi surfaces. . . . .	72
4.4	Effective Cu $d_{x^2-y^2}$ Wannier-type functions and the hopping integrals of a single-band model of $\text{La}_2\text{CuO}_4$ in T (left panels) and T' (right panels) structures. (a) Wannier type functions projected on to $\text{CuO}_2$ plane ( $ab$ plane) and (b) Wannier-type functions projected on to plane perpendicular to $\text{CuO}_2$ plane ( $ac$ plane). Lobes of opposite signs are colored as black and gray. (c) In-plane hopping integrals in the basis of effective Wannier-type functions, plotted as a function of Cu-Cu distances, measured in unit of lattice constant ( $a_{\text{lat}}$ ). . . . .	73
4.5	DMFT spectral function at $T=580$ K (thick line) and the LDA DOS (thin line) $\text{La}_2\text{CuO}_4$ in T (left panel) and T' (right panel) structures. The zero of the energy is set at $\mu$ . . . . .	76
5.1	The Fe sublattice ordering of $\text{Sr}_{2-x}\text{La}_x\text{FeMoO}_6$ . Shown are the A-type(left panel) and G-type (right panel) antiferromagnetic arrangement of Fe spins. In case of A-type antiferromagnetism the Fe spins in-plane are ferromagnetically coupled while Fe spins between two adjacent plans are antiferromagnetically coupled. For G-type antiferromagnetism, the Fe spins are antiferromagnetically coupled both out-of-plane and inplane. The shaded box indicate the unit cell of two formula unit supercell. . . .	82
5.2	The energy difference between FM and AFM-A phase plotted as a function of La concentration. The FM phase becomes unstable beyond a critical concentration of La both within GGA and GGA+U. . . . .	84
5.3	The GGA density of states corresponding to SFMO, SLFMO, L3SFMO, and LFMO in ferromagnetic configuration. The density of states projected onto Fe, Mo, and O are represented by solid black, green (gray), and shaded gray area. The upper and lower panels correspond to majority- and minority-spin channels. Zero of the energy is set at the GGA Fermi energy. . . . .	86

5.4	Schematic showing the mechanism stabilizing the AFM phase over FM phase. As the La doping is increased, the Fermi level ( $E_f$ ) shifts toward right. . . . .	87
5.5	The density of states corresponding to SFMO, SLFMO, L3SFMO, and LFMO in the A-type antiferromagnetic configuration. The density of states projected onto Fe, Mo, and O are represented by solid black, green (gray), and shaded gray area. Zero of the energy is set at the GGA Fermi energy. . . . .	88
5.6	DOS for LFMO in FM and AFM-A phase, using GGA+U. . . . .	89
5.7	Top panels: Positioning of various energy levels as obtained by NMTO-downfolding calculation before and after switching on the hybridization between the magnetic and nonmagnetic ions. Bottom panels: Effective Mo $t_{2g}$ Wannier orbitals corresponding to massively downfolded NMTO Hamiltonian in the down-spin channel. Shown are the orbital shapes (constant amplitude surfaces) with lobes of opposite signs colored as blue (dark gray) and cyan (light gray). The central part of the Wannier orbitals are shaped according to Mo $t_{2g}$ symmetry while the tails are shaped according to Fe $t_{2g}$ and O- $p$ symmetries. Significant amount of weights are seen in O and Fe site which reflects the strong hybridization between Fe, Mn, and O. For LFMO, finite weights are seen also at La sites, occupying the hollows formed between Mo-O and Fe-O bonds, which is of La $3z^2$ character. . . . .	92
5.8	The energy differences between the FM and G-type AFM phase (solid line) and the FM and A-type AFM phase (dashed line) plotted as a function of the number of conduction electrons, as obtained by exact diagonalization of the low-energy Hamiltonian for a $8 \times 8 \times 8$ lattice. Only the region outside the hashed regions, from carrier concentration 1 to 3 is of relevance for $\text{Sr}_{2-x}\text{La}_x\text{FeMoO}_6$ . . . . .	95
5.9	The ferromagnetic $T_c$ (solid line) and the antiferromagnetic transition temperature $T_N$ (dashed line) plotted as a function of the number of conduction electrons, as obtained by exact diagonalization of the low-energy Hamiltonian for a $8 \times 8 \times 8$ lattice. As in Fig. 5.8, the region outside the hashed regions, from carrier concentration 1 to 3 is of relevance for $\text{Sr}_{2-x}\text{La}_x\text{FeMoO}_6$ . . . . .	96

6.1	Left Panels: GGA DOS projected onto Cr $d$ (black solid lines), B' $d$ (Red/Grey solid lines) and O $p$ (shaded area). Zero of the energy is set at $E_F$ . The numbers within the boxes indicate the Cr $t_{2g}$ contribution in the bands crossing $E_F$ , with respect to that of B'. Right Panel: Calculated net magnetic moment and magnetic moments at Cr, B' and O sites. The numbers within the bracket denote the result of GGA+SO calculations, the first entry being the spin moment and the second entry being the orbital moment. From top to bottom, the plots correspond to SCWO, SCRO and SCOO respectively. . . . .	102
6.2	The energy level diagram (upper panel) and massively downfolded Wannier functions (lower panels) for $\text{Sr}_2\text{CrB}'\text{O}_6$ series. For Wannier function plots, constant value surfaces have been plotted with two oppositely signed lobes colored differently. From left to right in lower panel, the plots correspond to SCWO, SCRO and SCOO respectively. The numbers in the energy level diagram are in unit of eV. . . . .	103
6.3	PM - FM energy differences plotted as a function of valence electron count, as obtained in exact diagonalization calculation. The diamond (square) symbols connected by dashed (solid) line correspond to calculations corresponding to Hamiltonian, without (with) $J_2$ term. . . . .	107
6.4	The polar Kerr effect . . . . .	108
6.5	Right and left-handed circularly polarized component of a plane polarized light beam. . . . .	108
6.6	Left panel: Density of states of $\text{Sr}_2\text{CrB}'\text{O}_6$ system (B'=W,Re,Os) computed within the framework of GGA including SO coupling. Black and cyan lines and shaded brown area indicate partial density of states corresponding to Cr- $d$ , B'- $d$ , and O- $p$ . Arrows indicate various possible optical transitions. Right panel: Calculated reflectivity spectra for $\text{Sr}_2\text{CrB}'\text{O}_6$ series. . . . .	111
6.7	Left panel: Absorptive and dispersive parts of the calculated diagonal optical conductivity of $\text{Sr}_2\text{CrB}'\text{O}_6$ . Right panel: Calculated polar Kerr rotation spectra for $\text{Sr}_2\text{CrB}'\text{O}_6$ . The inset shows the Faraday spectrum in unit of $10^6$ deg/cm for insulating $\text{Sr}_2\text{CrOsO}_6$ . . . . .	112
7.1	Magnetic susceptibility $\chi(T)$ data as measured by Nyrrisa <i>et.al.</i> [10], at 1 T on zero-field (ZFC) and field cooling (FC). Insets show a field dependent magnetization data at 5 K (upper right). . . . .	117
7.2	temperature dependence of the dielectric constant at 10 KHz for 0, 0.1 and 1 T applied field. Taken from Ref.[10]. . . . .	117

7.3	Crystal structure viewed along the pseudocubic [111] direction revealing the high-temperature rhombohedral structure of LNMO. The violet (dark gray) and orange (light gray) colored octahedra denote the NiO <sub>6</sub> and MnO <sub>6</sub> octahedra, respectively. The La atoms shown as big balls sit in the hollow formed by NiO <sub>6</sub> and MnO <sub>6</sub> octahedra. . . . .	118
7.4	DOS of LNMO in geometry optimized rhombohedral and monoclinic phases. . . . .	120
7.5	All super exchange interactions between Ni- <i>d</i> states and Mn- <i>d</i> states. The upper panel corresponds to superexchange interactions between half-filled Ni <i>e<sub>g</sub></i> and half-filled Mn <i>t<sub>2g</sub></i> states, while the lower panel corresponds to superexchange interactions between half-filled Ni <i>e<sub>g</sub></i> and empty Mn <i>e<sub>g</sub></i> states. . . . .	122
7.6	Overlap between effective $x^2 - y^2$ orbitals, placed at neighboring NiO <sub>6</sub> and MnO <sub>6</sub> octahedra of LNMO calculated in the monoclinic phase, showing the superexchange path mediated by the corner-shared O. Plotted are the orbital shapes (constant-amplitude surfaces) with lobes of opposite signs colored as black (magenta) and white (cyan), respectively, for Mn (Ni). . . . .	123
7.7	Phonon spectra of rhombohedral LNMO in FM (top panel) and FIM (bottom panel) states. The arrows show the shifting of dominant IR-active phonon modes. The inset shows the displacement of atoms corresponding to the lowest frequency IR-active mode. The angle between the dotted lines connecting the Ni-O (at the center of the oxygen octahedra) and O-Mn (rightmost corner of the cell) is affected by this phonon. . . .	125
7.8	Energy level positions of Ni and Mn <i>d</i> levels with respect to Fermi energy $E_f$ as obtained in DFT calculation. The upper (lower) panel corresponds to ferromagnetic (ferrimagnetic) spin arrangement between Ni and Mn spins. . . . .	129

7.9 (a) Atomic structure of  $\text{La}_2\text{NiMnO}_6$  in the equilibrium configuration compared to the structure where Ni atom has been moved along the rhombohedral  $x$  axis. The green, yellow and orange balls mark the positions of Ni, Mn, and O atoms. The lighter and darker green balls indicate the positions of Ni at equilibrium and that after displacement. The movement of Ni atom strongly influences the  $\angle\text{Ni-O-Mn}$ , increasing it one quadrant and decreasing it in the opposite quadrant from the equilibrium  $\angle\text{Ni-O-Mn}$ . (b) The rhombohedral global coordinate system and the oxygen-based octahedral coordinate system. The unprimed and primed coordinate systems represent the rhombohedral coordinate system ( $z$  axis pointing along the pseudocubic  $[111]$  direction) and the oxygen-based octahedral coordinate system ( $z'$  axis pointing along one of the Ni-O bond and  $x'$  axis pointing along the Ni-O bond approximately perpendicular to it.) (c) Plot of effective Ni  $y'z'$  Wannier functions. Plotted are the orbital shapes (constant amplitude surfaces) with the lobes of opposite signs colored as red (light gray) and blue (dark gray). The upper two panels correspond to calculations in the equilibrium (left panel) and Ni displaced (right panel) conditions in the ferromagnetic phase, while the lower panels correspond to calculations in the equilibrium (left panel) and Ni displaced (right panel) conditions in the ferrimagnetic phase. The arrows marked in the Wannier functions in the ferromagnetic phase show the sense of rotation of the orbital tails. . . . . 130

# List of Tables

3.1	Cu-Cu hopping parameters corresponding to the downfolded Cu- $d_{x^2-y^2}$ Hamiltonian in NMTO-Wannier function basis. Interactions of strength larger than 1 meV are listed. . . . .	58
5.1	Optimized cell parameters and the atomic positions for Sr <sub>2</sub> FeMoO <sub>6</sub> and La <sub>2</sub> FeMoO <sub>6</sub> . Fe and Mo ions are situated at the high-symmetry Wykoff positions $2a$ and $2b$ , given by (0,0,0) and (0.0, 0.0, 0.5), respectively. For $I4/mmm$ symmetry Sr/La also sites in the high-symmetry Wykoff position given by (0.5, 0.0, 0.25) but sits in a general position for $P21/n$ symmetry. . . . .	83
5.2	Magnetic moments at Fe and Mo sites, and the total magnetic moment in FM and AFM-A phase of Sr <sub>2-x</sub> La <sub>x</sub> FeMoO <sub>6</sub> in a two formula unit calculation. S3LFMO, SLFMO, and SL3FMO refer to Sr <sub>1.5</sub> La <sub>0.5</sub> FeMoO <sub>6</sub> , SrLaFeMoO <sub>6</sub> , and Sr <sub>0.5</sub> La <sub>1.5</sub> FeMoO <sub>6</sub> , respectively. . . . .	85
5.3	Total energy differences per unit formula in eV between FM and AFM-A, and between FM and AFM-G for various doping of La, as obtained within eight formula unit supercell calculations. . . . .	90
5.4	Hopping matrix elements in eV between Fe- $t_{2g}$ and Mo- $t_{2g}$ . Only the hopping matrix elements of magnitude larger than 0.01 eV are listed. The onsite matrix elements are given by 0.005 (0.008) eV, 0.0 (0.0) eV, 0.0 (0.0) eV for Fe- $xy$ , Fe- $yz$ and Fe- $xz$ respectively, and 1.018 (1.057) eV, 1.007 (1.053) eV, 1.007 (1.053) eV for Mo- $xy$ , Mo- $yz$ and Mo- $xz$ respectively. All numbers inside the bracket are for LFMO and those outside are for SFMO. The energies for a given compound is measured with respect to the lowest energy state. The small differences between numbers involving $xy$ and that of $yz$ and $xz$ reflect the tetragonality present in the systems. . . . .	93
7.1	Energy-minimized structural parameters of LNMO. Lattice constants have been kept constant at the experimental values. . . . .	119

7.2	Calculated Born effective charge tensors at the La, Ni, Mn and O sites of $\text{La}_2\text{NiMnO}_6$ at FM and FiM phases. Note the presence of large, off-diagonal elements which are anti-symmetric specially in case of Ni. Changing the magnetic ordering between Ni and Mn from FM to FiM has profound effect in terms of making the anti-symmetric off-diagonal components at Ni weaker. . . . .	127
-----	---	-----



# Chapter 1

## Introduction

### 1.1 General introduction about Oxides

Complex oxides, especially Transition Metal Oxides (TMO) present a class of materials exhibiting a variety of structures and properties. The outstanding range of electronic and magnetic properties exhibited by transition metal oxides is particularly noteworthy.

The basic structural unit of this class of materials is metal-oxygen polyhedra ( $MO_n$ , where M is the TM atom, O is the oxygen and  $n$  is an integer) such as octahedra, square pyramid, square planar, tetrahedra, pentagonal bipyramid, trigonal bipyramid *etc* (some of these structural units are presented in Fig. 1.1). The strong tendency of surrounding oxygens towards the negative valence, remove the  $s$  electrons from the TM atom and subject the  $d$  orbitals of TM ions to an anisotropic field, known as Crystal field. Under the influence of this field each  $d$  orbital is affected differently and how a particular  $d$  orbital will be affected depends upon the geometry of the oxygen surrounding. This results into splitting of the energy levels of the five fold degenerate (including spin, 10-fold degenerate)  $d$  orbitals in the atomic limit. The strength of this splitting, known as crystal field splitting, depends on the following factors:

- Symmetry of the oxygen cage.
- Strength of TM-O covalency.

The most common geometry is the octahedral geometry, where six oxygen ligands form an octahedron around the metal ion as shown in Fig. 1.1(b). For a cubic structure the  $d$ -orbitals split into two sets : a higher energy level of two-fold (including spin, four-fold) degenerate  $e_g$  orbital and a lower energy level of three-fold (including spin, six-fold) degenerate  $t_{2g}$  orbitals. For a perfect octahedral symmetry, the lobes of the  $e_g$  orbitals, formed by  $d_{x^2-y^2}$  and  $d_{3z^2}$  orbitals, are pointed directly towards the oxygen atoms and therefore feel stronger electrostatic field than the  $t_{2g}$  orbitals, which are constituted by  $d_{xy}$ ,  $d_{yz}$  and  $d_{zx}$  orbitals with lobes directed in between two oxygen atoms. If the degenerate  $e_g$  states are occupied partially, it generally leads to further lifting of degeneracy of the ground state. The perfect octahedral geometry distort spontaneously driven by the combined effect of two phonon modes  $Q_2$  and  $Q_3$ , as represented in Fig. 1.2. This spontaneous distortion removes the degeneracy and reduce the energy of the system to stable energy. This effect is known as Jahn-Teller effect, named after Hermann Jahn

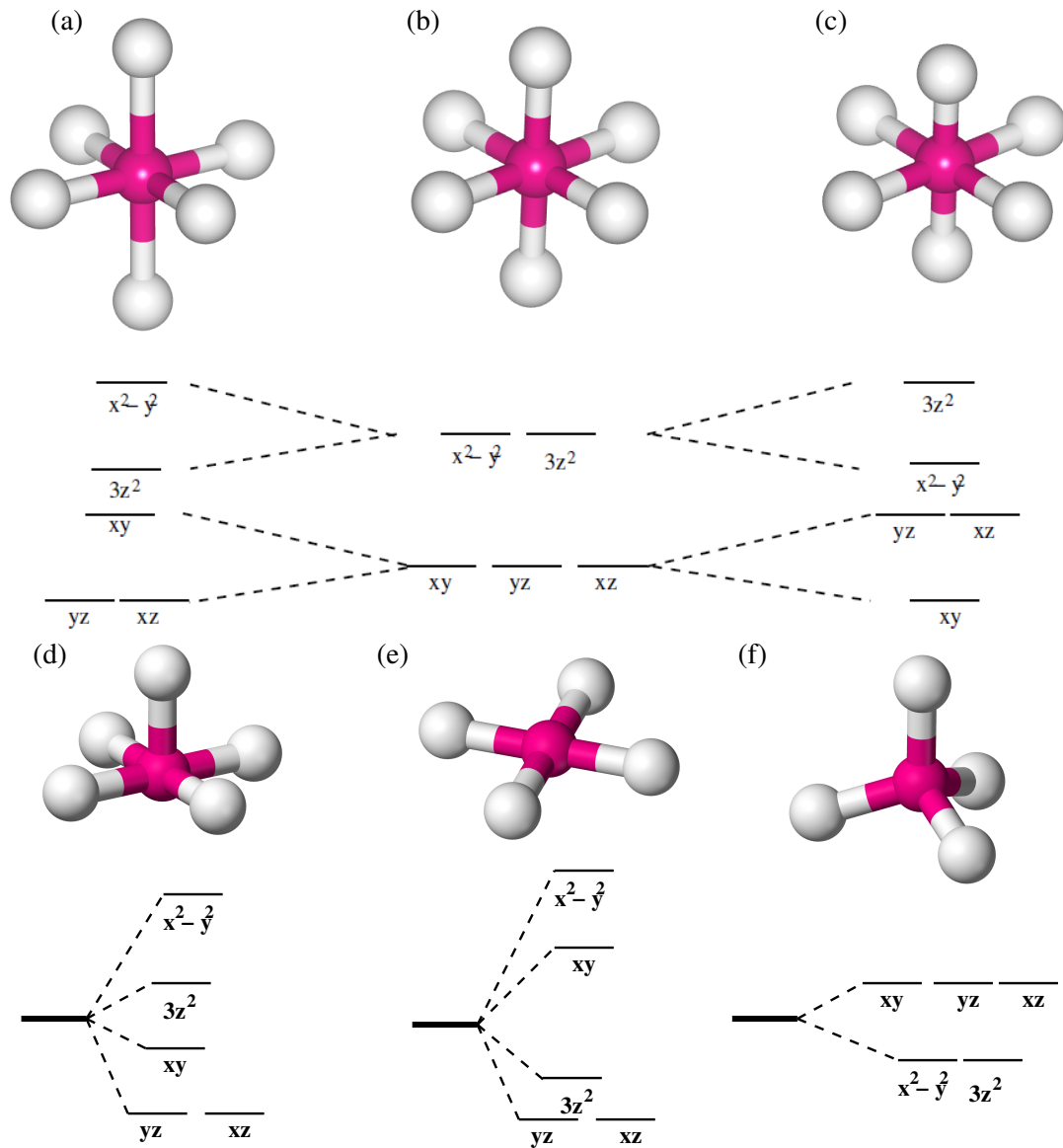


Fig. 1.1: Symmetry and corresponding Crystal field splitting of  $d$  levels for some known regular TM-O polyhedra: (b) Octahedra, (d) Square pyramid, (e) Square planar, (f) Tetrahedra. Panels (a) and (c) show the additional splitting in the  $d$  levels due to tensile and compressive JT distortions in octahedral symmetry respectively.

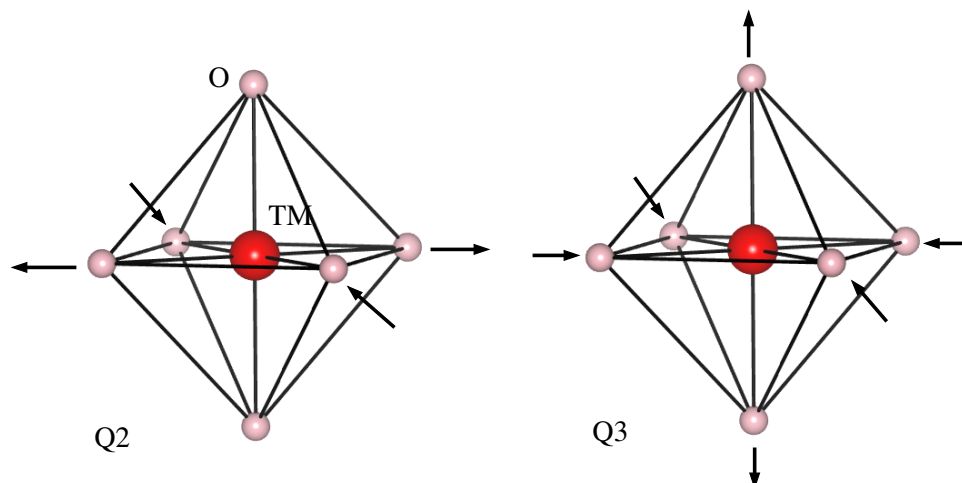


Fig. 1.2: The two Jahn-Teller modes  $Q_2$  and  $Q_3$ .

and Edward Teller, who first give the full explanation of this effect [1]. The energy level diagram for tetragonal Jahn-Teller distortion is shown in Fig. 1.1(a) and (c).

Two extensions of octahedral geometry are square pyramidal and square planar symmetry. The first one can be achieved by the removal of one of the apical oxygen ions along  $z$  axis, the second symmetry is result of removal of both apical oxygens of an octahedra along  $z$  axis. The respective structures and energy level diagrams are shown in Figs. 1.1(d) and (e).

The nature of crystal field splitting is exactly opposite in case of tetrahedral geometry compared to octahedral symmetry. The  $e$  orbitals in this case are energetically more stabilized than  $t_2$ , as shown in Fig. 1.1(f). The splitting pattern can be explained by an analogous line of reasoning as explained for the octahedral symmetry. The crystal field splitting is much less in this case than octahedral symmetry because of the fact that none of the  $d$  orbitals are exactly directed towards the ligand atoms.

In transition metals, the energy scale associated with crystal field splitting is typically much smaller than the bandwidth, however in case of TMO the crystal field splitting is comparable with the band width of  $d$  orbitals and may compete with Hund's exchange energy ( $J_H$ ) and the  $d$  orbital valence bandwidth to create many dramatic effects, such as metal-insulator transition, low spin to high spin transition with application of external perturbations, like temperature, pressure, doping.

In TMOs, as the direct overlap between TM  $d$  orbitals is negligibly small, the  $d$  electrons only can move through hybridization with oxygen  $2p$ -bands. The magnitude of this indirect overlap depends on the following factors:

- The orientation of the  $d$  orbitals with respect to the connecting O  $p$  orbitals, that are responsible for the low energy phenomenon.

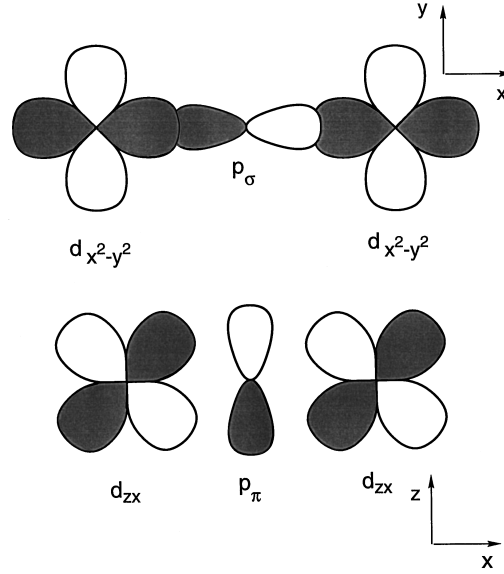


Fig. 1.3: Examples of configurations for transition-metal  $d$  orbitals which are bridged by ligand  $p$  orbitals (Taken from Ref.[2]).

- The relative position of oxygen  $p$ -levels ( $\epsilon_p$ ) and transition metal  $d$ -levels ( $\epsilon_d$ ), *i.e.* the value of charge transfer energy  $\Delta = \epsilon_d - \epsilon_p$ .

For example in case of early  $3d$  transition metal (Ti, V, Cr, Mn) oxides having octahedral surrounding of oxygen ions the Fermi level lies in the manifold of  $t_{2g}$  bands. Therefore the net overlap between two adjacent TM  $d$  orbital takes place through the hybridization between  $t_{2g}$  bands and oxygen  $2p$  bands. As the  $t_{2g}$  orbitals point away from the oxygen  $2p$  orbital it forms weak  $\pi$  hybridization with oxygen (as shown in the bottom panel of Fig. 1.3). Furthermore, low nuclear charge of early TM, makes the relative energy difference of  $d$  and  $p$  bands large. On the other hand in case of late  $3d$  TM (Fe, Co, Ni, Cu) based oxides, for the same octahedral symmetry, as the  $t_{2g}$  levels are completely occupied,  $e_g$  levels play the main role to create interesting physical phenomenon. Because of the favorable geometric orientation of the  $e_g$  orbital with respect to oxygen  $2p$  orbital, as shown in the top panel of Fig. 1.3, the hybridization is stronger. Additionally, the larger charge on the TM nuclei decreases the chemical potential of  $d$  electrons and thus the relative energy difference of  $d$  and  $p$  bands.

The TM- $d$  orbitals in Transition metal oxides, possess a strong intra-atomic Coulomb interaction which support local magnetic moment, as well as a strong hybridization with oxygen which leads to formation of delocalized band. These two effects compete to form a broad range of physical properties. The TMOs are found to show conductivities ranging from good metals (e.g.  $\text{RuO}_2$ ,  $\text{ReO}_3$ ,  $\text{LaNiO}_3$ ) to strong insulators (e.g.  $\text{BaTiO}_3$ ) and often show phenomenon like metal-insulator transition (e.g.  $\text{V}_2\text{O}_3$ ,  $\text{La}_{1-x}\text{Sr}_x\text{VO}_3$ ). They show a wide range of magnetic properties ranging from ferromagnetism (e.g.  $\text{CrO}_2$ ,

La<sub>0.5</sub>Sr<sub>0.5</sub>MnO<sub>3</sub>) to anti ferromagnetism (e.g. NiO, LaCrO<sub>3</sub>) to ferrimagnetism (e.g. La<sub>2</sub>NiMnO<sub>6</sub>) to complicated spiral magnetism (YMnO<sub>3</sub>, YMn<sub>2</sub>O<sub>5</sub>). In addition, temperature, pressure, field or doping induced change in magnetic as well as spin and orbital states has been observed in this class of materials (e.g. La<sub>0.5</sub>Ca<sub>0.5</sub>MnO<sub>3</sub>, LaCoO<sub>3</sub>). Many oxides possess switchable orientation states as in ferroelectric (e.g. BaTiO<sub>3</sub>, KNbO<sub>3</sub>) and ferroelastic (e.g. Gd<sub>2</sub>(MoO<sub>4</sub>)<sub>3</sub>) materials. Some of the oxides exhibit more than one primary ferroic order parameter (ferromagnetism, ferroelectricity, ferroelasticity) simultaneously in a single phase, known as multiferroic material (e.g. BiFeO<sub>3</sub>, TbMn<sub>2</sub>O<sub>5</sub>). They show effect such as Colossal magnetoresistance (CMR) (e.g. Sr<sub>2</sub>FeMoO<sub>6</sub>) and Giant magnetoresistance (GMR) as well as high temperature superconductivity (e.g. Ba<sub>x</sub>La<sub>5-x</sub>Cu<sub>5</sub>O<sub>5(3-y)</sub>, La<sub>2-x</sub>Sr<sub>x</sub>CuO<sub>4</sub>). In the following we list some important classes of TMO discussed in recent literature based on their properties.

⇒ *Ferroics*: Materials possessing two or more orientation states or domains that can be switched from one to another through the application of one or more appropriate forces belong to a general class called ferroics. Three known ferroic orders are : ferromagnetism, ferroelectricity and ferroelasticity. Ferromagnetic materials exhibit a long-range ordering phenomenon at the atomic level which causes the unpaired electron spins to line up parallel to each other. Some examples of ferromagnetic oxides with high transition temperature ( $T_c$ ) are : CrO<sub>2</sub> ( $T_c = 386$  K), Sr<sub>2</sub>FeMoO<sub>6</sub> ( $T_c = 450$  K), Y<sub>3</sub>Fe<sub>5</sub>O<sub>12</sub> ( $T_c = 560$  K) *etc.*

In a ferroelectric, spontaneous electric polarization is altered by the application of an electric field. ferroelectric materials can be used to make capacitors with tunable capacitance. By symmetry considerations they are required to be also piezoelectric and pyroelectric. The combined properties of ferroelectricity, piezoelectricity, and pyroelectricity make ferroelectric capacitors very useful, e.g. for sensor applications. Ferroelectric capacitors are used in medical ultrasound machines, high quality infrared cameras, fire sensors, sonar, vibration sensors and even fuel injectors on diesel engines. PbTiO<sub>3</sub>, BaTiO<sub>3</sub>, KNbO<sub>3</sub> and the Bi<sub>2</sub>A<sub>n-1</sub>B<sub>n</sub>O<sub>3n+3</sub> family of oxides are ferroelectrics, whereas PbZrO<sub>3</sub> and NaNbO<sub>3</sub> are antiferroelectrics.

In a ferroelastic, the direction of spontaneous strain in a domain is switched by the application of mechanical stress. The properties of domains and their walls in a ferroelastic material can be very useful in mineral physics and mineralogy research. Examples of ferroelastic and antiferroelastic TMOs are LaCoO<sub>3</sub> and LaMnO<sub>3</sub>, respectively.

In a multiferroic material more than one above mentioned ferroic order exist in a single phase and may couple to each other, as demonstrated in Fig. 1.4. In recent years most of the research on multiferroics has focused on materials that combine some form of magnetic order (ferromagnetic, antiferromagnetic, non-collinear, ...) with ferroelectricity, so that the term "multiferroics" is now often used synonymous with "magnetic ferroelectrics". Multiferroics have immense potential for technological device applications and at the same time they pose very interesting and rich fundamental physics problems. Examples

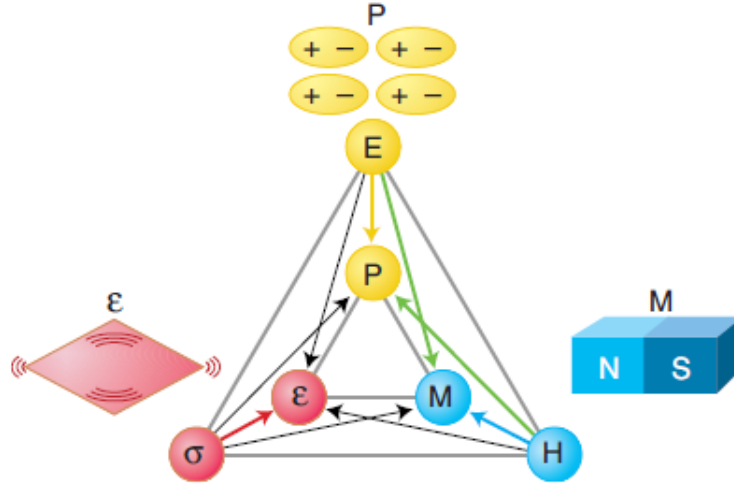


Fig. 1.4: Schematic diagram showing the coexistence of at least two ferroic forms of ordering leads to additional interactions. From Ref:[4].

of such materials are :

Ferroelectric-ferromagnetic:  $\text{Bi}_9\text{Ti}_3\text{Fe}_5\text{O}_{27}$

Ferroelectric-antiferromagnetic:  $\text{YMnO}_3$ ,  $\text{HoMnO}_3$

Antiferroelectric-antiferromagnetic:  $\text{BiFeO}_3$

It is also possible to induce such ferroic order in material by means of many external perturbations, known as secondary ferroics. For example  $\text{SrTiO}_3$ , where ferroelectricity can be induced through application of epitaxial strain.

$\implies$  *Superconductors* : Superconductors, those who show zero electrical resistivity below a certain temperature and form a perfect diamagnet, are known since 1911 after discovery of superconductivity in mercury by Kamerlingh-Onnes, for which the transition temperature was found to be  $\sim 4.2$  K. Subsequently, many metals, alloys and inter-metallic compounds were found, but the highest  $T_c$  was limited to 23.2 K in the  $\text{Nb}_3\text{Ge}$  alloy [5]. The discovery of the high-temperature superconductivity in 1986 in  $\text{Ba}_x\text{La}_{5-x}\text{Cu}_5\text{O}_{5(3-y)}$  [6] with  $T_c \sim 30$  K has opened a new era of research in superconducting materials. This invention leads to discovery of several superconductors which show superconductivity at temperature higher than boiling point of liquid-nitrogen temperature (77K). This was first achieved by Chu and co-workers [7] for nominal composition  $\text{Y}_{1.2}\text{Ba}_{0.8}\text{CuO}_{4-y}$ , where reported  $T_c$  was 92 K. Later on different groups [8]-[10] identified that the composition responsible for the superconductivity at 90 K is  $\text{YBa}_2\text{CuO}_{7-y}$ .

The success of discovery of superconductivity above boiling point of liquid nitrogen provide immense encouragements to search new superconducting materials. Following this path in 1988 Maeda *et.al.* [11] reported 105 K transition temperature in the multiphase sample Bi-Sr-Ca-CuO compound. The highest  $T_c$  of 110 K was obtained in the Bi-Sr-

Ca-CuO compound having composition  $\text{Bi}_2\text{Sr}_2\text{Ca}_2\text{Cu}_3\text{O}_{10}$  [12, 13]. Later many other cuprates were discovered which exceed this value of  $T_c$ , such as Tl-Ba-Ca-CuO (120 K) [14],  $\text{HgBa}_2\text{Ca}_2\text{Cu}_3\text{O}_x$  (133 K) [15],  $\text{HgBa}_2\text{Ca}_2\text{Cu}_2\text{O}_x$  (153 K) [16].

Iron-based superconductors is another bunch of materials that has gained many serious attention recently in the field of High- $T_c$  superconductivity. Interest in their superconducting properties began in 2006 with the discovery of superconductivity in LaFePO at 4 K [18] and gained much greater attention in 2008 after the analogous material LaFeAs(O,F)[17] was found to superconducting up to 43 K under pressure [19]. By replacing the La atoms with other rare-earth elements and modulating the structural parameters, new superconductors were discovered and  $T_c$  was quickly enhanced in  $\text{SmFeAsO}_{1-x}\text{F}_x$ ,  $\text{CeFeAsO}_{1-x}\text{F}_x$ ,  $\text{PrFeAsO}_{1-x}\text{F}_x$ , and  $\text{NdFeAsO}_{1-x}\text{F}_x$ , to above 50 K [20]-[23].

$\implies$  *Materials exhibiting Colossal magnetoresistance (CMR)* : The magnetoresistance (MR) is defined as the change of electrical resistance of a material upon application of magnetic field. It is generally defined by,

$$MR = [\Delta\rho/\rho(O)] = [\rho(H) - \rho(O)]/\rho(O) \quad (1.1)$$

where  $\rho(H)$  and  $\rho(O)$  are the resistivities at a given temperature in the presence and absence of a magnetic field,  $H$ , respectively. It has been observed that the mixed-valent oxide of Manganese, called 'rare-earth Manganites' that undergo a ferromagnetic to paramagnetic transitions upon increasing the temperature, exhibit a high negative MR ( $\sim 80\text{-}90\%$ ) close to the  $T_c$ , at a field of a few Tesla [24]. This phenomenon is called 'Colossal Magnetoresistance' (CMR). These materials have continuously drawn attention from the physicists because of an extremely rich and intriguing phase diagram, and several unusual transport and optical properties. At low temperatures, a variety of phases such as antiferromagnetic insulator (AI), ferromagnetic insulator (FI), ferromagnetic metal (FM), charge and orbitally ordered insulator (COI), *etc* are found. There occurs several metal insulator transitions in this compound, as a function of doping, temperature, and magnetic field. While the CMR in the manganese oxides have been hot topic of research for past several years, a number of systems other than manganese oxide based perovskites have been synthesized which have shown to develop CMR or TMR (tunneling magnetoresistance) effects. These include systems like perovskite-derived Ruddlesden-Popper phases  $\text{Ln}_{2-x}\text{Sr}_{1+x}\text{Mn}_2\text{O}_7$  (where Ln is a trivalent rare-earth), double perovskites  $\text{Sr}_2\text{FeMoO}_6$  and  $\text{Sr}_2\text{FeReO}_6$ , (Tl, In)-manganese pyrochlores, chalcospinel as such  $\text{FeCr}_2\text{S}_4$  and  $\text{Fe}_{0.5}\text{Cu}_{0.5}\text{Cr}_2\text{S}_4$ , layered rare-earth iodide like  $\text{GdI}_2$ .

## 1.2 Theoretical methods to study oxides

In order to explain the above mentioned properties it is necessary to understand the underlying electronic structure first, which is complex in general and difficult to calcu-

late because of the strong electron-electron correlation effect. On theoretical front, this problem has been attacked from two point of views:

1. On one hand, using *ab-initio* calculations which take into account all the structural and chemical aspect correctly, but based on single particle approximation where the electron-electron correlation is treated in a mean field manner, such as Hartree-Fock or Density functional theory (DFT).
2. On the other hand, using models such as Hubbard or Anderson impurity models, which treat the important electron-electron correlation in a improved way, but the parameters of the model Hamiltonian are vastly unknown.

Both approaches have made tremendous progress in the last decades. The DFT calculations within local density approximation (LDA), in which the correlation as well as exchange interaction of the Coulomb interaction is only treated by means of a local density, is unexpectedly successful to explain physical properties of many materials, implying that electronic correlations are rather weak in these materials. But it fails sometimes to describe properties of materials where electronic correlation is strong, such as transition metal oxides. One of the crucial reason for this failure is that the problem of self-interaction is treated in a averaged way in LDA, which is explicitly taken into account in both Self interaction correction (SIC) method [25] and Hartree-Fock method [26]. Both the methods are quite successful to improve the localized description of  $d$  electrons in TMOs. However, a serious problem of these methods is the absence of Coulomb interaction screening effects that leads to strong overestimation of effective Coulomb parameter  $U$  [27, 28]. As a result the energy gap values obtained following these methods are always overestimated. The problem of screening is addressed in a rigorous way in the GW approximation (GWA) [29, 30], in which one electron spectrum is modified by self energy that is defined by Greens function  $G$  and screened energy dependent Coulomb interaction potential  $W$ . This approach is based on many-electron theory with perturbation series preserving first order term in  $W$ . Many real materials including simple metals, semiconductors and insulators are well described within GW calculations. With certain approximations good results were also obtained for Mott insulators such as NiO [31]. However this method has two major shortcomings: (i) it can not describe properly strongly correlated metals where higher order terms in  $W$  need to be included, (ii) it requires significant computer time expenses.

As the electronic and magnetic properties of many strongly correlated systems are primarily controlled by a limited number of states lying near the Fermi level, one can combine the DFT based first principles electronic structure calculations with many body models, formulated in the restricted Hilbert space of states close to the Fermi level. Such a construction is expected to describe the effects that are not captured by LDA. The basic steps of this approach can be summarized by the flow chart given in Fig. 1.5. One

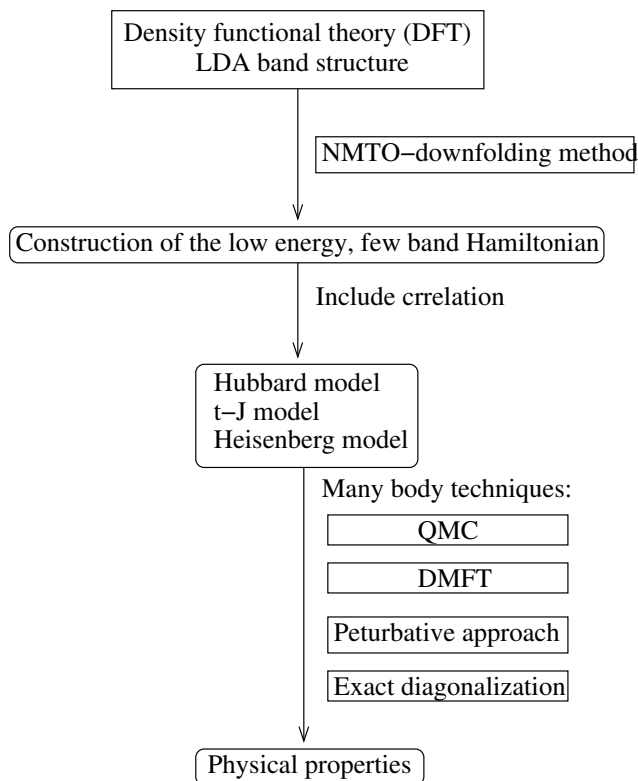


Fig. 1.5: Schematic diagram of the combined approach.

of the crucial step is the construction of one-electron part of the model Hamiltonian in a well localized Wannier basis. To do so, one of the promising way is the  $N^{th}$  order muffin tin orbital (NMTO) based downfolding method [32], which provides maximally localized Wannier functions without explicitly calculating the corresponding Bloch functions. This method derives a low-energy Hamiltonian by an energy selective, downfolding process that integrates out the high energy degrees of freedom. The effective orbitals that define the low energy Hamiltonian is nothing but the Wannier functions and they are maximally localized through the construction. Then the many body Hamiltonian constructed in the basis of these DFT derived Wannier functions can be solved in terms of many body methods like, quantum Monte Carlo method [33], exact diagonalization (ED), dynamical mean field theory (DMFT) [34]. A detail description of theoretical methods involved in such an approach is given in Chapter-2.

### 1.3 Systems under study

♣ *Low dimensional quantum spin systems* : Quantum spin systems are compounds in which spins are small in value ( $S=1/2, 1$ ) and therefore leads to the reduction of the

relevant degrees of freedom to a spin variable  $S_i$ , such as in Heisenberg Hamiltonian,

$$H = \sum_{i,j} J_{ij} \mathbf{S}_i \cdot \mathbf{S}_j \quad (1.2)$$

where  $\mathbf{S}_i$  is the spin operator located at the lattice site  $i$  and  $J_{ij}$  denotes the strength of the exchange interaction. The quantum fluctuations are therefore important and leads to properties that are not obtained in their classical counterparts.

A strong motivation of studying such systems has been driven by the importance for understanding the mechanism of high  $T_c$  superconductivity as well as for their applications in the field of quantum computers. Though these systems are structurally three dimensional, but the anisotropy in the interaction between magnetic ions reduce the effective dimension of the underlying magnetic structure of such systems and provide a simple model to study many phenomena of general interest: magnetic field induced quantum phase transitions and critical points, the frustration (*i.e.* the effect of competing interactions) and the effect of doping impurities. For quantum spin system based on transition metal oxides the factors that reduce the effective dimension are :

- An enlarged distance or missing bridging oxygen between two TM sites.
- A TM-O-TM path with an angle different from  $180^\circ$ .
- Lone pair active cations such as  $\text{As}^{3+}$ ,  $\text{Se}^{4+}$ ,  $\text{Te}^{4+}$ ,  $\text{Pb}^{2+}$  *etc.*

In this thesis we focus on a special class of low dimensional quantum spin systems (QSS) that exhibit a gap in their spin excitation spectra. The magnitude of the gap ( $\Delta$ ) is the difference between a singlet (total spin  $S=0$ ) ground state and a triplet ( $S=1$ ) excited state and proportional to the strongest exchange interaction ( $J$ ) between two magnetic ions (*i.e.*  $\Delta \lesssim J$ ). They have spin-disordered ground states, *i.e.* the spin-spin correlations in the ground state are short -ranged, which can broadly be described as quantum spin liquids (QSL). Formation of such states is favored by quantum fluctuations, which is inversely proportional to the effective dimension of the system and spin at each magnetic site. In experiments, the presence of the gap  $\Delta$  is confirmed through measurement of properties like susceptibility,  $\chi$ , which goes to zero exponentially at low temperature ( $T$ ) as,

$$\chi \sim \exp(-\Delta/k_B T) \quad (1.3)$$

Some well known examples of spin gap (SG) AFMs are given below:

1. *Spin-Peierls compounds*: A spin-Peierls chain is a Heisenberg, AF,  $S=1/2$  chain on an elastic lattice, which at low temperature show a spontaneous dimerization of the lattice allowing a lowering of the magnetic free energy due to the formation of a spin-singlet ground state and opening of a finite energy gap in the magnetic excitation

spectrum. The magnitude of the gap is related to the degree of dimerization and hence to the degree of lattice distortion. The critical temperature below which the spin-Peierls transition takes place, is given by  $T_{SP} \sim |J| \exp(-1/\lambda)$ , where  $J$  is the exchange interaction between adjacent spins and  $\lambda$  is the electron-phonon coupling.

As the presence of interchain interactions typically drives quasi-1D systems towards long range magnetic order, only a selected family of compounds with particularly strong spin-phonon coupling have been found to exhibit a spin-Peierls transition. For example many organic materials: TTF-CuBDT [35]-[36], TTF-CuS<sub>4</sub>C<sub>4</sub>(CF<sub>3</sub>)<sub>4</sub> [37, 38], MEM-(TCNQ)<sub>2</sub> [39] *etc*, where large inter-chain separation and weak van der Waals interaction between adjacent flat organic molecules favor the dominance of magnetoelastic effects over inter-chain ordering. The first transition metal oxide based system which show spin-Peierls transition was CuGeO<sub>3</sub> [40] and later on many TMOs have been found, such as NaV<sub>2</sub>O<sub>5</sub> [41], TiOBr and TiOCl [42] *etc*, which show spin-Peierls or spin-Peierls like (combined with charge or orbital ordering) transition.

2. *Spin ladders*: A spin ladder system consists of two or more spin chains coupled by rungs (Fig. 1.6). The nearest neighbor intra-chain and rung exchange interactions are of strengths of  $J_C$  and  $J_R$  respectively. The ground state of these systems depends on the number of spin chains. If the number of the legs is even, the ground state becomes non-magnetic with a finite energy gap to the excited states [43]; if it is odd, the energy gap collapses [44]. To understand this situation Dagotto *et.al.* [45] assumed a simple limit for a spin 1/2 system in which the exchange coupling  $J_R$  is much stronger than the coupling along the chains. The advantage of this idealization is that the intra-chain coupling in this case can be treated as a perturbation and therefore the exact ground state is the product state of singlets along the rungs, which is given by,

$$|\psi_s\rangle = (|\uparrow\downarrow\rangle - |\downarrow\uparrow\rangle)/\sqrt{2} \quad (1.4)$$

An  $S=1$  excitation may be created by promoting one of the rung singlet to the  $S=1$  triplet,

$$|\psi_t\rangle = [|\uparrow\uparrow\rangle, (|\uparrow\downarrow\rangle - |\downarrow\uparrow\rangle)/\sqrt{2}, |\downarrow\downarrow\rangle] \quad (1.5)$$

The weak coupling along the chains gives rise to a propagating  $S=1$  magnon with a dispersion,

$$w(k) = J_R + J_C \cos k \quad (1.6)$$

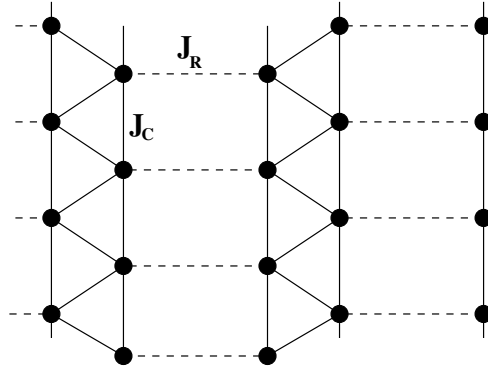


Fig. 1.6: The simplest ladder model consists of two spin chains.  $J_C$  and  $J_R$  represents the exchange coupling along the spin chain and along the rung of the ladder respectively.

The generated spin gap is,

$$\Delta = w(\pi) \simeq J_R - J_C \quad (1.7)$$

The two spin correlations decay exponentially along the chains showing that the ground state is a quantum spin liquid.

The first experimentally realized series of even and odd-leg ladder structures was provided by the family of compounds  $\text{Sr}_{n-1}\text{Cu}_{n+1}\text{O}_{2n}$  consists of planes of weakly-coupled ladders of  $(n+1)/2$  chains [46, 47]. For  $n=3$  and 5, one gets the two-chain and three chain ladder compounds  $\text{SrCu}_2\text{O}_3$  and  $\text{Sr}_2\text{Cu}_3\text{O}_5$  respectively. While in case of  $\text{SrCu}_2\text{O}_3$  the susceptibility shows a exponential decay at low temperature, which is a signature of spin gap, the second compound ( $\text{Sr}_2\text{Cu}_3\text{O}_5$ ) shows a gapless excitation spectrum. Experimental studies confirm this theoretically predicted difference between even and odd-leg  $S=1/2$  Hiesenberg AFM ladders [48].

3. *Haldane gap antiferromagnets:* Haldane first proposed that, in contrast to the the gapless ground state of a chain with half-odd-integer spin (which follow Lieb-Schultz-Mattis theorem [49]), the chains with integer spins have a gap in the excitation spectra, which is called Haldane gap [50]. This leads to important differences in the correlation functions. In the first case they show power law behavior and in the second case exponential behavior. This conjecture has been backed up with considerable experimental and theoretical evidence [51]. Many Haldane gap (HG) AFMs have been discovered so far, which include many TM oxide based materials, such as  $S=1$  compound  $\text{Y}_2\text{BaNiO}_5$  [52] and  $\text{Tl}_2\text{Ru}_2\text{O}_7$  [53].  $\text{Y}_2\text{BaNiO}_5$  [52] is a charge transfer insulator containing  $\text{Ni}^{+2}$  ( $S=1$ ) chain. The ground state of this system is spin disordered and the spin excitation spectrum is separated by a HG of magnitude from the ground state.

To study a low-dimensional QSS it is necessary to gain knowledge of the spin model, which will define the underlying exchange network of the system. Since often the nature of this exchange network is not possible to extract from the crystal structure, a microscopic investigation for this purpose is essential, which is carried for a spin-gapped system  $\text{CuTe}_2\text{O}_5$  in Chapter 3.

♣ *High-temperature Cuprate superconductors:*

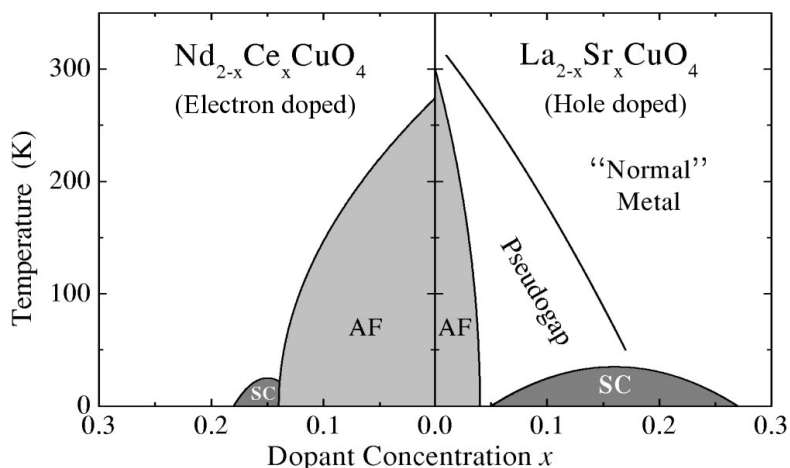


Fig. 1.7: Phase diagram of electron and hole doped superconductors, showing superconductivity (SC), antiferromagnetic (AF), pseudogap, and normal-metal regions. Taken from Ref-[55].

The parent compounds of high-temperature cuprate superconductors with general chemical formula  $\text{R}_2\text{CuO}_4$  (R is a rear-earth element) are known to be antiferromagnetic charge-transfer insulators. The structure is formed by square planar copper-oxygen ( $\text{CuO}_2$ ) layer separated by charge reservoir layers. The superconducting order originates from the two-dimensional charge dynamics of the doped charge carriers in the  $\text{CuO}_2$  planes. The two-dimensional AFM order gets subsided with the concentration of doping and superconducting order sets in as the doping concentration increases beyond a critical value. The carrier introduced into the cuprates is either an electron or a hole. While the hole-doped superconductors have been studied extensively from both theoretical and experimental approaches, the electron-doped cuprates are small in number and less explored. Although the superconducting order parameter of electron-doped is of the same symmetry as in case of hole-doped cuprates, namely  $d_{x^2-y^2}$ , but they differ in many respects. Most remarkable difference has been observed in their phase diagrams with respect to the doping concentration, which exhibit an asymmetric behavior (as shown in Fig. 1.7).

Considering the phase diagram for hole-doped compound  $\text{La}_{2-x}\text{Sr}_x\text{CuO}_4$  and electron-doped compound  $\text{Nd}_{2-x}\text{Ce}_x\text{CuO}_4$  as shown in Fig. 1.7, the noticeable differences are:

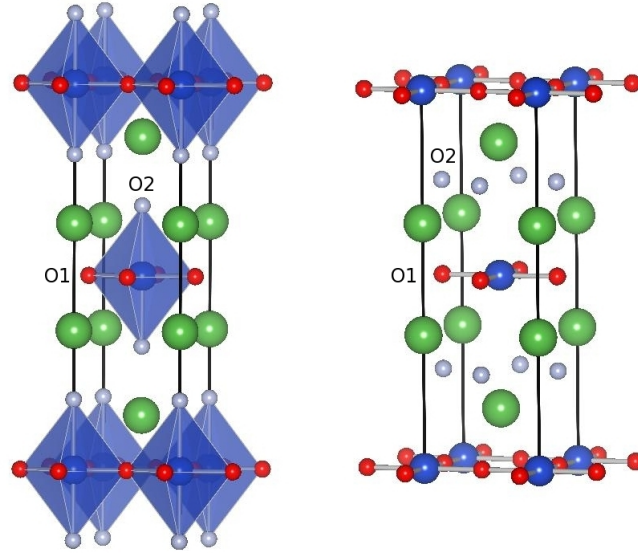


Fig. 1.8: Crystal structure of T (left panel) and T' (right panel) structures. The rare-earth, Cu, and O atoms are represented by the large, mediums and small sized balls, respectively. The in-plane and out-of-plane oxygen atoms are represented by dark and light shades, respectively.

1. While the antiferromagnetic order disappears with a small carrier concentration ( $x \sim 3\%$ ) in the hole doped cuprate  $\text{La}_{2-x}\text{Sr}_x\text{CuO}_4$  (LSCO), it persists up to  $x=0.15$  for the electron doped cuprate  $\text{Nd}_{2-x}\text{Ce}_x\text{CuO}_4$ .
2. The electron doping range for superconductivity is much narrower than hole doped compounds.
3. These two ground states occur in much closer proximity to each other and may even coincide unlike in the hole-doped materials.

The crystal structure of the parent compounds corresponding to hole doped and electron doped compounds are also different. The parent materials for hole doped cuprate crystallize in T structure which has  $\text{CuO}_6$  octahedra, whereas for electron doped they crystallize in T' structure that is characterized by a shift of oxygen (O2) in the apical position to the position directly below or above the oxygen (O1) in the  $\text{CuO}_2$  plane (see Fig. 4.2). The T structure is formed with large rare-earth ions, such as  $\text{La}^{3+}$  ions, while the T' structure is formed with smaller rare-earth ions, such as  $\text{Pr}^{3+}$ ,  $\text{Nd}^{3+}$ ,  $\text{Sm}^{3+}$ ,  $\text{Eu}^{3+}$ , and  $\text{Gd}^{3+}$  [56]. Interestingly,  $\text{La}_2\text{CuO}_4$  lies almost at the borderline of the T-phase stability and serves as the parent compound for hole-doped superconducting cuprates as well as for electron doped superconducting cuprates. Recently it has also shown that while  $\text{La}_2\text{CuO}_4$  in the T structure is strongly insulating, the same in T' structure appears to be conducting with a difference in resistivity of orders of magnitude [57]. While this finding hints toward an interesting implication on mechanism of superconductivity, the experimental situation

is faced with difficulties [58] such as the issue of strain effect (since the fabrication was carried out by thin-film synthesis technique), oxygen content of the sample, *etc.* Therefore for the benefit of understanding the mechanism of high-temperature superconductivity we have carried out investigation of the electronic structure of  $\text{La}_2\text{CuO}_4$  in T and T' phase using first principles techniques, which is devoid of experimental difficulties concerning synthesis. Details of this investigation has been given in Chapter-4.

♣ **Double perovskite system:** The general formula of a Double perovskite oxide compound is  $\text{AA}'\text{BB}'\text{O}_6$ , where A and A' represent large electropositive rare-earth cation, B and B' represent small TM cations. The structure is basically defined by the arrangement of the B cation sublattice and three known forms of such arrangements are: random, rock salt, and layered. Most of the Double perovskites, synthesized so far are of random type. The B and B' cations order crystallographically, if their normal oxidation states, number of valence electrons and ionic radii are considerably different. They mostly order in rock salt manner, which is formed by an alternate arrangement of corner sharing  $\text{BO}_6$  and  $\text{B}'\text{O}_6$  octahedra along all three crystallographic axes (see Fig. 1.9).

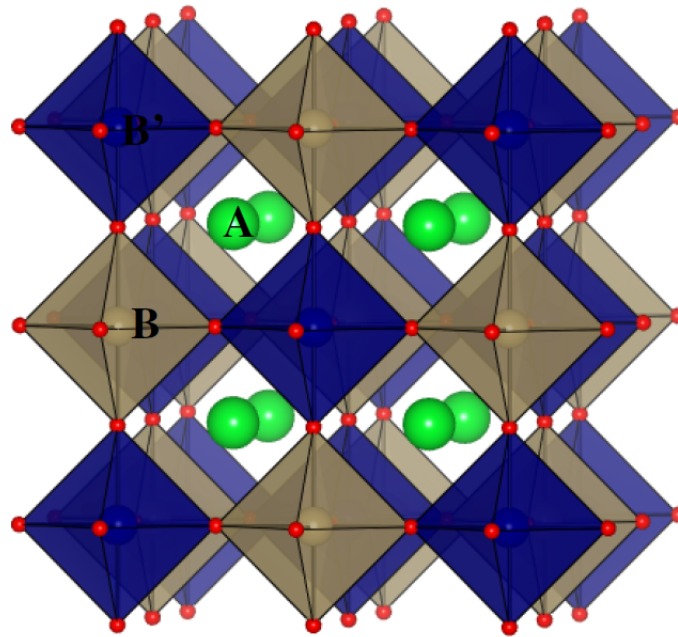


Fig. 1.9: A rock-salt ordered double perovskite structure ( $\text{A}_2\text{BB}'\text{O}_6$ ).

The ideal structure is cubic, but undergoes symmetry lowering due to structural distortions. The source of distortions can be of many origins, such as,

- Due to the mismatch of the relative sizes of the cations, which can be quantified in

terms of tolerance factor  $f$ , defined as

$$f = \frac{\frac{r_A + r_{A'}}{2} + r_O}{\sqrt{2}\left(\frac{r_B + r_{B'}}{2} - r_O\right)} \quad (1.8)$$

where  $r_A$ ,  $r_{A'}$ ,  $r_B$ ,  $r_{B'}$  and  $r_O$  are the ionic radii of the respective A, A', B, B' and oxygen ions respectively. The ideal cubic structure is obtained for  $f=1$  and for  $f < 1$  a  $\text{GdFeO}_3$  kind of distortion takes place originates from the cooperative tilting rotation of  $\text{BO}_6$  octahedra.

- The First order Jahn-Teller distortions, solely of electronic origin, occurs due to the presence of partially filled degenerate  $t_{2g}$  or  $e_g$  states and is particularly strong in case of  $e_g$  symmetry, as discussed earlier.
- Other structural distortions are based on off-centering mechanisms, such as second order Jahn-Teller distortion operates on the  $d^0$  cations at the octahedral B/B' site and drives the ion to go out-of-centre. Another mechanism is lone-pair effect, which operates in perovskite with A site cations with  $ns^2$  valence electronic configuration, for example  $\text{Pb}^{2+}$ ,  $\text{Bi}^{3+}$ .

The choice of B and B' ions, provide the tunability of B-O-B' interaction, giving rise to a variety of magnetic properties such as ferromagnetism, antiferromagnetism, ferrimagnetism, and electronic properties such as metallic, half metallic, and insulating [59, 60], as illustrated in table inserted in Fig 1.3.

Perhaps the most studied member of this series that arose much interest is  $\text{Sr}_2\text{FeMoO}_6$  (SFMO), where magnetic Fe sites and non-magnetic Mo sites are arranged in a rock-salt manner (Fig. 1.9). The unusually high ferromagnetic transition temperature in SFMO was rationalized [61, 62] in terms of a kinetic-energy driven mechanism which produces a negative spin polarization at otherwise nonmagnetic site such as Mo. Very recently, an kinetic-energy driven antiferromagnetic phase has been predicted beyond certain doping concentration for a 2D dimensional and single band model electron doped system [63]. This prediction has been verified by taking into account all the structural and chemical aspects correctly of a real system in Chapter-5. The trivalent La ion doped  $\text{Sr}_2\text{FeMoO}_6$  exactly meets the criteria of such system, where doping with  $x$  amount of  $\text{La}^{3+}$  ion corresponds to doping of  $x$  electron per formula unit in the conduction band.

The discovery of above room temperature ferromagnetic transition temperature in  $\text{Sr}_2\text{FeMoO}_6$  also promotes many intensive research to search new double perovskite materials with higher  $T_c$  through the variation of the metallic/magnetic ions on the B and B' sites as well as by electron doping. Though sufficient attempts have been dedicated to both,  $T_c$  was found to be boosted much more efficiently by moving to different choices of B and B' ions. The microscopic understanding of this increase, however, has not been

material	crystallographic structure lattice parameters [Å]	$f$	magnetic order $T_C$ or $T_N$ [K]	$M_{\text{sat}}(5 \text{ K})$ ( $\mu_B/\text{f.u.}$ )	MR at 50 kOe [%] ( $T < 10 \text{ K}$ )
$\text{Ca}_2\text{CrMoO}_6$	orthorhombic, $a = 5.49$ $b = 5.36$ , $c = 7.70$ (Ref. 36)	0.954(3+/5+)	$T_C = 148$ (Ref. 36)		
$\text{Sr}_2\text{CrMoO}_6$	$Fm\bar{3}m$ , $a = 7.84$ (Ref. 37)	1.009 (3+/5+)	$T_C = 450$ (Ref. 37)	0.5 (Ref. 13)	-5(40 K) (Ref. 37)
$\text{Ba}_2\text{CrMoO}_6$		1.070 (3+/5+)			
$\text{Ba}_3\text{Cr}_2\text{MoO}_9$	$P6_3/mmc$ , $a = 5.69$ , $c = 1.39$ (Ref. 28)		paramagnetic (Ref. 28)		
$\text{Ca}_2\text{CrReO}_6$	$P2_1/n$ , $a = 5.38$ , $b = 5.46$ $c = 7.65$ , $\beta = 90^\circ$ (Ref. 2)	0.952 (3+/5+)	$T_C = 360$ (Ref. 2)	0.82 (Ref. 2)	
$\text{Sr}_2\text{CrReO}_6$	$I4/mmm$ , $a = 5.52$ , $c = 7.82$ (Ref. 2)	1.006 (3+/5+)	$T_C = 635$ (Ref. 2)	0.86 (Ref. 2)	
$\text{Ba}_2\text{CrReO}_6$		1.067 (3+/5+)			
$\text{Ba}_3\text{Cr}_2\text{ReO}_9$	hexagonal, $a = 4.94$ , $c = 13.8$ (Ref. 38)				
$\text{Ca}_2\text{CrWO}_6$	$P2_1/n$ , $a = 5.39$ , $b = 5.45$ $c = 7.66$ , $\beta = 90.1^\circ$	0.945 (3+/5+)	$T_C = 161$	1.34	-9
$\text{Sr}_2\text{CrWO}_6$	$Fm\bar{3}m$ , $a = 7.82$	0.99 (3+/5+)	$T_C = 458$	1.11	-48
$\text{Ba}_2\text{CrWO}_6$	$P\bar{6}2c$ , $a = 5.70$ , $c = 13.99$	1.059 (3+/5+)	$T_C = 145$	0.02	0
$\text{Ba}_3\text{Cr}_2\text{WO}_9$	$P\bar{6}2c$ , $a = 5.69$ , $c = 13.99$ (Ref. 28)		paramagnetic (Ref. 28)		
$\text{Sr}_2\text{MnMoO}_6$	$Fm\bar{3}m$ , $a = 8.01$ (Ref. 13)	0.999 (3+/5+) 0.958 (2+/6+)	$T_N = 12$ (Ref. 39)		
$\text{Sr}_2\text{MnReO}_6$	$Fm\bar{3}m$ , $a = 8.00$ (Ref. 40)	0.997 (3+/5+) 0.949 (2+/6+)	$T_C = 120$ (Ref. 40)		-10 (Ref. 40) (100 K)
$\text{Ba}_2\text{MnReO}_6$	$Fm\bar{3}m$ , $a = 8.18$ (Ref. 40)	1.057 (3+/5+) 1.006 (2+/6+)	$T_C = 120$ (Ref. 40)		+14 (Ref. 40) (80 K)
$\text{Ca}_2\text{MnWO}_6$	$P2_1/n$ , $a = 5.46$ , $b = 5.65$ $c = 7.80$ , $\beta = 90.2^\circ$ (Ref. 41)	0.936 (3+/5+) 0.904 (2+/6+)	$T_C = 45$ $T_N = 16$ (Ref. 41)		
$\text{Sr}_2\text{MnWO}_6$	$P4_2/n$ , $a = 8.012$ , $c = 8.01$ (Ref. 42)	0.990 (3+/5+) 0.956 (2+/6+)	$T_C = 40$ $T_N = 13$ (Ref. 42)		
$\text{Ba}_2\text{MnWO}_6$	$Fm\bar{3}m$ , $a = 8.20$ (Ref. 43)	1.049 (3+/5+) 1.014 (2+/6+)	$T_C = 45$ $T_N = 10$ (Ref. 43)		
$\text{Ca}_2\text{FeMoO}_6$	$P2_1/n$ , $a = 5.41$ , $b = 5.52$ , $c = 7.71$ , $\beta = 90.0^\circ$ (Ref. 31)	0.946 (3+/5+)	$T_C = 365$ (Ref. 31)	3.51 (Ref. 31)	-29 (Ref. 44)
$\text{Sr}_2\text{FeMoO}_6$	$I4/mmm$ , $a = 5.58$ , $c = 7.89$ (Ref. 20)	1.000 (3+/5+)	$T_C = 420$ (Ref. 20)	3.7 (Ref. 45)	-37 (Ref. 5)
$\text{Ba}_2\text{FeMoO}_6$	$Fm\bar{3}m$ , $a = 8.06$ (Ref. 30)	1.060 (3+/5+) 1.030 (2+/6+)	$T_C = 367$ (Ref. 30)	3.53 (Ref. 31)	-25 (Ref. 46) (8 kOe)
$\text{Ca}_2\text{FeReO}_6$	$P2_1/n$ , $a = 5.40$ , $b = 5.52$ $c = 7.68$ , $\beta = 90.02^\circ$ (Ref. 47)	0.943 (3+/5+)	$T_C = 540$ (Ref. 48)	2.24 (Ref. 49)	0 (Ref. 47)
$\text{Sr}_2\text{FeReO}_6$	$Fm\bar{3}m$ , $a = 7.89$ (Ref. 47)	0.997 (3+/5+)	$T_C = 400$ (Ref. 50)	2.7 (Ref. 7)	-26 (Ref. 47)
$\text{Ba}_2\text{FeReO}_6$	$Fm\bar{3}m$ , $a = 8.06$ (Ref. 47)	1.057 (3+/5+)	$T_C = 315$ (Ref. 49)	3.04 (Ref. 49)	-8 (Ref. 47)
$\text{Ba}_3\text{Fe}_2\text{ReO}_9$	hexagonal, $a = 5.03$ , $c = 14.10$ (Ref. 38)				
$\text{Sr}_2\text{FeWO}_6$	$P2_1/n$ , $a = 5.65$ , $b = 5.61$ $c = 7.94$ , $\beta = 89.99^\circ$ (Ref. 51)	0.969 (2+/6+)	$T_N = 40$ (Ref. 52)		
$\text{Ba}_2\text{FeWO}_6$	$I4m$ , $a = 5.75$ , $c = 8.13$ (Ref. 51)	1.028 (2+/6+)	$T_N \approx 20$ (Ref. 51)		

Fig. 1.10: Structure, tolerance factor ( $f$ ), and magnetic properties of various double perovskites. Taken from Ref:[59].

achieved. In Chapter-6 we probe this issue through density functional theory (DFT) based calculations together with exact diagonalization of model Hamiltonian constructed in a first-principles derived Wannier function basis. Chapter-7 contains a study of the electronic and magnetic properties of the ferromagnetic semiconducting double perovskite compound  $\text{La}_2\text{NiMnO}_6$ , which shows a magnetic near room temperature and has been reported to exhibit an interesting magnetic field sensitive dielectric anomaly as a function of temperature [64].

Finally, in Chapter-8 we sum up all the important results made in this thesis.

# References

- [1] H. Jahn and E. Teller, *Phys. Rev.* **49**, 874 (1936).
- [2] M. Imada, A. Fujimori and Y. Tokura, *Reviews of Modern Physics* **70**, 1039 (1998).
- [3] H. K. Onnes. *Akad van Waterschapper (Amsterdam)* **14**, 818 (1911).
- [4] N. A. Spaldin and M. Fiebig, *Science* **309**, 391 (2005).
- [5] J. R. Gavaler. *Appl. Phys. Lett.* **23**, 480 (1973).
- [6] J. G. Bednorz and K. A. Müller, *Zeitschrift für Physik B* **64**, 189 (1986).
- [7] C. W. Chu, P. H. Hor, R. L. Merg, L. Gao and Z. J. Huang. *Science* **235**, 567 (1987).
- [8] R. J. Cava, B. Batlogg, R. B. van Dover, D. W. Murphy, S. Sunshine, T. Siegrist, J. P. Remeika, E. A. Rietman, S. Zahurak, and G. P. Espinosa, *Phys. Rev. Lett.* **58**, 1676 (1987).
- [9] R. M. Hazen, L. W. Finger, R. J. Angel, C. T. Prewitt, N. L. Ross, H. K. Mao, C. G. Hadidiacos, P. H. Hor, R. L. Meng, and C. W. Chu, *Phys. Rev. B* **35**, 7238 (1987).
- [10] C. N. R. Rao, P. Ganguly, A. K. Raychaudhuri, R. A. Mohan Ram, K. Sreedhar, *Nature* **326**, 856 (1987)
- [11] H. Meada, Y. Taraka, M. Fukutomi, T. Asano, *Jpn. J. Appl. Phys.* **27**, L209 (1988).
- [12] R. M. Hazen, C. T. Prewitt, R. J. Angel, N. L. Ross, L. W. Finger, C. G. Hadidiacos, D. R. Veblen, P. J. Heaney, P. H. Hor, R. L. Meng, Y. Y. Sun, Y. Q. Wang, Y. Y. Xue, Z. J. Huang, L. Gao, J. Bechtold, and C. W. Chu, *Phys. Rev. Lett.* **60**, 1174 (1988).
- [13] J. M. Tarascon, W. R. McKinnon, P. Barboux, D. M. Hwang, B. G. Bagley, L. H. Greene, and G. W. Hull, Y. LePage, N. Stoffel and M. Giroud, *Phys. Rev. B* **38**, 8885 (1988)
- [14] Z. Z. Sheng, A. M. Hermann, and A. El Ali, C. Almasan, J. Estrada, and T. Datta, R. J. Matson, *Phys. Rev. Lett.* **60**, 937 (1988).

- [15] A. Schilling, M. Cantoni, J. D. Guo, H. R. Ott, *Nature* **363**, 56 (1993).
- [16] C. W. Chu, L. Gao, F. Chen, Z. J. Huang, R. L. Meng, Y. Y. Xue, *Nature* **365**, 323 (1993).
- [17] Y. Kamihara, T. Watanabe, M. Hirano, and H. Hosono, *Journal of the American Chemical Society* **130**, 3296 (2008).
- [18] Y. Kamihara, H. Hiramatsu, M. Hirano, R. Kawamura, H. Yanagi, T. Kamiya, and H. Hosono. *J. Am. Chem. Soc.* **128** (31), 10012 (2006).
- [19] H. Takahashi, K. Igawa, K. Arii, Y. Kamihara, M. Hirano, H. Hosono. *Nature* **453** (7193), 376 (2008).
- [20] X. H. Chen, T. Wu, G. Wu, R. H. Liu, H. Chen, D. F. Fang, *Nature* **453**, 761 (2008).
- [21] G. F. Chen, Z. Li, D. Wu, G. Li, W. Z. Hu, J. Dong, P. Zheng, J. L. Luo, N. L. Wang, *Phys. Rev. Lett.* **100**, 247002 (2008).
- [22] Z. A. Ren, J. Yang, W. Lu, W. Yi, G. C. Che, X. L. Dong, L. L. Sun, Z. X. Zhao, *Mater. Res. Innovations* **12**, 105 (2008).
- [23] Z. A. Ren, J. Yang, W. Lu, W. Yi, X. L. Shen, Z. C. Li, G. C. Che, X. L. Dong, L. L. Sun, F. Zhou, Z. X. Zhao, *Europhys. Lett.* **82**, 57002 (2008).
- [24] *Colossal Magnetoresistive Oxides*, ed. Y. Tokura (Gordon and Breach, Amsterdam, 2000).
- [25] A. Svane and O. Gunnarsson, *Phys. Rev. Lett.* **65**, 1148 (1990).
- [26] S. Massida, M. Posternak and A. Baldereschi, *Phys. Rev. B* **48**, 5058 (1993).
- [27] O. Gunnarsson, O. K. Andersen, O. Jepsen and J. Zaanen, *Phys. Rev. B* **39**, 1708 (1989).
- [28] V. I. Anisimov and O. Gunnarsson, *Phys. Rev. B* **43**, 7570 (1991).
- [29] L. Hedin, *Phys. Rev.* **139**, A796 (1965).
- [30] L. Hedin and S. Lundqvist, *Solid State Physics* vol **23**, ed H. Ehrenreich, F. Seitz and D. Turnbull (New York: Academic) p:1 (1969).
- [31] F. Aryasetiawan and O. Gunnarsson, *Phys. Rev. Lett.* **74**, 3221 (1995).
- [32] O. K. Andersen and T. Saha-Dasgupta, *Phys. Rev. B* **62**, R16219 (2000).
- [33] K. Louis and C. Gros, *Phys. Rev. B* **70**, 100410(R) (2004).

- 
- [34] A. Georges, G. Kotliar, W. Krauth, and M. J. Rozenberg, *Rev. Mod. Phys.* **68**, 13 (1996).
- [35] J. W. Bray, H. R. Hart, L. V. Interrante, I. S. Jacobs, J. S. Kasper, G. D. Watkins, S. H. Wee, J. C. Bonner, *Phys. Rev. Lett.* **35**, 744 (1975).
- [36] I. S. Jacobs, J. W. Bray, H. R. Hart, L. V. Interrante, J. S. Kasper, G. D. Watkins, D. E. Prober, J. C. Bonner, *Phys. Rev. B* **14**, 3036 (1976).
- [37] J. W. Bray, H. R. Hart Jr., L. V. Interrante, I. S. Jacobs, J. S. Kasper, G. D. Watkins, S. H. Wee and J. C. Bonner, *Phys. Rev. Lett.* **35**, 744 (1975).
- [38] I. S. Jacobs, J. W. Bray, H. R. Hart Jr., L. V. Interrante, J. S. Kasper, G. D. Watkins, D. E. Prober and J. C. Bonner, *Phys. Rev. B* **14**, 3036 (1976).
- [39] S. Huizinga, J. Kommandeur, G.A. Sawatzky, B.T. Thole, K. Kopinga, W.J.M. de Jonge, J. Roos, *Phys. Rev. B* **19**, 4723 (1979).
- [40] M. Hase, I. Terasaki, and K. Uchinokura, *Phys. Rev. Lett.* **70**, 3651 (1993); J. P. Pouget, L. P. Regnault, M. Ain, B. Hennion, J. P. Renard, P. Veillet, G. Dhahlenne, and A. Revcolevschi, *ibid.* **72**, 4037 (1994).
- [41] M. Isobe, Y. Ueda, *J. Phys. Soc. Japan* **65**, 1178 (1996).
- [42] J. P. Clancy, B. D. Gaulin, and F. C. Chou, *Phys. Rev. B* **81**, 024411 (2010), see the references given in this paper.
- [43] T. Barnes, E. Dagotto, J. Riera, and E. S. Swanson. *Phys. Rev. B*, **47**, 3196, (1993).
- [44] S. Gopalan, T. M. Rice, and M. Sigrist. *Phys. Rev. B*, **49**, 8901, (1994).
- [45] E. Dagotto, J. Riera and D. J. Scalapino, *Phys. Rev. B* **50**, 5744 (1992); E. Dagotto and A. Mareo, *Phys. Rev. B* **38**, 5087 (1988).
- [46] T. M. Rice, S. Gopalan and M. Sigrist, *Europhys. Lett.* **23**, 445 (1993).
- [47] Z. Hiroi, M. Azuma, M. takano and Y. Bando, *J. Solid State Chem.* **95**, 230 (1991).
- [48] E. Dagotto, and T. M. Rice, *Science* **271**, 618 (1996).
- [49] E. Lieb, T. D. Schultz and D. C. Mattis, *Ann. Phys.* **16**, 407 (1961).
- [50] F. D. M. Haldane, *Phys. Rev. Lett.* **50**, 1153 (1983); *Phys. Lett. A* **93**, 464 (1983).
- [51] I. Affleck, *J. Phys.: Condens. Matter* **1**, 3047 (1989).
- [52] J. F. Di Tusa, S. -W. Cheong, J. -H. Park, G. Aeppli, C. Broholm, and C. T. Chen, *Phys. Rev. Lett.* **73**, 1857 (1994).

- [53] S. Lee, J.-G. Park, D. T. Adroja, D. Khomskii, S. Streltsov, K. A. McEwen, H. Sakai, K. Yoshimura, V. I. Anisimov, D. Mori, et al. *Nature Materials* **5**, 471 (2006).
- [54] J. Deisenhofer, R. M. Eremina, A. Pimenov, T. Gavrilova, H. Berger, M. Johnsson, P. Lemmens, H.-A. Krug von Nidda, A. Loidl, K.-S. Lee, and M.-H. Whangbo, *Phys. Rev. B* **74**, 174421 (2006).
- [55] A. Damascelli, Z. Hussain and Z. Shen, *Rev. Mod. Phys.* **75**, 473 (2003).
- [56] H. Muller-Buschbaum and W. Wollsglaser, *Z. Anorg. Allg. Chem.* **414**, 76 (1975).
- [57] A. Tsukada, Y. Krockenberger, M. Noda, H. Yamamoto, D. Manske, L. Alff, and M. Naito, *Solid State Comm* **133**, 427 (2005).
- [58] P. G. Radaelli, J. D. Jorgensen, A. J. Schultz, B. A. Hunter, J. L. Wagner, F. C. Chou, and D. C. Johnston, *Phys. Rev. B* **48**, 499 (1993); H. Sato and M. Naito, *Physica C* **274**, 221 (1997).
- [59] J. B. Philipp, P. Majewski, L. Alff, A. Erb, R. Gross, T. Graf, M. S. Brandt, J. Simon, T. Walther, W. Mader, D. Topwal, and D. D. Sarma, *Phys. Rev. B* **68**, 144431 (2003).
- [60] D. D. Sarma, *Curr. Opin. Solid State Mater. Sci.* **5**, 261 (2001).
- [61] D. D. Sarma, P. Mahadevan, T. Saha-Dasgupta, S. Ray, and A. Kumar, *Phys. Rev. Lett.* **85**, 2549 (2000).
- [62] J. Kanamori and K. Terakura, *J. Phys. Soc. Jpn.* **70**, 1433 (2001).
- [63] P. Sanyal and P. Majumdar, *Phys. Rev. B* **80**, 054411 (2009).
- [64] N. S. Rogado, J. Li, A.W. Sleight, and M. A. Subramanian, *Adv. Mater.* **17**, 2225 (2005).

# Chapter 2

## Theoretical methods

### 2.1 Introduction

A real system consists of heavy positively charged particles (nuclei) and lighter negatively charged particles (electrons) and the basic interaction among them is electrostatic or Coulombic. Then the problem that we have to deal with is many body problem that can be described by the many body Hamiltonian:

$$H = -\sum \frac{\hbar^2}{2M_I} \nabla_I^2 - \sum \frac{\hbar^2}{2m_i} \nabla_i^2 + \frac{e^2}{2} \sum_{I,J} \sum_{J \neq I} \frac{Z_I Z_J}{|\mathbf{R}_I - \mathbf{R}_J|} + \frac{e^2}{2} \sum_{i,j} \sum_{j \neq i} \frac{1}{|\mathbf{r}_I - \mathbf{r}_J|} - e^2 \sum_I \sum_i \frac{Z_I}{|\mathbf{R}_I - \mathbf{r}_i|} \quad (2.1)$$

where,  $\mathbf{R}_I = \{\mathbf{R}_I, I = 1, \dots, P\}$  is the coordinate set of  $P$  ions and  $\mathbf{r}_i = \{\mathbf{r}_i, i = 1, \dots, N\}$  is that of electrons.  $Z_I$  and  $M_I$  are charge and mass of ion cores and  $m$  is electron mass. The first and second term represent the kinetic energy of ion ( $T_N(\mathbf{R})$ ) and electron ( $T_e(\mathbf{r})$ ), respectively and last three terms represent coulomb interaction between ions ( $V_{II}(\mathbf{R})$ ), electrons ( $V_{ee}(\mathbf{r})$ ), ions and electrons ( $V_{ext}(\mathbf{R}, \mathbf{r})$ ), respectively. To find out the corresponding many body wave function  $\psi_n(\mathbf{R}, \mathbf{r})$  we need to solve the Schrödinger's equation:

$$H\psi_n(\mathbf{R}, \mathbf{r}) = \varepsilon_n \psi_n(\mathbf{R}, \mathbf{r}) \quad (2.2)$$

The two-body nature of coulomb interaction prevents this equation to be solved exactly even for very small systems. Therefor some approximations need to be carried out. In 1927, Born and Oppenheimer [1] simplified the problem in the first step by decoupling the motion of ions and electrons. They argued that, electrons being much lighter than ions, moves much faster in solid than that of ions. Therefore ions can be considered as fixed with respect to electron motion. Thus for a fixed ionic configuration the Hamiltonian for a system of  $N$  interacting electrons takes the form

$$H_{el} = T_e(\mathbf{r}) + V_{II}(\mathbf{R}_a) + V_{ext}(\mathbf{r}; \mathbf{R}_a) + V_{ee}(\mathbf{r}) \quad (2.3)$$

where the constant ion-ion interaction term  $V_{II}(\mathbf{R}_a)$  is called Madelung energy and is calculated classically. Though the quantum many body problem obtained after this approximation is much simpler than the original one, but still far too difficult to solve.

Several approaches exist to transform this many body problem to an effective single particle problem, in which the system of interacting electrons are mapped into a system of non-interacting quantum mechanical particles that approximates the behavior of original system. Two distinct approaches have been put forward in this direction: wave function based approaches [2, 3, 4] like Hartree, Hartree-Fock, configuration-interaction *etc*, and density functional theory [5, 6, 7]. The theoretical study carried out in this thesis is primarily Density functional theory (DFT) based, a description of which is given in §: 2.2.

Following the combined approach that has been described in the introductory chapter we used the  $N^{th}$  order muffin tin orbital (NMTO) method to calculate the single-particle parts of correlated Hamiltonian, such as hopping integrals, on site energies, which is discussed in §: 2.3. Finally, the techniques to solve the correlated Hamiltonian, like Stochastic Series expansion (SSE) of quantum Monte Carlo method, Dynamical Mean Field theory (DMFT) and exact diagonalization (ED) are described in §: 2.4.

## 2.2 Density Functional theory (DFT)

Density functional theory (DFT) is one of the most successful approach to theoretical prediction of structures and properties of atoms, molecules and solids with an eventual aim of designing of new materials. Within DFT [5, 6] all aspects of the electronic structure of a system of  $N$  interacting electrons in an external coulomb potential  $V_{ext}$ , created by the fixed ionic configuration are completely determined by the electronic charge density  $\rho(\mathbf{r})$ , which is a function of position of a single electron. This is a drastic simplification, since the many-body wave functions  $\Psi(\mathbf{r})$ , which is function of  $3N$  variable, need not to be explicitly specified. Although the root of density functional theory is in the Thomas-Fermi model [8, 9], modern DFT rests on two fundamental mathematical theorems proved by Kohn and Hohenberg [5] and the derivation of a set of equations by Kohn and Sham [6].

### Hohenberg-Kohn (HK) theorem

The first theorem of HK states that, there is an one to one correspondence between external potential  $V_{ext}$  and the ground state electron density  $\rho(\mathbf{r})$ , *i.e.* the external potential is uniquely determined by the electron density of a system. An immediate consequence is that the ground state expectation value of any observable  $\hat{O}$  is a unique functional of the exact ground state electron density :

$$\langle \Psi | \hat{O} | \Psi \rangle = O[\rho] \tag{2.4}$$

Considering  $\hat{O}$  to be the Hamiltonian  $\hat{H}$ ,

$$\hat{H} = \hat{T} + \hat{V} + \hat{V}_{ext} \tag{2.5}$$

where  $\hat{T}$  is the kinetic energy term and  $\hat{V}$  represents the electron electron Coulomb interaction, the ground state total energy takes the form,

$$E[\rho(\mathbf{r})] = F[\rho(\mathbf{r})] + \int V_{ext}(\mathbf{r})\rho(\mathbf{r})d\mathbf{r} \quad (2.6)$$

The first term,

$$F[\rho(\mathbf{r})] = \langle \Psi | \hat{T} + \hat{V} | \Psi \rangle \quad (2.7)$$

is the universal density functional for any many electron system.

The second theorem of HK defines an important property of the energy functional : The exact ground state energy ( $E_0$ ) is given by the global minimum of  $E[\rho(\mathbf{r})]$ , and the ground state density is the density that minimizes  $E[\rho(\mathbf{r})]$ . That is, for a trial density  $\tilde{\rho}(\mathbf{r})$  such that  $\tilde{\rho}(\mathbf{r}) \geq 0$  and  $\int \tilde{\rho}(\mathbf{r})d\mathbf{r} = N$ ,

$$E_0 \leq E[\tilde{\rho}(\mathbf{r})] \quad (2.8)$$

## Kohn-Sham equations

In the energy functional the main unknown part is the universal functional  $F[\rho]$ , which consists of all many body interactions. Kohn and Sham introduced a further development on the universal functional  $F[\rho]$  by mapping the  $\rho(\mathbf{r})$  of "interacting  $N$  electrons" into that of a system of non-interacting electrons. For this system of non-interacting electrons the universal functional  $F[\rho]$  can be written as,

$$F[\rho(r)] = T_0[\rho(\mathbf{r})] + \frac{e^2}{2} \int \frac{\rho(\mathbf{r})\rho(\mathbf{r}')}{|\mathbf{r} - \mathbf{r}'|} d\mathbf{r}d\mathbf{r}' + E_{xc}[\rho(\mathbf{r})] \quad (2.9)$$

where  $T_0[\rho(\mathbf{r})]$  is the functional for the kinetic energy (KE) of a the non-interacting electrons and the second term is the classical electrostatic contribution (the Hartree term). All many body effects have been now accumulated in the last term  $E_{xc}[\rho(\mathbf{r})]$ , known as the exchange correlation energy.

The energy functional takes form:

$$E_{KS}[\rho] = \int V_{ext}(r)\rho(r)dr + T_0[\rho(\mathbf{r})] + \frac{e^2}{2} \int \frac{\rho(\mathbf{r})\rho(\mathbf{r}')}{|\mathbf{r} - \mathbf{r}'|} d\mathbf{r}d\mathbf{r}' + E_{xc}[\rho(\mathbf{r})] \quad (2.10)$$

The corresponding KS Hamiltonian can be written as:

$$H_{KS} = \left( \frac{-\hbar^2}{2m} \right) \nabla^2 + V_{eff} \quad (2.11)$$

where

$$\begin{aligned} V_{eff}(\mathbf{r}) &= V_{ext}(\mathbf{r}) + \int \frac{\rho(\mathbf{r}')}{|\mathbf{r} - \mathbf{r}'|} d\mathbf{r}' + \frac{\delta E_{xc}[\rho]}{\delta \rho(\mathbf{r})} \\ &= V_{ext} + V_{Hartree} + V_{xc} \end{aligned} \quad (2.12)$$

The exact ground state density  $\rho(\mathbf{r})$  of  $N$  electron system is:

$$\rho(\mathbf{r}) = \sum_{i=1}^N |\psi_i(\mathbf{r})|^2 \quad (2.13)$$

where the single-particle wave functions  $\psi_i(\mathbf{r})$  are the  $N$  lowest-energy solutions of the Kohn- Sham equation,

$$\hat{H}_{KS}\psi_i(\mathbf{r}) = \epsilon_i\psi_i(\mathbf{r}) \quad (2.14)$$

Since the Hartree part and the exchange-correlation term depend on the density  $\rho(\mathbf{r})$ , which in turn depends on the solution of KS equations ( $\psi_i(\mathbf{r})$ ), the Kohn-Sham equations need to be solved iteratively until the solution is self consistent. The procedure is the following: some starting density  $\rho_0$  is guessed, and a initial KS Hamiltonian  $H_{KS1}$  is constructed with it. The eigenvalue problem is solved, which results in a set of  $\psi_1$  from which a new density  $\rho_1$  can be derived. If the new density differs from the old one by an amount more than a given critical value, the density for the next step is evaluated through the mixing of these two densities depending on the choice of mixing scheme. It is used to construct the Hamiltonian for next iteration, which will yield a  $\rho_2$ , *etc.* The procedure will continue until the density converge to a final density  $\rho_f$  which generates a  $H_{KSf}$  which yields as solution again  $\rho_f$ . This final density is then consistent with the Hamiltonian (see the flow chart given in Fig. 2.1).

## Extension to spin polarized systems

For spin polarized systems the electron density is composed of two independent spin densities,

$$\rho = \rho_{\uparrow} + \rho_{\downarrow} \quad (2.15)$$

As the exchange-correlation ( $xc$ ) potential is different for each spin channel, it transforms to the form,

$$V_{xc,s}[\rho_{\uparrow}, \rho_{\downarrow}] = \frac{\delta E_{xc}[\rho_{\uparrow}, \rho_{\downarrow}]}{\delta \rho_s(\mathbf{r})} \quad (2.16)$$

where  $s$  denotes spin degrees of freedom ( $\uparrow$  or  $\downarrow$ ). The spin polarized KS equations are:

$$\left[ \left( \frac{-\hbar^2}{2m} \right) \nabla^2 + V_{eff,s} \right] \psi_{i,s}(\mathbf{r}) = \epsilon_{i,s} \psi_{i,s}(\mathbf{r}) \quad (2.17)$$

Thus there are two sets of single electron wave functions, one for spin up electrons and one for spin down electrons.

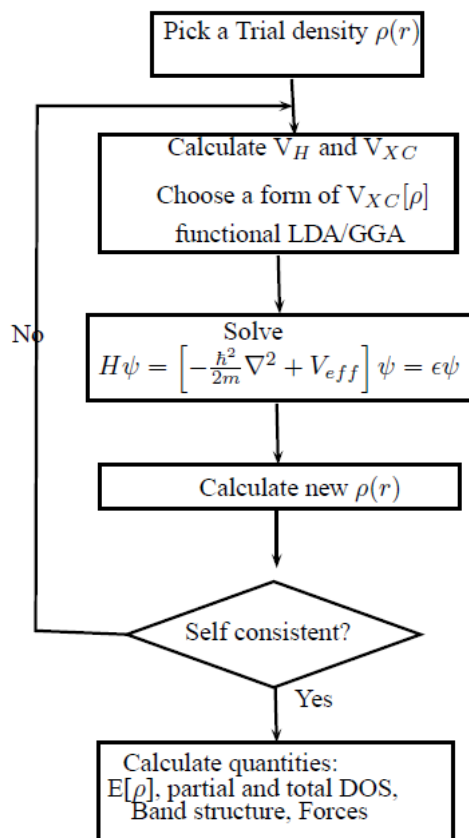


Fig. 2.1: DFT self consistent cycle.

### 2.2.1 Exchange correlation functional

As  $xc$  energy  $E_{xc}$ , which includes all many body interactions, has a very complicated expression which is not known explicitly, approximations are needed to convert the  $xc$  energy functional to some known form. Up to now, many simplified forms of this functional have been proposed, where most of them are based on local or quasi local approximation, in which the  $xc$  energy at position  $\mathbf{r}$  depends on the local charge density or the local charge density and its first derivative.

#### Local density approximation

The simplest of these descriptions is called the Local Density Approximation (LDA), where the  $xc$  energy of a real system is expressed by the electronic charge density corresponds to that of a homogeneous electron gas. Therefore the  $xc$  energy is given by,

$$E_{xc}^{LDA} = \int \varepsilon_{xc}^{LDA}(\rho(\mathbf{r}))\rho(\mathbf{r})d\mathbf{r} \quad (2.18)$$

where  $\varepsilon_{xc}[\rho]$  is the exchange-correlation energy per electron in a homogeneous gas with electron density  $\rho(\mathbf{r})$ . In practice, the  $xc$  energy density is always treated as a sum of

individual exchange and correlation contributions,

$$\varepsilon_{xc}^{LDA}(\rho) = \varepsilon_x^{LDA}(\rho) + \varepsilon_c^{LDA}(\rho) \quad (2.19)$$

In a uniform electron gas, the exchange part  $\varepsilon_x^{LDA}[\rho]$  is given by the Dirac's expression,

$$\varepsilon_x^{LDA}(\rho) = -\frac{0.458}{r_s} \quad (2.20)$$

here  $r_s$  is the mean interelectronic distance and given by,

$$\frac{4\pi}{3}r_s^3 = \rho^{-1} \quad (2.21)$$

The correlation part is more complex and E.P.Wigner [10] first estimated it by,

$$\varepsilon_c^{LDA} \approx \frac{0.44}{r_s + 7.8} \quad (2.22)$$

Later, Ceperlay and Alder [11] gave more accurate estimate based on the quantum Monte Carlo simulations. This correlation functional is exact within numerical accuracy and has been parametrized by Perdew and Zunger [12], Vosko- Wilk -Nusair [13], John P. Perdew and Yue Wang [14] *etc.*

For spin polarized system the  $xc$  energy density depends not only on the electron density  $\rho$ , but also depends on the magnetization density  $\zeta = (\rho^\uparrow - \rho^\downarrow)/(\rho^\uparrow + \rho^\downarrow)$ . It is in general evaluated by the interpolation between the fully-polarized ( $\varepsilon_{xc}^P$ ) and unpolarized ( $\varepsilon_{xc}^U$ )  $xc$  energy densities using the interpolation function that depends on  $\zeta$ . Excellent approximate expressions for the interpolation function  $f(\zeta)$  are available, such as proposed by Barth and Hedin [15], by Vosko *et.al.* [13].

By construction, LDA is expected to work well with systems in which the electronic charge density is slowly varying, but surprisingly it gives quite good results also in case of non-homogeneous systems (see review by R.O. Jones and O. Gunnarsson [16]). The reasons for such a surprising work is suggested to be related with facts that:

- Only the spherical average of the  $xc$  hole influences the energy, *i.e.*  $xc$  energy is given by,

$$E_{xc}[\rho] = -\frac{1}{2} \int \rho(\mathbf{r}) \left( \frac{1}{R(\mathbf{r})} \right) d\mathbf{r} \quad (2.23)$$

where,

$$\frac{1}{R(\mathbf{r})} = \int \frac{\tilde{\rho}_{xc}(r, r')}{|r - r'|} dr' \quad (2.24)$$

and  $\tilde{\rho}_{xc}$  is the  $xc$  hole, which is expressed in terms of pair correlation function  $\tilde{g}(r, r')$  as,

$$\tilde{\rho}_{xc}(r, r') = \rho(r')[\tilde{g}(r, r') - 1] \quad (2.25)$$

- LDA fulfills the sum rule that  $xc$  hole contain exactly one electron, *i.e.*

$$\int \tilde{\rho}_{xc}^{LDA}(\mathbf{r}, \mathbf{r}') d\mathbf{r}' = \int \rho(\mathbf{r}) \tilde{g}[|\mathbf{r} - \mathbf{r}'|, \rho(\mathbf{r})] d\mathbf{r}' = -1 \quad (2.26)$$

LDA is quite successful to explain phenomenon that involves energies related to the motion of ions, *i.e.* of the order of 1 eV and fails to reproduce phenomenon that involves very small energy scales, for example the phenomenon of superconductivity involves energy scales of a few degrees kelvin.

### Generalized gradient approximation

One natural way to take into account the inhomogeneities in the electron density to some extent is to make  $xc$  energy depend not only on the local value of the density, but also on the gradient of density. Within generalized gradient approximation, the  $xc$  energy functional can be expressed as,

$$E_{xc}^{GGA}[\rho] = \int \varepsilon_{xc}(\rho(\mathbf{r}), |\nabla \rho(\mathbf{r})|) \rho(\mathbf{r}) d\mathbf{r} = \int \rho(\mathbf{r}) \varepsilon_{xc}[\rho(\mathbf{r})] F_{xc}[\rho(\mathbf{r}), \nabla \rho(\mathbf{r})] d\mathbf{r} \quad (2.27)$$

where the function  $F_{xc}$  is an enhancement factor that modifies the LDA expression.

One of the widely used form of  $F_{xc}$  was given by Perdew-Wang (PW91) [17] in 1991. Later on, a particularly simple form was introduced by Perdew, Bruke and Ernzerhof (PBE) [18] by modifying PW91, which simplifies PW91 significantly though retaining the important features of PW91.

Although GGA performs better than LDA to produce many physical properties, such as the structural, magnetic properties of real materials, the systematic improvement is not obvious. For example, it overestimates the electric polarization for a polar system [19]. In spite of the improved treatment of the inhomogeneities of electron density, it is not sufficient to describe the properties of the systems where local electron electron correlation is strong and plays the significant role to determine many properties, such as in case of transition metal oxides. Therefore to take the local Coulomb interaction into account, it is necessary to go beyond LDA/GGA.

### LDA+U

”LDA+U” involves LSDA or GGA type calculations coupled with an additional orbital dependent interaction in a Hartree-Fock like manner. The additional interaction is usually considered only for highly localized orbitals, such as  $d$  and  $f$  orbitals. The generalized LDA+U functional is defined as follows:

$$E^{LDA+U}[\rho^\sigma(\mathbf{r}), \{n^\sigma\}] = E^{LSDA/GGA}[\rho(\mathbf{r})] + E^U[\{n_m^{I,\sigma}\}] - E_{dc}[n^{I,\sigma}] \quad (2.28)$$

where the  $n_m^{I,\sigma}$  are orbital occupancies for atom  $I$  experiencing the on-site Hubbard interactions,  $m$  is the magnetic quantum number,  $\sigma$  is the spin index and  $n^{I,\sigma} = \sum_m n_m^{I,\sigma}$ . The last term is included to correct the double counting. For the Hartree-Fock like term  $E^U[\{n_m^{I,\sigma}\}]$  Liechtenstein *et.al.* [20] has formulated a rotationally invariant form,

$$E^U[\{n_m^{I,\sigma}\}] = \frac{1}{2} \sum_{\{m\},\sigma} \langle m_1 m_3 | \frac{1}{|\mathbf{r} - \mathbf{r}'|} | m_2 m_4 \rangle n_{m_1 m_2}^\sigma n_{m_3 m_4}^{-\sigma} - \left( \langle m_1 m_3 | \frac{1}{|\mathbf{r} - \mathbf{r}'|} | m_2 m_4 \rangle - \langle m_1 m_3 | \frac{1}{|\mathbf{r} - \mathbf{r}'|} | m_4 m_2 \rangle \right) n_{m_1 m_2}^\sigma n_{m_3 m_4}^\sigma \quad (2.29)$$

The matrix elements can be expressed in terms of complex spherical harmonics and effective Slater integrals  $F^k$  [21] as,

$$\langle m_1 m_3 | \frac{1}{|\mathbf{r} - \mathbf{r}'|} | m_2 m_4 \rangle = \sum_k a_k(m_1, m_2, m_3, m_4) F^k \quad (2.30)$$

where  $0 \leq k \leq 2l$  and

$$a_k(m_1, m_2, m_3, m_4) = \frac{4\pi}{2k+1} \sum_{q=-k}^k \langle l m_1 | Y_{kq} | l m_2 \rangle \langle l m_3 | Y_{kq}^\dagger | l m_4 \rangle \quad (2.31)$$

For  $d$  electrons one needs  $F^0$ ,  $F^2$  and  $F^4$  and these can be specified by two adjustable parameters in term of effective on site Coulomb and Stoner parameters  $U$  and  $J$  through the relations,

$$U = F^0 \quad (2.32)$$

$$J = \frac{F^2 + F^4}{14} \quad (2.33)$$

For  $f$  electrons the expression for  $J$  is ,

$$J = \frac{286F^2 + 195F^4 + 250F^6}{6435} \quad (2.34)$$

Within this approach the double counting correction term is expressed as,

$$E_{dc}[n^{I,\sigma}] = \frac{1}{2} U N(N-1) - \frac{1}{2} J [N^\uparrow(N^\uparrow - 1) + N^\downarrow(N^\downarrow - 1)] \quad (2.35)$$

where  $N^\sigma = \text{Tr}(n_{m_1 m_2}^\sigma)$  and  $N = N^\uparrow + N^\downarrow$ .

Later, Dudarev *et.al.* [22] presented a simplified approach, in which the total energy functional is expressed as,

$$E_{LSDA+U} = E_{LSDA} + \frac{U-J}{2} \sum_\sigma \left[ \left( \sum_{m_1} n_{m_1}^\sigma \right) - \left( \sum_{m_1 m_2} n_{m_1 m_2}^\sigma n_{m_2 m_1}^\sigma \right) \right] \quad (2.36)$$

In this approach only the difference ( $U-J$ ) is used.

The applicability of LSDA+U approach depends on the choice of values of  $U$  and  $J$ . Though there exists constraint DFT approach to calculate the  $U$  and  $J$  values from an *ab initio* way, it is often found to over estimate the values. The most common way to determine the parameter  $U$  therefore lies in seeking a good agreement of calculated properties with the experimental results.

### 2.2.2 Different DFT based first principles methods

To solve the single-particle Kohn-Sham Eqn.( 2.14) and to obtain the eigenvalues (band structure) and eigenfunctions, one has to choose an appropriate basis set  $\{\phi_\alpha(\mathbf{r})\}$  to expand the KS wave-functions  $\Psi_i(\mathbf{r})$ ,

$$\Psi_i(\mathbf{r}) = \sum_{\alpha} C_{\alpha}^i \phi_{\alpha}(\mathbf{r}) \quad (2.37)$$

The choice of the basis set  $\{\phi_\alpha(\mathbf{r})\}$  depends on the specification of a given problem, such as the crystal symmetry, the nature of the involved elements of the periodic table. Several basis methods have been developed in last four decades and are widely used for band structure calculations of solids. Depending on the choice of basis functions these methods can be broadly classified into two categories, fixed basis set method and partial basis set method.

#### (a) Methods using fixed basis sets

This method is based on energy independent basis sets or fixed basis sets, like tight binding method using linear combination of atomic orbitals (LCAO) type basis [23], orthogonalized plane wave (OPW) method within a pseudopotential scheme using plane waves orthogonalized to core states as the basis set [24, 25], which transform the KS equations ( 2.14) to the eigenvalue problem,

$$\sum_{\beta} (\tilde{H}_{\alpha\beta} - \varepsilon_i \tilde{O}_{\alpha\beta}) \tilde{C}_{\beta}^i = 0, \quad j = 1, 2, \dots, N \quad (2.38)$$

where,

$$\tilde{H}_{\alpha\beta} = \int d^3r \phi_{\alpha}^*(\mathbf{r}) \hat{H}(\mathbf{r}) \phi_{\beta} \quad (2.39)$$

$$\tilde{O}_{\alpha\beta} = \int d^3r \phi_{\alpha}^*(\mathbf{r}) \phi_{\beta} \quad (2.40)$$

#### Plane wave basis pseudopotential method

Many first principles methods based on DFT adopt plane waves as the basis functions to solve KS equation. The reasons for high demand are the following:

- The basis set is independent of atom position and species.
- Forces acting on atoms are equal to Hellman-Feynman forces, no basis set correction to the forces is needed.
- It takes advantages for efficient algorithms, like the Fast Fourier Transformation (FFT).

One major problem, though is that: a large number of plane waves is required to describe the wave functions close to nucleus, defined as core region. This is due to two reasons: first, the electrons in this region are tightly bound to the nucleus and second, the wave functions in this region are rapidly oscillating due to the orthogonality requirements with the valence electron wave functions. One way to circumvent this problem is to replace the strong Coulomb potential of the nucleus and the effects of the tightly bound core electrons by an effective ionic potential acting on the valence electrons, known as pseudopotential.

The general procedure for obtaining a pseudopotential begins by solving the all electron (AE) radial Schrödinger equation for a chosen atomic configuration, *i.e.* for a given distribution of electrons in the atomic energy levels. This is called the reference configuration:

$$\left[ \frac{1}{2} \frac{d^2}{dr^2} + \frac{l(l+1)}{2r^2} + V_{eff}[\rho] \right] r\phi_{AE}^{nl}(\mathbf{r}) = \epsilon_{nl} r\phi_{AE}^{nl}(\mathbf{r}) \quad (2.41)$$

One can generate a pseudo wavefunction  $\phi_{ps}^{nl}$  corresponding to  $\phi_{AE}^{nl}$ , so that it becomes node-less inside the core region of radius  $r_c$  and matches exactly with the AE wavefunction  $\phi_{AE}^{nl}$  for  $r \geq r_c$ . After constructing the pseudo wavefunction the pseudopotential can be generated by inverting the Schrödinger equation,

$$V_{ps}^l(\mathbf{r}) = \epsilon_l - \frac{l(l+1)}{2r^2} + \frac{1}{2r\phi_{ps}^l} \frac{d^2}{dr^2} [r\phi_{ps}^l] \quad (2.42)$$

The pseudopotential is finally obtained by subtracting the Hartree and exchange-correlation potential calculated only for the valence electrons:

$$V_{ps}^{(ion)l} = V_{ps}^l - V_{Hartree}[\rho_{ps}] - V_{xc}[\rho_{ps}] \quad (2.43)$$

There are two principle criteria to judge the goodness of a pseudopotential: (i) Transferability: a pseudopotential is transferable if it works reasonably well in different environments. (ii) Softness: a pseudopotential is soft if it requires less number of plane waves.

To make these two criteria to be fulfilled several methods have been developed. There are two kinds of pseudopotential that are widely used: norm conserving pseudopotential and ultrasoft pseudopotential.

- ♣ **Norm conserving pseudopotential:** Norm conserving pseudopotentials (NCP) [26] are constructed with an extra constraint that the pseudo-wave function must ensure that the charge within the core radius is same for the pseudo and all-electron wave function, *i.e.*,

$$\int |\phi_{AE}^{nl}(\mathbf{r})|^2 d\mathbf{r} = \int |\phi_{ps}^{nl}(\mathbf{r})|^2 d\mathbf{r} \quad (2.44)$$

NCP works well for most elements except for some first period  $2p$  and  $3d$  elements. In these case the pseudo and the all-electron wave functions are almost identical.

- ♣ **Ultra soft pseudopotential:** With the requirement of norm conservation, it is not possible to make a pseudopotential dramatically soft. A completely new idea of removing norm conserving requirement was introduced by Vanderbilt [27] with a motivation to introduce soft pseudopotential. Vanderbilt's ultrasoft pseudopotential can reduce significantly the number of plane waves to express the pseudo wave functions, at the expense of a much more complex formulation of the algorithm. Relaxation of the norm-conservation condition make possible to form each smooth pseudowavefunction independently, within the constraint of matching the wave functions at the radius  $r_c$ . Therefore one can choose much larger  $r_c$  value than for a norm-conserving pseudopotential, where the desired accuracy is taken care of by additional auxiliary functions and overlap operators. The Vanderbilt's pseudopotentials are implemented in a number of DFT computer codes such as VASP [28]-[29], PWscf [30].

### (b) Methods using partial basis sets and muffin-Tin approximation

The crucial approximation that these methods are based on is the Muffin-tin (MT) sphere approximation. In this approximation the potential around each atom is treated as spherically symmetric within a radius  $S_R$  and the same is considered to be constant in between muffin-tin (MT) spheres, called interstitial region (as illustrated in Fig. 2.2). A single MT potential can be written as:

$$v_{ext}(\mathbf{r}_R) = \begin{cases} v(r_R) & \text{for } r_R \leq S_R, r_R = |\mathbf{r} - \mathbf{R}| \\ -v_0 & \text{for } r_R > S_R \end{cases} \quad (2.45)$$

The basis set therefore consists of two parts: the rapidly varying part of the wavefunctions in the MT region (where the potential is spherically symmetric) is represented by a radial solution of the Schrödinger equation at energy  $\epsilon$  ( $\phi_{Rl}(\epsilon)$ ) times spherical harmonics, known as partial waves, whereas the smoothly varying part of the wavefunctions in the interstitial region (where the potential is constant) is represented by plane wave or other smoothly varying functions. To generate a well behaved basis through out the



spheres are replaced by space-filling atomic spheres, called Wigner-Seitz (WS) spheres. In this limit of  $\kappa \rightarrow 0$ ,  $\eta_l \rightarrow (r_R/S_R)^{-l-1}$  with logarithmic derivative  $D = -l - 1$  and  $j_l \rightarrow (r_R/S_R)^l$  with  $D = l$ . With the above mentioned approximation a single MTO can be expressed as,

$$\chi_{RL}^\alpha(r_R, \epsilon) = \phi_{RL}(r_R, \epsilon)N_{RL}^\alpha(\epsilon) + \sum_{R'L'} j_{l'}^\alpha(r_{R'})[P_{R'L'}^\alpha(\epsilon)\delta_{R'L',RL} - S_{R'L',RL}^\alpha] \quad (2.48)$$

$N_{RL}^\alpha$  is the normalization factor,  $P_{RL}^\alpha$  is the potential function and the superscript  $\alpha$  represents the screening constant which control the range of MTO. The relationship between the potential function  $P_{RL}^\alpha$ ,  $\alpha$  matrix and the logarithmic derivative  $D_{RL}$ , is

$$[P_{RL}^\alpha]^{-1} = \left[ 2(2l + 1) \frac{D_l + l + 1}{D_l - 1} \right]^{-1} - \alpha \quad (2.49)$$

The last term of Eqn. 2.48 expresses the tail of the MTO centered on the sphere of radius  $S_{R'}$ . This term depends only on the structure and positions of the atoms through the structure matrix  $S^\alpha$  and not on the type of atoms occupying the sites. In terms of canonical structure constant  $S^0$ ,  $S^\alpha$  is given by,

$$S^\alpha = S^0(1 - \alpha S^0)^{-1} \quad (2.50)$$

The energy dependence of the MTO basis leads to general ASA-KKR secular equations:

$$\det|P_{R'L'}^\alpha(\epsilon)\delta_{R'L',RL} - S_{R'L',RL}^\alpha| = 0 \quad (2.51)$$

Finally following Andersen's approach of linearization the LMTO basis functions can be written as,

$$\chi_{RL}^\alpha = \phi_{RL}(r_R) + \sum \dot{\phi}_{R'L'}^\alpha(r_{R'})h_{R'L',RL}^\alpha \quad (2.52)$$

where, the functions  $\dot{\phi}_{R'L'}^\alpha(r_{R'})$  are linear combination of  $\phi$  and  $\dot{\phi}$  having the form,

$$\dot{\phi}_{R'L'}^\alpha = \dot{\phi}_{R'L'} + \phi_{R'L'}o^\alpha \quad (2.53)$$

$o^\alpha$  is the non-diagonal overlap matrix. The matrix  $h^\alpha$  is given by

$$h^\alpha = C^\alpha - \epsilon_\nu + (\Delta^\alpha)^{1/2}S^\alpha(\Delta^\alpha)^{1/2} \quad (2.54)$$

where  $C^\alpha$  and  $\Delta^\alpha$  are the diagonal potential matrices. They depend on the potential inside the sphere, the chosen screening parameter  $\alpha$  and on the sphere radii. The band center parameter  $C^\alpha$  is given by,

$$C^\alpha = \epsilon_\nu - \frac{P^\alpha(\epsilon_\nu)}{\dot{P}^\alpha(\epsilon_\nu)} \quad (2.55)$$

and the band width is given by

$$\sqrt{(\Delta^\alpha)} = \frac{1}{P^\alpha(\epsilon_\nu)} \quad (2.56)$$

Each set of screened LMTO's is characterized by the set of screening constant  $\alpha_{Rl}$  and these can be determined so as to give the LMTO set short range. The site independent set of screening constants

$$\alpha = \left\{ \begin{array}{lll} 0.3485 & l = 0 & (s) \\ 0.05303 & l = 1 & (p) \\ 0.010714 & l = 2 & (d) \end{array} \right\} \quad (2.57)$$

for *spd* screening have been found numerically [35] to give short ranged envelope functions for all, reasonably homogeneous, three-dimensional structures. The corresponding LMTO sets are referred to as *tight-binding*(TB) sets. The two-centre nearly orthogonal TB-Hamiltonian is:

$$H_{RL,R'L'}^{(1)} = \epsilon_\nu \delta_{RR'} \delta_{LL'} + h_{RL,R'L'}^\alpha \quad (2.58)$$

For the purpose of self-consistency, particularly for open structures, it is necessary to go beyond ASA to attain desired accuracy. It is done by introducing a correction term, named combined correction. The corrected Hamiltonian is:

$$\begin{aligned} H^{(2)} &= \epsilon_\nu + h^\alpha - (\kappa_\nu^2 + v_0) \partial_{\kappa^2} h^\alpha \\ &= C^\alpha + (\Delta^\alpha)^{1/2} S^\alpha (\Delta^\alpha)^{1/2} - (\kappa_\nu^2 + v_0) \partial_{\kappa^2} h^\alpha \end{aligned} \quad (2.59)$$

$$(2.60)$$

### ★ Linearized Augmented Plane Wave method

The linearized version of Augmented Plane Wave (LAPW) basis, following Andersen's linearization approach, is expressed as:

$$\chi_{\mathbf{q}}(\mathbf{r}, \epsilon) = \begin{cases} \sum_{l,m} \left( A_{lm,R}^q \phi_{LR}(r_R, \epsilon_\nu) + B_{lm,R}^q \dot{\phi}_{LR}(r_R, \epsilon_\nu) \right) & \text{for } r_R \leq S_R \\ e^{i(\mathbf{q} \cdot \mathbf{r})} & \text{for } r_R > S_R \end{cases} \quad (2.61)$$

where the coefficients  $A_{lm,R}^q$  and  $B_{lm,R}^q$  can be determined by matching these solutions in magnitude and slope at the sphere boundary. To do so the plane wave solution in the interstitial is required to expand in terms of Bessel functions  $j_l(r_R, q)$ . In principle a large number of  $l$  values are required for exact matching, but to keep the problem tractable one truncates this number at some value  $l_{max}$ . Therefore in band structure calculations based on LAPW basis set a crucial parameter is  $l_{max}$  for which a reasonable choice is needed. The condition that allows a good choice of  $l_{max}$  is :

$$R_i K_{max} = l_{max} \quad (2.62)$$

where  $R_i$  is the radius of  $i^{th}$  MT sphere and  $K_{max}$  determines the cut-off for the plane waves. The accuracy of the basis is controlled by the quantity  $R_i^{min} K_{max}$ , where  $R_i^{min}$  is the smallest MT sphere radius in the unit cell.

In this method the core states, those do not participate in chemical bonding, are treated as in free atoms, but subject to the potential due to the valence states. The problem arises in order to treat the semi-core states, which lie in between core and valence states. For example, due to hybridization, Fe atom in *bcc* lattice will have a non-negligible amount of  $4p$ -character in its valence states that are about 0.2 Ry below the Fermi level. But the  $3p$ -states that are 4.3 Ry below the Fermi level are not entirely confined in the core too. It is not clear how  $\epsilon_{l=1}^{Fe}$  should be chosen: close to  $3p$ , close to  $4p$  or at an intermediate value? In order to solve this problem an additional basis functions can be added. They are called "local orbitals" [36] and consist of a linear combination of two radial functions at two different energies and one energy derivative at one of these energies:

$$\phi_{lm}^{LO} = \left( A_{lm,R} \phi_{LR}(r_R, \epsilon_{\nu 1}) + B_{lm,R} \dot{\phi}_{LR}(r_R, \epsilon_{\nu 1}) + C_{lm,R} \phi_{LR}(r_R, \epsilon_{\nu 2}) \right) \quad (2.63)$$

The coefficients are determined by the requirements that  $\phi^{LO}$  should be normalized and should have zero value and slope at the sphere boundary. Though adding local orbitals increases the LAPW basis set size, still their number is quite small compared to typical LAPW basis set size of a few hundred functions.

The problem with the APW method was the energy dependence of the basis set, which is removed in the LAPW+LO method, but at the cost of a somewhat larger basis set size. Sjöstedt, Nordstrom and Singh [37] proposed the so called APW+lo method, in which the basis set is energy independent though still have the same size as in the APW method. In this sense, APW+lo combines the good features of APW and LAPW+LO method. The APW+lo basis set contains two kind of functions. The first kind is the standard APW basis with the partial wave evaluated at a fixed energy  $\epsilon_{\nu}$ . The other part of this basis is local orbitals, which is defined differently from that used in connection with the LAPW method. We abbreviate this local orbital as 'lo' instead of 'LO' used in connection with LAPW. The local orbitals are defined as:

$$\phi_{lm}^{lo} = \left( A_{lm,R}^{lo} \phi_{LR}(r_R, \epsilon_{\nu 1}) + B_{lm,R}^{lo} \dot{\phi}_{LR}(r_R, \epsilon_{\nu 1}) \right) \quad (2.64)$$

The two coefficients are determined by normalization and by requiring that the local orbital has zero value at the MT boundary and not zero slope. Hence, both the APW and the local orbital are continuous at the sphere boundary, but the first derivatives of both functions are discontinuous at sphere boundary. This new scheme converges practically to

identical results as the LAPW method [39], but allows to reduce “ $R_i^{min} K_{max}$ ” drastically, thus the corresponding computational time too.

The LAPW based computer code that has been used in the present study is Wien2k [38].

### (c) PAW method

The Projector Augmented Wave (PAW) method is a general approach for the all electron solution, proposed by Blöchl [40]. The unique features of this method is combination of the formal simplicity of plane wave pseudopotential approach and the versatility of the LAPW method.

A transformation  $\tau$  is used to map the true wave function  $\psi$  onto smooth auxiliary wave function  $\tilde{\psi}$ . An augmentation region  $\Omega_R$  is defined. Outside this region, the true wave functions coincides with auxiliary wave functions, while inside this region, the true wave function is given by  $\psi = \tau\tilde{\psi}$ . The transformation  $\tau$  is defined as identity plus a localized atom-centered contribution  $\hat{\tau}_R$ ,

$$\tau = 1 + \hat{\tau}_R \quad (2.65)$$

Within each augmentation region, each valence wavefunction  $\psi$  can be expanded as the sum of atomic partial waves  $\phi_m(r)$  such as

$$\psi(r) = \sum_m c_m \phi_m(r) \quad (2.66)$$

where the atomic partial waves only include the valence states that are orthogonalized to the core wave functions of the atom. For each partial wave there is a auxiliary partial wave  $\tilde{\phi}_m$  given by,

$$\phi_m = \tau\tilde{\phi}_m \quad (2.67)$$

All the auxiliary partial waves should be identical with  $\phi_m$  beyond certain radius since the transformation only acts locally in the core region. Demanding the transformation to operate on an arbitrary auxiliary wavefunction, one is able to expand the auxiliary wavefunction into the auxiliary partial waves with the same coefficient  $c_m$ , as,

$$\tilde{\psi} = \sum_m c_m \tilde{\phi}_m \quad (2.68)$$

Starting from Eqn. 2.66, the all electron wavefunction can be expressed as,

$$\psi = \tilde{\psi} + \sum_m c_m (\phi_m - \tilde{\phi}_m) \quad (2.69)$$

The projection operator  $\tilde{P}_m$  is then defined by,

$$c_m = \langle \tilde{P}_m | \tilde{\psi} \rangle \quad (2.70)$$

The projection operator probes the local character of the auxiliary wave function in the atomic region. From the above equation, one can derive,

$$\sum_m |\tilde{\psi}\rangle \langle \tilde{P}_m| = 1 \quad (2.71)$$

which is valid within the augmentation region. In order to determine the projector operator fully one needs to add another condition for the projector operator,

$$\langle \tilde{P}_m | \tilde{\phi}_{m'} \rangle = \delta_{mm'} \quad (2.72)$$

In terms of projector operators the transformation is expressed as,

$$\tau = 1 + \sum_m (|\phi_m\rangle + |\tilde{\phi}_m\rangle) \langle \tilde{p}_m| \quad (2.73)$$

The true wave function can be expressed as,

$$\psi = \tilde{\psi} + \sum_m (\phi_m - \tilde{\phi}_m) \langle \tilde{p}_m | \tilde{\psi} \rangle \quad (2.74)$$

By using transformation  $\tau$ , any operator  $A$  in the original AE space can also be cast into  $\tilde{A}$  by,

$$\tilde{A} = \tau^* A \tau \quad (2.75)$$

The KS equation is similarly transformed into,

$$(\tilde{H} - \varepsilon \tilde{S}) |\tilde{\psi}_i\rangle = 0 \quad (2.76)$$

where  $\tilde{H} = \tau^* H \tau$  is the pseudopotential Hamiltonian and  $S = \tau^* \tau$  is the pseudopotential overlap operator.

We used PAW method as implemented in VASP [28]-[29].

## 2.3 $N^{th}$ Order Muffin Tin Orbital (NMTO) - a down-folding method

To calculate the single electron part - the orbitals, hopping integrals and on-site terms, of a correlated Hamiltonian, one needs to extract low energy, few band Hamiltonian from the all band Hamiltonian. This is achieved through downfolding technique. The downfolding technique is based on the division of the space of a basis set into two subsets, lower  $|l\rangle$  and higher  $|s\rangle$ , and reduction of the full Hamiltonian  $H$  into the lower subset of the Hamiltonian  $\tilde{H}_l$  in such a way that lowest  $l$  eigenvalues of  $H$  and eigenvalues of

$\tilde{H}_{ll}$  are same. The formation of  $\tilde{H}_{ll}$  introduces additional energy dependence through the expression:

$$\tilde{H}_{ll}(\epsilon) = H_{ll} - H_{lh}(H_{hh} - \epsilon)^{-1}H_{hl} \quad (2.77)$$

In LMTO method it is implemented in the KKR equation, via the transformation of the structure matrix  $S^\alpha$  into  $\beta$  representation,

$$S_{ll}^\beta = S_{li}^\alpha + S_{li}^\alpha(P_{ii}^\alpha - S_{ii}^\alpha)^{-1}S_{il}^\alpha \quad (2.78)$$

The additional energy dependence is taken care of by the linearization procedure in construction of LMTO. Though the implementation of downfolding in LMTO helps to resolve the problem of ghost bands, but it does not provide an accurate way to do a massive downfolding, where the downfolded bands span in a very narrow energy window. The shortcomings of LMTO method in general can be listed as follows:

- The basis is complete to  $(\epsilon - \epsilon_\nu)$  ( *i.e.* 1<sup>st</sup> order) inside the sphere while it is only complete to  $(\epsilon - \epsilon_\nu)^0 = 1$  ( 0<sup>th</sup> order ) in the interstitial, which is inconsistent. This is made consistent by removing the interstitial region, through introduction of ASA.
- For open systems non-ASA corrections (Combined correction) is also included in the Hamiltonian and in the Overlap matrices. but,
  1. This makes the formalism heavy.
  2. Basis must often be increased by multi-panel calculation.
- The expansion of the Hamiltonian  $H$  in the orthogonal representation as a power series in the two-centered tight-binding Hamiltonian  $h$  :

$$\langle \chi | (H - \epsilon_\nu) | \chi \rangle = h - hoh + \dots \quad (2.79)$$

is obtained only within ASA and excluding downfolding.

Recently a more sophisticated method, based on  $N^{\text{th}}$  order muffin tin orbital (NMTO) basis [41], has been formulated, which overcomes these shortcomings and provides a way to describe the downfolded band structure with high accuracy within a chosen energy window. It uses the partial waves,  $\phi_{RL}(\epsilon, r_R)$  in the atomic sphere, but instead of Neumann function it uses Screened spherical waves (SSWs) as its tail part. The screening technique that has been adopted is described as follows:

- It introduces a hard sphere of radius  $a$  and a phase shifted partial wave solution  $\phi_{RL}^{\alpha 0}(\epsilon, r_R)$  (shown by the green line in Fig. 2.3), which matches the value and slope

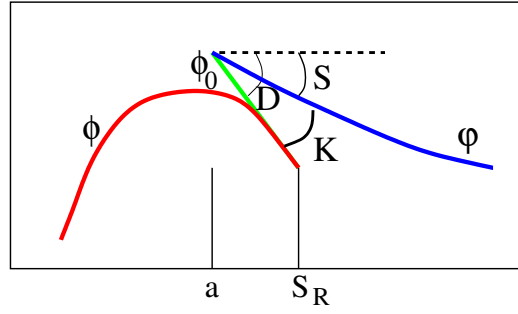


Fig. 2.3: Constituents of Kink partial wave (KPW),  $\phi$ ,  $\phi_0$  and  $\varphi$ .

of  $\phi$  at  $S_R$ , but their curvatures differ. At the hard sphere,  $\phi_{RL}^{\alpha 0}(\epsilon, r_R)$  is joined continuously but with a kink to the SSW,  $\varphi_{RL}^{\alpha}(\epsilon, \mathbf{r})$ , shown by the blue line in Fig. 2.3.

The combined form of these contributions known as the Kink Partial Wave (KPW), is given as,

$$\psi_{RL}^{\alpha}(\epsilon, r_R) = [\phi_{RL}^{\alpha}(\epsilon, r_R) - \phi_{RL}^{\alpha 0}(\epsilon, r_R)]Y_L(\hat{r}_R) + \varphi_{RL}^{\alpha}(\epsilon, \mathbf{r}) \quad (2.80)$$

The members of the NMTO basis set  $\chi_{R'L'}^{(N)}$  is constructed by Lagrange interpolation of  $\psi_{RL}^{\alpha}(\epsilon, r_R)$  evaluated at the energy points  $\epsilon_0, \dots, \epsilon_N$  (as shown in Fig. 2.4),

$$\chi_{R'L'}^{(N)} = \sum_{n=0}^N \sum_{RL \in A} \psi_{RL}^{\alpha}(\epsilon_n, r_R) L_{nRL, R'L'}^{(N)} \quad (2.81)$$

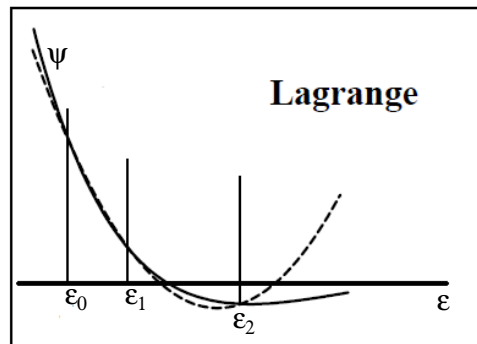


Fig. 2.4: The Nth order approximation to the energy dependence of a partial wave for a discrete (Lagrange) mesh.

The constructed basis set is therefore energy selective and localized in nature. The energy selective nature of the basis set provides the way to select a narrow energy window from full LDA band structure accurately and the accuracy can even be tuned with the

choice of the number of energy points (N). NMTO-downfolding technique also provides the underlying Wannier or Wannier-like basis, which are nothing but the effective orbitals defining the low energy Hamiltonian. If the selected bands are isolated from other bands, the orthonormalized NMTOs are the Wannier functions. However, for the strongly hybridized bands the NMTOs define a Wannier-like basis.

## 2.4 Many body techniques

The inclusion of the missing correlated part along with the LDA low energy Hamiltonian defines the many body model Hamiltonians, such as Generalized Hubbard model, Heisenberg model, t-J model *etc.* To solve these models three many body techniques have been used in this thesis, as discussed below.

### 2.4.1 Stochastic series expansion of quantum Monte Carlo method

The central quantity to be sampled in a Quantum Monte Carlo (QMC) simulation is the partition function  $Z$ :

$$Z = Tr[exp(-\beta H)] \quad (2.82)$$

where  $\beta$  is the inverse temperature ( $\beta = 1/T$ ) and  $H$  is the underlying Hamiltonian. In Stochastic series expansion (SSE) [42, 43, 44] one expands  $Z$  into a power series by choosing a basis  $|\alpha\rangle$ ,

$$Z = \sum_{\alpha} \sum_{n=0}^{\infty} \frac{(-\beta)^n}{n!} \langle \alpha | H^n | \alpha \rangle \quad (2.83)$$

For an isotropic  $S = 1/2$  Heisenberg model,

$$H = J \sum_{\langle i,j \rangle} \mathbf{S}_i \cdot \mathbf{S}_j \quad (2.84)$$

The standard basis set is defined as,

$$|\alpha\rangle = |S_1^z, S_2^z, \dots, S_N^z\rangle, \quad S_i^z = \pm 1/2 \quad (2.85)$$

where  $N$  is the number of spins in the system and  $J$  denotes the exchange parameter between two adjacent spins.

For the construction of the SSE configuration space the Hamiltonian can be written as,

$$H = -J \sum_{b=1}^M [H_{1,b} - H_{2,b}] \quad (2.86)$$

where  $H_{1,b}$  and  $H_{2,b}$  are the diagonal and off-diagonal bond operators respectively, corresponding to an interacting spin pair  $\langle i(b), j(b) \rangle$ ,

$$H_{1,b} = \frac{1}{4} - S_{i(b)}^z S_{j(b)}^z \quad (2.87)$$

and

$$H_{2,b} = \frac{1}{2}(S_{i(b)}^+ S_{j(b)}^- + S_{i(b)}^- S_{j(b)}^+) \quad (2.88)$$

In terms of bond operators the SSE partition function is,

$$Z = \sum_{\alpha} \sum_{S_L} \frac{\beta^n (L-n)!}{L!} \langle \alpha | \prod_{i=1}^L H_{a_i, b_i} | \alpha \rangle \quad (2.89)$$

where  $S_L$  denotes a sequence of operator indices;  $S_L = [a_1, b_1], [a_2, b_2], \dots, [a_L, b_L]$ , with  $a_i \in \{1, 2\}$  and  $b_i \in \{1, \dots, M\}$  or  $[a_i, b_i] = [0, 0]$ , and  $n$  is the number of  $[0, 0]$  elements in  $S_L$ .

As the bond operators do not commute with each other, a Quantum Monte Carlo (QMC) procedure is required to use to sample the terms  $\{\alpha, S_L\}$ . We use the "operator loop update" scheme, as proposed by Sandvik [42, 43, 44], which consists of two steps:

1. local substitution of single diagonal operator,  $[0, 0]_p \longleftrightarrow [1, b]_p$ .
2. change the operator type, diagonal to off-diagonal, for any number of diagonal and off-diagonal operators,  $[1, b]_{p_1}, [1, b]_{p_2}, \dots, [1, b]_{p_m} \longleftrightarrow [2, b]_{p_1}, [2, b]_{p_2}, \dots, [2, b]_{p_m}$ .

For details on the "operator loop update" technique see Ref.[42], [43], [44].

## 2.4.2 Dynamical Mean Field Theory (DMFT)

DMFT [45] maps the many-body crystal problem defined by the Hubbard Hamiltonian onto an effective self-consistent quantum impurity problem, which deals with a set of local quantum mechanical degrees of freedom that interacts with a bath created by all other degrees of freedom on other sites, see Fig. 2.5. This approximation is exact in the limit of infinite dimensions.

The corresponding local Green's function matrix is calculated via the  $k$ -integrated Dyson equation,

$$G(\omega_n) = \sum_k [(\omega_n + \mu)I - H^{LDA}(k) - \Sigma(\omega_n)]^{-1} \quad (2.90)$$

In the above  $H^{LDA}(k)$ , is the few band description of the LDA band structure defined in an Wannier function basis. The chemical potential  $\mu$  is defined self-consistently through the total number of electrons.  $\omega_n = (2n+1)\pi/\beta$  are the Matsubara frequencies with  $\beta$  as the inverse temperature ( $\beta = 1/T$ ).  $\Sigma$  is the selfenergy matrix and related to the local Green's function ( $G$ ) and bath Green's function ( $\mathcal{G}$ ) through the expression:

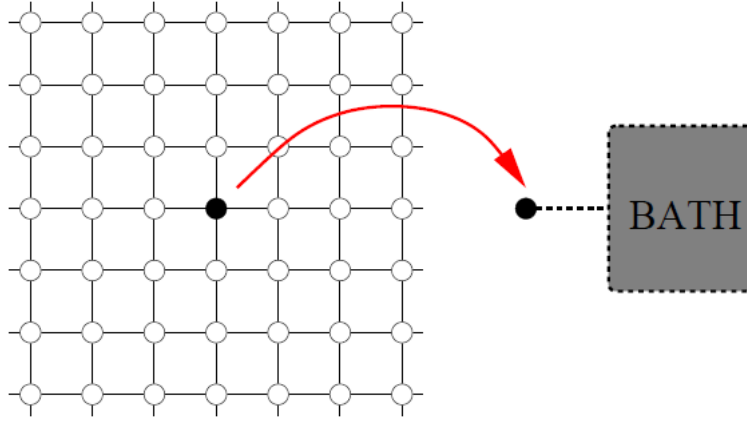


Fig. 2.5: The DMFT replaces a the full lattice of a correlated electron system with a single impurity site coupled to a self consistent bath (Taken from Ref.[45]).

$$\Sigma = \mathcal{G}^{-1} - G^{-1} \quad (2.91)$$

The local Green's function therefore has to be calculated self-consistently with the condition that implies the local Green's function to be the same as the corresponding solution of the quantum impurity problem:

$$G(\tau - \tau') = 1/Z \int D[c, c] e^{S_{eff}} c(\tau) c(\tau') \quad (2.92)$$

where the effective action  $S_{eff}$  is defined in terms of the bath Green's function  $\mathcal{G}$ , which describes the energy, orbital, spin, and temperature-dependent interaction of a particular site with the rest of the medium. The partition function  $Z$  is defined as,

$$Z = \int D[c, c] e^{S_{eff}} \quad (2.93)$$

The DMFT self consistent flow chart is shown in Fig. 2.6. The first step is to guess value of the input  $\Sigma$  and then calculate  $\mathcal{G}$  from Eqn. 2.90 and 2.91. The next step is the most difficult part of the self consistent cycle, *i.e.* to get the solution of the quantum impurity problem. Several impurity problem solver techniques have been proposed, like Iterated Perturbation Theory (IPT), Numerical Renormalization Group (NRG), Exact diagonalization (ED), Quantum Monte Carlo (QMC) *etc.* Once the impurity problem is solved, we get  $G$ , which together with  $\mathcal{G}$  yields a new  $\Sigma$  from Eqn. 2.91. In the present study we use QMC, as the quantum impurity solver, which is numerically an exact method, but requires an extrapolation, to calculate quantities involving real frequencies.

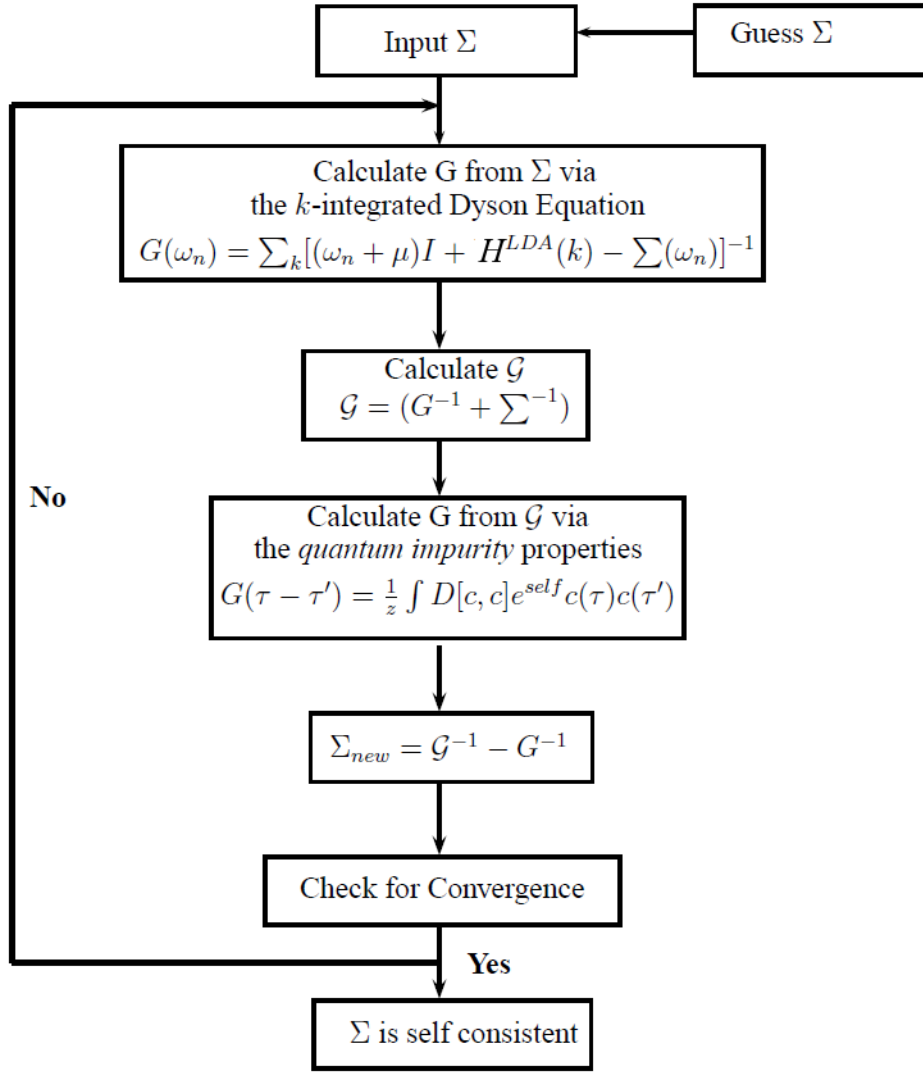


Fig. 2.6: Flowchart of the DMFT self consistent cycle.

### 2.4.3 Exact diagonalization method

This is a technique to provide a numerically exact solution, with a few caveats. In this technique, instead of considering the entire lattice, one considers a finite-sized cluster, which can be solved exactly on a computer. One first enumerates the degrees of freedom available, for which one can consider the states that contribute more in the essential physics of the system, *i.e.* the low lying single-particle states only. Then next crucial step is to choose a suitable basis to write the Hamiltonian, for which a preferable choice is the localized Wannier functions. If the interactions are strictly of four-fermion type, then the basis has to be in Fock space, and can only be written in terms of Slater Determinants or

a linear combination of them. The rank of the corresponding Hamiltonian grows as,

$$d = \frac{n!}{m!(m-n)!} \quad (2.94)$$

where  $n$  is the total number of states and  $m$  is the total number of particles. Obviously, the time involved in diagonalizing such a Hamiltonian increases very quickly with  $n$ , and only very small clusters can be diagonalized. However, if it is possible to separate the interaction term into quadratic parts in different sectors of the Hilbert space, using some symmetry, then the computational effort is reduced substantially. The model that has been solved using this many body technique in this thesis, *i.e.* the two-sublattice Kondo model is defined as,

$$\begin{aligned} H = & \epsilon_B \sum_{i \in B} b_{i\sigma\alpha}^\dagger b_{i\sigma\alpha} + \epsilon_{B'} \sum_{i \in B'} b_{i\sigma\alpha}'^\dagger b_{i\sigma\alpha}' \\ & - t_{BB'} \sum_{\langle ij \rangle \sigma, \alpha} b_{i\sigma, \alpha}^\dagger b_{j\sigma, \alpha}' - t_{B'B'} \sum_{\langle ij \rangle \sigma, \alpha} b_{i\sigma, \alpha}'^\dagger b_{j\sigma, \alpha} \\ & - t_{BB} \sum_{\langle ij \rangle \sigma, \alpha} b_{i\sigma, \alpha}^\dagger b_{j\sigma, \alpha} + J \sum_{i \in A} \mathbf{S}_i \cdot b_{i\alpha}^\dagger \vec{\sigma}_{\alpha\beta} b_{i\beta} \end{aligned} \quad (2.95)$$

The  $b^\dagger$  and  $b$ 's refer to the creation and annihilation operators, respectively, that operate on the sites belong to sublattice one. The same operators for the sites belong to the second sublattice are represented as  $b'^\dagger$  and  $b'$ . We have considered the hopping integrals upto second nearest neighbor, *i.e.*  $t_{bb'}$ ,  $t_{b'b'}$  and  $t_{bb}$ . Therefore the Hamiltonian matrix is already sparse. Nevertheless, it will be strictly tridigonal only for 1 dimension and nearest neighbor hopping. In higher dimensions, the matrix is band diagonal and may be further reduced to tridigonal form by Householder transformations. Then it can be diagonalized easily by QR algorithm [47, 48, 49].

## 2.5 Outline of the present study

The various theoretical approaches that have been employed in various chapters are as follows:

- In **Chapter-3** a model is proposed to explain the underlying magnetic structure of  $\text{CuTe}_2\text{O}_5$  through NMTO calculation and is solved using SSE technique of quantum Monte Carlo method. The observables that have been calculated are magnetic susceptibility, magnetization and magnetic specific heat.
- In **Chapter-4** we carried out a combined approach of LDA+DMFT calculations to investigate the electronic structure of  $\text{La}_2\text{CuO}_4$  in T and T' phase.

- In **Chapter-5**, to explain the kinetic energy driven antiferromagnetism in  $\text{Sr}_2\text{FeMoO}_6$  we use a first principles derived two-sublattice double exchange model and solve it with Exact diagonalization technique.
- In **Chapter-6**, we explored the origin of the ferromagnetic  $T_c$  trend in Cr-based double perovskite series,  $\text{Sr}_2\text{CrB}'\text{O}_6$  (B0=W/Re/Os), based on DFT calculations. To support our investigation we also adopted model Hamiltonian approach, which turned out to be a contribution of two-sublattice double exchange model and the super exchange model. The established model has been solved with Exact diagonalization technique. Additionally we explore the possibility of large magneto-optic signals in these materials, fully based on DFT calculations.
- The study on insulating ferromagnetic double perovskite  $\text{La}_2\text{NiMnO}_6$  described in **Chapter-7**, is entirely DFT based. The magnetic exchanges have been calculated using the extended Kugel-Khomskii model of super exchange using NMTO derived hopping integrals and site energies. For  $\Gamma$  point phonon and dielectric response calculations we use Density functional perturbation theory (DFPT).

# References

- [1] M. Born, and J. R. Oppenheimer, Zur Quantentheorie der Molekeln, Ann. Physik **84**, 457 (1927).
- [2] D. R. Hartree, Proc. Cambridge Phil. Soc. **24**, 89, 111 (1928).
- [3] C. C. J. Roothaan, Rev. Mod. Phys. **23**, 69 (1951).
- [4] N. W. Ashcroft and N. D. Mermin, Solid State Physics (Thomson Learning, Toronto, 1976).
- [5] P. Hohenberg and W. Kohn, Phys. Rev. B **136**, 864 (1964).
- [6] W. Kohn and L. J. Sham, Phys. Rev. A **140**, 1133 (1965).
- [7] "Nobel Lecture: Electronic structure of matterwave functions and density functionals" by W. Kohn, Reviews of Modern Physics, Vol. **71**, No. 5, 1253.
- [8] L. H. Thomas (1927). "The calculation of atomic fields". Proc. Cambridge Phil. Soc. **23** (5): 542548.
- [9] E. Fermi "Un Metodo Statistico per la Determinazione di alcune Priopriet dell'Atomo". Rend. Accad. Naz. Lincei **6**: 602607 (1927).
- [10] E. Wigner, Phys. Rev. **46**, 1002 (1934).
- [11] D.M. Ceperley and B.J. Alder, Phys. Rev. Lett. **45**, 566 (1980).
- [12] J.P. Perdew and A. Zunger, Phys. Rev. B **23**, 5048 (1981).
- [13] S. J. Vosko, L. Wilk, M. Nusair, "Accurate spin-dependent electron liquid correlation energies for local spin density calculations: A critical analysis", Can. J. Phys. **58**, 1200 (1980).
- [14] J. P. Perdew, Y. Wang, Phys. Rev. B, **45**, 13244 (1992).
- [15] von U. Barth, L. Hedin, J. Phys. C: Solid State Phys. **5**, 1629(1972).

- 
- [16] R.O. Jones and O. Gunnarson. The density functional formalism, its applications and prospects. *Rev. Mod. Phys.* **61**, 689 (1989).
- [17] J. P. Perdew, in *Electronic Structure of Solids 91*, edited by P. Ziesche and H. Eschrig (Akademie Verlag, Berlin, 1991), p. 11.
- [18] J. P. Perdew, K. Burke and M. Ernzerhof, *Phys. Rev. Lett.* **77**, 3865 (1996).
- [19] Y. Umeno, B. Meyer, C. Elsasser, and P. Gumbsch, *Phys. Rev. B* **74**, 060101(R) (2006).
- [20] A. I. Liechtenstein, V. I. Anisimov and J. Zaane, *Phys. Rev. B* **52**, R5467 (1995).
- [21] B. R. Judd 1963 *Operator Techniques in Atomic Spectroscopy* (New York: McGraw-Hill).
- [22] S. L. Dudarev, G. A. Botton, S. Y. Savrasov, C. J. Humphreys and A. P. Sutton, *Phys. Rev. B* **57**, 1505 (1998).
- [23] J. C. Slater and G. F. Koster, *Phys. Rev.* **94**, 1498 (1954).
- [24] W. C. Herring, *Phys. Rev.* **57**, 1169 (1940); W. C. Herring and A. G. Hill, *Phys. Rev.* **58**, 132 (1940).
- [25] J. C. Phillips and L. Kleinman, *Phys. Rev.* **116**, 287 (1959).
- [26] D.R. Hamann, M. Schluter and C. Chiang, *Phys. Rev. Lett.* **43**, 1494 (1979).
- [27] D. Vanderbilt, *Phys. Rev. B* **41**, 7892 (1985).
- [28] G. Kresse and J. Hafner, *Phys. Rev. B* **47**, 558 (1993).
- [29] G. Kresse and J. Furthmuller, *Phys. Rev. B* **54**, 11169 (1996).
- [30] S. Baroni *et.al.*, <http://www.pwscf.org/>.
- [31] E. P. Wigner and F. Seitz, *Phys. Rev.* **46**, 509 (1934).
- [32] T. L. Loucks, *Augmented Plane Wave Methods*, (Benjamin, New York, 1967).
- [33] J. Koringa, *Physica* **13**, 392 (1947); J. Koringa, *Phys. Rev.* **238**, 341 (1994).
- [34] O. K. Andersen, *Phys. Rev. B* **12**, 3060 (1975), and *The Electronic Structure of Complex Systems* (Plenum, New York, 1984); H. L. Skriver, *The LMTO Method* (Springer, New York, 1984).
- [35] O. K. Andersen and O. Jepsen, *Phys. Rev. B* **52**, 2571 (1984).

- 
- [36] D. Singh, Phys.Rev. B 43, 6388 (1991).
- [37] E. Sjöstedt, L. Nordström and D. J. Singh, Solid State Commun. **114**, 15 (2000).
- [38] P. Blaha, K. Schwarz, G. K. H. Madsen, D. Kvasnicka, and J. Luitz, computer code WIEN2K, (2001).
- [39] G. K. H. Madsen, P. Blaha, K. Schwarz, E. Sjöstedt and L. Nordström Phys. Rev. B, **64**, 195134 (2001).
- [40] P. E. Blöchl, Phys. Rev. B **50**, 17953 (1994).
- [41] O. K. Andersen and T. Saha-Dasgupta, Phys. Rev. B **62**, R16219 (2000).
- [42] A. W. Sandvik, Phys. Rev. B **59**, R14157 (1999).
- [43] A. Dorneich and M. Troyer, Phys. Rev. E **64**, 066701 (2001).
- [44] K. Louis and C. Gros, Phys. Rev. B **70**, 100410(R) (2004).
- [45] A. Georges, G. Kotliar, W. Krauth, and M. J. Rozenberg, Rev. Mod. Phys. **68**, 13 (1996).
- [46] A. Georges, Lectures on the Physics of Highly Correlated Electron Systems VIII (2004) 3, American Institute of Physics Conference Proceedings Vol. **715**.
- [47] J. G. F. Francis, "The QR Transformation, I", The Computer Journal **4**, 265 (1961).
- [48] J. G. F. Francis, "The QR Transformation, II" The Computer Journal **4**, 332 (1962).
- [49] V. N. Kublanovskaya, "On some algorithms for the solution of the complete eigenvalue problem," USSR Computational Mathematics and Mathematical Physics **1**, 637 (1963).

# Chapter 3

## Proposed low-energy model Hamiltonian for the spin-gapped system $\text{CuTe}_2\text{O}_5$

Content of this chapter has been published in: Hena Das, T. Saha-Dasgupta, C. Gross and R. Valenti, Phys. Rev. B, **77**, 224437 (2008) (*Editor's suggestion*).

### 3.1 Introduction

Transition metal oxides based on  $3d^9$  copper  $\text{Cu}^{2+}$  ions reveal a striking diversity of magnetic structures depending on the effective magnetic dimensionality of the system [1]. Therefore a crucial piece of information needed in the process of understanding these systems is the connection between the underlying chemical complexity of the compound and the spin lattice. Often, this relation is not obvious from structural considerations and one needs to rely on *ab-initio* based calculations that has proven to be very successful in deriving the underlying spin model of a large number of low-dimensional quantum spin systems including cuprates [2, 3, 4], vanadates [5, 6] and titanates [8, 9].

Introduction of lone pair cations, like  $\text{As}^{3+}$ ,  $\text{Se}^{4+}$ ,  $\text{Te}^{4+}$ ,  $\text{Pb}^{2+}$  or  $\text{Bi}^{3+}$ , in between  $\text{Cu}^{2+}$ - $\text{O}^{2-}$ - $\text{Cu}^{2+}$  superexchange path, was suggested as a fruitful path to reduce the magnetic dimensionality and to create new magnetic structures [10, 11]. For example  $\text{Cu}_2\text{Te}_2\text{O}_5\text{X}_2$  ( $\text{X}=\text{Cl}, \text{Br}$ ), where the effective magnetic dimension is reduced to extreme limit of quasi-zero dimension by the magnetic insulation via  $\text{Te}^{4+}$  ions[12]. There are many more examples of such systems, like  $\text{Cu}_4\text{Te}_5\text{O}_{12}\text{Cl}_4$ [13, 14],  $\text{Cu}_3(\text{SeO}_3)_2\text{Cl}_2$ [15],  $\text{Cu}_3\text{TeO}_6$  *etc.* Recently, in an attempt to analyze the effect of lone-pair cations such as  $\text{Se}^{4+}$  or  $\text{Te}^{4+}$  on the magnetic dimensionality of  $\text{Cu}^{2+}$ -based systems, the magnetic properties of  $\text{CuTe}_2\text{O}_5$  were investigated [1].  $\text{CuTe}_2\text{O}_5$  is structurally a Cu(II)-dimer system separated by Te ions. Magnetic susceptibility measurements show a maximum at  $T_{max} = 56.5$  K with an exponential drop at lower temperatures signaling the opening of a spin gap (see Fig. 3.1(a)). The behavior at high temperatures follows the Curie law with a Curie-Weiss temperature of  $\theta = -41$  K [1], which indicates that the dominant interactions in this system are antiferromagnetic. Electron spin-resonance (ESR) studies suggest that the structural dimers of  $\text{CuTe}_2\text{O}_5$  do not coincide with the magnetic dimers [16]. To determine the underlying magnetic structure Deisenhofer *et.al.* [16] fitted their susceptibility data considering three model spin systems:

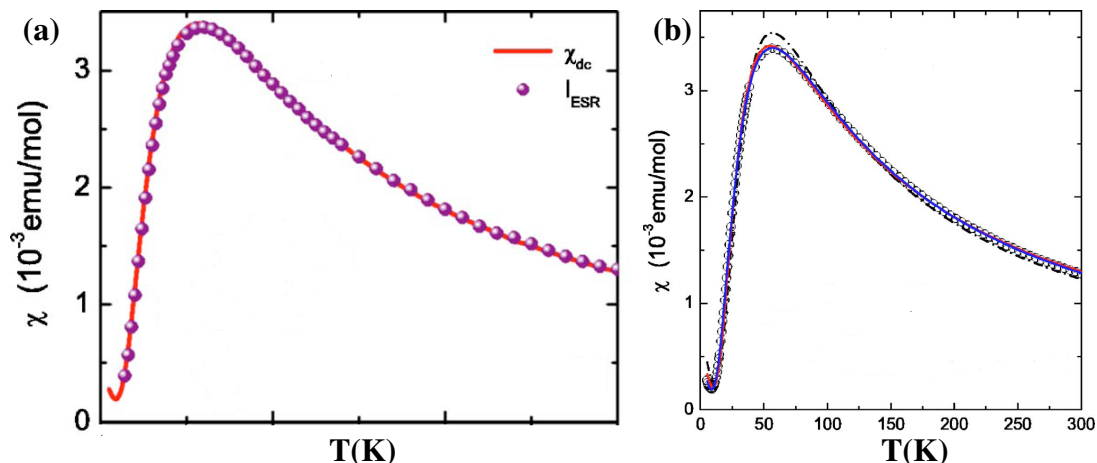


Fig. 3.1: (a)Temperature dependences of the ESR intensity and the dc susceptibility. (b)Temperature dependences of the spin susceptibility (circles) in  $\text{CuTe}_2\text{O}_5$ . The lines are best fits obtained by the models : (1)A pure dimer model (black dashed line), (2)An alternating spin chain model (blue solid line), (3)Interacting dimer model (red solid line). Taken from Ref.[16].

- A pure dimer model, in which only two sites are magnetically coupled and are magnetically isolated from rest of the sites. A schematic diagram of a antiferromagnetic dimer system is shown in Fig. 3.2.

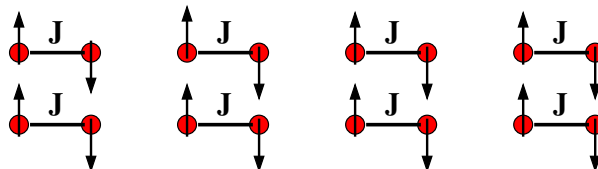


Fig. 3.2: An antiferromagnetic dimer system with intra dimer interaction strength  $J$ .

The dimer susceptibility as driven by Bleaney and Bowers (BB)[17] is given by,

$$\chi(T) = \frac{Ng^2\mu_B^2}{k_B T} [3 + \exp(J/k_B T)]^{-1} \quad (3.1)$$

where  $J$  denotes the intradimer exchange coupling,  $g$  is the effective  $g$  factor, and  $k_B$  is the Bohr magneton.

- An alternating spin chain model, an infinite one dimensional system with alternate exchange interaction between two magnetic ions of different magnitude and may be of different sign. A schematic representation of an alternating antiferromagnetic chain is shown in Fig. 3.3.

Numerical method [18] was used to solve the spin-1/2 alternating Heisenberg antiferromagnetic model.

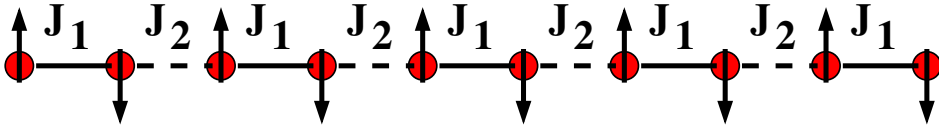


Fig. 3.3: An alternating antiferromagnetic spin chain with alternating exchange constants  $J_1$  and  $J_2$ .

- Interacting dimer model, in which the exchange interaction between two adjacent dimers ( $J'$ ) is non-negligible. The magnetic susceptibility is defined by a mean-field modification of the Bleaney-Bowers equation [19],

$$\chi(T) = \frac{Ng^2\mu_B^2}{k_B T} [3 + \exp(J/k_B T) + J'/k_B T]^{-1} \quad (3.2)$$

As fitting the susceptibility data to all of these three models showed good agreement with the experimental data [16] (see Fig. 3.1(b)), the determination of the magnetic structure from the fitting was not unambiguous. Further detailed investigation of the magnetic exchange paths using the extended Hückel tight-binding (EHTB) [20, 21] method was also carried out. This study suggested that:

1. the strongest interaction is between Cu ions which are sixth nearest neighbors ( $J_6$ ) and is of antiferromagnetic supersuperexchange type mediated by a O-Te-O bridge.
2. the next strongest interaction is of antiferromagnetic superexchange (SE) type within the structural dimer ( $J_1$ ), yielding a ratio  $J_1 / J_6 = 0.59$  [16].

Based on these findings, Deisenhofer *et.al.* [16] proposed an alternating spin-chain model as the simplest possible model for  $\text{CuTe}_2\text{O}_5$ .

Given the existence of many possible Cu-Cu interaction paths in this material whose relative importance may not be necessarily captured in EHTB study, we performed *ab-initio* density-functional theory (DFT) calculations and applied the Nth order muffin-tin orbital (NMTO)-downfolding technique in order to derived the low-energy spin model for  $\text{CuTe}_2\text{O}_5$ , the validity of which had been checked by computing the magnetic susceptibility with quantum Monte Carlo technique and comparing it with available experimental data.. This chapter is outlined as follows: in §: 3.2 we discuss the crystal structure of  $\text{CuTe}_2\text{O}_5$ . §: 3.6 present *ab initio* DFT electronic structure of  $\text{CuTe}_2\text{O}_5$ . In §: 3.4 we discuss the effective model Hamiltonian obtained with the NMTO downfolding method. QMC results for magnetic susceptibility, magnetization and specific heat are described in §: 3.5 and finally in §: 8 we present our conclusions with future outlook.

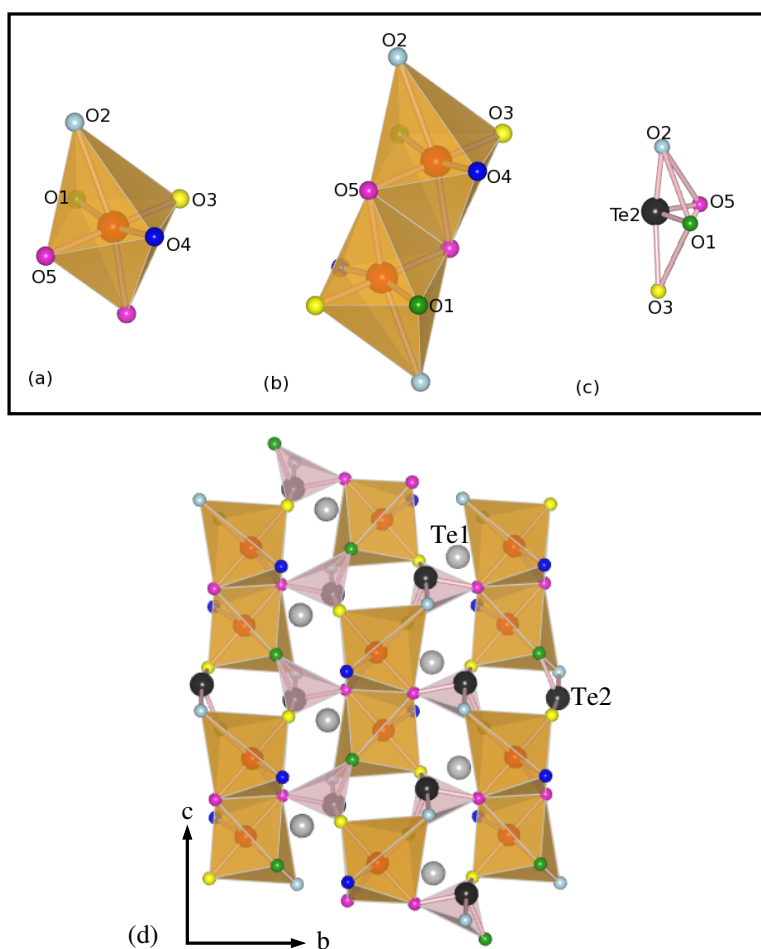


Fig. 3.4: Building units of  $\text{CuTe}_2\text{O}_5$ . (a)  $\text{CuO}_6$ -distorted octahedron. (b)  $\text{Cu}_2\text{O}_{10}$ -structural dimer unit. (c)  $\text{TeO}_4$ -tetrahedra. (d) Crystal structure of  $\text{CuTe}_2\text{O}_5$ . The largest balls represent Te1 and Te2. Te1 and Te2 are shown in gray and black colors, respectively. Cu atoms are represented by medium sized balls, situated at the center of the distorted octahedra. The smallest balls denote the oxygen atoms.

## 3.2 Crystal structure

$\text{CuTe}_2\text{O}_5$  crystallizes in the monoclinic space group  $P21/c$  (Ref. [22]) with lattice parameters  $a = 6.871 \text{ \AA}$ ,  $b = 9.322 \text{ \AA}$ ,  $c = 7.602 \text{ \AA}$ , and  $\beta = 109.08^\circ$ . It is built out of  $\text{CuO}_6$  distorted octahedra (Fig. 3.4(a)), with six inequivalent oxygens O1, O2, O3, O4, O5, and O5' surrounding each Cu(II) ion. Each  $\text{CuO}_6$  octahedron is elongated along the O2-O5' axis, with distances  $d_{\text{Cu-O5}'} = 2.303 \text{ \AA}$  and  $d_{\text{Cu-O2}} = 2.779 \text{ \AA}$ . The Cu-O distances in the  $\text{CuO}_4$  plane range from  $d_{\text{Cu-O5}} = 1.948 \text{ \AA}$  to  $d_{\text{Cu-O3}} = 1.969 \text{ \AA}$ . Two neighboring  $\text{CuO}_6$  octahedra share an edge to form a  $\text{Cu}_2\text{O}_{10}$  structural dimer (Fig. 3.4(b)). The oxygen octahedra of two Cu(II) ions within a given structural dimer are rotated by  $180^\circ$  with respect to each other.

The structural dimers form a chain like structure running almost parallel to the crystallographic  $c$  axis. These chains pile along the crystallographic  $b$  axis (Fig. 3.4(d)).

The  $\text{Te}_1$  atoms are situated between two successive  $\text{Cu(II)}$ -structural dimer chains, while the  $\text{Te}_2$  atoms are located in between two  $\text{Cu}_2\text{O}_{10}$  structural dimers along a given chain. The local oxygen environment of the Te atoms forms a  $\text{TeO}_4$  tetrahedra (Fig. 3.4(c)). The layers containing these chains in the  $bc$  plane are stacked approximately along the crystallographic  $a$  axis with hardly any connection between the layers.

### 3.3 Electronic structure

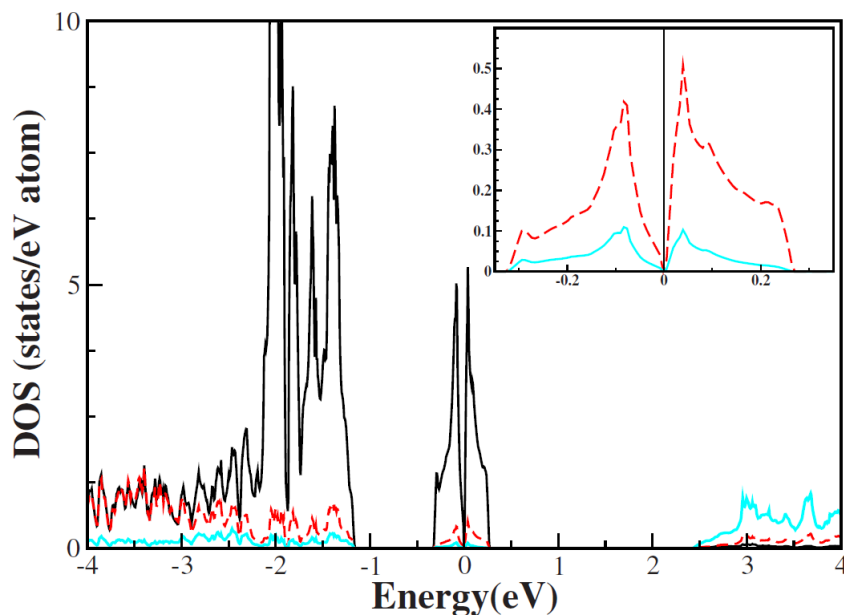


Fig. 3.5: Partial density of states of Cu  $d$  (in black full lines), O  $p$  (in red dashed lines), and Te  $p$  (in cyan or gray full lines) orbitals for  $\text{CuTe}_2\text{O}_5$ . The inset shows the density of states for O  $p$  and Te  $p$  in the energy range close to  $E_F$ , dominated by Cu  $d_{x^2-y^2}$  character.

In order to analyze the electronic behavior of  $\text{CuTe}_2\text{O}_5$  we carried out first principles Density functional theory based calculations within the local density approximation (LDA) by employing both the WIEN2K code based on the full-potential linearized augmented plane-wave (LAPW) method and the Stuttgart TBLMTO-47 code based on the linear muffin-tin orbital (LMTO) method. The calculated band structures agree well with each other within the allowed error bars of the various approximations involved in these two methods. Fig. 3.5 and 3.6 show the non-spinpolarized density of states (DOS) and band structures, respectively, of  $\text{CuTe}_2\text{O}_5$ . The orbital contributions to the valence and conduction bands in the band structure and the DOS were determined by defining the local reference frame with the local  $z$  axis pointing along Cu-O2 bond and the local  $y$  axis pointing almost parallel to the Cu-O5 bond.

The predominant feature of the band structure is the isolated manifold of four bands

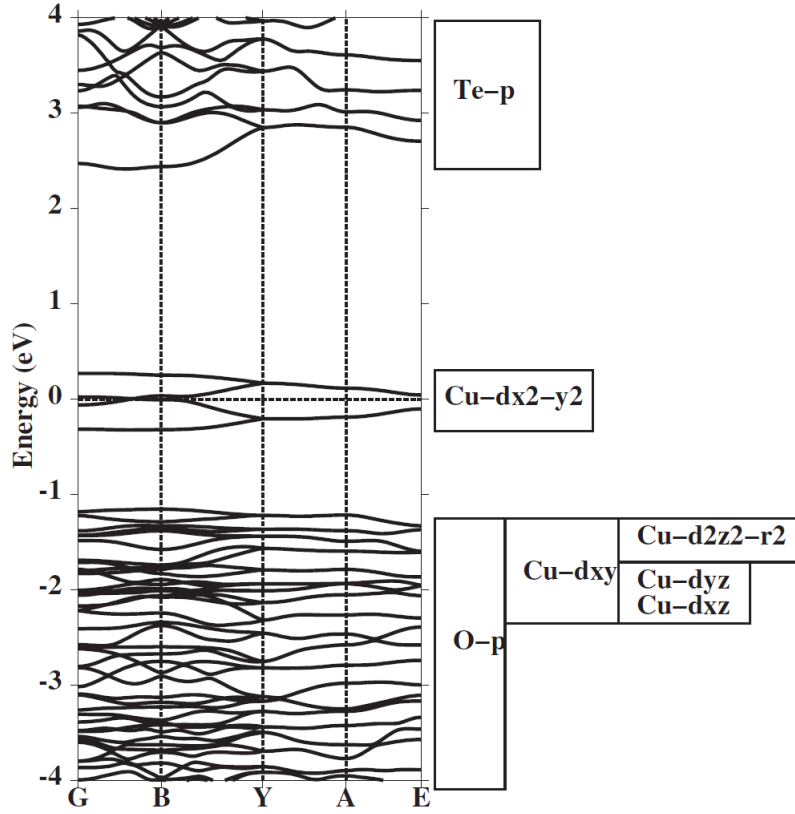


Fig. 3.6: LDA band structure of CuTe<sub>2</sub>O<sub>5</sub> plotted along various symmetry directions of the monoclinic lattice. The zero of the energy has been set up at the LDA Fermi energy. The dominant orbital contributions in various energy ranges are shown in boxes on the right-hand side. The various Cu  $d$  characters are shown in the local reference frame as described in the text.

crossing the Fermi level ( $E_F$ ), formed by Cu  $d_{x^2-y^2}$  orbitals corresponding to the four Cu atoms in the unit cell, admixed with O  $p$  states. These bands are half filled and separated from the low lying O  $p$  and non- $d_{x^2-y^2}$  Cu valence bands by a gap of about 0.8 eV and from the Te  $p$ -dominated high lying conduction bands by a gap of about 2.2 eV, with the zero of energy set at the LDA Fermi level. We note that in the low-energy scale, the LDA results lead to a metallic state. Introduction of missing correlation effects beyond LDA, for instance, with the LDA+U functional, is expected to drive the system insulating, as our LDA+U calculations corroborated.

The valence band shows Cu  $d_{xy}$ ,  $d_{yz}$ ,  $d_{zx}$  and  $d_{3z^2-r^2}$  character dominated bands in the energy range between -2.2 and -1.2 eV, while the O  $p$ -dominated bands are in the energy range between -4 and -1.2 eV. The contribution of O2 character in the conduction bands crossing the Fermi level is found to be small compared to other oxygens because of the large Cu-O2 bond length. The Te1  $p$  and Te2  $p$  states show a non-negligible contribution to the bands crossing the Fermi energy, as pictured in the inset of Fig. 3.5 and play an important role in mediating the Cu-Cu exchange interaction as will be demonstrated in

what follows.

### 3.4 Derivation of Low-energy model Hamiltonian

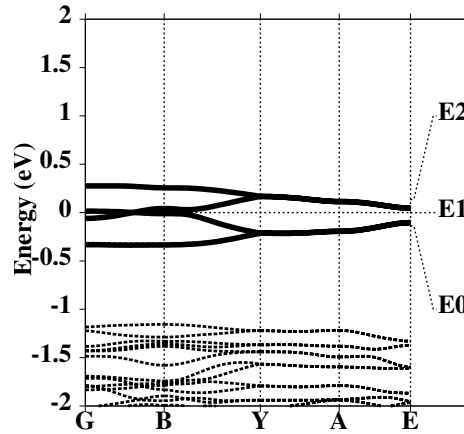


Fig. 3.7: Bands obtained with downfolded Cu  $d_{x^2-y^2}$  basis (solid lines) compared to full LDA band structure (dashed lines).  $E_0$ ,  $E_1$  and  $E_2$  mark the energy points used in NMTO calculation.

We derived the low-energy Hamiltonian using NMTO downfolding method, defined in the basis of the effective Cu  $d_{x^2-y^2}$  orbitals by keeping only the  $d_{x^2-y^2}$  orbital for each Cu atom in the unit cell and integrating out all the rest. We show the downfolded bands in Fig. 3.7 in comparison to the full LDA band structure. With the choice of three energy points  $E_0$ ,  $E_1$  and  $E_2$ , downfolded bands are indistinguishable from the Cu  $d_{x^2-y^2}$  dominated bands of the full LDA calculation.

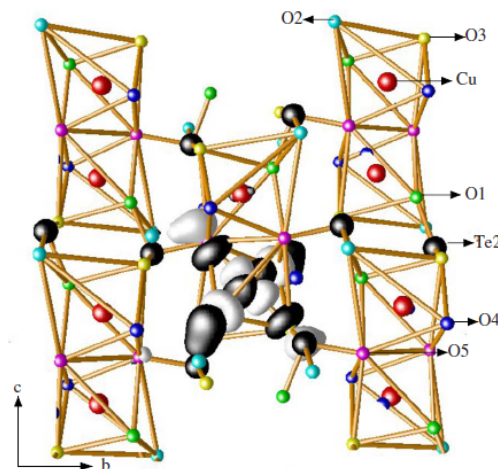


Fig. 3.8: Effective Cu  $d_{x^2-y^2}$  orbital with lobes of opposite signs colored as black and white. The  $d_{x^2-y^2}$  orbital is defined with the choice of local reference frame as described in the text.

The corresponding Wannier function is plotted in Fig. 3.8. The central part has the  $3d_{x^2-y^2}$  symmetry with the choice of the local coordinate system as stated above, while the tails are shaped according to O  $p_x/p_y$ . The Cu  $d_{x^2-y^2}$  orbital forms strong  $pd$  antibonds with the O  $p_x/p_y$  tails. O  $p_x/p_y$  tails bend toward the Te2 atom, which indicates the importance of hybridization effects from the Te cations and enhances the Cu-Cu interaction placed at different structural dimers  $\text{Cu}_2\text{O}_{10}$ .

Table 3.1: Cu-Cu hopping parameters corresponding to the downfolded Cu- $d_{x^2-y^2}$  Hamiltonian in NMTO-Wannier function basis. Interactions of strength larger than 1 meV are listed.

hopping	Cu-Cu distances in Å	Hopping parameters in meV
$t_1$	3.18	38.7
$t_3$	5.32	11.0
$t_4$	5.58	112.9
$t_5$	5.83	13.7
$t_6$	6.20	59.9
$t_7$	6.43	4.9

Table 3.1 shows the various dominant effective hopping integrals  $t_{ij}$  with magnitude greater than 1 meV between the Cu(II) ions at sites  $i$  and  $j$ . The notation for the various hoppings is shown in Fig. 3.9 where the subindex of  $t_n$  corresponds to the  $n^{\text{th}}$  Cu neighbors. The strongest hopping integral,  $t_4$ , is found to be between those two Cu(II) ions which are placed at different structural dimers and the interaction is mediated by two O-Te-O bridges.  $t_1$ , which denotes the hopping integral between two Cu(II) ions situated within the same structural dimer unit, is found to be about 1/3 of the strongest hopping integral ( $t_4$ ). The second strongest hopping term,  $t_6$ , mediated by one O-Te-O bridge is about 1/2 of  $t_4$ . Fig. 3.9(b) shows the interaction paths in the  $ab$  plane, which are weak in general and can be neglected. In particular, we mention as examples the hopping integrals  $t_3$  and  $t_7$ , which are approximately 1/10 and 1/25 of the strongest hopping term ( $t_4$ ), respectively. In the following we discuss the origin of the various dominant interaction paths.

### ♣ Strongest hopping term $t_4$

The strongest hopping term,  $t_4$ , mediated by two O-Te-O bridges is associated to a Cu-O-Te-O-Cu supersuper exchange path generating the spin-spin coupling  $J_4$ . The strength of a supersuper exchange interaction through an exchange path of type Cu-O-L-O-Cu (e.g., L=Te) depends sensitively on how the O-L-O linkage orients the two magnetic orbitals (*i.e.*, the  $d_{x^2-y^2}$  orbitals) centered at two Cu sites and also on how the tails of the magnetic orbitals, which have contributions from the orbitals of the ligand atom L,

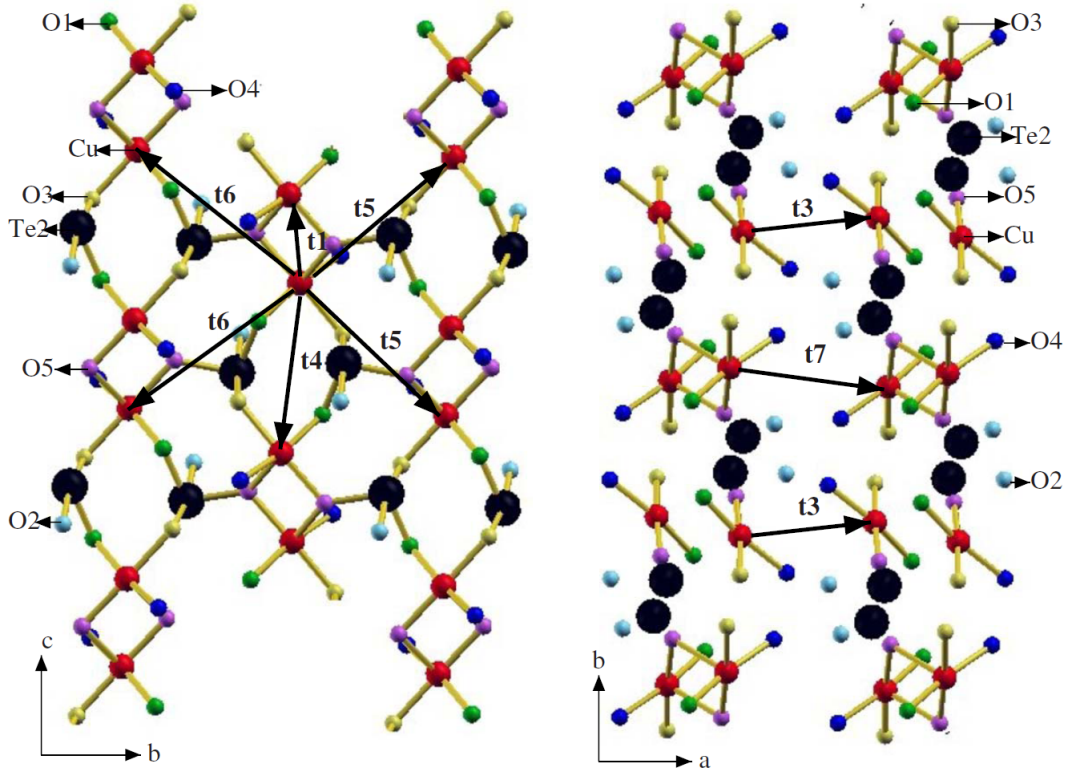


Fig. 3.9: Cu-Cu interaction paths  $t_n$ . The color convention is the same as Fig. 3.4.

are oriented with respect to the central part. In Fig. 3.10 we show the Wannier function plot corresponding to  $t_4$ , where the effective Cu  $d_{x^2-y^2}$ -like Wannier orbitals are at the Cu sites between which we found the strongest interaction. The O  $p_x/p_y$  tails bend toward the Te atoms forming O-Te-O ligand paths which are responsible for the strong Cu-Cu bonding.

### ♣ Second strongest hopping term $t_6$

The hopping integral  $t_6$  describes the next strong Cu-Cu interaction path, which is mediated via one O-Te-O bridge and responsible for the Cu-O-Te-O-Cu supersuper exchange interaction generating the spin-spin coupling  $J_6$ . Fig. 3.11 shows the Wannier plots of the Cu  $d_{x^2-y^2}$  downfolded NMTOs. Here the oxygen tails bend toward the interconnecting  $\text{TeO}_2$  unit to provide an interaction pathway between the two Cu sites as in the  $t_4$  path. However the strength of this interaction is expected to be weaker than  $t_4$  since there is only one, instead of two O-Te-O interaction path.

### ♣ Structural intradimer hopping term $t_1$

$t_1$  corresponds to the intradimer Cu-Cu interaction path which is mediated by O5-O5' atoms. In Fig. 3.12 we show the Wannier function plot, where the effective Cu  $d_{x^2-y^2}$

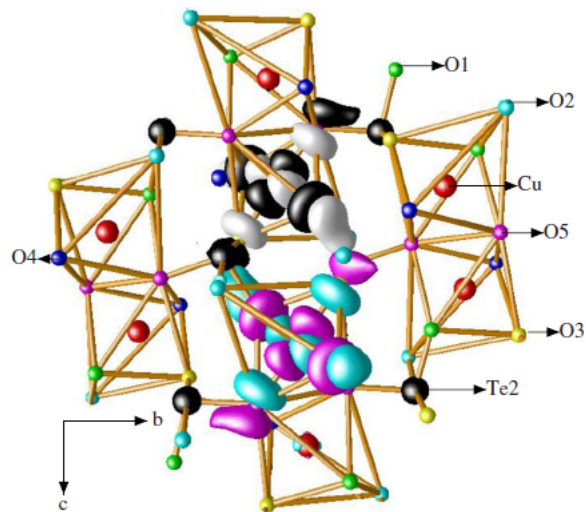


Fig. 3.10: Effective orbital corresponding to the downfolded NMTOs, placed at two Cu sites situated at two different structural dimer units corresponding to the  $t_4$  interaction. Lobes of orbitals placed at different Cu sites are colored differently. Lobe colored black (white) at one Cu site represents the same sign as that colored magenta (cyan) at other Cu site.

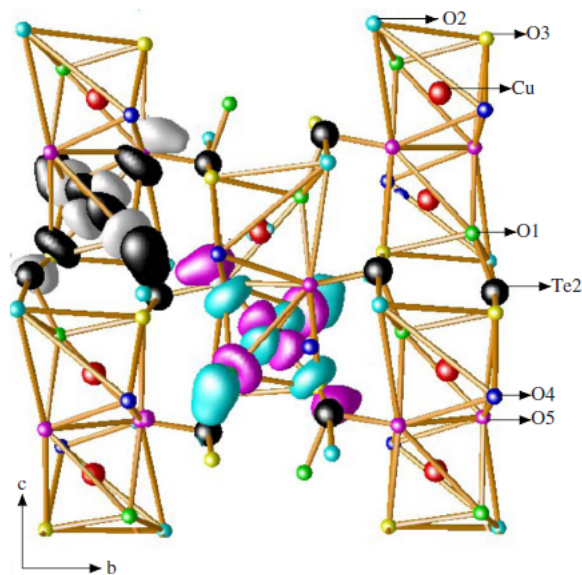


Fig. 3.11: Effective orbital corresponding to the downfolded NMTOs, placed at two Cu sites situated at two different structural dimer units corresponding to the  $t_6$  hopping term. Color convention is the same as in Fig. 3.10

-like Wannier orbitals are placed at the Cu sites of the same structural dimer unit. As we stated above, each structural dimer unit is made of two edge sharing  $\text{CuO}_6$  distorted octahedra. In the case of the first octahedron O5 is situated on the basal plane of the octahedron and O5  $p_x/p_y$  form  $pd\sigma$  antibond with the Cu  $d_{x^2-y^2}$  orbital, whereas O5' is situated at the apical position for this octahedron. The reverse is true for the second octahedron. Therefore Cu  $d_{x^2-y^2}$  orbitals of two  $\text{Cu}^{2+}$  sites placed at the same structural dimer unit are misaligned, which is responsible for the weak Cu-Cu intradimer interaction. We note that the internal parameters associated with atomic positions of Cu, O5 and O5' are such that the Cu-O5-Cu and Cu-O5'-Cu angles turn out to be close to  $90^\circ$  ( $96.76^\circ$ ). The Cu-Cu interaction within the structural dimer, which is weak in general, is therefore in the borderline where a sign change in the exchange interaction from antiferromagnetic to ferromagnetic may occur [23].

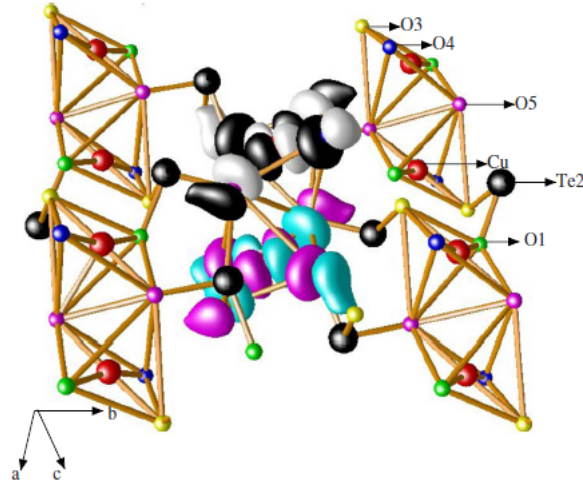


Fig. 3.12: Cu  $d_{x^2-y^2}$  downfolded NMTOs, placed at two Cu sites situated within the same structural dimer. The O2 sites with long Cu-O2 bond lengths have been removed for better view. Color convention is the same as in Fig. 3.10.

### ♣ Proposed low energy model Hamiltonian

The description of the spin model for  $\text{CuTe}_2\text{O}_5$  as obtained from the NMTO-downfolding technique turned out to be that of a system of coupled dimers in a two-dimensional (2D) grid (see Fig. 3.13). We reduced the underlying spin model to that of a 2D model, because the interlayer couplings were estimated to be 2 orders of magnitude smaller than the intralayer couplings. Inclusion of the coupling corresponding to  $t_5$  has also been found to have marginal effects. The corresponding spin-1/2 Heisenberg Hamiltonian on a  $N_1 \times N_2$  lattice is:

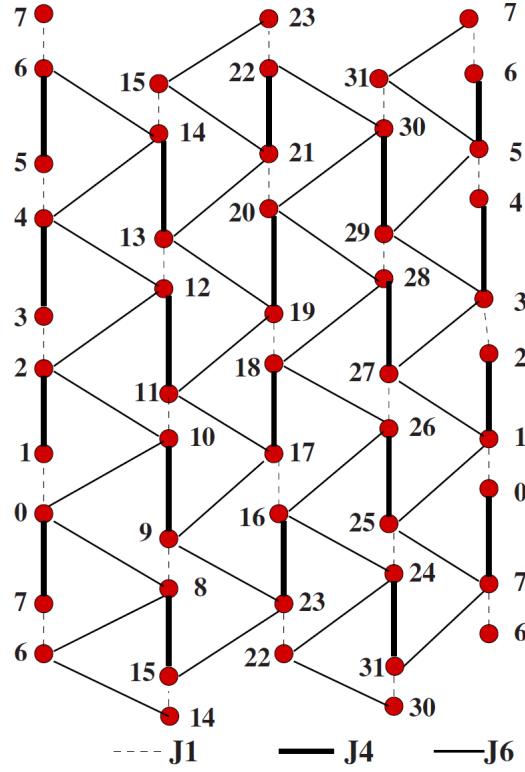


Fig. 3.13: The 2D coupled dimer model shown on a  $8 \times 4$  (32 site) lattice. Periodic boundary conditions have been applied on both directions. The thick, thin and dashed lines represent the strongest  $J_4$ , the next strong  $J_6$  and the weak structural intradimer interaction  $J_1$ , respectively. The site index  $k$  is given by  $k=N_1(l+m)$ , where  $m$  runs over number of rows in the square lattice ( $m=0,1,\dots,N_1$ ) and  $l$  runs over the number of columns in the square lattice ( $l=0,1,\dots,N_2$ ).

$$\begin{aligned}
 H = & J_1 \sum_{j=0}^{N_2-1} \sum_{i=0}^{\frac{N_1}{2}-1} (\mathbf{S}_{2i,j} \mathbf{S}_{2i+1,j}) + J_4 \sum_{j=0}^{N_2-1} \sum_{i=0}^{\frac{N_1}{2}-1} (\mathbf{S}_{2i+1,j} \mathbf{S}_{2i+2,j}) \\
 & + J_6 \sum_{j=0}^{\frac{N_2}{2}-1} \sum_{i=0}^{\frac{N_1}{2}-1} [(\mathbf{S}_{2i,2j} \mathbf{S}_{2i,2j+1} + \mathbf{S}_{2i,2j} \mathbf{S}_{2i+2,2j+1}) \\
 & + (\mathbf{S}_{2i+1,2j} \mathbf{S}_{2i+1,2j-1} + \mathbf{S}_{2i+1,2j} \mathbf{S}_{2i+3,2j-1})] \quad (3.3)
 \end{aligned}$$

where  $J_1$ ,  $J_4$ , and  $J_6$  are the exchange integrals corresponding to the hopping paths  $t_1$ ,  $t_4$ , and  $t_6$ , respectively. Interestingly, this model reduces to the model grid that describes the magnetic behavior of  $\text{CaCuGe}_2\text{O}_6$  when  $J_1 = 0$ . In that case, the two-dimensional model has (using the present notation) two critical points at  $J_6 \approx -0.9J_4$  and  $J_6 \approx 0.55J_4$  [2].

### 3.5 Susceptibility, magnetization and specific heat

In order to check the goodness of our proposed model, we calculated the magnetic susceptibility as well as magnetization and specific-heat properties by considering the above mentioned spin-1/2 Heisenberg model. The analysis of model (Eq. 3.3) was done by the quantum Monte Carlo method (stochastic series expansion) [24]-[26] on a  $20 \times 20$  lattice. While the NMTO-downfolding technique gives us an estimation for hopping parameters, it does not provide directly values of exchange integrals. The exchange coupling,  $J$ , can be expressed in general as a sum of antiferromagnetic and ferromagnetic contributions,  $J = J^{AFM} + J^{FM}$ . In the limit of large correlation, typically valid for Cu based system, the antiferromagnetic contribution,  $J^{AFM}$ , is related to the hopping integral  $t$  by the second-order perturbation relation  $J^{AFM} = 4t^2/U$ , where  $U$  is the effective on-site Coulomb repulsion. In absence of a satisfactory approach for computing  $J$  directly, in the following we considered the NMTO-downfolding inputs to built up the model and starting point for relative estimates of various exchange interactions. We defined the parameters,

$$\alpha_1 = \frac{J_6}{J_4}, \alpha_2 = \frac{J_1}{J_4} \quad (3.4)$$

which measure the ratio of the interdimer  $J_6$  and structural intradimer  $J_1$  interactions with respect to the exchange interaction which was suggested from the downfolding calculations to be the strongest  $J_4$ .

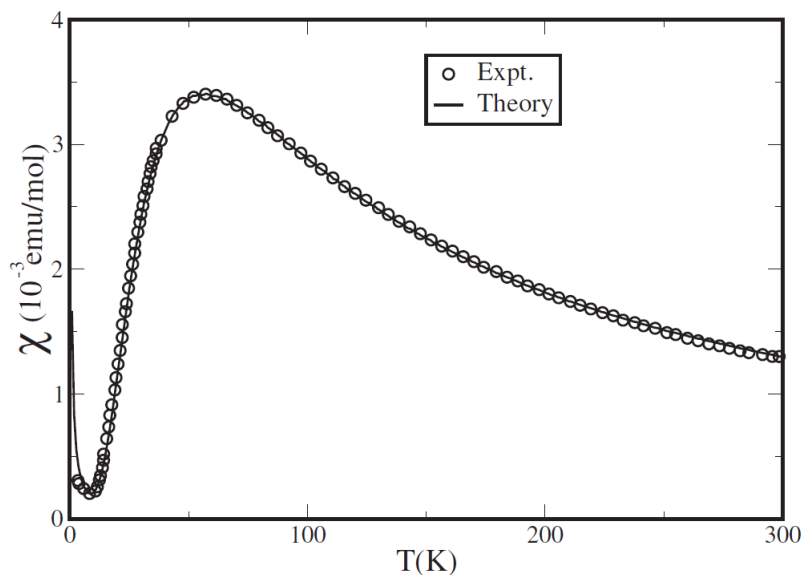


Fig. 3.14: Temperature dependence of magnetic susceptibility for  $\text{CuTe}_2\text{O}_5$ . The circles correspond to experimental data (Ref.[16]) and the solid line corresponds to calculated susceptibility based on a 2D-coupled dimer model.

The optimal values of  $\alpha_1$  and  $\alpha_2$  as well as the strength of the primary interaction  $J_4$  and the effective  $g$  factor were obtained by fitting the QMC results for the susceptibility,

$$\chi^{th} = \langle (S^z - \langle S^z \rangle)^2 \rangle \quad (3.5)$$

with the experimental susceptibility [in (emu/mol)] at intermediate to high temperatures via [27]  $\chi = 0.375(g^2/J)\chi^{th}$ . To simulate the low-temperature region of the susceptibility data, we included the respective Curie contribution from impurities as  $\chi^{CW} = C_{imp}/T$ . The calculated susceptibility in comparison to experimental data is shown in Fig. 3.14.

The best fit corresponds to the intradimer exchange integral  $J_4=92.4$  K, very close to the value proposed by Deisenhofer *et.al.* [16] for the strongest dimer coupling. The optimal value of the  $g$  factor=2.17 was found to be slightly larger than the spin only value of  $g=2$ , in agreement with ESR measurements [16]. The optimal values for the coupling ratios in Equ. 3.4 were found to be  $\alpha_1=0.27$  and  $\alpha_2=0.07$ , rather close to the estimates, 0.28 and 0.11, respectively, obtained using the second-order perturbation relationship between exchange interaction ( $J$ ) and the hopping integral ( $t$ ) given by the NMTO-downfolding study. The theoretically estimated ratio of strongest interdimer and structural intradimer interaction, given by  $\alpha_2$ , was found to be in good agreement with that obtained from the analysis of recent electron-spin-resonance measurements by Eremina *et.al.* [28]. The weak  $J_1$  interaction turned out to be of antiferromagnetic nature giving rise to a positive sign for  $\alpha_2$ .

With the stochastic series-expansion implementation of the quantum Monte Carlo method, it is possible to simulate quantum spin models in an external field. In Fig. 3.15, we present the computed magnetization as a function of temperature  $M(T)$  for various magnetic fields strengths and in Fig. 3.16 we show the comparison of  $M(T)$  for the model proposed in this work and the alternating chain model of Deisenhofer *et.al.* [16] for  $H=12.7$  T and  $H=31.7$  T. Two models show distinctly different behavior at moderate to high magnetic fields. In the inset of Fig. 3.15 we show the magnetization curve for  $\text{CuTe}_2\text{O}_5$  as a function of applied magnetic field up to the saturation field at  $T=10$  K. While it would be admittedly difficult to reach the saturation field experimentally, part of this data may be directly compared with experiment.

We also calculated the specific heat  $C_v(T)$  for both models and the results are presented in Fig. 3.17. While the overall qualitative shapes of the  $C_v(T)$  versus temperature curves for both models are similar, there are important quantitative distinctions which capture the different nature of the models. Our above computed thermodynamic quantities provide a useful framework to test the validity of our proposed model in terms of further experimental measurements.

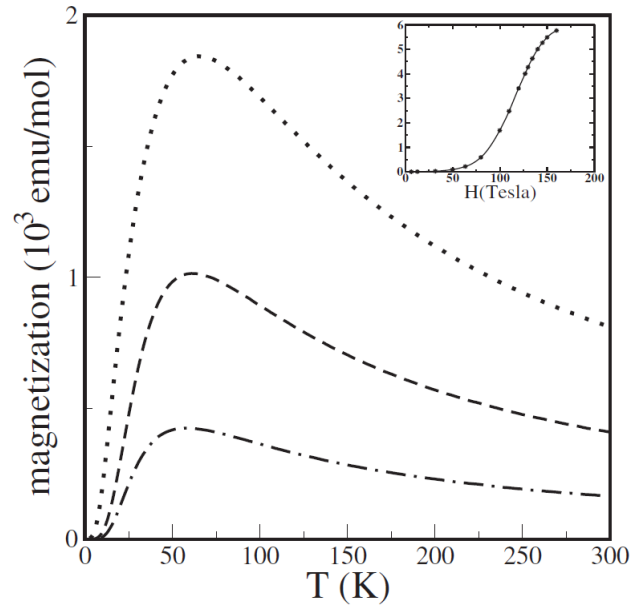


Fig. 3.15: Magnetization plotted as a function of temperature for the 2D-coupled dimer model of  $\text{CuTe}_2\text{O}_5$  in an applied magnetic field of strengths  $h/J=0.2, 0.5, 1.0$  (bottom to top) which correspond to  $H=12.7, 31.7, 63.4$  T. The inset shows the magnetization versus  $H$  upto the saturation magnetic field at  $T=10$  K.

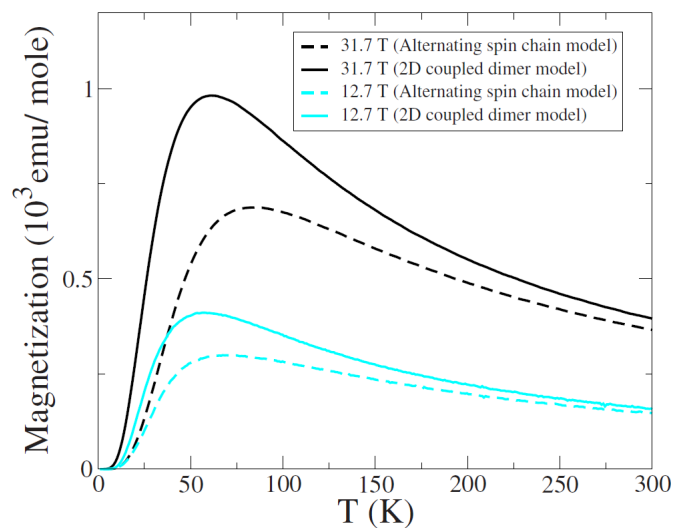


Fig. 3.16: Magnetization plotted as a function of temperature for the 2D-coupled dimer model of  $\text{CuTe}_2\text{O}_5$  and the alternating chain model of Ref.[16] for two values of the magnetic field  $H=12.7$  T and  $H=31.7$  T.

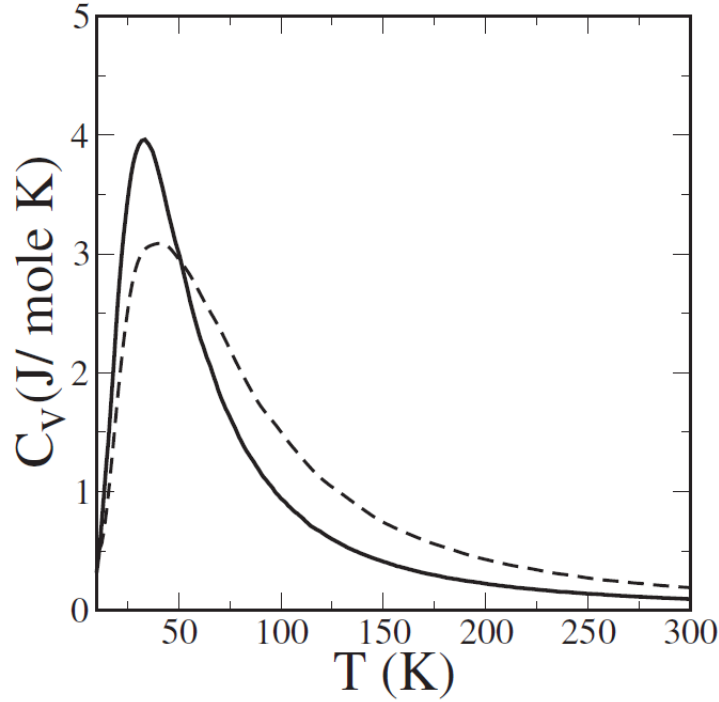


Fig. 3.17: Specific heat plotted as a function of temperature for  $\text{CuTe}_2\text{O}_5$  for the 2D-coupled dimer model (solid line) and the model of Ref.[16] (dashed line).

### 3.6 Summary and outlook

The analysis of the electronic structure of  $\text{CuTe}_2\text{O}_5$  by first-principles NMTO-downfolding calculations as well as the calculation and examination of susceptibility data by the QMC method lead to a unique description of this system as a 2D coupled dimer model. The strongest Cu-Cu interaction is between Cu pairs belonging to different structural dimer units and connected by two O-Te-O bridges. Two additional in-plane interactions of about  $1/3$  and  $1/10$  of the strongest interaction have been found; the latter one being the structural intradimer interaction. This leads to a somewhat different model compared to recent theoretical considerations in Ref.[16], which suggest an alternating spin-chain system with strong interdimer and intradimer couplings as the simplest possible model for the  $\text{CuTe}_2\text{O}_5$ . Based on our proposed model, we calculated the magnetization and specific heat which may be compared with new experimental measurements. We hope that our work will stimulate further experimental studies.

# References

- [1] P. Lemmens, G. Guntherodt, and C. Gros, Phys. Rep. **375**, 1 (2003).
- [2] R. Valent, T. Saha-Dasgupta, and C. Gros, Phys. Rev. B **66**, 054426 (2002).
- [3] S. Derakhshan, H. L. Cuthbert, J. E. Greedan, B. Rahaman, and T. Saha-Dasgupta, Phys. Rev. B **76**, 104403 (2007).
- [4] C. Gros, P. Lemmens, M. Vojta, R. Valenti, K. Y. Choi, H. Kageyama, Z. Hiroi, N. V. Mushnikov, T. Goto, M. Johnsson, and P. Millet, *ibid.* **67**, 174405 (2003).
- [5] T. Saha-Dasgupta, R. Valent, F. Capraro, and C. Gros, Phys. Rev. Lett. **95**, 107201 (2005).
- [6] R. Valent and T. Saha-Dasgupta, Phys. Rev. B **65**, 144445 (2002).
- [7] R. Valent, T. Saha-Dasgupta, J. V. Alvarez, K. Pozgajcic, and C. Gros, Phys. Rev. Lett. **86**, 5381 (2001).
- [8] P. Lemmens, K. Y. Choi, R. Valent, T. Saha-Dasgupta, E. Abel, Y. S. Lee, and F. C. Chou, New J. Phys. **7**, 74 (2005).
- [9] T. Saha-Dasgupta, R. Valenti, H. Rosner, and Claudius Gros, Europhys. Lett. **67**, 63 (2004).
- [10] M. Johnsson, K.W. Tornroos, F. Mila, and P. Millet, Chem. Mater. **12**, 2853 (2000).
- [11] M. Herak, H. Berger, M. Prester, M. Miljak, I. Zivkovic, O. Milat, D. Drobac, S. Popovic, and O. Zaharko, cond-mat/0507684 (2005).
- [12] P. Lemmens, K.-Y. Choi, E.E. Kaul, C. Geibel, K. Becker, W. Brenig, R. Valenti, C. Gros, M. Johnsson, P. Millet, and F. Mila, Phys. Rev. Lett. **87**, 227201 (2001).
- [13] B. Rahaman, H. O. Jeschke, R. Valent, and T. Saha-Dasgupta, Phys. Rev. B **75**, 024404 (2007).
- [14] R. Takagi, M. Johnsson, V. Gnezdilov, R. K. Kremer, W. Brenig, and P. Lemmens, Phys. Rev. B **74**, 014413 (2006).

- [15] P. Millet, B. Bastide, M. Johnsson, *Solid State Commun.* **113**, 719 (2000).
- [16] J. Deisenhofer, R. M. Eremina, A. Pimenov, T. Gavrilova, H. Berger, M. Johnsson, P. Lemmens, H.-A. Krug von Nidda, A. Loidl, K.-S. Lee, and M.-H. Whangbo, *Phys. Rev. B* **74**, 174421 (2006).
- [17] B. Bleaney and K. D. Bowers, *Proc. R. Soc. London, Ser. A* **214**, 451 (1952).
- [18] D. C. Johnston, R. K. Kremer, M. Troyer, X. Wang, A. Klumper, S. L. Budko, A. F. Panchula, and P. C. Canfield, *Phys. Rev. B* **61**, 9558 (2000).
- [19] T. Nakajima, H. Mitamura, and Y. Ueda, *J. Phys. Soc. Jpn.* **75**, 054706 (2006).
- [20] For recent reviews, see M.-H. Whangbo, H.-J. Koo, and D. J. Dai, *Solid State Chem.* **176**, 417 (2003); M.-H. Whangbo, D. Dai, and H.-J. Koo, *Solid State Sci.* **7**, 827 (2005).
- [21] R. Hoffmann, *J. Chem. Phys.* **39**, 1397 (1963).
- [22] K. Hanke, V. Kupcik, and O. Lindqvist, *Acta Crystallogr., Sect. B: Struct. Crystallogr. Cryst. Chem.* **29**, 963 (1973).
- [23] J. B. Goodenough, *Phys. Rev.* **100**, 564 (1955); J. Kanamori, *J. Phys. Chem. Solids* **10**, 87 (1959); P. W. Anderson, *Solid State Phys.* **14**, 99 (1963).
- [24] A. W. Sandvik, *Phys. Rev. B* **59**, R14157 (1999).
- [25] A. Dorneich and M. Troyer, *Phys. Rev. E* **64**, 066701 (2001).
- [26] K. Louis and C. Gros, *Phys. Rev. B* **70**, 100410(R) (2004).
- [27] D. C. Johnston, R. K. Kremer, M. Troyer, X. Wang, A. Klumper, S. L. Budko, A. F. Panchula, and P. C. Canfield, *Phys. Rev. B* **61**, 9558 (2000).
- [28] R. Eremina, T. P. Gavrilova, N.-A. Krug von Nidda, A. Pimenov, J. Deisenhofer, and A. Loidl, *Phys. Solid State* **50**, 283 (2008).

# Chapter 4

## Electronic structure of $\text{La}_2\text{CuO}_4$ in the T and T' crystal structures.

Content of this chapter has been published in: Hena Das and T. Saha-Dasgupta, Phys. Rev. B **79**, 134522 (2009).

### 4.1 Introduction

As we have mentioned in the introductory chapter of this thesis, the undoped compound  $\text{La}_2\text{CuO}_4$  serves as the parent compound of the hole-doped cuprate superconductors, e.g.,  $\text{La}_{2-x}\text{Ba}_x\text{CuO}_4$ , which crystallizes in  $\text{K}_2\text{NiF}_4$ -type T structure [1], as well as the parent compound of the electron-doped cuprate superconductors, e.g.,  $\text{La}_{2-x}\text{Ce}_x\text{CuO}_{4+y}$ , which however crystallize in  $\text{Nd}_2\text{CuO}_4$ -type T' structures [2]. For the benefit of understanding the mechanism of high-temperature superconductivity (HTS), it would have been interesting to study the properties of the parent compounds in both hole-doped and electron-doped cases. The situation, however, is complicated by the fact that the preparation of undoped T'-structured parent compound is hindered by the structural phase transition to T structure occurring around  $x \approx 0.05$  [3]. One trick to synthesize  $\text{La}_2\text{CuO}_4$  in the T' phase is to the replacement of La by smaller but isovalent ions, such as Y, Lu, Sm, Gd. . . [4]. The interesting observation was, the structural phase transition from T to T' is coupled to a change in resistivity of several orders of magnitude.  $\text{La}_2\text{CuO}_4$  in the T' structure is strongly metallic ( $d\rho/dT > 0$ ), while in the T structure it is insulating ( $d\rho/dT < 0$ ) (see Fig. 4.1). While this finding hints toward an interesting implication on mechanism of superconductivity, the experimental situation is faced with difficulties [6] such as the issue of strain effect (since the fabrication was carried out by thin-film synthesis technique), oxygen content of the sample, *etc.* Therefore we took the task of investigating electronic structure of  $\text{La}_2\text{CuO}_4$  in T and T' using first-principles techniques, which is devoid of experimental difficulties concerning synthesis. A description of this investigation has been summarized in this chapter.

It is widely accepted that correlation plays a significant role in the correct description of the electronic structure of cuprates [7]. The density-functional based theories within the local-density approximation (LDA) on the other hand are expected to take into account the structural and chemical intricacies which is needed for the study involving comparison

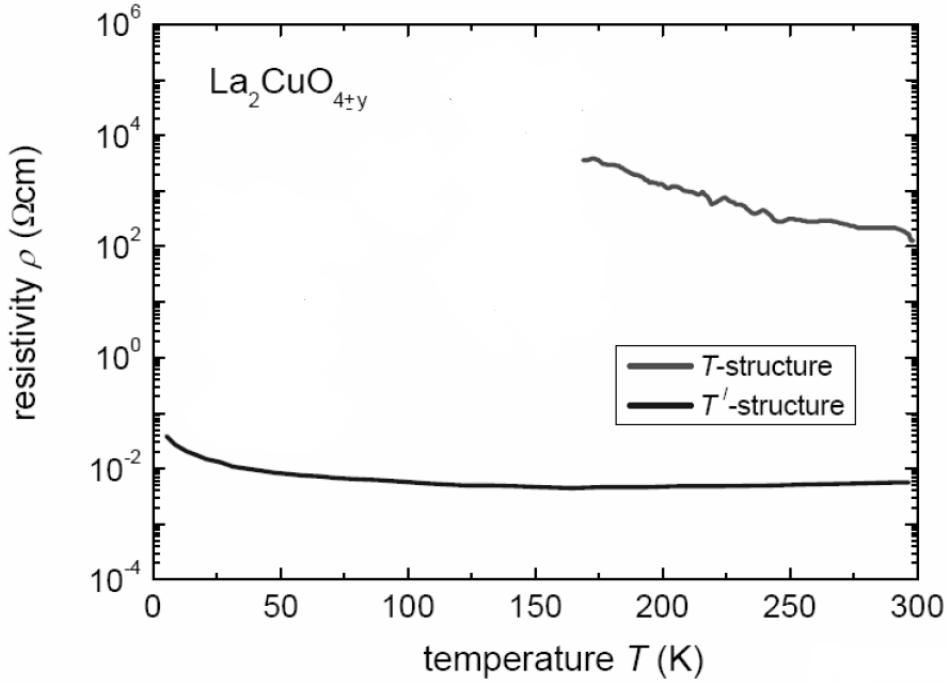


Fig. 4.1: Comparison of resistivity of  $\text{La}_2\text{CuO}_{4\pm y}$  thin films with the T- and T'-structure for  $y \sim 0$  (taken from Ref.[5]). The very high resistivity in the T' phase below 150 K was not measurable with their experimental set up.

of electronic structure of  $\text{La}_2\text{CuO}_4$  in two different crystal structures. We therefore carried out calculations combining these two aspects within the framework of LDA+dynamical mean field theory (DMFT). The choice of DMFT for the many-body part is driven by the fact that the many-body formulation of DMFT takes fully into account the temporal fluctuations, though freezes the spatial fluctuations. This aspect makes it ideally suited to describing correlated metals as well as insulators, as is needed for the present problem.

## 4.2 Structural details

Both T and T' crystal structures of  $\text{La}_2\text{CuO}_4$  are determined to be in body-centered tetragonal I4/mmm structure [8]. La, Cu, and the plane oxygen (O1) occupy the identical symmetry positions in T and T' given by  $4e [(0,0,\pm u_{La})]$ ,  $2a [(0,0,0)]$  and  $4c [(0,1/2,0),(1/2,0,0)]$ , respectively. As we have discussed before in our introductory chapter, the two structures differ in the position of the out-of-plane oxygen (O2) (see Fig. 4.2). In case of T structure, O2 occupies the position directly below or above Cu (given by  $4e$ ) while for T' it occupies the position directly below or above O1 (given by  $4d$  positions). This results into structures consisting of square  $\text{CuO}_2$  planes without any apical oxygen in T' structure instead of two-dimensional (2D) array of  $\text{CuO}_6$  octahedra in T structure. The in-plane lattice parameter shows an expansion with a slightly smaller  $c/a$  ratio in case of T' structure

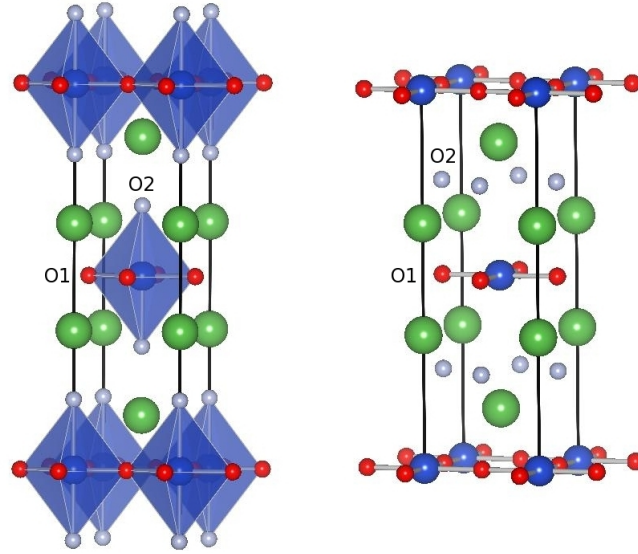


Fig. 4.2: Crystal structure of T (left panel) and T' (right panel) structures. The rear-earth, Cu, and O atoms are represented by the large, mediums and small sized balls, respectively. The in-plane and out-of-plane oxygen atoms are represented by dark and light shades, respectively.

( $a=4.005 \text{ \AA}$ ,  $c=12.550 \text{ \AA}$ ) compared to T structure ( $a=3.803 \text{ \AA}$ ,  $c=13.150 \text{ \AA}$ ), resulting into about 6% expansion in volume [9].

### 4.3 One-particle electronic structure

Fig. 4.3 shows the LDA band structure of  $\text{La}_2\text{CuO}_4$  in T and T' structures calculated in linear muffin-tin-orbital basis projected on to Cu  $d_{x^2-y^2}$  character. We find that, while the basic electronic structure is similar between T and T' structures with a single  $pd\sigma$  antibonding band arising out of Cu  $d_{x^2-y^2}$  and O1  $p\sigma$  crossing the Fermi energy ( $E_F$ ), the details of the low-energy features are markedly different in two cases in terms of the position and shape of the saddle point. The obtained band structure in T' structure is found to be similar to that of reported band structure of isostructural  $\text{Nd}_2\text{CuO}_4$  [10]. This happens due to change in position of the out-of-plane oxygen, O2. O2, which is positioned directly below O1 for T' structure, develops a strong hybridization with O1 resulting into O1  $p_z$ -O2  $p_z$  band lying close to  $E_F$ . The O2  $p_x - p_y$  originating from square O2<sub>2</sub> layer in T' structure also is energetically positioned close to  $E_F$ . In case of T structure on the other hand the conduction band is significantly mixed with Cu  $3z^2$  and O2  $p_z$  character due to short Cu-O2 distance, with O2 serving the purpose of apical oxygen in  $\text{CuO}_6$  octahedra. The resulting difference in case of T' structure pushes down the energy of the saddle point and changes the shape of the 2D Fermi surface from square oriented in  $(\pi, \pi)$  direction in T structure to a rounded square oriented in  $(\pi, 0)$  direction

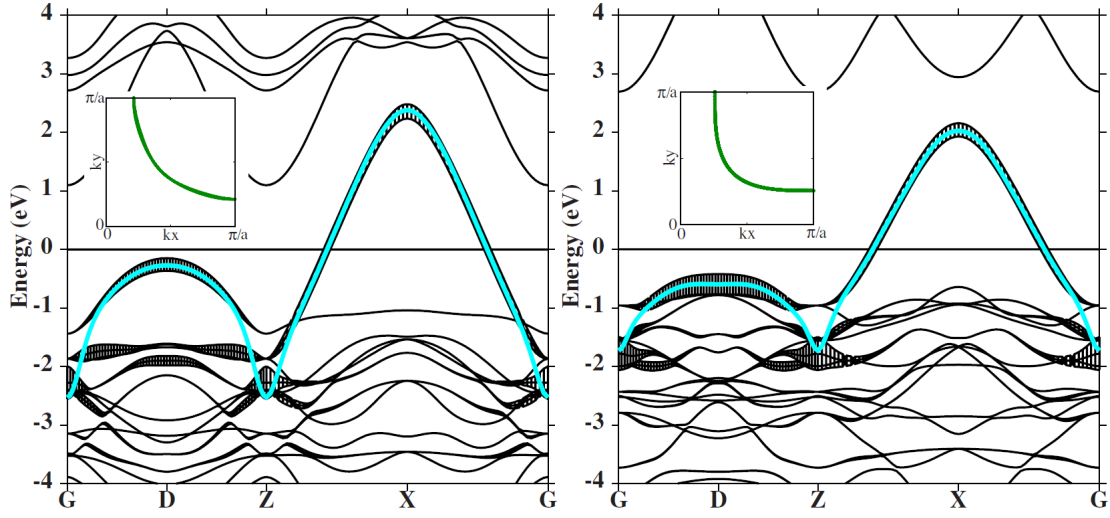


Fig. 4.3: Band structure of  $\text{La}_2\text{CuO}_4$  in T (left panel) and  $T'$  (right panel) structures plotted along the high symmetry points of the body centered tetragonal BZ. The fatness associated with each band is proportional to the orbital character of Cu  $d_{x^2-y^2}$ . The single band shown as thick line is the effective one band obtained by NMTO downfolding technique. The inset shows the corresponding Fermi surfaces.

in  $T'$  structure (see inset of Fig. 4.3).

As discussed above, the low-energy-band structures are described by a single  $p d \sigma$  antibonding band. This gives rise to a single sheet in the Fermi surface which is also seen in the photoemission experiment [11]. It is therefore natural that most theories of HTS cuprates [12] are based on single-band  $t-t'-t''-U$ -like or  $t-t'-t''-J$ -like model with an effective Cu  $d_{x^2-y^2}$ -like orbital per  $\text{CuO}_2$  layer.  $t$ ,  $t'$ ,  $t''$ , ..... denote the nearest-neighbor, second-nearest-neighbor, third nearest-neighbor and further nearest-neighbor hopping integrals, respectively, on a square lattice with Cu ions. In order to derive a single-band one-particle Hamiltonian, we performed NMTO downfolding calculations by integrating out all the degrees of freedom other than Cu  $d_{x^2-y^2}$ . Such an approach for single-band modeling of hole-doped cuprates [13] has been found to be highly successful. The resulting single band for  $\text{La}_2\text{CuO}_4$  in T and  $T'$  structures, in comparison to full LDA band structure, is also shown in Fig. 4.3.

In Figs. 4.4(a) and (b), we show the plot of such Wannier-type functions for both T and  $T'$  structure projected on to the  $\text{CuO}_2$  plane and perpendicular to the  $\text{CuO}_2$  plane, respectively. The Wannier-type functions have the central Cu  $d_{x^2-y^2}$  symmetry, which antibonds to O1  $p\sigma$  in its immediate neighborhood a general feature of the electronic structure of HTS cuprates. The tails extending to further neighbors reflect the structure specific trend between T and  $T'$ . The immediate feature to notice is that the Wannier-type functions of  $T'$  structure appears to be more delocalized in plane and more compact out of plane compared to that of T structure. If one interprets the hopping integrals as overlap integrals for such Wannier-type functions, one may realize that this larger amplitudes at

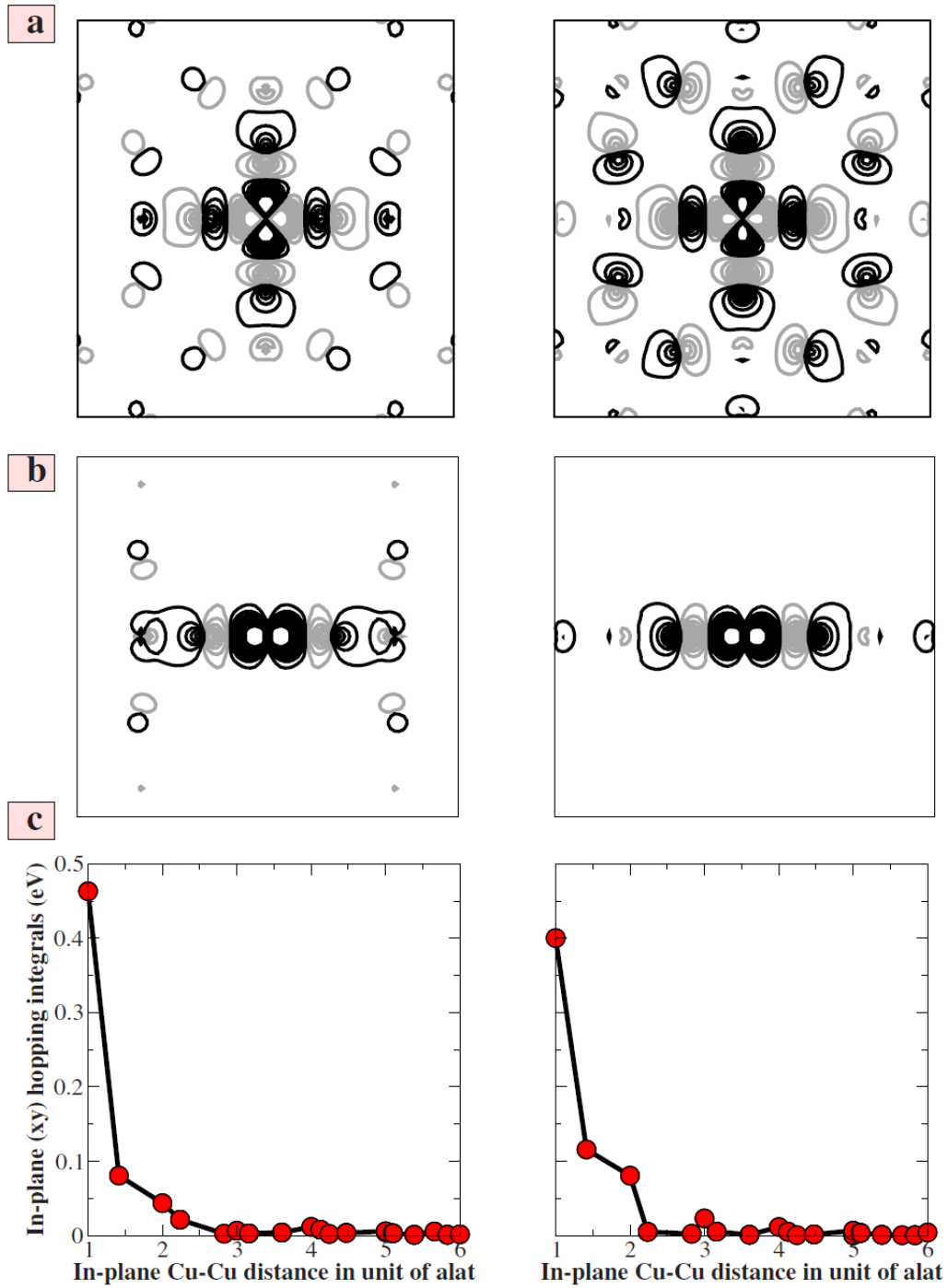


Fig. 4.4: Effective Cu  $d_{x^2-y^2}$  Wannier-type functions and the hopping integrals of a single-band model of  $\text{La}_2\text{CuO}_4$  in T (left panels) and T' (right panels) structures. (a) Wannier type functions projected on to  $\text{CuO}_2$  plane ( $ab$  plane) and (b) Wannier-type functions projected on to plane perpendicular to  $\text{CuO}_2$  plane ( $ac$  plane). Lobes of opposite signs are colored as black and gray. (c) In-plane hopping integrals in the basis of effective Wannier-type functions, plotted as a function of Cu-Cu distances, measured in unit of lattice constant (alat).

the further neighbor oxygen results into larger further neighbor in-plane hoppings in a one-band model. The plot of the functions seen from side (c.f. Fig. 4.4(b)) shows the out-of-plane orbital characters of the conduction-band Wannier-type functions. Considering the case of T structure, starting from the central Cu atom and going in the a direction, we see Cu  $d_{x^2-y^2}$  antibond to neighboring O1  $p_x$ , which itself anti-bonds to  $3z^2$  on the next Cu. From here and moving along the  $c$  direction, we see also  $3z^2$  antibond to O2  $p_z$ , which itself bonds to further neighbor La orbitals. For T' structure we find about the same amount of Cu  $d_{x^2-y^2}$  and nearly same amount of O1 character but negligible Cu  $3z^2$  and certainly no O2  $p_z$  since due to symmetry O2  $p_z$  cannot bind to Cu  $d_{x^2-y^2}$  any more. We on other hand find with diffused Cu  $s$  character that causes inflation of the black lobe of O1-like tail compared to the gray lobe. Constructing the real space Hamiltonians in the basis of the above discussed Wannier-type functions for the conduction band, as shown in Fig. 4.4(c), exhibit a reduction in nearest-neighbor hopping interaction  $t$  in T' structure compared to T structure, which is governed by the increase in Cu-O1 bond length in case of T' structure compared to T structure. We however, notice an enhancement of the next-nearest-neighbor hopping,  $t'$ , and other longer-ranged hoppings,  $t''$ , and so on in T' structure compared to T structure in agreement with conclusions drawn on basis on the plot of Wannier-type functions. The spread of the single-band Wannier function and the resulting tight-binding Hamiltonian may be expressed in terms of the so-called range parameter,  $r$ , as introduced in Ref.[13]. The  $r$ -parameter is found to be 0.14 for T structure and 0.4 for T' structure. As has been found in Ref.[13], the range is intimately connected to the energy of axial orbital, a hybrid between Cu  $s$ ,  $3z^2$ , and apical oxygen  $p_z$ , which is governed by the distance of apical oxygen to  $\text{CuO}_2$  plane. In cases of short distances of apical oxygen to  $\text{CuO}_2$  plane, finite mixing of Cu  $s$  with Cu  $3z^2$  and apical oxygen  $p_z$  character causes the energy of the hybrid axial orbital to be pushed up in energy which in turn reduces the range of the in-plane hoppings. While such a scenario is valid for T-structured  $\text{La}_2\text{CuO}_4$ , in absence of the apical oxygen in T' structure such mechanism is not operative for T'-structured  $\text{La}_2\text{CuO}_4$ , giving rise to the long range of the in-plane hoppings.

## 4.4 LDA+DMFT results and discussion

In the next step, we carried out dynamical mean field theory (DMFT) calculations on the 2D single-band Hubbard Hamiltonian given by,

$$H = \sum_{i,j,\sigma} t_{i,j} c_{i\sigma}^\dagger c_{j\sigma} + U \sum_i n_{i\uparrow} n_{i\downarrow} - \mu \sum_i n_i \quad (4.1)$$

where  $t_{i,j}$ s are the single-particle hopping interaction between the effective Cu  $d_{x^2-y^2}$  as obtained in downfolded NMTO-Wannier-type function basis.  $n_{i\sigma} = c_{i\sigma}^\dagger c_{i\sigma}$ , where  $c_{i\sigma}^\dagger$

creates a  $\sigma$ -spin electron at site  $i$  and  $U$ , is the Hubbard interaction. The double-counting correction is absorbed in the chemical-potential shift  $\mu$ . The quantum impurity problem within DMFT in our calculations was solved by the numerically exact quantum Monte Carlo (QMC) scheme [14]. The computational effort becomes prohibitive rather quickly as one lowers the temperature since in order to maintain the accuracy of the calculation one needs to increase the imaginary time slices as one increases  $\beta$ . The results reported in the following are done for  $\beta = 30$  (in unit of  $\text{eV}^{-1}$ ) with 290 slices in imaginary time and 100 000 QMC sweeps. The maximum entropy method [15] had been used for analytical continuation of the diagonal part of the Greens function matrix to the real energy axis to get the DMFT spectral density.

The choice of Hubbard  $U$  is a delicate issue in the whole calculation scheme. The choice of  $U$  for a given compound depends on the choice of representation basis and therefore depends on the model used for the description of the compound. The  $U$  is expected to be significantly screened in case of a single-band model due to the much delocalized character of the effective single-band Wannier-type function. The Slater integral computed in the basis of the computed Wannier-type functions [16] show significant reduction compared to that calculated using constraint density-functional calculations [17] for cuprates. This is also in accordance with the recent proposal by Comanac *et.al.* [18] obtained combining DMFT studies and analysis of optical spectra of cuprates that the correlation strength in the cuprates is actually smaller than the critical  $U$  for a Mott transition in the non-magnetic sector. In the calculations reported in the following, we fixed the value of  $U$  to 4.5 eV. We kept the same value of  $U$  between the T and T' structures although the T' structure is expected to have a lower  $U$  value compared to T structure due to the more delocalized nature in case of T' structure.

The calculated spectrum as presented in Fig. 4.5 show formation of lower and upper Hubbard bands, signaling the correlated nature of the compounds. Interestingly, for T' structure we find simultaneous presence of Hubbard sub-bands and a coherent quasiparticle peak, compared to that of an insulator as found in the case of T-structured  $\text{La}_2\text{CuO}_4$ . We note that the conclusions drawn are based on the finite temperature calculations, carried out at a temperature of 580 K. Since the overall bandwidths of the single-electron spectra for both T and T' are about 4 eV and the  $U$  value used in the DMFT calculations is 4.5 eV, which may be about or slightly less than the critical  $U$  value for the Mott transition, the T=0 state might be metallic even for the T-structured  $\text{La}_2\text{CuO}_4$ , as hinted in Ref.[18]. It will be therefore fair to claim that the T-structured  $\text{La}_2\text{CuO}_4$  has a lower coherence temperature (lower than 580 K) compared to that of the T'-structured  $\text{La}_2\text{CuO}_4$ , indicating the more metallic character of the T'-structured  $\text{La}_2\text{CuO}_4$  compared to T structure.

We further note that the bandwidth of the single-particle density of states (DOS) for T' structure is somewhat smaller compared T structure. Nevertheless our finite temperature

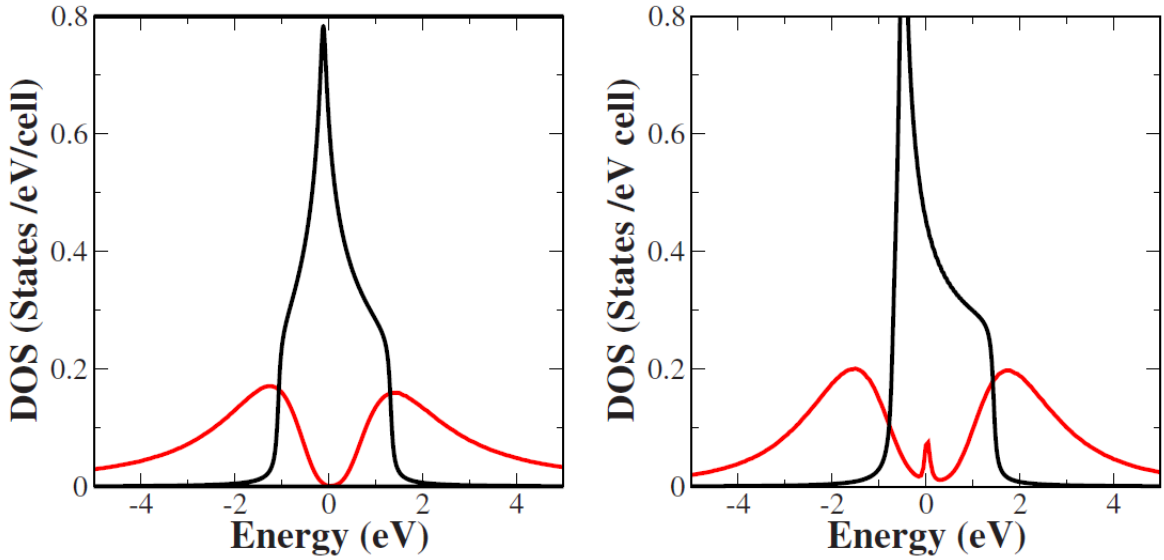


Fig. 4.5: DMFT spectral function at  $T=580$  K (thick line) and the LDA DOS (thin line)  $\text{La}_2\text{CuO}_4$  in T (left panel) and  $T'$  (right panel) structures. The zero of the energy is set at  $\mu$ .

calculations find the metallic solution of the  $T'$  structure and the insulating solution of the T structure. This apparently counterintuitive result may be explained in terms of the fact that, instead of the bandwidth alone, what matters is the shape of the single-particle density of states, a good measure being the second moment of the density of states. The band energy is therefore measured [19] by  $(\frac{\mu_2}{\mu_0})$ , where  $\mu_2$  and  $\mu_0$  are the second and zeroth moments of the density of states. We found the second moment is determined by the interplay between the bandwidth, governed by the nearest-neighbor hopping parameter  $t$  and the range parameter  $r$ . For  $T'$  structure although the bandwidth is smaller than T structure, the  $r$  value is larger compared to T structure, which makes the second moment to be larger and hence the band energy to be larger.

## 4.5 Summary and outlook

To conclude, using combination of LDA to take into account the composition and structural aspect, and DMFT to take into account the correlation aspect, we have studied the electronic structure of T- and  $T'$ -structured  $\text{La}_2\text{CuO}_4$ . Our calculation shows the change in position of the out-of-plane oxygen between T and  $T'$  structures, resulting into significant changes in the one-particle electronic structure. Upon incorporation of correlation effect, these differences translate into insulating solution in case of T structure and correlated metallic situation in case of  $T'$  structure for calculations carried out at a temperature of 580 K. This indicates higher coherence temperature and therefore more metallic character for  $T'$  structure compared to T structure. Our study suggest that both

---

T- and T'-structured cuprates are close to or even below the critical  $U$  for Mott transition, and therefore far from a very strong-coupling regime, a fact which has been also suggested in Ref.[18]. As a result, the delicate band structure differences between T- and T'-structured  $\text{La}_2\text{CuO}_4$  cause the interesting effect of the more metallic character in one case over the other. Our findings seem to support the initial experimental studies made by Tsukada *et.al.* in this context. This should be explored more carefully in the future. Our LDA+DMFT calculations do not take into account the presence of antiferromagnetic fluctuations. We carried out antiferromagnetic LDA+U calculations, that gave rise to a small energy gap of  $\approx 0.1$  eV for T'-structured  $\text{La}_2\text{CuO}_4$ , compared to energy gap of 1.8 eV for T-structured  $\text{La}_2\text{CuO}_4$ . However, the values of the band gaps are overestimated, which is a general drawback of LDA+U approach, it shows T' phase to be more metallic than T. Therefore, the obtained results may be considered as the effect of correlation on the single-particle band structure arising out of presence and absence of apical oxygen in T and T' structures. Our study nevertheless provides useful hint to future studies.

# References

- [1] J. G. Bednorz and K. A. Müller, *Z. Phys. B: Condens. Matter* **64**, 189 (1986).
- [2] A. Sawa, M. Kawasaki, H. Takagi, and Y. Tokura, *Phys. Rev. B* **66**, 014531 (2002).
- [3] M. Naito and M. Hepp, *Jpn. J. Appl. Phys., Part 1* **39**, L485 (2000).
- [4] A. Tsukada, Y. Krockenberger, M. Noda, H. Yamamoto, D. Manske, L. Alff, and M. Naito, *Solid State Commun.* **133**, 427 (2005).
- [5] A. Tsukada, Y. Krockenberger, M. Noda, H. Yamamoto, D. Manske, L. Alff, and M. Naito, *Solid State Comm.* **133**, 427 (2005).
- [6] P. G. Radaelli, J. D. Jorgensen, A. J. Schultz, B. A. Hunter, J. L. Wagner, F. C. Chou, and D. C. Johnston, *Phys. Rev. B* **48**, 499 (1993); H. Sato and M. Naito, *Physica C* **274**, 221 (1997).
- [7] P. W. Anderson, *Science* **235**, 1196 (1987).
- [8] Y. Tokura, H. Takagi, and S. Uchida, *Nature (London)* **337**, 345 (1989).
- [9] A. Tsukada, T. Greibe, and M. Naito, *Phys. Rev. B* **66**, 184515 (2002).
- [10] S. Massidda, N. Hamada, Jaejun Yu, and A. J. Freeman, *Physica C* **157**, 571 (1989).
- [11] N. P. Armitage, F. Ronning, D. H. Lu, C. Kim, A. Damascelli, K. M. Shen, D. L. Feng, H. Eisaki, Z.-X. Shen, P. K. Mang, N. Kaneko, M. Greven, Y. Onose, Y. Taguchi, and Y. Tokura, *Phys. Rev. Lett.* **88**, 257001 (2002).
- [12] F. C. Zhang and T. M. Rice, *Phys. Rev. B* **37**, 3759 (1988).
- [13] E. Pavarini, I. Dasgupta, T. Saha-Dasgupta, O. Jepsen, and O. K. Andersen, *Phys. Rev. Lett.* **87**, 047003 (2001).
- [14] J. E. Hirsch and R. M. Fye, *Phys. Rev. Lett.* **56**, 2521 (1986).
- [15] M. Jarrell and J. E. Gubernatis, *Phys. Rep.* **269**, 133 (1996).
- [16] W. Heitler and F. London, *Z. Phys.* **44**, 455 (1927).

- [17] O. Gunnarsson, O. K. Andersen, O. Jepsen, and J. Zaanen, *Phys. Rev. B* **39**, 1708 (1989).
- [18] A. Comanac, L. D. Medici, M. Capone, and A. J. Millis, *Nat. Phys.* **4**, 287 (2008).
- [19] F. Ducastelle, *Order and Phase Stability in Alloys, Cohesion and Structure*, edited by F. R. de Boer and D. G. Pettifor (North-Holland, Amsterdam, 1991), Vol. **3**.

# Chapter 5

## Evidence of kinetic-energy-driven antiferromagnetism in double perovskites.

Content of this chapter has been published in: Prabuddha Sanyal, Hena Das, and T. Saha-Dasgupta, Phys. Rev. B **80**, 224412 (2009).

### 5.1 Introduction

The discovery of room-temperature tunneling magnetoresistance (MR) and half-metallic ferromagnetic behavior of  $\text{Sr}_2\text{FeMoO}_6$  (SFMO) oxides with a Curie temperature  $T_c$  of about 400 K [1]-[6] has opened the possibility of designing spintronics materials operating at room temperature. However, unlike colossal magnetoresistive compounds as manganites, this MR does not arise from electron-phonon interactions. Rather, it is extrinsic, of tunnelling magnetoresistive origin. Since the report of the large MR effect and high magnetic transition temperature, a number of experimental studies such as NMR [7], X-ray emission spectroscopy [8], Hall measurements [9] and magnetic measurements [10] have been carried out to characterize various properties of this material. There have been also a number of theoretical studies involving both first-principles calculations [11]-[14] as well as model calculations [15]-[20]. The unusually high ferromagnetic transition temperature in  $\text{Sr}_2\text{FeMoO}_6$  and related material such as  $\text{Sr}_2\text{FeReO}_6$  was rationalized [11, 17] in terms of a kinetic-energy driven mechanism which produces a negative spin polarization at otherwise nonmagnetic site such as Mo or Re. Following this idea, a double-exchange like two-sublattice model was introduced and studied by different groups [15, 16],[18]-[20]. While most of the studies [15, 16, 19] were restricted only to ferromagnetic phase, some of the studies [16, 20] were extended to other competing magnetic phases too. Very recently [21], the problem has been studied in detail in terms of a full numerical solution of spin-fermion model and as well as in terms of reduced, classical magnetic model. These studies predict that when the competing magnetic phases are taken into account, the electron-doped model systems beyond a certain doping prefers to have antiferromagnetic (AFM) arrangement of Fe spins compared to ferromagnetic (FM) arrangement of the undoped system. The predicted antiferromagnetic phase in electron-doped system is kinetic-energy-driven rather than superexchange driven, as is the case, for example, in  $\text{Sr}_2\text{FeWO}_6$  (SFWO) [22], which is an insulating antiferromagnet with Néel temperature of

$\approx 20$  K. The superexchange-driven antiferromagnetic phase is necessarily insulating while the kinetic-energy-driven AFM phase may not be so. The prediction of such an antiferromagnetic phase of different origin is therefore of significance. While the kinetic-energy-driven antiferromagnetic phases have been suggested in hole-doped rare-earth manganites (e.g., the charge-exchange phase at half doping [23]), to the best of our knowledge, till date no reports of such analogous phases in double perovskites exist, thereby, opening up the possibility of experimental exploration in this front. However, the aforementioned model calculations were carried out in two dimension and with single band, which was justified by the assumption that the dominant nearest-neighbor B-B' interactions are operative between orbitals of same symmetry and within a given plane. These restrictions are not strictly true. Furthermore, the magnetic ordering in real material is three dimensional. A full three-dimensional, all-orbital calculation without these approximations, is therefore necessary to put the possible existence of the AFM phase in firm footing.

Considering the above-mentioned points, it is therefore, of interest to study the problem of electron doping using first-principles density-functional theory (DFT) -based calculations. The first-principles calculations which take into account all the structural and chemical aspects correctly is expected to provide more realistic scenario and verification of predictions made by model calculations. The Sr ions in SFMO can be substituted for trivalent cations, such as La, leading to  $\text{Sr}_{2-x}\text{La}_x\text{FeMoO}_6$ . This would cause electron doping in the system, with  $1 + x$  electron per formula unit in the conduction band, compared to 1 electron per formula unit in the undoped SFMO situation. To our knowledge, there exists very few first-principles study of the La-doped SFMO system. Few studies [24, 25] that exist explored only the ferromagnetic phase, did not consider the other competing magnetic phases and were restricted mostly to Sr-rich part of the phase diagram. Motivated by the findings of the model calculations [23], we considered it worthwhile to span the whole concentration range from  $x = 0.0$  (*i.e.*,  $\text{Sr}_2\text{FeMoO}_6$ ) to  $x = 2.0$  (*i.e.*,  $\text{La}_2\text{FeMoO}_6$ ) and to study the relative stability of the various magnetic phases as one increases the carrier concentration through the increased doping of La.

The chapter is organized in the following manner: §: 5.2 contains the details of calculations. §: 5.3 is devoted to results which consist of four subsections: 5.3.1: structural details, 5.3.2: total-energy calculations, electronic structure, and relative stability of various magnetic phases in doped compounds, 5.3.3: determination of lowenergy, few-orbital Hamiltonian by NMTO downfolding and 5.3.4: calculations of magnetic phase diagram and magnetic transition temperatures in terms of low-energy Hamiltonian. The paper concludes with §: 5.4 containing summary and outlook.

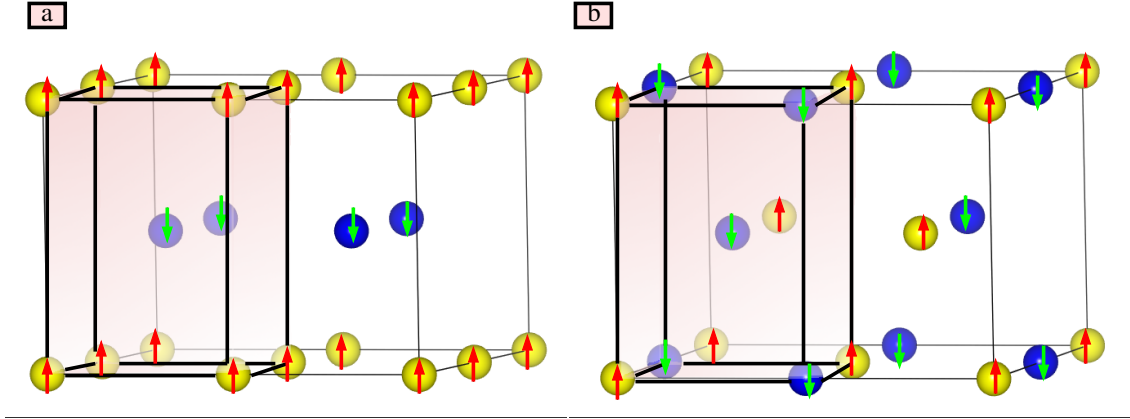


Fig. 5.1: The Fe sublattice ordering of  $\text{Sr}_{2-x}\text{La}_x\text{FeMoO}_6$ . Shown are the A-type (left panel) and G-type (right panel) antiferromagnetic arrangement of Fe spins. In case of A-type antiferromagnetism the Fe spins in-plane are ferromagnetically coupled while Fe spins between two adjacent plans are antiferromagnetically coupled. For G-type antiferromagnetism, the Fe spins are antiferromagnetically coupled both out-of-plane and inplane. The shaded box indicate the unit cell of two formula unit supercell.

## 5.2 Computational Details

The first-principles DFT calculations were carried out using the plane-wave pseudopotential method implemented within VASP. We considered exchange-correlation functionals within generalized gradient approximation (GGA) and GGA+U. We used projector-augmented wave potentials and the wave functions were expanded in the plane-wave basis with a kinetic-energy cutoff of 450 eV. Reciprocal-space integration was carried out with a k-space mesh of  $6 \times 6 \times 6$ . Two sets of supercell calculations were carried out, one with two formula unit and another with eight formula unit. The two formula unit supercells with two inequivalent Fe atoms can accommodate the ferromagnetic spin alignment of Fe spins and the A-type antiferromagnetic spin alignments of Fe spins. The eight formula unit supercells with eight inequivalent Fe atoms in the unit cell, in addition to FM and A-type AFM, can accommodate G-type antiferromagnetic ordering of Fe spins (see Fig. 5.1).

For extraction of a few-band tight-binding Hamiltonian out of full DFT calculation which is used as input to multiorbital, low-energy Hamiltonian-based calculations, we carried out NMTO-downfolding calculations. The constructed multi-orbital, low-energy Hamiltonian solved by means of real space based exact diagonalization technique for finite-size lattice of dimensions  $4 \times 4 \times 4$ ,  $6 \times 6 \times 6$ , and  $8 \times 8 \times 8$ .

Table 5.1: Optimized cell parameters and the atomic positions for  $\text{Sr}_2\text{FeMoO}_6$  and  $\text{La}_2\text{FeMoO}_6$ . Fe and Mo ions are situated at the high-symmetry Wykoff positions  $2a$  and  $2b$ , given by  $(0,0,0)$  and  $(0.0, 0.0, 0.5)$ , respectively. For  $I4/mmm$  symmetry Sr/La also sites in the high-symmetry Wykoff position given by  $(0.5, 0.0, 0.25)$  but sits in a general position for  $P21/n$  symmetry.

SFMO				LFMO							
a	5.57			a	5.78			a	5.65		
b	5.57			b	5.78			b	5.63		
c	7.80			c	7.75			c	7.95		
								$\beta$	90.04		
	x	y	z		x	y	z		x	y	z
Sr	0.5	0.0	0.25	La	0.5	0.0	0.25	La	0.010	0.002	0.259
O1	0.248	0.248	0.0	O1	0.245	0.245	0.0	O1	0.504	0.000	0.255
O2	0.0	0.0	0.248	O2	0.0	0.0	0.245	O2	0.248	0.257	0.003
								O3	0.253	0.244	0.497

## 5.3 Result and discussions

### 5.3.1 Structural details

$\text{Sr}_2\text{FeMoO}_6$  crystallizes in body-centered tetragonal space group with  $I4/mmm$  symmetry. The crystal structure of SFMO is well characterized. The crystal structure of La doped  $\text{Sr}_2\text{FeMoO}_6$  on the other hand is controversial. Some of the study [26, 27] reports that though  $I4/mmm$  symmetry is retained for small doping of La, for doping beyond  $x = 0.4$  or so, the symmetry changes to  $P21/n$ . The other measurements [24] however reports that all compounds of  $\text{Sr}_{2-x}\text{La}_x\text{FeMoO}_6$  for  $x=0, 0.25, 0.5,$  and  $1.0$  crystallize in  $I4/mmm$  symmetry. Unfortunately, the information of the detailed crystal structure data are limited due to the facts that (a) the compounds till now have been synthesized only for La concentrations less than or equal to 1, (b) increasing concentration of La leads to increased disorder which prohibits accurate measurement of the underlying symmetry. While in the following, we have primarily reported the results assuming  $I4/mmm$  symmetry, we have also carried out calculation for  $P21/n$  symmetry for the end member,  $\text{La}_2\text{FeMoO}_6$  (LFMO). The crystal structure corresponding to  $P21/n$  symmetry for  $\text{La}_2\text{FeMoO}_6$  was obtained starting with initial parameters of  $x=0.4$  as reported in Ref.[28] and then performing total-energy optimization of the initial structure. The  $P21/n$  symmetry structure has been found to be energetically lower in energy by 90 meV than the corresponding  $I4/mmm$ -symmetry structure. However, as described later, the

primary conclusion of our results is found to remain unaffected by this possible change in symmetry. Table 5.1 shows the theoretically optimized crystal structures obtained using plane-wave basis of SFMO and that of LFMO assuming  $I4/mmm$  symmetry as well as  $P21/n$  symmetry. Optimization has been carried out both in terms of GGA and GGA+U. The results are found to differ only marginally. The values quoted in Table I were obtained with GGA.

The volume for LFMO is found to expand with respect to that of SFMO, in agreement with experimental trend [24, 26] of increasing volume with increased La doping. Assuming  $I4/mmm$  symmetry, as is seen from Table 5.1, the internal parameters corresponding to oxygen positions, which are the only free parameters within  $I4/mmm$  space group, change little upon changing Sr by La. The unit-cell volume for various intermediate members of the series obtained by interpolation from the optimized lattice parameters of the end members using Vegard's law,  $120.99 \text{ \AA}^3$  for SFMO,  $123.27 \text{ \AA}^3$  for  $\text{Sr}_{1.5}\text{La}_{0.5}\text{FeMoO}_6$ , and  $125.56 \text{ \AA}^3$  for  $\text{SrLaFeMoO}_6$ , agree well with the experimental data available for  $I4/mmm$  symmetry in terms of volume expansion, given by 121.4, 124.0, and  $124.88 \text{ \AA}^3$ , respectively [24]. The crystal structure for the doped compounds in the assumed  $I4/mmm$  symmetry for the intermediate concentration values are, therefore, obtained by using Vegard's law for interpolation of cell parameters keeping the atomic positions fixed.

### 5.3.2 Total energy, electronic structure, and relative stability of magnetic phases

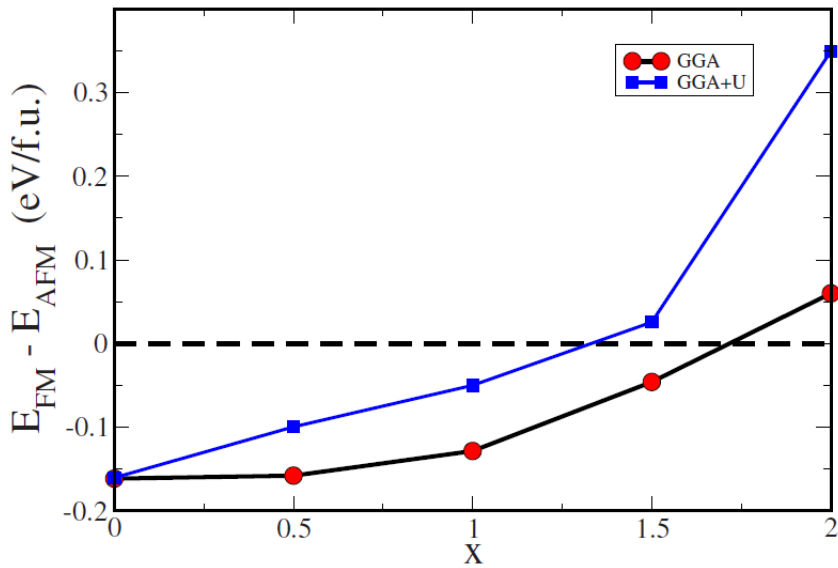


Fig. 5.2: The energy difference between FM and AFM-A phase plotted as a function of La concentration. The FM phase becomes unstable beyond a critical concentration of La both within GGA and GGA+U.

First, we carried out total-energy calculations of  $\text{Sr}_{2-x}\text{La}_x\text{FeMoO}_6$  in  $I4/mmm$  symmetry for the FM alignment of Fe spins and the AFM alignment of Fe spins. The energy difference between FM and AFM-A spin configuration per formula unit as a function of La concentration is plotted in Fig. 5.2, for both GGA and GGA+U calculation. Focusing on to GGA results first, as is evident from Fig. 5.2, the stability of the FM phase with respect to AFM configuration is gradually reduced as the La concentration is increased. As the concentration is increased beyond  $x=1.5$  or so, the FM phase becomes unstable and the AFM phase becomes the ground state, in agreement with prediction of model calculations [20, 21]. The total and magnetic moments at Fe and Mo sites, as obtained within GGA, are listed in Table 5.2. The net magnetic moment at the FM phase reduces as the La concentration is increased, which is due to the increased moment at the Mo site. Such behavior has been also observed in experiment [24]. Especially, photoemission studies have confirmed that electron injection occurs at the Mo site, increasing the moment on that site [29]. While the moment at the Fe site stays more or less the same between ferromagnetic and antiferromagnetic phases, the magnetic moment at the Mo site is found to be systematically smaller in the AFM phase compared to FM phase.

Table 5.2: Magnetic moments at Fe and Mo sites, and the total magnetic moment in FM and AFM-A phase of  $\text{Sr}_{2-x}\text{La}_x\text{FeMoO}_6$  in a two formula unit calculation. S3LFMO, SLFMO, and SL3FMO refer to  $\text{Sr}_{1.5}\text{La}_{0.5}\text{FeMoO}_6$ ,  $\text{SrLaFeMoO}_6$ , and  $\text{Sr}_{0.5}\text{La}_{1.5}\text{FeMoO}_6$ , respectively.

		SFMO	S3LFMO	SLFMO	SL3FMO	LFMO
FM	Fe	3.68	3.59	3.53	3.50	3.52
	Mo	-0.23	-0.45	-0.71	-0.80	-0.85
	Total	4.0	3.5	3.0	2.5	2.0
AFM	Fe	3.69	3.60	3.52	3.42	3.50
	Mo	-0.05	-0.03	-0.04	-0.18	-0.70
	Total	0.0	0.0	0.0	0.0	0.0

In order to check the influence of the possible change in crystal symmetry that may happen between SFMO and LFMO, we calculated the total-energy difference between FM and AFM-A spin configurations, assuming LFMO in  $P21/n$  symmetry with theoretically optimized structure. The calculated  $E_{FM}-E_{AFM-A}$  came out to be 0.094 eV per formula unit, confirming the stabilization of AFM phase for LFMO. While the possible change in crystal symmetry from  $I4/mmm$  to  $P21/n$  for La-rich samples is expected to change the precise La concentration at which FM to AFM transition happens, the general trend of AFM phase becoming progressively more favorable upon increasing La doping therefore would remain hold good.

Fig. 5.3 shows the GGA density of states corresponding to FM phase of SFMO, LFMO,

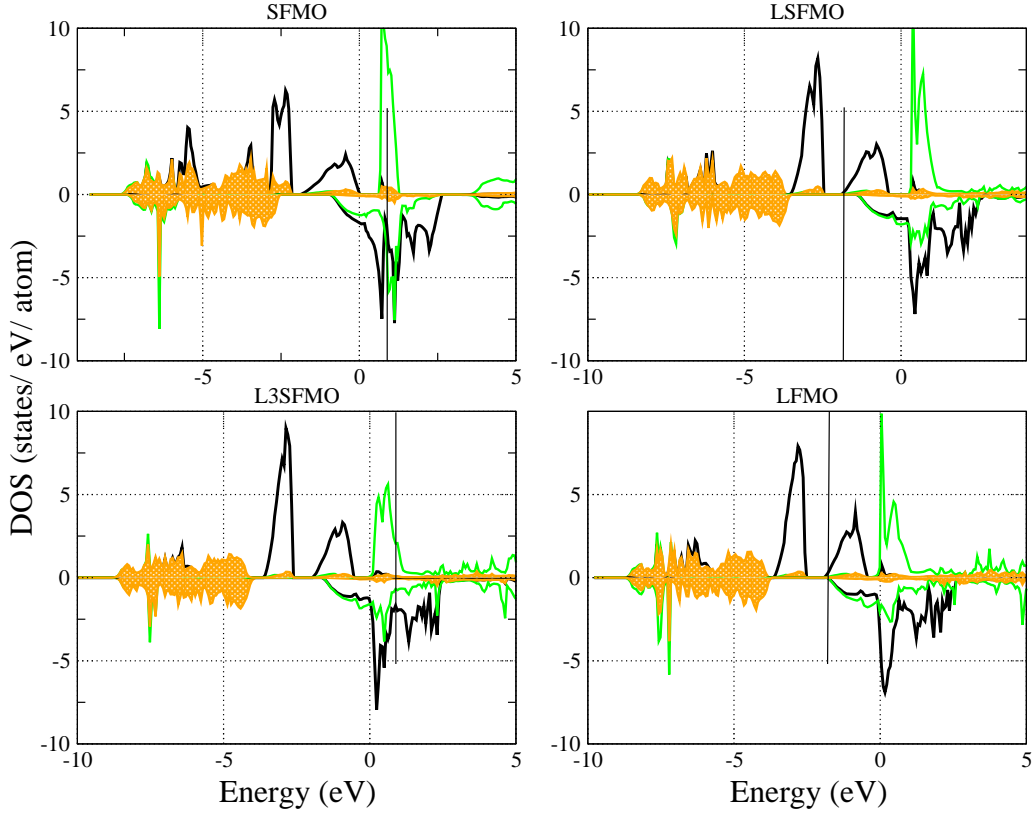


Fig. 5.3: The GGA density of states corresponding to SFMO, SLFMO, L3SFMO, and LFMO in ferromagnetic configuration. The density of states projected onto Fe, Mo, and O are represented by solid black, green (gray), and shaded gray area. The upper and lower panels correspond to majority- and minority-spin channels. Zero of the energy is set at the GGA Fermi energy.

and the doped compounds,  $\text{SrLaFeMoO}_6$  and  $\text{Sr}_{0.5}\text{La}_{1.5}\text{FeMoO}_6$  in  $I4/mmm$  symmetry. Focusing on the well-studied [11] DOS of SFMO, we find that the Fe  $d$  states are nearly full (empty) in the majority (minority)-spin channel while the Mo  $d$  states are nearly empty in the majority-spin channel and partially filled in the minority-spin channel. This is in conformity with the halfmetallic character of the compound and also with the nominal  $\text{Fe}^{3+}$  and  $\text{Mo}^{5+}$  valences. Due to the octahedral oxygen surrounding of Fe and Mo atoms, the Fe  $d$  and Mo  $d$  states are split up into  $t_{2g}$  and  $e_g$ , the highly delocalized state crossing the Fermi level in the minority-spin channel being of mixed Fe  $t_{2g}$ -Mo  $t_{2g}$  character. The empty Mo  $t_{2g}$  states in the majority-spin channel is found to be highly localized giving rise to peaked structure positioned at about 1 eV above the Fermi energy. As each of the Sr atoms is replaced by a La atom, one extra electron is introduced in the system which populates the hybridized Fe  $t_{2g}$ -Mo  $t_{2g}$  state in the minority-spin channel, keeping the overall structure of the density of states intact. The Fermi level therefore progressively moves up like a rigid-band fashion as  $x$  is increased and eventually hits the Van Hove singularity of the Mo  $t_{2g}$  states in the majority-spin channel. The FM solution becomes unstable at this point. This is schematically shown in the left panel

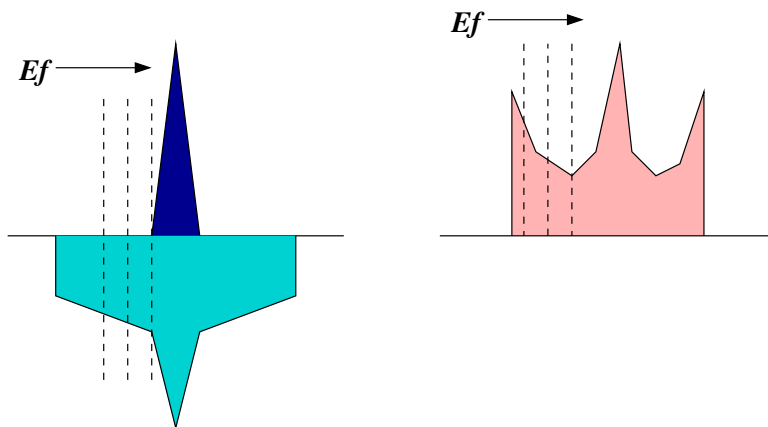


Fig. 5.4: Schematic showing the mechanism stabilizing the AFM phase over FM phase. As the La doping is increased, the Fermi level ( $E_f$ ) shifts toward right.

of Fig. 5.4. Interestingly the DOS corresponding to the mixed Fe  $t_{2g}$ -Mo  $t_{2g}$  character in the minority-spin channel also exhibits the singularity at the same energy due to the essentially two-dimensional-like nature of the hoppings between Mo  $t_{2g}$  and Fe  $t_{2g}$  Wannier functions as will be discussed in the following section.

Fig. 5.5 shows the density of states of SFMO, LFMO, and the doped compounds, SrLaFeMoO<sub>6</sub> and Sr<sub>0.5</sub>La<sub>1.5</sub>FeMoO<sub>6</sub> in the antiferromagnetic A phase, as calculated within GGA. In the two formula unit supercells, there are two inequivalent Fe atoms, Fe1 and Fe2, whose spins are antiferromagnetically oriented. The majority channel of Fe1 therefore is identical to the minority channel of Fe2 and vice versa. The induced moments at two inequivalent Mo sites also become antiferromagnetically aligned, giving rise to a net AFM arrangement with a zero total moment. Shown in Fig. 5.5, are therefore, the partial DOS corresponding to one of the sublattice since that of the other sublattice is identical with majority and minority spins reversed. We find that the Mo-Fe hybridized state crossing the Fermi level, has a three peak Van Hove structure. This arises because of the fact that due to creation of sublattices in the AFM phase, the Mo hopping becomes restricted to a reduced dimension as the Mo electrons can effectively hop to Fe sites with a specific orientation of Fe spins and not in another. Interestingly, such a three-peak structure formation is also seen in model calculation (see Fig. 5.3 of Ref.[21]). As found in the case of FM DOS, the gross features of the density of states remain unchanged with the La doping apart from the upward shift of the Fermi energy. Reaching LFMO, the Fermi level lands up in the dip of the three-peak structured DOS, justifying the stability of the antiferromagnetic phase, as shown in the schematic of Fig. 5.4.

The antiferromagnetic state becomes energetically favorable, when the filling is such that it starts populating the Mo states in the majority-spin channel of the FM DOS, which is highly localized due to the strong preference of the Mo-Fe hopping in one spin channel and not in another. The antiferromagnetic configuration of Fe spins, on the other

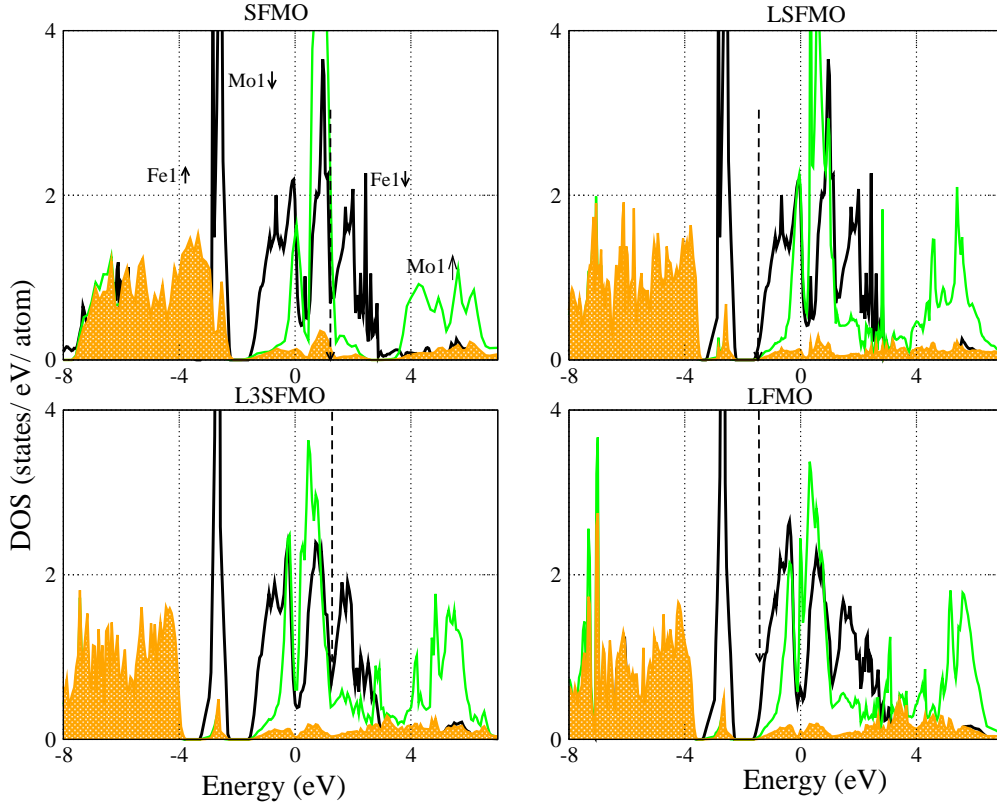


Fig. 5.5: The density of states corresponding to SFMO, SLFMO, L3SFMO, and LFMO in the A-type antiferromagnetic configuration. The density of states projected onto Fe, Mo, and O are represented by solid black, green (gray), and shaded gray area. Zero of the energy is set at the GGA Fermi energy.

hand, allows both Mo down-spin as well as up-spin electron to hop, albeit in different sublattices, thereby stabilizing the AFM phase through kinetic-energy gain.

In order to check the influence of the missing correlation effect in GGA, we also carried out GGA+U calculations with a typical U value [30] of 4 eV and J value of 1 eV, applied at the Fe site. The calculated energy difference between FM and AFM-A configuration as a function of La doping is shown in Fig. 5.2, along with GGA results. The application of U is found to increase the relative stability of AFM phase due to the increased superexchange contribution to antiferromagnetism in addition to kinetic-energy-driven antiferromagnetism.

In Fig. 5.6, we show the GGA+U DOS for LFMO, plotted for both FM and AFM-A phases. It is observed that the gross features of the DOS close to Fermi energy, remain similar to GGA, in particular, the Fermi energy in the FM phase remains pinned to the unoccupied Mo  $t_{2g}$  level in the FM phase. However, the hybridization between the Fe and Mo decreases. Nevertheless, the antiferromagnetic state is still found to have a finite density of states at Fermi energy, signifying the dominance of kinetic-energy-driven contribution over that of superexchange.

As already mentioned, considering the two formula unit supercell, the possible AFM

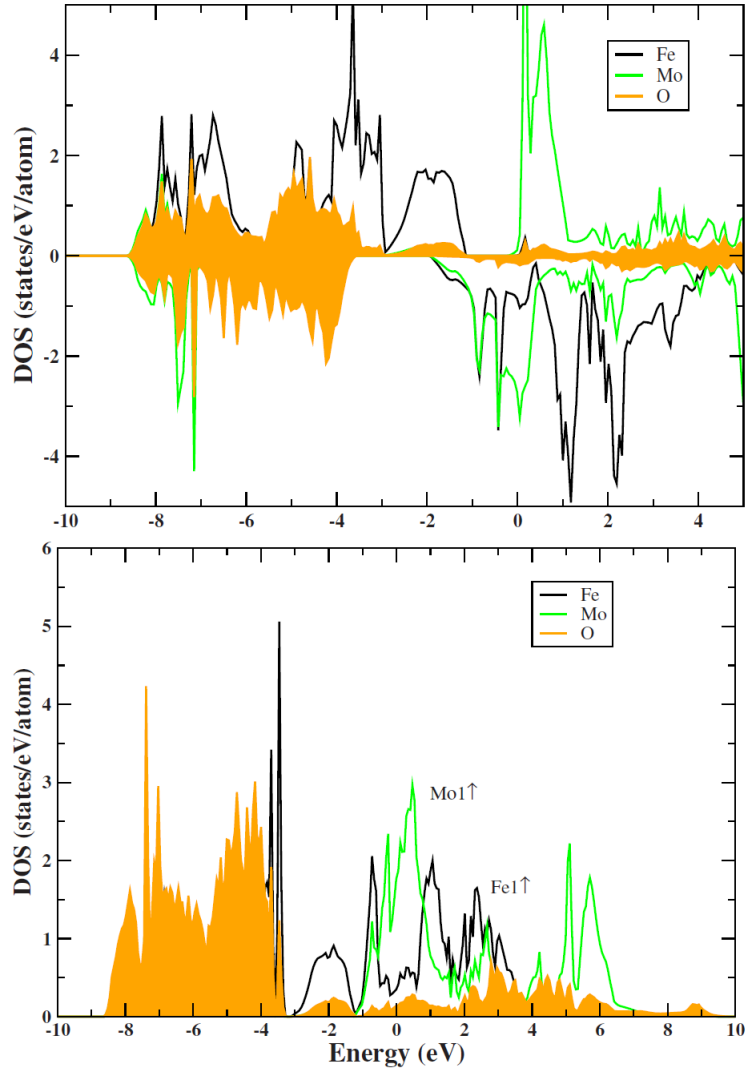


Fig. 5.6: DOS for LFMO in FM and AFM-A phase, using GGA+U.

arrangement that can be achieved is of A type. In order to achieve the G-type AFM ordering involving both in-plane and out-of-plane AFM ordering, one needs to increase the size of the supercell to at least eight formula unit. Eight formula unit supercells also allow to probe the concentration range intermediate to  $x=1.5$  and  $x=2.0$ , the region where the crossover from FM to AFM happens. Since the qualitative conclusions remain unchanged between GGA and GGA+U, the eight formula unit calculations were carried out only for GGA. The energy differences per formula unit obtained for different concentrations of La between FM and AFM-A, and between FM and AFM-G phases are listed in Table 5.3. As found in the calculations with two formula unit, the stability of the FM phase is found to gradually decrease as the La concentration increases. Among the two antiferromagnetic phases, the G-type AFM is found to be energetically very close to A-type AFM phase, with G-type AFM being the ground state at the end limit of doping i.e., for LFMO.

Table 5.3: Total energy differences per unit formula in eV between FM and AFM-A, and between FM and AFM-G for various doping of La, as obtained within eight formula unit supercell calculations.

	$\Delta E(\text{FM} - \text{AFM-A})$	$\Delta E(\text{FM} - \text{AFM-G})$
SFMO	-0.145	-0.147
SLFMO	-0.076	-0.073
$\text{Sr}_{0.5}\text{La}_{1.5}\text{FeMoO}_6$	-0.017	-0.008
$\text{Sr}_{0.375}\text{La}_{1.625}\text{FeMoO}_6$	0.014	0.006
$\text{Sr}_{0.25}\text{La}_{1.75}\text{FeMoO}_6$	0.037	0.032
$\text{Sr}_{0.125}\text{La}_{1.875}\text{FeMoO}_6$	0.057	0.052
LFMO	0.066	0.069

### 5.3.3 Determination of low-energy, few-orbital Hamiltonian

In order to probe the variation in La concentration in a continuous manner, it is perhaps more convenient to adopt a low-energy Hamiltonian approach. This would also allow one to calculate the physical properties such as magnetic transition temperatures, transport, and spin-wave spectra in a much more manageable way.

The multiorbital, low-energy Hamiltonian that is assumed to capture the essential physics of SFMO, should consist of the following ingredients:

1. A large core spin at the Fe site.
2. Strong coupling on the Fe site between the core spin and the itinerant electron, strongly preferring one spin polarization of the itinerant electron.
3. Delocalization of the itinerant electron on the Fe-Mo network.

From the above considerations, the representative Hamiltonian is given by,

$$\begin{aligned}
 H = & \epsilon_{Fe} \sum_{i \in B} f_{i\sigma\alpha}^\dagger f_{i\sigma\alpha} + \epsilon_{Mo} \sum_{i \in B'} m_{i\sigma\alpha}^\dagger m_{i\sigma\alpha} \\
 & - t_{FM} \sum_{\langle ij \rangle \sigma, \alpha} f_{i\sigma, \alpha}^\dagger m_{j\sigma, \alpha} - t_{MM} \sum_{\langle ij \rangle \sigma, \alpha} m_{i\sigma, \alpha}^\dagger m_{j\sigma, \alpha} \\
 & - t_{FF} \sum_{\langle ij \rangle \sigma, \alpha} f_{i\sigma, \alpha}^\dagger f_{j\sigma, \alpha} + J \sum_{i \in A} \mathbf{S}_i \cdot f_{i\alpha}^\dagger \vec{\sigma}_{\alpha\beta} f_{i\beta}
 \end{aligned} \tag{5.1}$$

The  $f$ s refer to the Fe sites and the  $m$ s to the Mo sites.  $t_{FM}$ ,  $t_{MM}$ , and  $t_{FF}$  represent the nearest-neighbor Fe-Mo, second nearest-neighbor Mo-Mo, and Fe-Fe hoppings, respectively, the largest hopping being given by  $t_{FM}$ .  $\sigma$  is the spin index and  $\alpha$  is the orbital index that spans the  $t_{2g}$  manifold. The difference between the  $t_{2g}$  levels of Fe and

Mo,  $\tilde{\Delta} = \epsilon_{Fe} - \epsilon_{Mo}$ , defines the charge-transfer energy. Since among the crystal-field split  $d$  levels of Fe and Mo, only the relevant  $t_{2g}$  orbitals are retained, the on-site and hopping matrices are of dimension  $3 \times 3$ . The  $\mathbf{S}_i$  are classical (large  $S$ ) core spins at the B site, coupled to the itinerant B electrons through a coupling  $J \gg t_{FM}$ .

Given the fact that  $J \gg t_{FM}$ , the Hamiltonian of Eqn. 5.1 can be cast into form appropriate for  $J \rightarrow \infty$ . This gives the following Hamiltonian, with spinless Fe conduction electrons and Mo electrons having both spin states,

$$\begin{aligned}
H = & t_{FM} \sum_{\langle ij \rangle_\alpha} \left( \sin\left(\frac{\theta_i}{2}\right) f_{i\alpha}^\dagger m_{j\uparrow\alpha} - e^{i\phi_i} \cos\left(\frac{\theta_i}{2}\right) f_{i\alpha}^\dagger m_{j\downarrow\alpha} \right) \\
& + h.c. + t_{MM} \sum_{\langle ij \rangle} m_{i\sigma\alpha}^\dagger m_{j\sigma\alpha} \\
& + t_{FF} \sum_{\langle ij \rangle} \cos(\theta_{ij}/2) (f_{i\sigma\alpha}^\dagger f_{j\sigma\alpha}) \\
& + \epsilon_{Fe} \sum_i f_{i\alpha}^\dagger f_{i\alpha} + \epsilon_{Mo} \sum_{i\sigma\alpha} m_{i\sigma\alpha}^\dagger m_{i\sigma\alpha}
\end{aligned} \tag{5.2}$$

This is the lowest-energy Hamiltonian. There is no longer any large coupling in the Hamiltonian, and the number of degrees of freedom has been reduced to three per Fe site and six per Mo, compared to original problem with six degrees of freedom at both Fe and Mo sites.  $m_{j\downarrow}$  and  $m_{j\uparrow}$  hop to different conduction-electron projections at the neighboring Fe sites so the effective hopping picks up a  $\theta_i$ ,  $\phi_i$ -dependent modulation. For example,  $\theta = 0$ ,  $\phi = 0$ , corresponds to FM configuration with all Fe core spins being up. Since the spin  $S$  is large and can be considered classical, one can consider different spin configurations (ferro, antiferro, and disordered) and diagonalize the system in real space, to obtain variational estimates of the ground state, and its stability.

We derived a Fe  $t_{2g}$ -Mo  $t_{2g}$ -only Hamiltonian by integrating out all the degrees of freedom other than Fe  $t_{2g}$  and Mo  $t_{2g}$  starting from a full DFT band structure and then performing NMTO-downfolding calculation. Calculations were carried out both in the spin-polarized and nonspinpolarized form. First of all, Fig. 5.7 illustrates the driving mechanism of magnetism in this class of compounds [31]. The top panels show the on-site energies of the real-space Hamiltonian defined in downfolded effective Fe-Mo basis for SFMO and LFMO in a spin-polarized calculation. As is seen, the  $t_{2g}$  levels of Mo appear in between the exchange-split Fe  $d$  states. Upon switching on the hybridization between Fe  $d$  and Mo  $t_{2g}$ , states of same symmetry and spin interact. As a result, Mo  $t_{2g}$  up-spin states are pushed up in energy and Mo  $t_{2g}$  down-spin states are pushed down in energy, introducing a renormalized, negative spin splitting at the Mo site. The normalized spin splitting at Mo site is estimated by massive downfolding procedure by keeping only Mo  $t_{2g}$  states active in the basis, as shown in the right half on the top panels in Fig. 5.7. We note that this to be true for both SFMO and LFMO. This in turn, once again, reconfirms the hybridization driven mechanism to be operative both in SFMO and LFMO, the only

difference being in the carrier concentration. This is in contrast to  $\text{Sr}_2\text{FeWO}_6$  where W  $t_{2g}$  levels are pushed above the exchange split Fe  $d$  levels. The increase in the number of conduction electrons for LFMO compared to SFMO, is reflected in the spin splitting at Mo site before switching of the hybridization, to be about three times larger in LFMO (0.37 eV) compared to that of SFMO (0.13 eV). The bottom panels of Fig. 5.7 show the plots of Wannier functions of the massively downfolded Mo  $t_{2g}$  in the down-spin channel which demonstrates the hybridization between Mo  $t_{2g}$  and Fe  $t_{2g}$  states.

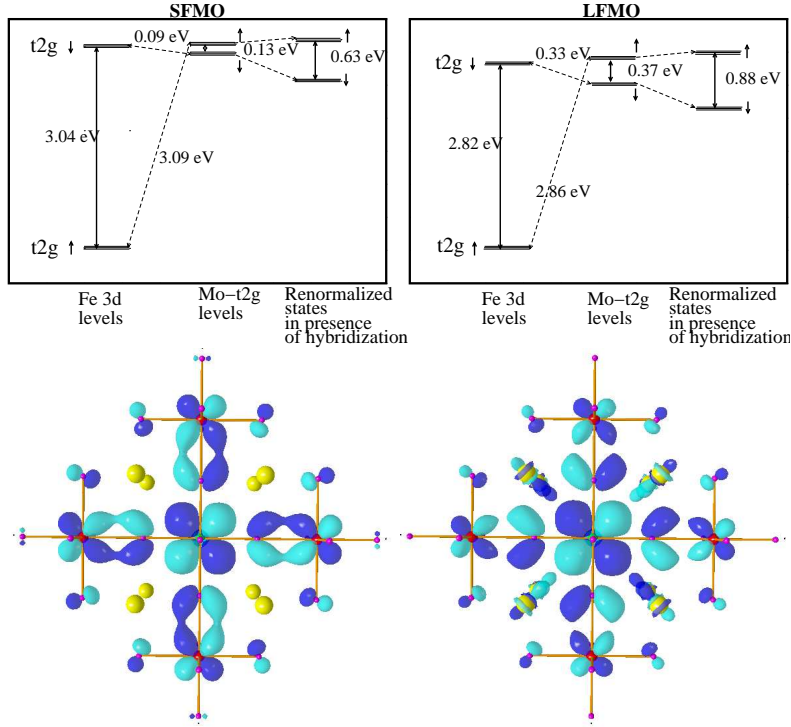


Fig. 5.7: Top panels: Positioning of various energy levels as obtained by NMTO-downfolding calculation before and after switching on the hybridization between the magnetic and nonmagnetic ions. Bottom panels: Effective Mo  $t_{2g}$  Wannier orbitals corresponding to massively downfolded NMTO Hamiltonian in the down-spin channel. Shown are the orbital shapes (constant amplitude surfaces) with lobes of opposite signs colored as blue (dark gray) and cyan (light gray). The central part of the Wannier orbitals are shaped according to Mo  $t_{2g}$  symmetry while the tails are shaped according to Fe  $t_{2g}$  and O- $p$  symmetries. Significant amount of weights are seen in O and Fe site which reflects the strong hybridization between Fe, Mn, and O. For LFMO, finite weights are seen also at La sites, occupying the hollows formed between Mo-O and Fe-O bonds, which is of La  $3z^2$  character.

Table 5.4 shows the hopping interactions between Fe and Mo, obtained in the basis of Fe and Mo  $t_{2g}$  Wannier functions constructed by NMTO-downfolding technique. The numbers inside the bracket are that of LFMO while those outside are that of SFMO. The examination of the hopping table reveals that the nearest-neighbor Fe-Mo hopping to be strongest, as expected. The second-nearest-neighbor Mo-Mo hopping is half as strong as the nearest-neighbor Fe-Mo hopping while the second-nearest-neighbor Fe-Fe hopping is about one fifth of the nearest-neighbor Fe-Mo hopping. The out-of-plane hoppings

Table 5.4: Hopping matrix elements in eV between Fe- $t_{2g}$  and Mo- $t_{2g}$ . Only the hopping matrix elements of magnitude larger than 0.01 eV are listed. The onsite matrix elements are given by 0.005 (0.008) eV, 0.0 (0.0) eV, 0.0 (0.0) eV for Fe- $xy$ , Fe- $yz$  and Fe- $xz$  respectively, and 1.018 (1.057) eV, 1.007 (1.053) eV, 1.007 (1.053) eV for Mo- $xy$ , Mo- $yz$  and Mo- $xz$  respectively. All numbers inside the bracket are for LFMO and those outside are for SFMO. The energies for a given compound is measured with respect to the lowest energy state. The small differences between numbers involving  $xy$  and that of  $yz$  and  $xz$  reflect the tetragonality present in the systems.

	Direction	xy,xy	yz,yz	xz,xz
1NN (Fe-Mo)	[100]	-0.26 (-0.26)	-0.02 (-0.04)	-0.26 (-0.26)
	[010]	-0.26 (-0.26)	-0.26 (-0.26)	-0.02 (-0.04)
	[001]	-0.02 (-0.04)	-0.26 (-0.25)	-0.26 (-0.25)
2 NN (Fe-Fe)	[110]	-0.05 (-0.06)	0.01 (0.00)	0.01 (0.00)
	[101]	0.00 (0.00)	0.01 (0.00)	-0.04 (-0.06)
	[011]	0.00 (0.00)	-0.04 (-0.06)	0.01 (0.00)
2 NN (Mo-Mo)	[110]	-0.11 (-0.12)	0.00 (0.01)	0.00 (0.01)
	[101]	0.01 (0.01)	0.00 (0.01)	-0.11 (-0.12)
	[011]	0.01 (0.01)	-0.11 (-0.12)	0.00 (0.01)
3NN (Fe-Mo)	[111]	0.01 (0.00)	0.00 (0.00)	0.00 (0.00)
4 NN (Fe-Fe)	[100]	0.01 (0.01)	0.01 (0.00)	0.01 (0.01)
	[010]	0.01 (0.01)	0.01 (0.01)	0.01 (0.00)
	[001]	0.01 (0.00)	0.01 (0.01)	0.01 (0.01)
4 NN (Mo-Mo)	[100]	0.01 (0.03)	0.01 (0.00)	0.01 (0.03)
	[010]	0.01 (0.03)	0.01 (0.03)	0.01 (0.00)
	[001]	0.01 (0.00)	0.01 (0.03)	0.01 (0.03)
5 NN (Fe-Mo)	[110]	-0.01 (-0.01)	0.00 (0.01)	0.00 (0.00)
	[101]	0.00 (0.01)	0.00 (0.00)	-0.01 (-0.01)
	[011]	0.00 (0.00)	-0.01 (-0.01)	0.00 (0.01)

which are of  $dd\delta$  kind are order of magnitude smaller than the in-plane  $dd\pi$  kind of hopping while interorbital hoppings are found to be negligibly small (less than 0.01 eV). This makes the hopping essentially two dimensional, as commented earlier. As is also evident, by replacing Sr by La, the essential material specific parameters of the low-energy Hamiltonian, as given in Eqn. 5.1 changes very little. This is shown pictorially in Fig. 5.7, where it is found that the relative energy positions of the  $t_{2g} \downarrow$  levels of Fe and Mo change very little in going from SFMO to LFMO. In the solution of low-energy Hamiltonians, to be described in the next section, calculations are therefore carried out assuming the hopping parameters corresponding to SFMO and varying the carrier concentration in a rigid-band fashion. The charge-transfer energy between Fe  $t_{2g}$  and Mo  $t_{2g}$  has been found to differ by about 5% which has been taken into account in these calculations.

### 5.3.4 Calculations of magnetic phase diagram and magnetic transition temperatures in terms of low-energy Hamiltonian

The hopping parameters and the on-site energies were taken out of DFT calculations, as listed in Table 5.4. For convenience of calculation, we have neglected the small tetragonality reflected in the parameters listed in Table 5.4. The dominant hopping interaction which is between nearest-neighbor Fe and Mo is found to be on the order of 0.3 eV while the spin-exchange splitting at Fe site as shown in Fig. 5.7, is on order of the 3 eV, an order of magnitude larger than the dominant hopping interaction. This justifies the assumption of  $J \rightarrow \infty$  limit as adopted in Eqn. 5.2. This makes the rank of the Hamiltonian to be diagonalized as  $9/2 \times N^3$  for a  $N \times N \times N$  lattice, because there are nine degrees of freedom per Fe-Mo pair, consisting of three at Fe site and six at Mo site.

The energy difference between ferromagnetic configuration and G-type and A-type antiferromagnetic configuration of Fe spins as a function of carrier concentration is plotted in Fig. 5.8. The negative values of the energy differences indicate the stability of the ferromagnetic phase while the positive values indicate the stability of the antiferromagnetic phase. The crossover happens for a value of conduction electrons equal to about  $\sim 2.6$ , corresponding to  $x=1.6$ , which agrees well with the results of eight formula unit supercell calculations, given the assumption of infinite Hunds coupling at Fe site and the finite-size effect. This agreement is nontrivial since the effective Hamiltonian has only 12 spin orbitals, and hence 12 bands, as compared to the 500 band calculation with eight formula unit supercells. This in turn, validates the construction of low-energy model Hamiltonian as given in Eqn. 5.2, in terms of correct identification of the essential contributing terms. This gives us confidence in the constructed low-energy model Hamiltonian, which can henceforth be used to calculate many other properties such as conductivity, susceptibility, magnetoresistance, including at finite temperature, which are not easily accessible within DFT.

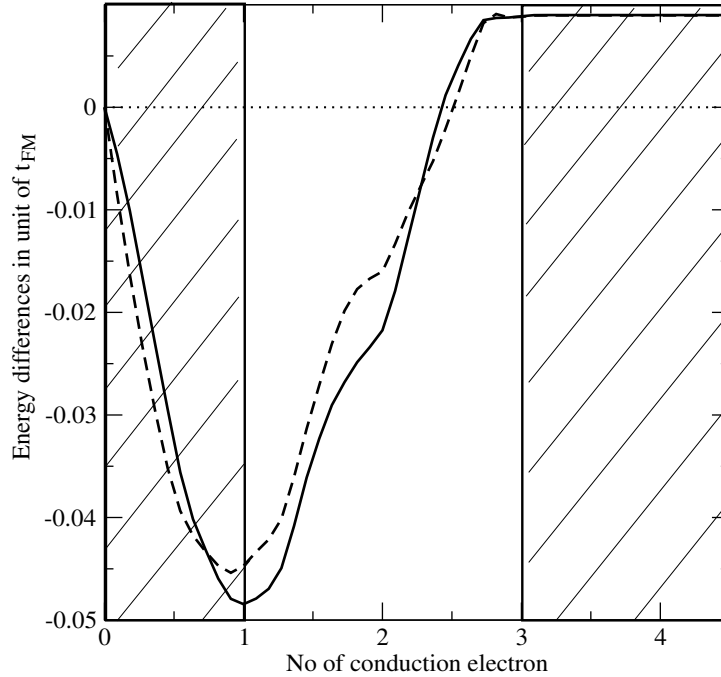


Fig. 5.8: The energy differences between the FM and G-type AFM phase (solid line) and the FM and A-type AFM phase (dashed line) plotted as a function of the number of conduction electrons, as obtained by exact diagonalization of the low-energy Hamiltonian for a  $8 \times 8 \times 8$  lattice. Only the region outside the hashed regions, from carrier concentration 1 to 3 is of relevance for  $\text{Sr}_{2-x}\text{La}_x\text{FeMoO}_6$ .

As an example, we have used the solutions of the lowenergy Hamiltonian to calculate the magnetic transition temperatures by calculating the difference between the paramagnetic phase and the relevant magnetic phases. The paramagnetic phase was simulated as disordered localmoment calculations, where the calculations were carried out for several ( $\sim 50$ ) disordered configurations of Fe spin and were averaged to get the energy corresponding to paramagnetic phase. We note that, such a calculation would have been rendered extremely difficult within ab initio owing to the computational time involved using large supercells, and also averaging them over myriad configurations. Fig. 6.3 shows the transition temperatures plotted as a function of carrier concentration. The ferromagnetic transition temperature at carrier concentration of 1, which corresponds to SFMO compound, is found to be 360 K in comparison to measured value of 410 K [12]. The ferromagnetic  $T_c$  is found to decrease upon increasing La concentration, and finally becomes zero. Upon suppression of ferromagnetic  $T_c$ , the transition temperature of the antiferromagnetic phase,  $T_N$  starts growing, hitting a maximum value for the end member, LFMO.

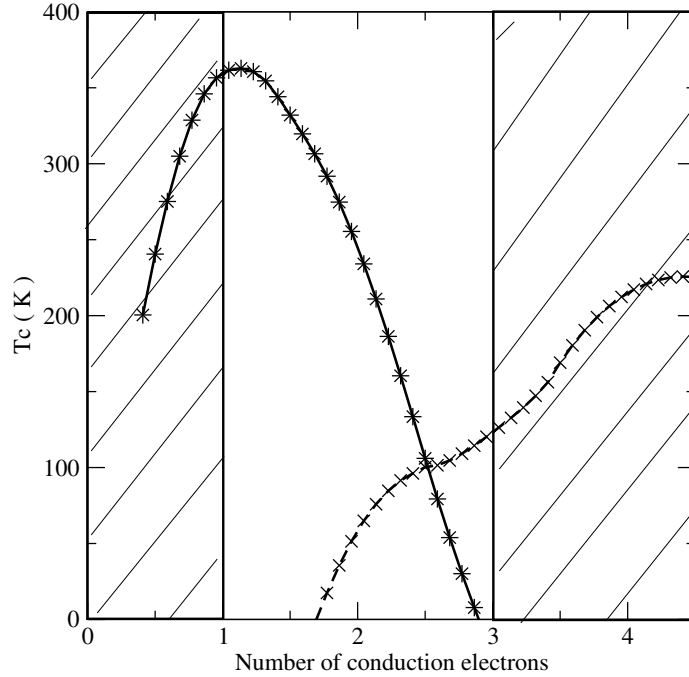


Fig. 5.9: The ferromagnetic  $T_c$  (solid line) and the antiferromagnetic transition temperature  $T_N$  (dashed line) plotted as a function of the number of conduction electrons, as obtained by exact diagonalization of the low-energy Hamiltonian for a  $8 \times 8 \times 8$  lattice. As in Fig. 5.8, the region outside the hashed regions, from carrier concentration 1 to 3 is of relevance for  $\text{Sr}_{2-x}\text{La}_x\text{FeMoO}_6$ .

## 5.4 Summary and outlook

Using the combination of first-principles DFT calculations and exact diagonalization calculations of low-energy Hamiltonians, we showed that the La-doped  $\text{Sr}_2\text{FeMoO}_6$  compounds become progressively more unstable toward ferromagnetism as the La concentration is increased. For the La-rich members of  $\text{Sr}_{2-x}\text{La}_x\text{FeMoO}_6$  series with  $x \sim 1.6$ , the ground state becomes antiferromagnetic. This antiferromagnetic phase is found to be governed by the kinetic-energy driven mechanism as operative in SFMO and achieved by change in carrier concentration. In contrast to the superexchange-driven antiferromagnetic phase found in case of double perovskite such as  $\text{Sr}_2\text{FeWO}_6$  [17], this antiferromagnetic phase presumably is metallic. Our DFT calculations found antiferromagnetic solutions with finite density of states at Fermi energy. The preliminary calculations of the matrix elements of the current operator also turned out to be nonzero. This will be taken up with more rigor in near future.

It is interesting to compare our results with dynamical mean-field theory (DMFT) calculations done by Chattopadhyay and Millis [15], using a one-band model Hamiltonian. This was, however, a single-site calculation, and hence there was no possibility of capturing an antiferromagnetic phase. Their  $T_c$  vs  $N$  plot for the ferromagnetic phase, however, was very similar to ours, as shown in Fig. 6.3, in the sense that the  $T_c$  first increased, and then

decreased with increasing filling, finally, becoming 0 at a filling close to 3. The additional and the most important finding of our study is that our calculations also demonstrate the cause of the vanishing  $T_c$ , namely, the emergence of the AFM phase.

# References

- [1] K.-I. Kobayashi, T. Kimura, H. Sawada, K. Terakura, and Y. Tokura, *Nature (London)* **395**, 677 (1998).
- [2] B. Garcia Landa, C. Ritter, M. R. Ibarra, J. Blasco, P. A. Algarabel, R. Mahendiran, and J. Garca, *Solid State Commun.* **110**, 435 (1999).
- [3] B. Martinez, J. Navarro, L. Balcells, and J. Fontcuberta, *J. Phys.: Condens. Matter* **12**, 10515 (2000).
- [4] D. D. Sarma, S. Ray, K. Tanaka, M. Kobayashi, A. Fujimori, P. Sanyal, H. R. Krishnamurthy, and C. Dasgupta, *Phys. Rev. Lett.* **98**, 157205 (2007).
- [5] C. L. Yuan, S. G. Wang, W. H. Song, T. Yu, J. M. Dai, S. L. Ye, and Y. P. Sun, *Appl. Phys. Lett.* **75**, 3853 (1999).
- [6] D. D. Sarma, E. V. Sampathkumaran, R. Sugata, R. Nagarajan, S. Majumdar, A. Kumar, G. Nalini, and T. N. Gururow, *Solid State Commun.* **114**, 465 (2000).
- [7] Cz. Kapusta, P. C. Riedi, D. Zajac, M. Sikora, J. M. De Teresa, L. Morellon, and M. R. Ibarra, *J. Magn. Magn. Mater.* **242-245**, 701 (2002).
- [8] K. Kuepper, M. Kadiroglu, A. V. Postnikov, K. C. Prince, M. Matteucci, V. R. Galakhov, H. Hesse, G. Borstel, and M. Neumann, *J. Phys.: Condens. Matter* **17**, 4309 (2005).
- [9] Y. Tomioka, T. Okuda, Y. Okimoto, R. Kumai, K.-I. Kobayashi, and Y. Tokura, *Phys. Rev. B* **61**, 422 (2000).
- [10] Dinesh Topwal, D. D. Sarma, H. Kato, Y. Tokura, and M. Avignon, *Phys. Rev. B* **73**, 094419 (2006).
- [11] D. D. Sarma, P. Mahadevan, T. Saha-Dasgupta, S. Ray, and A. Kumar, *Phys. Rev. Lett.* **85**, 2549 (2000).
- [12] Z. Szotek, W. M. Temmerman, A. Svane, L. Petit, and H. Winter, *Phys. Rev. B* **68**, 104411 (2003).

- 
- [13] V. Kanchana, G. Vaitheeswaran, M. Alouani, and A. Delin, Phys. Rev. B **75**, 220404(R) (2007).
- [14] I. V. Solovyev, Phys. Rev. B **65**, 144446 (2002).
- [15] A. Chattopadhyay and A. J. Millis, Phys. Rev. B **64**, 024424 (2001).
- [16] O. Navarro, E. Carvajal, B. Aguilar, and M. Avignon, Physica B **384**, 110 (2006).
- [17] J. Kanamori and K. Terakura, J. Phys. Soc. Jpn. **70**, 1433 (2001).
- [18] E. Carvajal, O. Navarro, R. Allub, M. Avignon, and B. Alascio, Eur. Phys. J. B **48**, 179 (2005).
- [19] L. Brey and M. J. Caldern, S. Das Sarma, and F. Guinea, Phys. Rev. B **74**, 094429 (2006).
- [20] J. L. Alonso, L. A. Fernandez, F. Guinea, F. Lesmes, and V. Martin-Mayor, Phys. Rev. B **67**, 214423 (2003).
- [21] P. Sanyal and P. Majumdar, Phys. Rev. B **80**, 054411 (2009).
- [22] Z. Fang, K. Terakura, and J. Kanamori, Phys. Rev. B **63**, 180407(R) (2001).
- [23] J. van den Brink, G. Khaliullin, and D. Khomskii, Phys. Rev. Lett. **83**, 5118 (1999).
- [24] A. Kahoul, A. Azizi, S. Colis, D. Stoeffler, R. Moubah, G. Schmerber, C. Leuvrey, and A. Dinia, J. Appl. Phys. **104**, 123903 (2008).
- [25] T. Saitoh, M. Nakatake, H. Nakajima, O. Morimoto, A. Kakizaki, Sh. Xu, Y. Moritomo, N. Hamada, and Y. Aiura, J. Electron Spectrosc. Relat. Phenom. **144-147**, 601 (2005).
- [26] J. Navarro, C. Frontera, Ll. Balcells, B. Martnez, and J. Fontcuberta, Phys. Rev. B **64**, 092411 (2001).
- [27] C. Frontera, D. Rubi, J. Navarro, J. L. Garcia-Munoz, J. Fontcuberta, and C. Ritter, Phys. Rev. B **68**, 012412 (2003).
- [28] Carlos Frontera (private communication).
- [29] J. Navarro, J. Fontcuberta, M. Izquierdo, J. Avila, and M. C. Asensio, Phys. Rev. B **70**, 054423 (2004).
- [30] Z. Zhang and S. Satpathy, Phys. Rev. B **44**, 13319 (1991).
- [31] T. Saha-Dasgupta, Molly De Raychaudhury, and D. D. Sarma, Phys. Rev. Lett. **96**, 087205 (2006).

# Chapter 6

## Study of magnetism and magneto-optic effect in Cr-based double perovskites

Content of this chapter has been published in: Hena Das, Prabuddha Sanyal, T. Saha-Dasgupta, D.D. Sarma, Phys. Rev. B, Hena Das, M. De-Raychaudhury, T. Saha-Dasgupta, Appl. Phys. Lett. **92**, 201912 (2008).

### 6.1 Introduction

Cr-based double perovskite series, namely  $\text{Sr}_2\text{CrB}'\text{O}_6$  ( $B' = \text{W}/\text{Re}/\text{Os}$ ), the family with spectacularly high  $T_c$ , the measured  $T_c$  shows a rapid increase as one moves from  $\text{Sr}_2\text{CrWO}_6$  (SCWO) [1] with  $T_c \approx 450$  K to  $\text{Sr}_2\text{CrReO}_6$  (SCRO) [2] with  $T_c \approx 620$  K to  $\text{Sr}_2\text{CrOsO}_6$  (SCOO) [3] with  $T_c \approx 725$  K. The  $B'$  ion which is in nominal 5+ valence state corresponds to  $5d^1$ ,  $5d^2$ ,  $5d^3$  configuration of W, Re and Os respectively. Taking the number of valence electrons as sole consideration, the situation of SCWO, SCRO, SCOO are comparable to that of  $\text{Sr}_2\text{FeMoO}_6$  (SFMO),  $\text{SrLaFeMoO}_6$  and  $\text{La}_2\text{FeMoO}_6$  (LFMO) respectively. However, the hybridization driven (HD) mechanism of magnetism used in the context of La doped SFMO, predicts decrease rather than the increase [4]. The Cr- $B'$  ( $B' = \text{W}, \text{Re}, \text{Os}$ ) series bear two fundamental differences compared to La-SFMO series: (1) the  $B'$  ions in Cr- $B'$  being  $5d$  transition metals exhibit significant spin-orbit (SO) coupling, (2) the three different chemical elements, namely W, Re and Os are involved in Cr- $B'$  series while for La-SFMO series the increased electron count is achieved without any changes in the B- $B'$  sublattice. In the first part of the present chapter, we present the study unraveling the dominant factor that causes the fundamental differences in magnetic properties of La-SFMO series and Cr- $B'$  like series, employing combination of DFT tools and the exact diagonalization of model Hamiltonian.

The presence of relatively large SO coupling make these materials suitable for magneto-optic applications with large signal. The magneto-optical Kerr effect (MOKE) in ferromagnets is an important phenomenon utilized for magneto-optical (MO) recording and optical communication. Search is on for suitable materials that exhibit large MOKE signals at high temperature for designing of improved devices. SCWO and SCRO with high  $T_c$  and  $B'$  site bearing substantial SO coupling are therefore potential candidates that

may satisfy the above criteria and can be used as functional MO disks. Similarly, SCOO, an insulator, may exhibit large Faraday signals. Unfortunately, there has not been any study of MO properties in this interesting class of materials with potential technological applicability. There have been reports of optical measurements in SCRO and SCWO, although they lack data in the far infrared region [6, 7]. Therefore we present the MO properties of  $\text{Sr}_2\text{CrB}'\text{O}_6$  series from a theoretical point of view in the second part of the chapter. To do so we have used the eigenvalues and wave functions generated from the full potential band structure calculations with SO included. We have calculated the various optical spectra, such as reflectivity and optical conductivity, and MO spectra, such as Polar Kerr and Faraday spectra.

## 6.2 Computational details

To find out the  $T_c$  trend in the Cr-B' series we have used density functional theory (DFT) based calculations together with exact diagonalization of Cr-B' model Hamiltonian constructed in a first-principles derived Wannier function basis. The first-principles DFT calculations were carried out using the plane wave pseudopotential method implemented within Vienna Ab-initio Simulation Package (VASP). The exchange-correlation functionals were approximated by generalized gradient approximation (GGA) and GGA+U. SO coupling has been included in the calculations in scalar relativistic form as a perturbation to the original Hamiltonian. We have used projected augmented wave (PAW) potentials and the kinetic energy cut-off for expansion of wavefunctions used was 450 eV. Reciprocal space integrations have been carried out with a k-space mesh of  $6 \times 6 \times 6$ . For extraction of a few-band, tight-binding Hamiltonian out of full DFT calculation which has been used as input to multi-orbital, low-energy Hamiltonian based calculations, we have carried out muffin-tin orbital (MTO) based NMTO-downfolding calculations. The constructed multi-orbital, spin-fermion Hamiltonian defined in the first-principles derived Wannier function basis has been solved by means of real space based exact diagonalization technique.

In order to investigate MO properties the band structure calculations have been carried out with no shape approximation to the potential and charge density. The basis has been chosen to be linearized augmented plane wave (LAPW) as implemented in the Wien2k code. Both local density approximation (LDA) and generalized gradient approximation (GGA) have been used as exchange-correlation functionals. For the number of plane waves, the criterion used was muffin-tin radius multiplied by Kmax (for the plane wave) yielding a value of 7.0. The k points used in the irreducible part of Brillouin zone was 256 (480 for optical calculations) and has been checked for convergence.

## 6.3 Investigation of the increasing trend in $T_c$

### 6.3.1 Examination of basic electronic structure

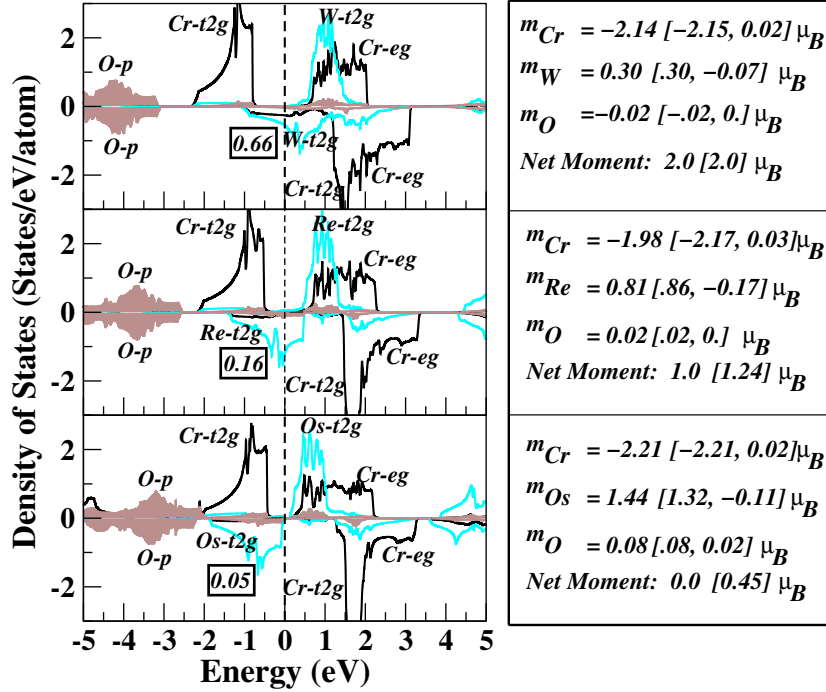


Fig. 6.1: Left Panels: GGA DOS projected onto Cr  $d$  (black solid lines), B'  $d$  (Red/Grey solid lines) and O  $p$  (shaded area). Zero of the energy is set at  $E_F$ . The numbers within the boxes indicate the Cr  $t_{2g}$  contribution in the bands crossing  $E_F$ , with respect to that of B'. Right Panel: Calculated net magnetic moment and magnetic moments at Cr, B' and O sites. The numbers within the bracket denote the result of GGA+SO calculations, the first entry being the spin moment and the second entry being the orbital moment. From top to bottom, the plots correspond to SCWO, SCRO and SCOO respectively.

In order to unravel the origin of magnetism in  $Sr_2CrB'O_6$  series, let us first critically examine the electronic density of states (DOS) of these compounds. Left panel of Fig. 6.1 shows the DOS, as obtained in spin-polarized DFT calculations within GGA. The states close to Fermi level ( $E_F$ ) are dominated by Cr and B'  $d$  states hybridized with O  $p$  states, while the O  $p$  dominated states separated from Cr and B'  $d$  dominated states occupy the energy range far below  $E_F$  and Sr  $s$  and  $d$  dominated state remain far above  $E_F$ . The  $d$  states of Cr and the B' ions are exchange split as well as crystal field split. The empty B'  $t_{2g}$  states in the up-spin channel appear in between the crystal field split Cr  $t_{2g}$  and  $e_g$  states, gaped from  $E_F$  while the B' states in the down spin channel hybridized with Cr  $t_{2g}$  states, either cross the Fermi level as in the case of W and Re compounds, or remain completely occupied, as in case of the Os compound. It is rather intriguing to notice that the hybridization between Cr  $t_{2g}$  and B'  $t_{2g}$  in the down spin channel, progressively gets weakened in moving from W to Re to Os compound. This may be appreciated by

considering the Cr contribution measured with respect to B' contribution for the states in the down spin channel close to  $E_F$ . For W, Re and Os compounds, it is found to be 66%, 16 % and 5% respectively. This is caused by the gradual moving down of the B' energy level, in moving from left to right of the periodic table across the same row (W  $\rightarrow$  Re  $\rightarrow$  Os), reflecting an increase in the ionic potential experienced by the 5d electrons with an increase in nuclear charge. As discussed later, the hopping interaction connecting Cr and B'  $t_{2g}$  states on the other hand remains similar across the series. Analyzing the DFT calculated magnetic moments, presented in the right panel of Fig. 6.1, we find the second interesting observation that the magnetic moment per electron at B' site, defined as  $m/d$ , where  $m$  is the calculated moment and  $d$  is the valence count at B', keeps growing from W to Re to Os. The increase in  $m/d$  becomes even more evident taking into account the magnetic moment at O site, which is small and point to Cr moment for SCWO, small (large) and point to Re (Os) moment for SCRO (SCOO). This prompts us to conclude that there is a growing intrinsic moment that develops at B' site following the dehybridization effect between Cr and B'.

### 6.3.2 NMTO-downfolding calculations

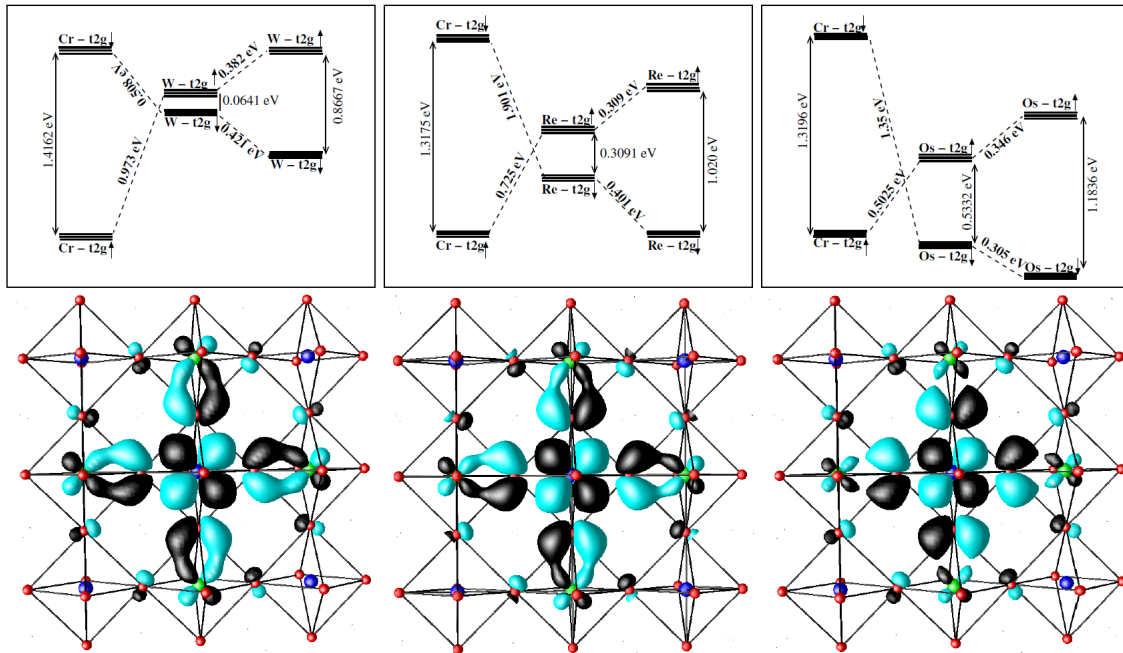


Fig. 6.2: The energy level diagram (upper panel) and massively downfolded Wannier functions (lower panels) for  $\text{Sr}_2\text{CrB}'\text{O}_6$  series. For Wannier function plots, constant value surfaces have been plotted with two oppositely signed lobes colored differently. From left to right in lower panel, the plots correspond to SCWO, SCRO and SCOO respectively. The numbers in the energy level diagram are in unit of eV.

In order to further analyze the findings of the electronic structure calculations, we

have carried out NMTO downfolding calculations. As a first step we downfolded O  $p$ , Sr as well as Cr and B'  $e_g$  degrees of freedom. This defines an effective basis consisting of Cr  $t_{2g}$  and B'  $t_{2g}$  states. In the second step, we applied massive downfolding, keeping only B'  $t_{2g}$  degrees of freedom active and downfolding all the rest including Cr  $t_{2g}$  degrees of freedom. On site matrix elements of the real space Hamiltonian defined in the Cr  $t_{2g}$ -B'  $t_{2g}$  basis and the massively downfolded basis give the energy level positions before and after switching on the hybridization between Cr and B' states, respectively. Fig. 6.2 summarizes the results for W, Re and Os compounds. The energy levels in the left half of each top panel depict the energy level positions in absence of hybridization between Cr  $t_{2g}$  and B'  $t_{2g}$  states while those in the right half of each top panel depict the normalized energy levels after the hybridization is switched on via the massive downfolding procedure. The lower panels exhibit the plots of the one of the  $t_{2g}$  ( $xy$ ) Wannier functions corresponding to massively downfolded Hamiltonian in the down spin channel. Examination of Fig. 6.2 brings out two aspects: Firstly, the progressive dehybridization effect, as discussed in the context of DOS plots, is evident in the plots of Wannier functions. The central parts of the Wannier functions are shaped according to B'  $xy$  symmetry and the tails of the Wannier functions sitting at neighboring sites are shaped according to O  $p$  and Cr  $t_{2g}$  symmetry. The tails reflecting the hybridization between the Cr  $t_{2g}$  and B'  $t_{2g}$ -O weaken as one moves from W to Re to Os compound. As a consequence, the ratio of renormalized spin splitting to that of the bare splitting at B' site reduces drastically from W (14.5) to Re (3.3) to Os (2.2). Secondly, considering the level splitting at B' site before switching on the hybridization, we find while the splitting at W is negligibly small confirming the nonmagnetic character of the B' site, those for Re and Os are found to be  $\approx 0.31$  eV and  $\approx 0.53$  eV, respectively. These values are significantly larger compared to what one would have expected considering  $d^2$  valence in Re and  $d^3$  valence in Os compared to  $d^1$  valence in case of W with 0.06 eV splitting, which would have given rise to splittings of 0.12 eV and 0.18 eV respectively. This confirms the presence of a growing intrinsic, local moment at B' site as one moves from W to Re to Os, driven by the dehybridization effect. The magnetism in Cr-B' series, therefore, needs to be understood as an interplay of two mechanisms: HD mechanism as operative in SFMO which causes renormalized, negative spin splitting within B' states that appear in between the exchange split Cr  $t_{2g}$  states, and the superexchange (SE) between the moment at Cr site and the intrinsic moment at B' site, which would align the moments at Cr and B' sites antiparallely. For W, the intrinsic moment being negligible, the magnetism is entirely driven by HD mechanism, while for the other extreme of Os, the hybridization effect is weak, SE having a rather large contribution. The presence of such intrinsic moment at 5d site is counterintuitive at a first glance. Comparing the situation, with the double perovskite  $\text{Sr}_2\text{ScReO}_6$ , for which the magnetism has been recently investigated [8], Re was found to possess a rather small intrinsic moment of size  $0.013 \mu_B$ . Our electronic structure calculations carried out for

$\text{Sr}_2\text{ScReO}_6$  find also a similarly small moment ( $0.03 \mu_B$ ). The unusual localized aspect of Re or Os, in case of Cr based compounds therefore arises due to the relative positioning of the Cr and B' energy levels, which narrows down the width of the B' states substantially in the up spin channel. The development of the intrinsic moment is thus helped by the delicate energy level structure responsible for the HD mechanism and would not have been present otherwise.

### 6.3.3 Total energy calculations

The calculations discussed so far, do not include Spin orbit correlation (SOC), which may be important. The numbers within the bracket in right panel of Fig. 6.1 show the individual spin and orbital moments as well as net moments as obtained in GGA+SO calculations. As expected, the orbital moments are large at B' site. Interestingly, we find while the net moment was zero for SCOO without SOC, it is the consideration of SOC that gives rise to a non-zero moment, due to the uncompensated orbital moment at B' site. Whether SOC has any influence on the trend within the  $T_c$ 's, therefore needs to be explored. Interplay of two driving mechanisms in W-Re-Os series, however, makes it difficult to extract the magnetic exchanges as energy difference between two specific magnetic configurations. The presence of finite, intrinsic moment at B' site, as is the case for Re and Os compounds, makes the moment at B' site frustrated in an antiferromagnetic (AFM) configuration of Cr spins. The finite presence of HD mechanism, on the other hand, disfavors stabilization of magnetic configurations with majority of B spins aligned parallelly to that of the moment at B' site. Admitting these difficulties, we carried out total energy calculations of the two possible spin configurations, one FM arrangement and another A-type AFM arrangement of Cr spins, with Cr spins between two adjacent planes are antiferromagnetically coupled, and are ferromagnetically coupled in plane. For the AFM calculations, the moment at B' site was found to be antiparallely (parallelly) aligned to the spins of in-plane (out-of-plane) Cr sites which are four (two) in number. As expected, the energy differences between FM and AFM configurations are found to be positive for all cases proving FM arrangement of Cr spins to be the stable phase. The values of the energy difference is found to increase from W to Re system (from 0.23 eV/formula unit to 0.25 eV/formula unit), and then decrease from Re to Os system (from 0.25 eV/formula unit to 0.24 eV/formula unit). Introduction of SO interaction though changes the individual energy differences by about 0.03 eV, the trend remains unaltered. This indicates that although the presence of substantial SOC at B' site is important for producing the large magneto-optical signals, it plays little role in setting up the trend in  $T_c$ . In order to examine the role of missing correlation effect in GGA, we have also carried out LDA+U calculations with a choice of U value of 3 eV at Cr site and 0.8 eV at B' site. Application of larger U at Cr site and relatively smaller one at B' sites, as expected from the relative band-widths, were found to preserve the general conclusions intact with more

localized character of d states at B' site, as expected.

### 6.3.4 Exact diagonalization study of model Hamiltonian

In view of the difficulty in stabilizing the appropriate excited state magnetic configuration, the stability of the FM arrangements of Cr spins may be measured as the energy difference between the FM spin configuration and the paramagnetic (PM) phase. The description of the PM phase needs consideration of different disordered spin configurations and averaging over a large number of them, which is almost impossible within the DFT framework. Such calculations are much easier to handle within a model Hamiltonian description. The model Hamiltonian, describing the interplay of the HD and SE mechanism may be written as,

$$\begin{aligned}
 H = & \epsilon_{Cr} \sum_{i \in B} f_{i\sigma\alpha}^\dagger f_{i\sigma\alpha} + \epsilon_{B'} \sum_{i \in B'} m_{i\sigma\alpha}^\dagger m_{i\sigma\alpha} \\
 & - t_{CB'} \sum_{\langle ij \rangle_{\sigma,\alpha}} f_{i\sigma,\alpha}^\dagger m_{j\sigma,\alpha} - t_{B'B'} \sum_{\langle ij \rangle_{\sigma,\alpha}} m_{i\sigma,\alpha}^\dagger m_{j\sigma,\alpha} \\
 & - t_{CC} \sum_{\langle ij \rangle_{\sigma,\alpha}} f_{i\sigma,\alpha}^\dagger f_{j\sigma,\alpha} + J \sum_{i \in Cr} \mathbf{S}_i \cdot f_{i\alpha}^\dagger \vec{\sigma}_{\alpha\beta} f_{i\beta} \\
 & + J_2 \sum_{i \in Cr, j \in B} \mathbf{S}_i \cdot \mathbf{s}_j
 \end{aligned}$$

where the  $f$ 's and  $m$ 's refer to the Cr  $t_{2g}$  and B'  $t_{2g}$  degrees of freedoms.  $t_{CB'}$ ,  $t_{B'B'}$ ,  $t_{CC}$  represent the nearest neighbor Cr-B', second nearest neighbor B'-B' and Cr-Cr hoppings respectively.  $\sigma$  is the spin index and  $\alpha$  is the orbital index that spans the  $t_{2g}$  manifold. The difference between the ionic levels,  $\Delta = \epsilon_{Cr} - \epsilon_{B'}$ , defines the on-site energy difference between Cr  $t_{2g}$  and B'  $t_{2g}$  levels.  $s_j$  is the intrinsic moment at the B' site. The first, six terms of the Hamiltonian, represent the HD mechanism, which consist of a large core spin at the Cr site ( $S_i$ ) and the coupling between the core spin and the itinerant electron delocalized over the Cr-B' network. Variants of this part has been considered by several authors [9, 10, 11] in the context of SFMO. The last term represents the SE mechanism, that consists of coupling between Cr spin and the intrinsic moment at B' site. The parameters of the model Hamiltonian are extracted out of DFT calculations through NMTO downfolding technique of constructing the real space Hamiltonian in the basis of effective Cr  $t_{2g}$  and B'  $t_{2g}$  degrees of freedom.  $t_{CB'}$ ,  $t_{B'B'}$  and  $t_{CC}$  hoppings are found to -0.35 eV, -0.12 eV and -0.08 eV respectively, with little variation within the W-Re-Os series.  $\Delta$ -s show a varying trend within the W-Re-Os series ( $\Delta^W = -0.66$  eV,  $\Delta^{Re} = 0.03$  eV,  $\Delta^{Os} = 0.26$  eV). The parameters involving  $J$  and  $J_2$  were obtained from the spin-splitting at Cr site and the extra splitting observed at B' site as compared to that expected from the electron filling effect and the splitting for W compound.

The constructed model was then solved using exact diagonalization on a lattice of dimension  $8 \times 8 \times 8$ . Calculations have been carried out as well for lattices of size  $4 \times 4$

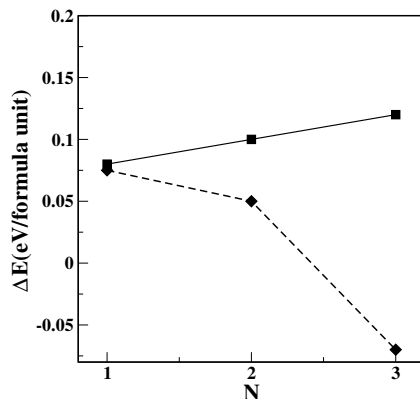


Fig. 6.3: PM - FM energy differences plotted as a function of valence electron count, as obtained in exact diagonalization calculation. The diamond (square) symbols connected by dashed (solid) line correspond to calculations corresponding to Hamiltonian, without (with)  $J_2$  term.

$\times 4$  and  $6 \times 6 \times 6$ . The trend is found to be the same as presented for  $8 \times 8 \times 8$ . Exact diagonalization was first carried out considering the  $B'$  site to be totally nonmagnetic, *i.e.* setting the last term to zero, which boils down to the same underlying model Hamiltonian as that of SFMO. The energy difference between the PM and FM is found to decrease with increasing number of valence electron, as shown by diamond symbols in Fig. 6.3. This is exactly the similar trend as found in a recent calculation on La doped SFMO [4], as well as in Ref.[5] with FM getting destabilized with increase of valence electrons. This trend of suppression of  $T_c$  upon increasing valence electron count is further amplified due to change in  $\Delta$  within the Cr- $B'$  series. This variation in  $\Delta$  in the present series is in contrast to the prescription given in Ref.[5] to achieve high  $T_c$ . Upon reaching valence electron count equal to 3 which corresponds to Os compound, FM becomes totally unstable, reflected in negative sign of the energy difference. We note a rather rapid decrease in moving from  $N=2$  case to  $N=3$  case. This may reflect the special situation of Os compound, with Cr  $t_{2g}^3$ - $B'$   $t_{2g}^3$  configuration, an ideal super-exchange situation with insulating solution, that adds on to the general trend. The situation gets dramatically changed upon inclusion of the growing localized magnetic nature of the  $B'$  site, as shown by square symbols in Fig. 6.3. Considering  $J_2$  values, as obtained in GGA calculations, we find that PM and FM energy difference, recovers the correct trend in moving from W to Re to Os as has been observed experimentally. Mapping the PM and FM energy difference to the mean field  $T_c$ , one obtains values 870 K, 1160 K and 1450 K for the W, Re and Os compounds respectively. Although the values are overestimated compared to experimental values, presumably due to the finite size effect of exact diagonalization calculation and the mean field formula, the trend is very well reproduced with  $T_c^{Re}/T_c^W = 1.33$  and  $T_c^{Os}/T_c^{Re} = 1.25$ , compared to experimental estimates of 1.38 and 1.17 respectively [1, 2, 3].

## 6.4 Investigation of magneto optical properties

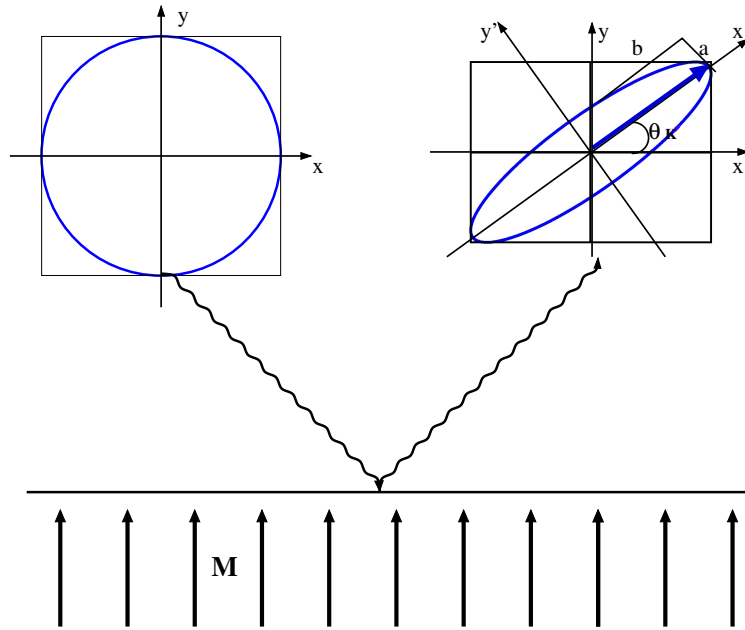


Fig. 6.4: The polar Kerr effect

Magnetic optics (MO) deal with phenomena arising as a result of interaction between light and matter when the latter has non zero magnetization. For example, when a plane polarized light reflects from a metal surface or transmits through a thin film which has non zero magnetization becomes elliptically polarized with a rotation of the plane of polarization. This effect due to reflection is called MO kerr effect and that due to transmission is called MO Faraday effect. The Kerr effect exists in three types of geometries: polar, longitudinal and transverse. Among these, the polar Kerr effect, where the direction of the magnetization  $\mathbf{M}$  is oriented perpendicular to the reflective surface and parallel to the plane of incidence (see Fig. 6.4), is by far the largest one and therefore this geometry is the most interesting one in connection with the technological application. Hence, we performed our theoretical investigations for the polar Kerr effect only.

### 6.4.1 Microscopic theory of magneto optical effect

A plane polarized light can be resolved into two oppositely polarized circular polarization:

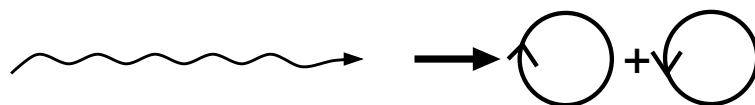


Fig. 6.5: Right and left-handed circularly polarized component of a plane polarized light beam.

When they interact with a magnetic medium the refractive indices for right and left-handed circular polarization become different. For polar Kerr magnetization geometry, the Kerr rotation ( $\theta_K$ ) and ellipticity ( $\eta_K$ ) in terms of the complex refractive indices ( $N_{\pm}$ ) for two circular components of opposite ( $\pm$ ) helicity is given by [14],

$$\frac{1 + \tan(\eta_K) e^{2i\theta_K}}{1 - \tan(\eta_K) e^{2i\theta_K}} = \frac{1 + N_+}{1 - N_-} \frac{1 - N_-}{1 + N_+} \quad (6.1)$$

The Faraday rotation ( $\theta_F$ ) and ellipticity ( $\eta_F$ ) can be expressed as [15],

$$\theta_F + i\eta_F = \frac{\omega d}{2c} (N_+ - N_-) \quad (6.2)$$

where  $c$  is the velocity of light in vacuum, and  $d$  is the thickness of the film.  $\omega$  is the frequency of the incoming/outgoing electromagnetic wave.

At optical frequencies the propagation of electromagnetic waves in magnetic materials is described by the dielectric tensor  $\varepsilon$ , or equivalently, with the optical conductivity tensor  $\sigma$ . With the magnetic moment in the  $z$  direction, the form of the optical conductivity tensor for cubic or tetragonal symmetry is,

$$\sigma = \sigma^{(1)} + i\sigma^{(2)} = \begin{pmatrix} \sigma_{xx} & \sigma_{xy} & 0 \\ \sigma_{yx} & \sigma_{yy} & 0 \\ 0 & 0 & \sigma_{zz} \end{pmatrix} \quad (6.3)$$

where  $\sigma_{xx} = \sigma_{yy}$  and  $\sigma_{xy} = -\sigma_{yx}$ . Note that even in the cubic case,  $\sigma_{zz}$  is not strictly equal to  $\sigma_{xx}$ . In terms of conductivities, the refractive indices are:

$$N_{\pm}^2 = 1 + \frac{4\pi i}{\omega} (\sigma_{xx} \pm i\sigma_{xy}) \quad (6.4)$$

Using this expression for  $N_{\pm}$  for small Kerr angles Eqn. 6.1 can be simplified to

$$\theta_K + i\eta_K \approx \frac{-\sigma_{xy}}{\sigma_{xx} \left(1 + \frac{4\pi i}{\omega} \sigma_{xx}\right)^{1/2}} \quad (6.5)$$

Similarly for small Faraday angle Eqn. 6.4 transforms Eqn. 6.2 in to a simplified form,

$$\theta_F + i\eta_F \approx \frac{2\pi d}{c} \frac{\sigma_{xy}}{\left(1 + \frac{4\pi i}{\omega} \sigma_{xx}\right)^{1/2}} \quad (6.6)$$

For a metal, the optical conductivity is sum of two contributions: (1) interband, (2) intraband. To calculate the interband contribution we used the dipole approximation, *i.e.*, the momentum transfer from the initial state to the final state was neglected. The interband contribution to the absorptive part of the optical conductivity  $\sigma_{\alpha\beta}^{(abs)}(\omega)$ , as a function of frequency  $\omega$  of the incoming/outgoing electromagnetic wave, in the random phase approximation is given by [16],

$$\begin{aligned}\sigma_{\alpha\beta}^{(abs)}(\omega) &= \frac{\Omega e^2}{4\pi^2 \hbar m^2 \omega} \sum_{nn'} \int d^3k \langle kn|p_\alpha|kn'\rangle \\ &\times \langle kn'|p_\beta|kn\rangle f_{kn}(1 - f_{kn'}) \delta(\epsilon_{kn'} - \epsilon_{kn} - \hbar\omega)\end{aligned}\quad (6.7)$$

We considered the transitions from occupied to unoccupied states only.  $e$  and  $m$  are the charge and mass of the electron,  $\Omega$  is the volume of the unit cell,  $\epsilon_{kn'}$  and  $\epsilon_{kn}$  are the eigenvalues of final state  $|kn'\rangle$  (unoccupied) and initial state  $|kn\rangle$  (occupied) at  $k^{th}$  point in the Brillouin zone.  $\langle kn|p_\alpha|kn'\rangle$  is the dipole matrix element with  $p_\alpha$  being the momentum operator in the  $\alpha^{th}$  direction.  $f_{kn}$  is the Fermi-distribution function ensuring that only transitions from occupied to unoccupied states are counted. Note that  $\sigma_{\alpha\alpha}^{(abs)}(\omega) = Re(\sigma_{\alpha\alpha}(\omega))$  (*i.e.* the real part), whereas  $\sigma_{\alpha\beta}^{(abs)}(\omega) = Im(\sigma_{\alpha\beta}(\omega))$  (*i.e.* the imaginary part).

The intraband contribution to the diagonal components of the conductivity is normally described by the Drude formula [17],

$$\sigma_D(\omega) = \frac{\omega_P^2}{4\pi[(1/\tau) - i\omega]}\quad (6.8)$$

The relaxation time  $\tau$ , characterizing the scattering of charge carriers, is dependent on the amount of vacancies and other defects, and will therefore vary from sample to sample. The unscreened plasma frequency  $\omega_P$  depends on the concentration of the charge carriers. We calculated the unscreened plasma frequency by integrating over the Fermi surface using the relation,

$$\omega_{P\alpha\alpha}^2 = \frac{8\pi e^2}{\Omega} \sum \langle kn\xi|p_\alpha|kn\xi\rangle \langle kn\xi|p_\alpha|kn\xi\rangle \delta(\epsilon_{kn\xi} - \epsilon_F)\quad (6.9)$$

where  $\epsilon_F$  is the Fermi energy and  $\xi$  is the spin. The dielectric tensor  $\epsilon_{\alpha\beta}$  is related to the optical conductivity tensor  $\sigma_{\alpha\beta}$  through the equation,

$$\epsilon_{\alpha\beta}(\omega) = \delta_{\alpha\beta} + \frac{4\pi i}{\omega} \sigma_{\alpha\beta}(\omega)\quad (6.10)$$

The reflectivity can be expressed as,

$$R(\omega) = \left| \frac{\sqrt{\epsilon_{\alpha\alpha}(\omega)} - 1}{\sqrt{\epsilon_{\alpha\alpha}(\omega)} + 1} \right|^2\quad (6.11)$$

## 6.4.2 Results and discussion

The basic electronic structure of this series in connection with GGA DOS has been discussed already. Two additional points to be noted:

- Inclusion of SO coupling mixes different spin channels which induces states in the gap around  $E_F$  in the majority spin channel in case of  $\text{Sr}_2\text{CrReO}_6$ , sufficient enough to nearly close the gap, making it an almost half-metallic situation as pointed out in Ref.[18].
- The O- $p$  dominated states separated from Cr and B'- $d$  dominated states appear in the energy range between -8 and -3 eV or so with a gap between O- $p$  dominated states and B/B'- $t_{2g}$  states which diminishes as one progresses from W to Re and finally vanishes for Os due to progressive shifting of B' level with respect to O- $p$  level.

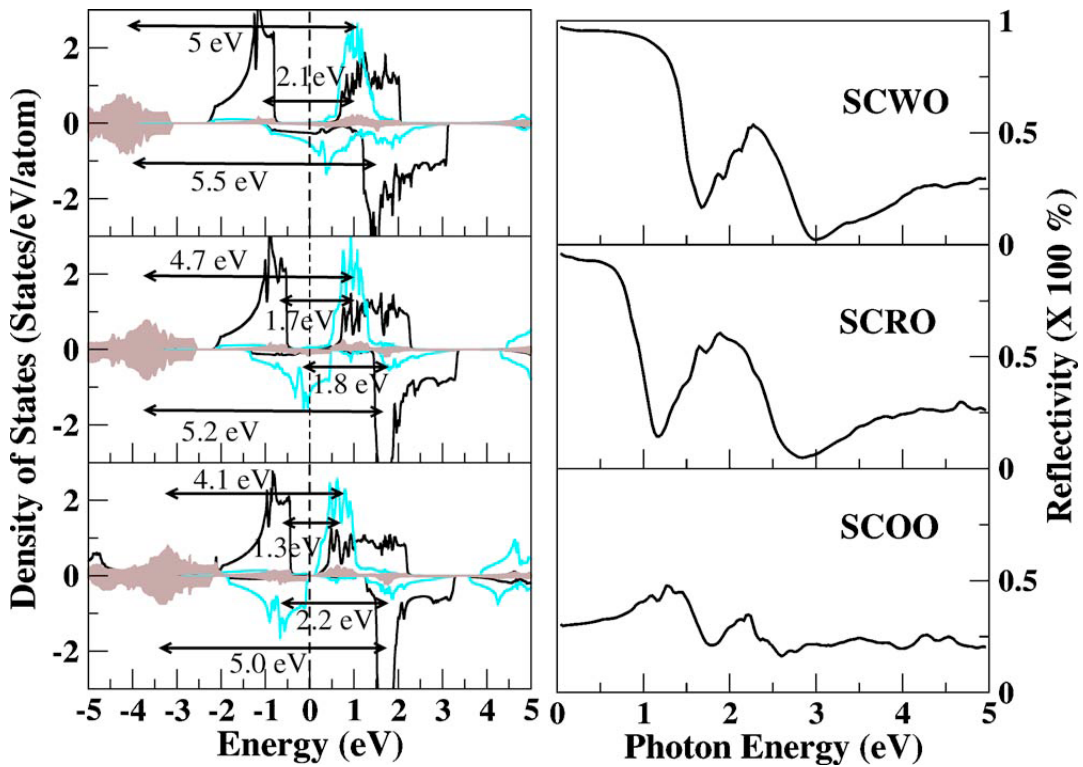


Fig. 6.6: Left panel: Density of states of  $\text{Sr}_2\text{CrB}'\text{O}_6$  system ( $B'=W, \text{Re}, \text{Os}$ ) computed within the framework of GGA including SO coupling. Black and cyan lines and shaded brown area indicate partial density of states corresponding to Cr- $d$ , B'- $d$ , and O- $p$ . Arrows indicate various possible optical transitions. Right panel: Calculated reflectivity spectra for  $\text{Sr}_2\text{CrB}'\text{O}_6$  series.

The left panel of Fig. 6.6 shows the various possible optical transitions with the low energy transitions being dominated by  $d-d$  transitions which can happen due to finite hybridization with O- $p$  and the relatively high energy transition being contributed by the  $d-p$  transitions, in agreement with the experimental findings. The right panel of Fig. 6.6 shows the computed reflectivity for all the three compounds. The computed reflectivity spectra in  $\text{Sr}_2\text{CrReO}_6$  with the Drude component calculated from bare plasma frequency, as given in band-structure calculation, show differences when compared to the available

experimental reflectivity spectrum as reported by Kato *et.al.* [19] In particular, the low energy behavior of the measured data indicates the system to be a bad metal which presumably may have been caused by the nature of the sample.

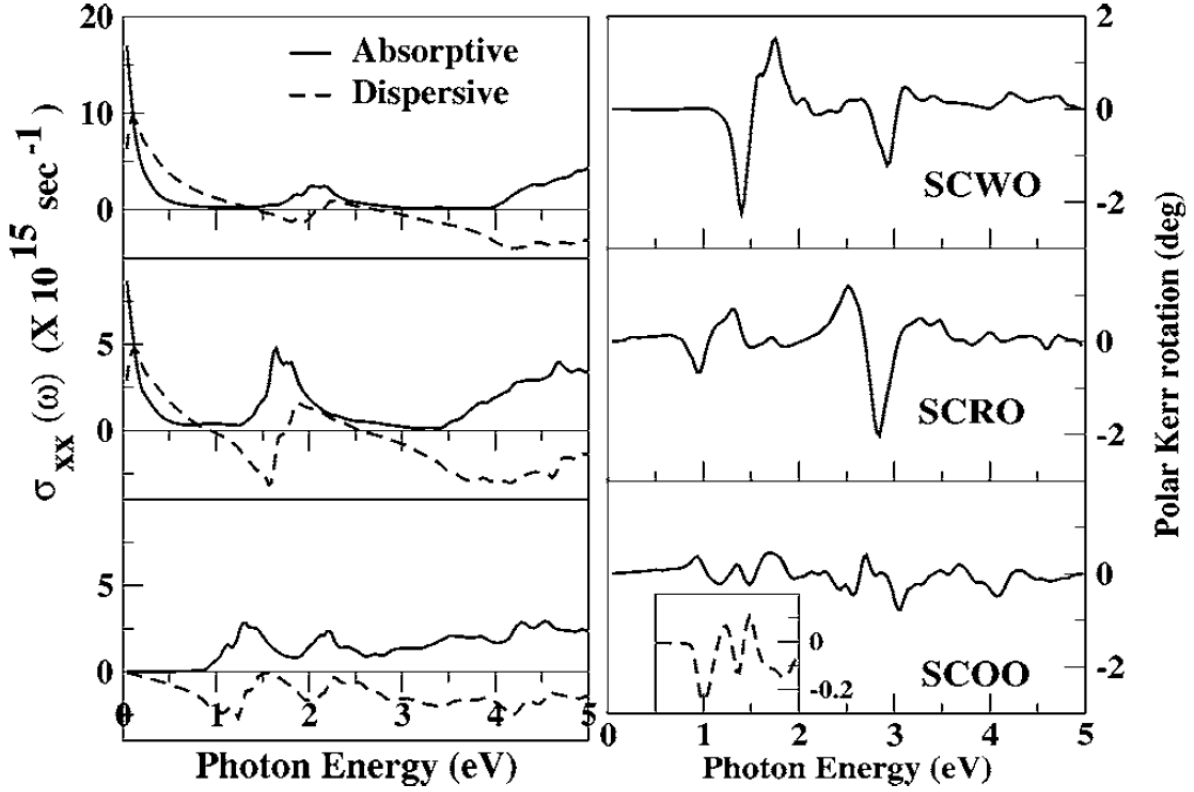


Fig. 6.7: Left panel: Absorptive and dispersive parts of the calculated diagonal optical conductivity of  $\text{Sr}_2\text{CrB}'\text{O}_6$ . Right panel: Calculated polar Kerr rotation spectra for  $\text{Sr}_2\text{CrB}'\text{O}_6$ . The inset shows the Faraday spectrum in unit of  $10^6 \text{ deg/cm}$  for insulating  $\text{Sr}_2\text{CrOsO}_6$ .

Fig. 6.7 shows the computed diagonal conductivity which follows the corresponding reflectivity spectra and the Kerr and Faraday rotation for the series. All interband transitions occurring at low energies are suppressed by the correction to the optical conductivity due to the Drude component for  $\text{Sr}_2\text{CrWO}_6$  and  $\text{Sr}_2\text{CrReO}_6$ . The  $d-d$  interband transition marked in the left panel of Fig. 6.6 gives rise to peak in the real part of the optical spectra observed in the range of 1.52.1 eV. The peak gets bifurcated for  $\text{Sr}_2\text{CrOsO}_6$  due to the combined effect of a larger spin splitting at B' site and enhanced hybridization from O- $p$  as compared to  $\text{Sr}_2\text{CrReO}_6$  and  $\text{Sr}_2\text{CrWO}_6$ . The change of hybridization is caused by the change in the charge transfer energy differences between B'- $d$  and O- $p$ . The spectra for  $\text{Sr}_2\text{CrWO}_6$  and  $\text{Sr}_2\text{CrReO}_6$  show a dip in the range of 34 eV due to the nonavailability of states within that range which gets filled up in  $\text{Sr}_2\text{CrOsO}_6$  due to the closure of gap between O- $p$  dominated states and B/B'- $t_{2g}$  caused by the enhanced  $d-p$  hybridization effect in case of  $\text{Sr}_2\text{CrOsO}_6$  as stated above. In presence of finite off-diagonal conduc-

tivity, large MO signals are expected to occur whenever diagonal conductivity reaches a small value prior to an absorbance due to interband transitions. In case of  $\text{Sr}_2\text{CrWO}_6$  and  $\text{Sr}_2\text{CrReO}_6$ , two such possibilities can arise, one at plasma edge and another at energy  $\approx 3$  eV, where the dip in diagonal conductivity is observed. Computed rotations show large values of  $-2.45^\circ$  and  $-1.25^\circ$  in case of  $\text{Sr}_2\text{CrWO}_6$  and  $-0.72^\circ$  and  $-2.10^\circ$  in case of  $\text{Sr}_2\text{CrReO}_6$ .  $\text{Sr}_2\text{CrOsO}_6$ , which does not have the plasma edge effect and exhibits the closure of the dip in the optical conductivity spectrum showing two small resonances at 1.2 and 2.7 eV. Interestingly,  $\text{Sr}_2\text{CrOsO}_6$  shows an optical gap of about 0.6 eV, and in this regime, light is mostly transmitted with a moderate value of reflectivity. At about 1 eV, it shows a Faraday rotation of about  $-0.25 \times 10^6$  deg/cm, which is of the same order as in Eu monochalcogenides [20, 21]. It is worth mentioning here that  $T_c$  in EuO and EuS are 69 and 16 K, respectively, while it is 725 K in case of  $\text{Sr}_2\text{CrOsO}_6$ .

## 6.5 Summary and outlook

we have studied the counter-intuitive  $T_c$  trend in Cr based double perovskites,  $\text{Sr}_2\text{CrB}'\text{O}_6$  ( $B'=\text{W}/\text{Re}/\text{Os}$ ). Analysis of the electronic and magnetic properties shows that the progressive enhancement of the  $T_c$  across the  $5d$  series should be understood as the interplay of two driving mechanisms: HD mechanism responsible for the negative spin splitting at  $B'$  site as in SFMO, and SE mechanism. The HD mechanism gets weaker as one moves along the series from W to Re to Os, due to the increased energy level separation of  $B'$  from Cr. SE, on the other hand, gets stronger in moving from SCWO to SCRO to SCOO due to the presence of growing intrinsic moment at  $B'$  site, following the dehybridization effect. The observation of uncompensated moment in SCOO arises due to the presence of SO. SCOO, in that sense, should be thought as a ferrimagnet rather than a ferromagnet. With this, we demystify the puzzling  $T_c$  trend in Cr- $B'$  double perovskite series.

Additionally we showed a large Kerr rotation of about  $2^\circ$ - $2.5^\circ$  in SCWO and SCRO in the visible light range that score over  $\text{Sr}_2\text{FeMoO}_6$  [22] in terms of applicability for industrial use as read heads or optical data storage devices. Moderately large Faraday signals found in  $\text{Sr}_2\text{CrOsO}_6$  makes it ideal for application in optical isolators as Faraday rotators. We hope that our study will stimulate experimental activity in this front. A crucial issue in this context is the control of the antisite disorder in terms of preparation of high quality ordered samples. Antisite disorders are known to alter the electronic structure of these materials substantially and are expected to change the value of the computed rotation. The reported antisite disorder of SCWO and SCRO are about 23% [23] and 15% [24], respectively. To get the desired effect, it is therefore essential to synthesize improved samples with reduced antisite disorder.

# References

- [1] J.B. Phillip *et. al.*, Phys. Rev.B, **68**, 144431 (2003).
- [2] H. Kato, T. Okuda, Y. Okimoto, Y. Tomioka, Y. Takenoya, A. Ohkubo, M. Kawasaki, and Y. Tokura, App. Phys. Lett **81**, 328 (2002).
- [3] Y. Krockenberger, K. Mogare, M. Reehuis, M. Tovar, M. Jansen, G. Vaitheeswaran, V. Kanchana, F. Bultmark, A. Delin, F. Wilhelm, A. Rogalev, A. Winkler, and L. Alff, Phys. Rev. B **75**, 020404 (2007).
- [4] Chapter-5 and references there in.
- [5] A. Chattopadhyay and A. J. Millis, Phys. Rev. B **64**, 024424 (2001).
- [6] J. B. Phillip, P. Majewski, L. Alff, A. Erb, R. Gross, T. Graf, M. S. Brandt, J. Simon, T. Walther, W. Mader, D. Topwal, and D. D. Sarma, Phys. Rev. B **68**, 144431 (2003).
- [7] H. Kato, T. Okuda, Y. Okimoto, Y. Tomioka, Y. Takeoya, A. Ohkubo, M. Kawasaki, and Y. Tokura, Appl. Phys. Lett. **81**, 328 (2002).
- [8] A Winkler, N Narayanan, D Mikhailova, K G Bramnik, H Ehrenberg, H Fuess, G Vaitheeswaran, V Kanchana, F Wilhelm, A Rogalev, A Kolchinskaya and L Alff, New J Phys **11** 073047 (2009).
- [9] J. L. Alonso, L. A. Fernandez, F. Guinea, F. Lesmes, and V. Martn-Mayor, Phys. Rev. B, **67**, 214423 (2003).
- [10] O. Navarro, E. Carvajal, B. Aguilar, M. Avignon, Physica B **384**, 110 (2006).
- [11] L. Brey, M. J. Caldern, S. Das Sarma, and F. Guinea, Phys. Rev. B **74**, 094429 (2006).
- [12] P. Sanyal, H. Das and T. Saha-Dasgupta, Phys. Rev. B **80**, 224412 (2009).
- [13] H. R. Hulme, Proc. Roy. Soc. (London) **A135**, 237 (1932); also O. Halpern, Ann Physik [5] **12**, 181 (1932).

- 
- [14] K. H. J. Buschow, in *Ferromagnetic Materials*, edited by E. P. Wohlfarth and K. H. J. Buschow North-Holland, Amsterdam, 1988!, Vol. **4**, Chap. 5.
- [15] W. Reim and J. Schoenes, in *Ferromagnetic Materials*, edited by K. H. K. Buschow and E. P. Wohlfarth Elsevier, New York, 1990!, Vol. **5**, Chap. 2.
- [16] C. S. Wang and J. Callaway, *Phys. Rev. B* **9**, 4897 (1974).
- [17] P. Drude, *Ann. Phys. (Leipzig)* **1**, 566 (1900); **3**, 369 (1900).
- [18] G. Vaitheeswaran, V. Kanchana, and A. Delin, *J. Phys.: Conf. Ser.* **29**, 50 (2006).
- [19] H. Kato, T. Okuda, Y. Okimoto, Y. Tomioka, Y. Takeoya, A. Ohkubo, M. Kawasaki, and Y. Tokura, *Appl. Phys. Lett.* **81**, 328 (2002).
- [20] D. B. Ghosh, M. De, and S. K. De, *Phys. Rev. B* **70**, 115211 (2004).
- [21] J. Schoenes, *Z. Phys. B* **20**, 345 (1974).
- [22] R. Vidya, P. Ravindran, A. Kjekshus, and H. Fjellvag, *Phys. Rev. B* **70**, 184414 (2004).
- [23] P. Majewski, S. Geprags, A. Boger, M. Opel, E. Arb, R. Gross, G. Vaitheeswaran, V. Kanchana, A. Delin, F. Wilhelm, A. Rogalev, and L. Alff, *Phys. Rev. B* **72**, 132402 (2005).
- [24] J. M. Michalik, J. M. De Teresa, C. Ritter, J. Blasco, D. Serrate, M. R. Ibarra, C. Kapusta, J. Freudenberger, and N. Kozlova, *E. Phys. Lett* **78**, 17006 (2007).

# Chapter 7

## Electronic Structure, phonons and dielectric anomaly and chemical origin of the Magneto-electro-structural coupling in ferromagnetic insulating double-perovskite $\text{La}_2\text{NiMnO}_6$ (LNMO)

Content of this chapter has been published in: Hena Das, U. V. Waghmare, T. Saha-Dasgupta and D. D. Sarma, Phys. Rev. Lett. **100**, 186402 (2008); Hena Das, U. V. Waghmare, T. Saha-Dasgupta and D. D. Sarma, Phys. Rev. B **79**, 144403 (2009).

### 7.1 Introduction

Ferromagnetic semiconductors and insulators are rare and mostly exhibit magnetic transition at very low temperatures, e.g., EuS (Curie temperature,  $T_c = 16$  K) [1], EuO ( $T_c = 77$  K) [2],  $\text{CdCr}_2\text{Se}_4$  ( $T_c = 130$  K) [3],  $\text{BiMnO}_3$  ( $T_c = 100$  K) [4],  $\text{SeCuO}_3$  ( $T_c = 25$  K) [5], which precludes their use in devices. Double perovskite  $\text{La}_2\text{NiMnO}_6$  (LNMO) offers an interesting case which is a ferromagnetic semiconductor with a Curie temperature close to room temperature [6]-[10]. Magnetic susceptibility measurements show a transition at a value of  $\sim 280$  K indicating the onset of ferromagnetic long-range ordering (see Fig. 7.1). The field dependence of the magnetization ( $\mathbf{M}$ ) of LNMO, shown in the inset of Fig. 7.1, shows highest saturated magnetization at 5 K and a 5 T applied magnetic field to be equal to  $4.96 \mu_B/f.u.$ , which is very close to the full magnetization of  $5.0 \mu_B/f.u.$  if one considers Ni to be in +2 state and Mn to be in +4 state.

Additionally, Nyrrisa *et.al.* [10] showed a large magnetic field induced changes in the dielectric properties of  $\text{La}_2\text{NiMnO}_6$  at temperature as high as 280 K, as shown in Fig. 7.2. Two important points to be noted are:

- The magnitude of the jump in dielectric constant is more than the electronic contribution of insulators such as LNMO.

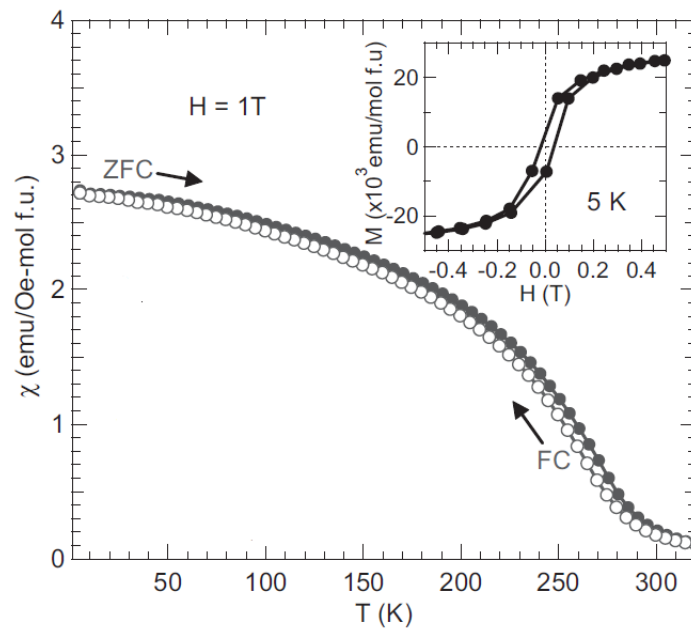


Fig. 7.1: Magnetic susceptibility  $\chi(T)$  data as measured by Nyrisa *et.al.* [10], at 1 T on zero-field (ZFC) and field cooling (FC). Insets show a field dependent magnetization data at 5 K (upper right).

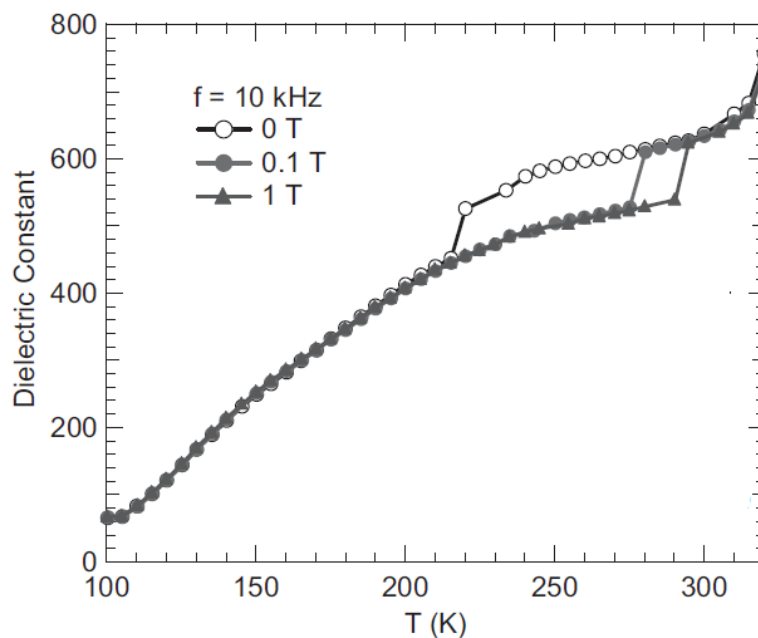


Fig. 7.2: temperature dependence of the dielectric constant at 10 KHz for 0, 0.1 and 1 T applied field. Taken from Ref.[10].

- The jump in the dielectric constant at  $H = 0$  T, occurs at a temperature  $T_{jump}$  below  $T_c$  and  $T_{jump}$  becomes closer to  $T_c$  upon application of a magnetic field.

The origin of such dielectric anomaly has been addressed in the first part of this chapter along with a explanation of the ferromagnetic behavior. In the second part we additionally investigate the Born effective charges  $Z^*$  that describe the coupling between electric field and atomic displacements for LNMO.

The chapter is organized as follows: §: 7.2 provides the structural details of LNMO. §: 7.3 contains the computational details. In §: 7.4, we describe the basic electronic structure of LNMO. §: 7.5 explains the ferromagnetic behavior in LNMO. The origin of the experimentally observed dielectric anomaly has been addressed in §: 7.7. §: 7.7 provides the calculated Born effective charges  $Z^*$  on LNMO and the microscopic understanding of the calculated Born effective charges has been investigated. We end the chapter with concluding remarks §: 7.8.

## 7.2 Structural details

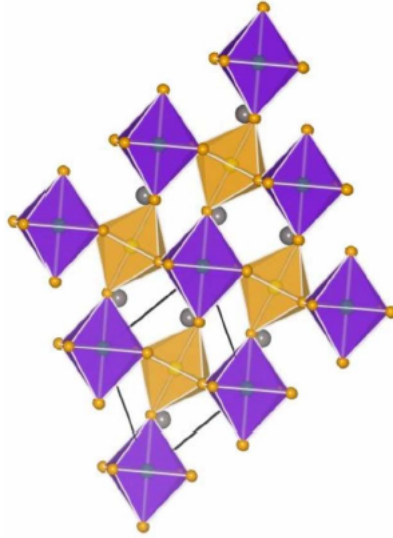


Fig. 7.3: Crystal structure viewed along the pseudocubic [111] direction revealing the high-temperature rhombohedral structure of LNMO. The violet (dark gray) and orange (light gray) colored octahedra denote the  $\text{NiO}_6$  and  $\text{MnO}_6$  octahedra, respectively. The La atoms shown as big balls sit in the hollow formed by  $\text{NiO}_6$  and  $\text{MnO}_6$  octahedra.

LNMO, having the general structure of a double ordered perovskite ( $\text{A}_2\text{BB}'\text{O}_6$ ), is distorted from the ideal double perovskite, and the amount of distortion changes as the temperature varies. The structure of  $\text{La}_2\text{NiMnO}_6$  is rhombohedral ( $R\bar{3}$ ) at high temperature (is shown in Fig. 7.3) and transforms to monoclinic ( $P2_1/n$ ) at low temperature, with

these two structures coexisting over a wide temperature range [11, 13]. In view of the fact that the positions of light atoms are often not well characterized within the experimental technique, we have carried out structural optimization of both rhombohedral (RH) and monoclinic (MC) phases where the internal degrees of freedom associated with La and O atoms have been optimized, keeping the lattice parameters fixed at experimentally determined values [11]. The relaxed structural parameters of the rhombohedral FM state (see Table 7.1) agree well within 3% with experimental ones proving the reliability of our calculation scheme. The position of O atoms, in particular, the x coordinate of O3 oxygen of the MC phase, however, differ noticeably (a deviation of about 22%) from the experimental values (compared Table 3 in Ref.[11]). Our results may provide basis to further refinement of the experimental structure. Each NiO<sub>6</sub> octahedra in the rhombohedral phase is tilted with respect to MnO<sub>6</sub> octahedra giving rise to the NiOMn bond angle of 157°. The tilting is further increased by 2° in the monoclinic phase.

Table 7.1: Energy-minimized structural parameters of LNMO. Lattice constants have been kept constant at the experimental values.

Rhombohedral						
a(Å)	b(Å)	c(Å)		x	y	z
5.474	5.474	5.474	La	0.24980	0.24980	0.24980
$\alpha$	$\beta$	$\gamma$	Ni	0.0	0.0	0.0
60.671	60.671	60.671	Mn	0.5	0.5	0.5
			O	0.81403	0.67182	0.25889
Monoclinic						
a(Å)	b(Å)	c(Å)		x	y	z
5.467	5.510	7.751	La	0.00838	0.03781	0.24968
$\alpha$	$\beta$	$\gamma$	Ni	0.0	0.5	0.0
			Mn	0.5	0.0	0.0
90.000	90.119	90.000	O1	0.22344	0.20903	0.04140
			O2	0.29189	0.27756	0.45700
			O3	0.42219	0.01454	0.24243

### 7.3 Computational details

We used a combination of two types of methods, namely, (a) muffin-tin orbital based linear muffin-tin orbital (LMTO) and Nth order muffintin orbital (NMTO) methods, and (b) plane wave-based methods. In the latter, we used ultrasoft pseudopotentials

with an energy cutoff of 25 Ry (150 Ry) on the plane wave basis for wave functions (charge density) and a  $6 \times 6 \times 6$  mesh of  $k$  points in sampling the Brillouin zone for a phase with the unit cell containing one formula unit and equivalent for other phases. In particular, the structural optimization and phonon calculations have been carried out using QUANTUM ESPRESSO and effective charges and dielectric response have been carried out using ABINIT. The analysis of hopping interactions by constructing effective orbitals, on the other hand, has been carried out within the framework of NMTO. In our LMTO and NMTO calculations, we have used four different empty spheres to achieve the space filling. We used a spin-polarized generalized gradient approximation (GGA) to the exchange correlation functional.

The computation of Born effective charges has been carried out with the plane-wave pseudopotential method as implemented in the ABINIT code. We have carried out the analysis of the contribution of the different set of bands to the BECs of different ions, a technique known as band-by-band decomposition [12]. In this technique, individual contributions are obtained by considering the Bloch functions associated with a particular set of bands as elements of overlap matrix.

## 7.4 Basic electronic structure

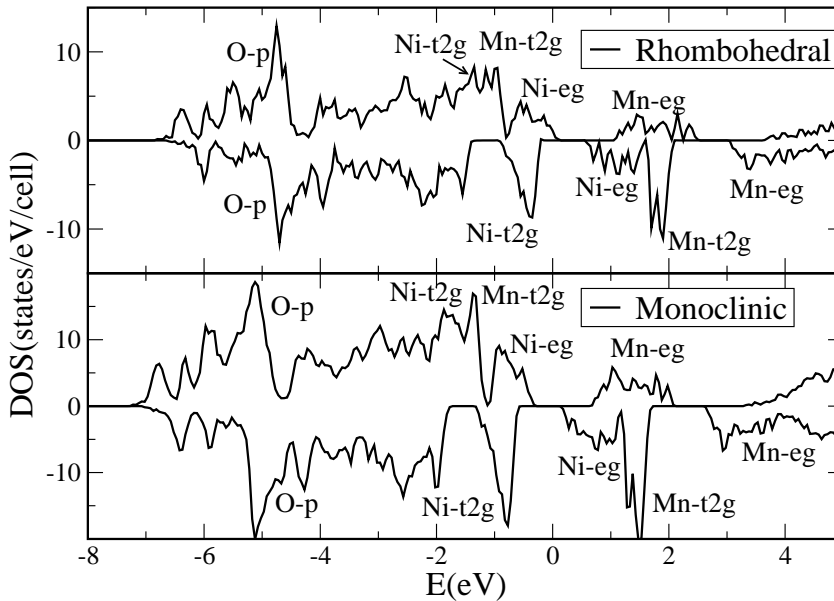


Fig. 7.4: DOS of LNMO in geometry optimized rhombohedral and monoclinic phases.

We determined the electronic structure of geometry optimized FM LNMO, for rhombohedral and monoclinic phases using the LMTO basis, as well as using the plane wave basis. Both methods resulted in similar features in the computed density of states and

band structures, and insulating solutions for both RH and MC phases. The spin resolved partial density of states (DOS) of LNMO in the rhombohedral phase, is shown in the topmost panel of Fig. 7.4. Below -2 eV the predominant contribution is from O-2*p* states. The octahedral surrounding of Mn and Ni atoms split the Mn- and Ni-*d* manifolds into *t*<sub>2*g*</sub> and *e*<sub>g</sub> levels. In the up-spin channel, the Ni-*t*<sub>2*g*</sub> and Ni-*e*<sub>g</sub> levels are found in the energy range  $\sim -2$  eV to Fermi energy and show a significant mixing with Mn-*d* states and O-*p* states. In the down-spin channel the Ni-*t*<sub>2*g*</sub> bands are located between O-*p* states and the Fermi level, while Ni-*e*<sub>g</sub> states lie  $\sim 1.2$  eV above the Fermi level. This corresponds to the nominal valence of Ni<sup>2+</sup> (*d*<sup>8</sup>: *t*<sub>2*g*</sub><sup>6</sup> *e*<sub>g</sub><sup>2</sup>). In the up-spin channel the Mn-*t*<sub>2*g*</sub> bands are localized between Ni-*t*<sub>2*g*</sub> and Ni-*e*<sub>g</sub> bands and are filled, while the Mn-*e*<sub>g</sub> bands are separated by a gap of  $\sim 2.5$  eV from the Mn-*t*<sub>2*g*</sub> bands and remain empty. In the down-spin channel, both Mn-*t*<sub>2*g*</sub> and Mn-*e*<sub>g</sub> bands are located above Fermi level in the energy range  $\sim 1.5$  to 5 eV. This leads to conclusion that the oxidation state of Mn is nominally 4+ (*d*<sup>3</sup>: *t*<sub>2*g*</sub><sup>3</sup> *e*<sub>g</sub><sup>0</sup>), which agree with the Mn NMR and x-ray absorption spectroscopy results [14, 15], though disagree with one of neutron diffraction study [13]. Our spinpolarized LMTO calculations gave a moment of 3.0  $\mu_B$  at the Mn site within a muffin-tin (MT) radius of 1.32 Å, which agree with the experimental value of 3.0  $\mu_B$  [10]. The magnetic moment at the Ni site, for a MT radius of 1.52 Å, is found to be 1.43  $\mu_B$ , which is less than the experimentally measured value of 1.9  $\mu_B$ . The residual moment is found to reside at the O sites giving rise to the total magnetization of 5.0  $\mu_B$  in agreement with the experimental value [10]. The spin resolved DOS in the monoclinic structure is shown in the bottommost panel of Fig. 7.4. The basic nature of the DOS is similar to that of rhombohedral phase of LNMO. The occupation of the Ni-*d* states and Mn-*d* states suggests again the nominal oxidation states of Ni and Mn ions to be 2+ and 4+ , respectively. The moments are found to be 2.91  $\mu_B$  within a MT radius of 1.38 Å at the Mn site, 1.35  $\mu_B$  at the Ni site within a MT sphere of radius 1.52 Å , and  $\sim 0.10$   $\mu_B$  (for 0.95 Å MT radius) at the O site, giving rise to  $\sim 5.0$ /f.u. total magnetic moment, which is again in agreement with the experimental findings.

## 7.5 Ferromagnetism - The extended Kugel-Khomskii model

LNMO being an insulator, the ferromagnetism in this compound is expected to be dominated by the localized superexchange kind of interaction, resulting from the interaction of the half-filled *d* orbital of one metal ion with the vacant *d* orbital of another metal ion through anion *p* orbital. We used an extended Kugel-Khomskii model [16] that includes the hybridization between half-filled Ni-*e*<sub>g</sub> orbitals and Mn-*t*<sub>2*g*</sub> orbitals, as well as the hybridization between half-filled Ni-*e*<sub>g</sub> orbitals and vacant Mn-*e*<sub>g</sub> orbitals, as illustrated

in Fig. 7.5. The interaction between Ni- $e_g$  and Mn- $t_{2g}$  is forbidden for parallel alignment between Ni and Mn spins, therefore the energy gain ( $E_{e,t}^{\uparrow\uparrow}$ ) is equal to zero. However this interaction is allowed for anti-parallel arrangement between Ni and Mn spins given by the energy gain,

$$E_{e,t}^{\uparrow\downarrow} = -4 \frac{\sum_{m,m'} (t_{e^m,t^{m'}})^2}{(U + \Delta_{e,t})} \quad (7.1)$$

where  $t_{e^m,t^{m'}}$  and  $\Delta_{e,t}$  represent the virtual hopping integral and on-site energy differences between Ni- $e_g$  and Mn- $t_{2g}$  states, respectively. The summation  $m, m'$  runs over all half-filled  $e_g$  and half-filled  $t_{2g}$  orbitals at Ni and Mn sites, respectively.  $U$  is the on-site Coulomb interaction and  $J_H$  denotes the Hund coupling.

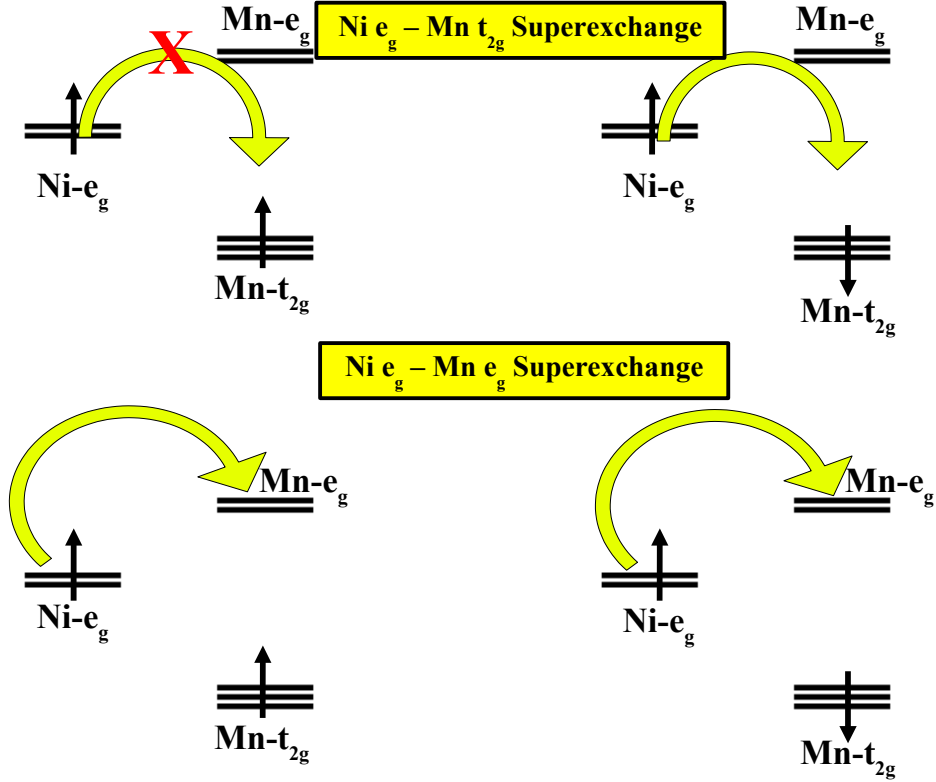


Fig. 7.5: All super exchange interactions between Ni- $d$  states and Mn- $d$  states. The upper panel corresponds to superexchange interactions between half-filled Ni  $e_g$  and half-filled Mn  $t_{2g}$  states, while the lower panel corresponds to superexchange interactions between half-filled Ni  $e_g$  and empty Mn  $e_g$  states.

On the other hand the interactions between half-filled Ni- $e_g$  orbitals and vacant Mn- $e_g$  orbitals are allowed for both parallel and anti-parallel alignments between Ni and Mn spins. The corresponding energy gains are,

$$E_{e,e}^{\uparrow\uparrow} = -4 \frac{\sum_{m,m'} (t_{e^m,e^{m'}})^2}{(U + \Delta_{e,e} - J_H)} \quad (7.2)$$

and

$$E_{e,e}^{\uparrow\downarrow} = -4 \frac{\sum_{m,m'} (t_{e^m, e^{m'}})^2}{(U + \Delta_{e,e})} \quad (7.3)$$

for parallel and anti-parallel alignments between Ni and Mn spins, respectively.  $t_{e^m, e^{m'}}$  and  $\Delta_{e,e}$  represent the virtual hopping integral and on-site energy differences between Ni- $e_g$  and Mn- $e_g$  states, respectively. The summation  $m, m'$  runs over all half-filled  $e_g$  and empty  $e_g$  orbitals at Ni and Mn sites, respectively. The virtual hopping of parallelly aligned spins is allowed and is favored over the virtual hopping of antiparallely aligned spins due to the energy gain via the Hund coupling  $J_H$ .

The net Ni-Mn interaction  $J_{Ni-Mn}$  is given by,

$$J_{Ni-Mn} = 4 \frac{\sum_{m,m'} (t_{e^m, t^{m'}})^2}{(U + \Delta_{e,t})} - 4 \frac{\sum_{m,m'} (t_{e^m, e^{m'}})^2 J_H}{(U + \Delta_{e,e} - J_H)(U + \Delta_{e,e})} \quad (7.4)$$

The construction of effective Ni- and Mn- $d$  orbitals carried out by integrating out O and La orbital degrees of freedom and keeping active only the Mn- and Ni- $d$  degrees of freedom, using NMTO downfolding method. This procedure generates the effective Ni- and Mn- $d$  orbitals (see Fig. 7.6), which takes into account the renormalization from the integrated-out O and also La degrees of freedom.

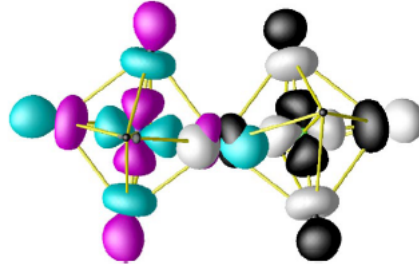


Fig. 7.6: Overlap between effective  $x^2 - y^2$  orbitals, placed at neighboring NiO<sub>6</sub> and MnO<sub>6</sub> octahedra of LNMO calculated in the monoclinic phase, showing the superexchange path mediated by the corner-shared O. Plotted are the orbital shapes (constant-amplitude surfaces) with lobes of opposite signs colored as black (magenta) and white (cyan), respectively, for Mn (Ni).

The computed sum of squares of the Ni- $e_g$ -Mn- $t_{2g}$  and Ni- $e_g$ -Mn- $e_g$  hopping interactions in the basis of NMTO-Wannier functions turned out to be about 0.02 eV and 0.2 eV, respectively. While the corresponding on-site energy difference  $\Delta_{e,t}$  and  $\Delta_{e,e}$  turned out to be about 0.25 eV and 1.9 eV, respectively. We considered a typical value of 4 eV and  $J_H$  of 0.9 eV. We assumed that the value of  $U$  and  $J_H$  to be the same between Ni and Mn. While  $J_H$  is fairly constant between different elements,  $U$  can vary. Mn is expected to have a smaller  $U$  value than Ni. Considering a  $U$  value of 3 eV for Mn and 5 eV for Ni, one gets an average  $U$  value of 4 eV. Putting these values in Eqn. 7.4 the net exchange interaction  $J_{Ni-Mn}$  between Ni and Mn came out to be ferromagnetic with a

value of about 5 meV. Changing  $U$  by 5% to 10%, we found that the calculated effective  $J_{Ni-Mn}$  turn out to have a value between 4 and 7 meV. The mean-field  $T_c$  computed with  $J_{Ni-Mn} = 4$  eV came out to be 350 K compared to experimental estimate of 280 K. We also attempted to extract the net magnetic coupling,  $J_{Ni-Mn}$ , by taking the total energy difference between two magnetic configuration: (1) parallel arrangement between Ni and Mn spins, ie FM arrangement. (2) Antiparallel arrangement between Ni and Mn spins, ie ferrimagnetic (FIM) arrangement. Local density approximation (LDA) total energy differences are, however, known to overestimate the value of  $J_{Ni-Mn}$  due to the local density approximation over binding problem. Our computed  $J_{Ni-Mn}$  turned out to be about 14 meV, which overestimate the perturbatively computed  $J_{Ni-Mn}$  by a factor of about 3. The introduction of spin-orbit coupling changes the magnitude of  $J_{Ni-Mn}$  by less than 1%, maintaining the FM nature of  $J_{Ni-Mn}$ .

## 7.6 Spin-phonon coupling-Origin of dielectric anomaly

As we have pointed out in the introductory section of this chapter, the electronic contribution to the dielectric constant  $\epsilon^\infty$  in LNMO is expected to be smaller than the magnitude of jump in the dielectric constant. To confirm this point we have calculated the electronic contribution  $\epsilon^\infty$  for FM and FIM magnetic configurations. Note that any other different spin arrangement other than the FM spin arrangement arrangement would have been equally qualified for this purpose. The charge states of Ni and Mn in the FIM state are found to remain same as that in the FM state. The computed values are equal to 22 and 20 for FM and FIM phases, respectively. Compare to the jump in dielectric constant, which is about 80, these values and difference in their magnitude are small.

Therefore we expect the origin of this coupling between magnetic field and dielectric response to emerge from the couplings between spin and structure, *i.e.*, phonons. To determine the coupling between spin and various phonons, we studied the response of optimized FM rhombohedral structure to changes in magnetic ordering: e.g., changes in phonon frequencies with changes in magnetic ordering. We determined changes in phonon frequencies upon changing the magnetic configuration from FM to FIM phase. Hellmann-Feynman forces acting on atoms in the FIM phase, giving us the lowest order coupling between spins and phonons, which is linear in atomic displacements. We found that these forces are equal and opposite for pairs of atoms; hence, this coupling is zero for any IR-active modes and should have no direct implications to the observed dielectric anomaly. Next, we determined the  $\Gamma$ -point phonons for the rhombohedral structure with FM and FIM ordering. Shifts in the phonon frequencies give the coupling between spins and atomic displacements at the second order. Since the rhombohedral structure is unstable at  $T = 0$  K, we find two marginally unstable modes ( $31i$  and  $19i$   $\text{cm}^{-1}$ ), which are IR inactive and couple strongly with spins: their frequencies change to  $64i$  and  $63i$   $\text{cm}^{-1}$  in the FIM

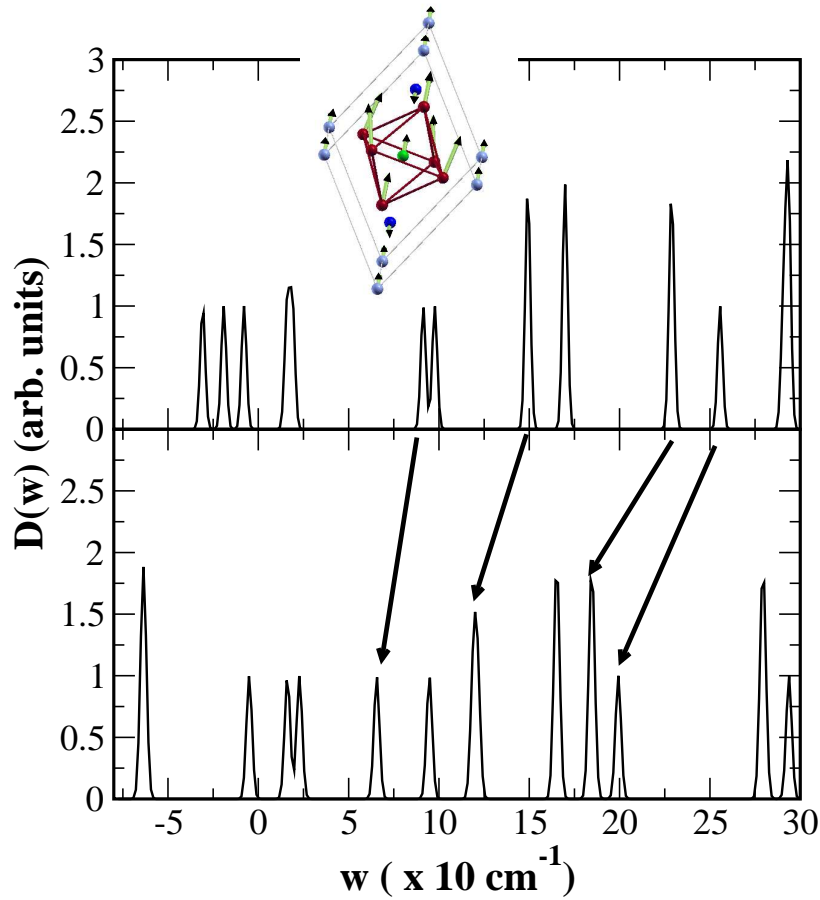


Fig. 7.7: Phonon spectra of rhombohedral LNMO in FM (top panel) and FIM (bottom panel) states. The arrows show the shifting of dominant IR-active phonon modes. The inset shows the displacement of atoms corresponding to the lowest frequency IR-active mode. The angle between the dotted lines connecting the Ni-O (at the center of the oxygen octahedra) and O-Mn (rightmost corner of the cell) is affected by this phonon.

phase. We find that frequencies of the lowest energy IR-active phonons soften from 91.3, 149, 228, and 255  $\text{cm}^{-1}$  in the FM phase to 65.5, 120, 184, and 199  $\text{cm}^{-1}$ , respectively (indicated by arrows in Fig. 7.7), exhibiting a strong coupling with spin. This may be compared with the recently studied case of  $\text{CdCr}_2\text{S}_4$  [17] where the significant polar mode was found only at a frequency of 300  $\text{cm}^{-1}$ . This results in a change in the static dielectric constant from 119 in the FM state to 221 in the FIM state, which is dominated by the softest IR-active mode (see inset of Fig. 7.7) with a contribution of 77 and 185, respectively. Atomic displacements in this softest mode are such that they would make the Ni-O-Mn angles closer to  $180^\circ$ , in an average sense, leading to enhancement of the superexchange interaction. The decrease in phonon frequency for the spin-paired Ni-Mn in the FIM phase compared to spin-antipaired Ni-Mn in the FM phase can be explained by analyzing the spin Hamiltonian  $JS_i \cdot S_j$  and noting that the magnetic superexchange

coupling  $J$  depends on Ni-O-Mn,  $\theta$ , as  $\cos^2(\theta)$ . Expanding  $\cos^2(\theta)$ , about the equilibrium value of Ni-O-Mn,  $\theta_0 \cong 157^\circ$ , and assuming  $\theta = \theta_0 + u$ ,  $u$  being the displacement, the spin-phonon coupling turns out to be positive for the term linear in  $u$  and negative for the term quadratic in  $u$ . The latter effectively gives a positive change in phonon frequency due to the additional negative sign, associated with the FM nature of the magnetic interaction [cf. Eqn. 7.4].

## 7.7 Born effective charges in LNMO

Dielectric response of a phonon is determined primarily by its frequency and the electric-dipole moment  $p$ . The latter is given by the Born effective charge [18] (BEC) tensor  $Z_{\kappa,\alpha\beta}^*$  through the relationship:

$$p_\alpha = Z_{\kappa,\alpha\beta}^* \tau_{\kappa,\beta} \quad (7.5)$$

where  $\tau_{\kappa,\beta}$  is the movement of an ion  $\kappa$  along the direction  $\beta$ . Physically,  $Z^*$  measures the microscopic current flowing across the sample while the ions are adiabatically displaced. Such currents are responsible for building up the spontaneous polarization when ions are displaced from the centrosymmetric position to the ferroelectric structure [19].

In another physical interpretation, it gives the force  $F$  the ion feels in the direction  $\alpha$  through interaction with the electric field  $E$  in direction  $\beta$ ,

$$F_{\kappa,\alpha} = Z_{\kappa,\alpha\beta}^* E_\beta \quad (7.6)$$

$Z^*$  is therefore a measure of the strength of electrostructural coupling of an insulating material. Being related to dynamical changes of the hybridization between various ions [20], values of  $Z^*$  are often found to be highly nontrivial and can reach values twice as large as the static nominal ionic charges. While in simple high-symmetry insulators, the  $Z^*$  matrix is typically isotropic with only nonzero identical diagonal components for a general case  $Z^*$  can have both diagonal and off-diagonal components which need not to be even symmetric.

Our calculated BECs of La, Ni, and Mn (shown in Table- 7.2) follow the rhombohedral site symmetry, with a threefold axis along pseudocubic [111] direction, while that at the O site is lowered, leading to strong anisotropy of the oxygen  $Z^*$  tensor. We found anomalously large charges at Mn site (+6 - +7, significantly larger compared to its nominal valence of +4), similar to earlier report on  $\text{CaMnO}_3$  [21]. The striking feature appears in the Born effective charges of Ni, which show anomalously large antisymmetric off-diagonal components in the Born effective charge matrix, though the diagonal elements have a value close to the nominal charge of Ni(+2). More interestingly we found that the largeness of these antisymmetric off-diagonal components depends sensitively upon the

Table 7.2: Calculated Born effective charge tensors at the La, Ni, Mn and O sites of  $\text{La}_2\text{NiMnO}_6$  at FM and FiM phases. Note the presence of large, off-diagonal elements which are anti-symmetric specially in case of Ni. Changing the magnetic ordering between Ni and Mn from FM to FiM has profound effect in terms of making the anti-symmetric off-diagonal components at Ni weaker.

	Ferromagnetic	Ferrimagnetic
$Z_{La}^{*(T)}$	$\begin{pmatrix} 4.52 & 0.0 & 0. \\ 0.0 & 4.52 & 0. \\ 0. & 0. & 4.38 \end{pmatrix}$	$\begin{pmatrix} 4.57 & -0.11 & 0. \\ 0.11 & 4.57 & 0. \\ 0. & 0. & 4.31 \end{pmatrix}$
$Z_{Ni}^{*(T)}$	$\begin{pmatrix} 2.48 & 3.23 & 0. \\ -3.23 & 2.48 & 0. \\ 0. & 0. & 2.24 \end{pmatrix}$	$\begin{pmatrix} 2.03 & 1.22 & 0. \\ -1.22 & 2.03 & 0. \\ 0. & 0. & 1.64 \end{pmatrix}$
$Z_{Mn}^{*(T)}$	$\begin{pmatrix} 6.44 & -0.37 & 0. \\ 0.37 & 6.44 & 0. \\ 0. & 0. & 6.52 \end{pmatrix}$	$\begin{pmatrix} 7.51 & -0.98 & 0. \\ 0.98 & 7.51 & 0. \\ 0. & 0. & 6.54 \end{pmatrix}$
$Z_{O1}^{*(T)}$	$\begin{pmatrix} -3.70 & -0.48 & 0.91 \\ 0.48 & -2.28 & -0.35 \\ 0.91 & 0.35 & -2.92 \end{pmatrix}$	$\begin{pmatrix} -3.67 & 0.21 & 0.93 \\ 0.21 & -2.54 & -0.22 \\ 1.01 & -0.18 & -2.80 \end{pmatrix}$
$Z_{O2}^{*(T)}$	$\begin{pmatrix} -2.64 & 0.14 & -0.15 \\ 1.09 & -3.35 & 0.97 \\ -0.76 & 0.62 & -2.92 \end{pmatrix}$	$\begin{pmatrix} -2.64 & 0.38 & -0.28 \\ 0.38 & -3.59 & 0.92 \\ -0.35 & 0.97 & -2.80 \end{pmatrix}$
$Z_{O3}^{*(T)}$	$\begin{pmatrix} -2.64 & -1.09 & -0.76 \\ -0.14 & -3.35 & -0.62 \\ -0.15 & -0.97 & -2.92 \end{pmatrix}$	$\begin{pmatrix} -3.03 & -0.60 & -0.65 \\ -0.60 & -3.21 & -0.70 \\ -0.66 & -0.79 & -2.80 \end{pmatrix}$

magnetic ordering between Ni and Mn. While the change in magnetic ordering from FM to FIM state affects almost all the matrix elements of Born effective charge tensor, the most significant change occurs in the offdiagonal component of the Born effective charge of Ni. This implies that the anomalous and antisymmetric Born effective charge of Ni is intimately connected with the magnetic coupling between Ni and Mn, thereby giving rise to a magnetism-dependent electrostructural coupling. The work by Massidda *et.al.* [22] in this context carried out for transition-metal monoxides showed the effect of magnetic anisotropy on  $Z^*$  in terms lowering of symmetry of the magnetic space group; while in the current example the magnetic ordering changes the hybridization and therefore influences the magnitude of the components of  $Z^*$  without effecting the symmetry. The effect is therefore of different origin than what has been described in Ref.[22].

We note that the  $Z^*$  of oxygen atoms also undergo interesting changes due to their hybridization with metal ions. The antisymmetric components of  $Z^*$  of oxygen atoms weaken (almost vanishes) significantly in the FIM state relative to FM one. Focusing on to Mn, we find that both diagonal and off-diagonal antisymmetric components are enhanced in the FIM phase compared to that in FM phase.

### 7.7.1 Electronic origin

Previous work [20] in connection with contributions of change in hybridization to the anomalous charge has shown that it originates primarily from a modification of the interactions between occupied and unoccupied electronic states. Examination of level diagram (Fig. 7.8) reveals that such situation arises in case of interaction between Ni  $t_{2g}$  and Mn  $t_{2g}$  symmetries, with Ni  $t_{2g}$  states being filled and Mn  $t_{2g}$  states being empty for the minority-spin channel in ferromagnetic case and for the majority-spin channel in case of ferrimagnetic spin alignment. Similarly it arises between Ni  $e_g$  and Mn  $e_g$  symmetries, with Ni  $e_g$  states being filled and Mn  $e_g$  states being empty for the majority-spin channel for both ferromagnetic and ferrimagnetic cases. Therefore we examine one of the Wannier functions centered on Ni and having  $t_{2g}$  symmetry in minority (majority) spin channel for the ferromagnetic (ferrimagnetic) phase for two cases: (a) equilibrium rhombohedral structure and (b) a structure distorted with Ni displaced by 1% of the lattice constant along the crystallographic x axis (see Fig. 7.9). We notice the central  $y'z'$  symmetry, defined in the local coordinate system with  $z'$  axis pointing along one of the Ni-O bond, while the tails in the immediate neighborhood are shaped according to oxygen  $p_{y'}$  and  $p_{z'}$  orbitals which form antibonds with the central Ni  $y'z'$  symmetry. The end of these tails consist of  $t_{2g}$  orbitals (largely unoccupied) of the next-nearest-neighbor Mn atoms, leading to a finite mixing of orbitals of Ni and Mn. The effective Ni-centered Wannier function is longer ranged in the ferromagnetic phase having a spread of  $\approx 3.6 \text{ \AA}$  compared to that in the ferrimagnetic phase, having a spread of  $\approx 2.7 \text{ \AA}$ . This is due to the fact that (cf. Fig. 7.8) Mn  $t_{2g}$  states are close in energy to Ni  $t_{2g}$  down-spin states ( $\Delta \approx 1.6 \text{ eV}$ ) in the

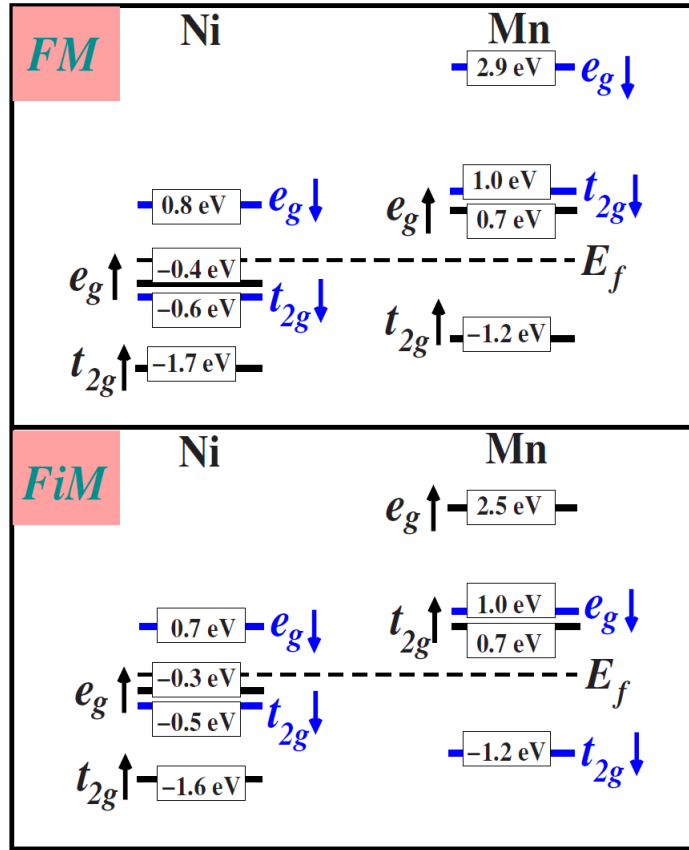


Fig. 7.8: Energy level positions of Ni and Mn  $d$  levels with respect to Fermi energy  $E_f$  as obtained in DFT calculation. The upper (lower) panel corresponds to ferromagnetic (ferrimagnetic) spin arrangement between Ni and Mn spins.

ferromagnetic phase while Mn  $t_{2g}$  states are farther away from Ni  $t_{2g}$  up-spin states ( $\Delta \approx 2.6$  eV) in the ferrimagnetic phase, resulting in stronger Ni-Mn hybridization in the ferromagnetic phase.

As the angle Ni-O-Mn increases in one quadrant and decreases in the opposite quadrant upon displacement of Ni atom (cf. Fig. 7.9(a)), oxygen-Mn bonding along the tails strengthens along one direction and weakens along the opposite direction implying a net transfer of charge. The most striking and key observation is that in addition to the net charge-transfer effect, the Mn  $t_{2g}$ -like tails rotate in quadrants that show accumulation of charge (see Fig. 7.9(c)). This mechanism is different from the charge transfer along a line through unit cell, and gives a shift in the center of Wannier function along  $y$  ( $-x$ ) direction when Ni atom is off-centered along  $x$  ( $y$ ) direction. The center of gravity of Wannier function with 1% displaced Ni atom along  $x$  direction shows a net displacement of about  $0.05 \text{ \AA}$  along  $y$  direction, which is about 1.5% of the lattice constant. Thus, this is responsible for the large off-diagonal component of the  $Z^*$  tensor of Ni. Change in the alignment of Ni and Mn spins from FM to FIM leads to weaker hybridization between Ni

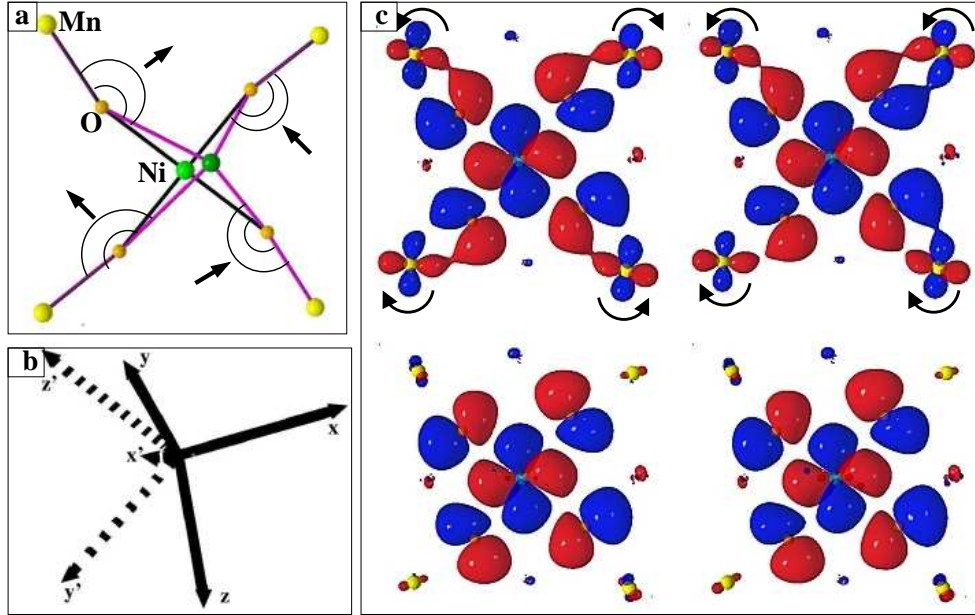


Fig. 7.9: (a) Atomic structure of  $\text{La}_2\text{NiMnO}_6$  in the equilibrium configuration compared to the structure where Ni atom has been moved along the rhombohedral  $x$  axis. The green, yellow and orange balls mark the positions of Ni, Mn, and O atoms. The lighter and darker green balls indicate the positions of Ni at equilibrium and that after displacement. The movement of Ni atom strongly influences the  $\angle\text{Ni-O-Mn}$ , increasing it one quadrant and decreasing it in the opposite quadrant from the equilibrium  $\angle\text{Ni-O-Mn}$ . (b) The rhombohedral global coordinate system and the oxygen-based octahedral coordinate system. The unprimed and primed coordinate systems represent the rhombohedral coordinate system ( $z$  axis pointing along the pseudocubic  $[111]$  direction) and the oxygen-based octahedral coordinate system ( $z'$  axis pointing along one of the Ni-O bond and  $x'$  axis pointing along the Ni-O bond approximately perpendicular to it.) (c) Plot of effective Ni  $y'z'$  Wannier functions. Plotted are the orbital shapes (constant amplitude surfaces) with the lobes of opposite signs colored as red (light gray) and blue (dark gray). The upper two panels correspond to calculations in the equilibrium (left panel) and Ni displaced (right panel) conditions in the ferromagnetic phase, while the lower panels correspond to calculations in the equilibrium (left panel) and Ni displaced (right panel) conditions in the ferrimagnetic phase. The arrows marked in the Wannier functions in the ferromagnetic phase show the sense of rotation of the orbital tails.

and Mn, and hence a much smaller antisymmetric component of the  $Z^*$ . Examination of BEC tensor shows diagonal component of Mn to be more anomalous compared to that of Ni, which is explained in terms of the dynamical charge transport from/to oxygen atoms. Mn being in  $d^3$  state, is more  $d^0$  like compared to Ni, which is in  $d^8$  state. Using simple criterion of capacity of an orbital available to exchange charge with  $O^2$ , one finds that the maximum permitted values for  $Ni^{2+}$  in  $d^8$  state is +2, and that for  $Mn^{3+}$  in  $d^3$  state is +5, allowing for a maximum value of BEC of +4 and +8 for Ni and Mn, respectively.

### 7.7.2 Comparison with other compounds

$LiNbO_3$ , very similar in structure with rhombohedral symmetry to LNMO, was also reported [23] to exhibit a large antisymmetric component of Born charge tensor of Nb. As Nb is in the  $d^0$  state in  $LiNbO_3$ , following the orbital filling criterion, the magnitude of the diagonal components of  $Z_{Nb}^*$  (8.3) is much larger than the off-diagonal ones (2.1), in contrast to LNMO. Due to symmetry, the antisymmetric components of  $Z^*$  of two Nb ions in  $LiNbO_3$  are opposite in sign and cancel, in contrast to very disparate magnitudes of the antisymmetric components of  $Z^*$  of Ni and Mn in LNMO. The band-by-band decomposition technique [12] for analysis of  $Z^*$  in case of LNMO reveals that the antisymmetric component of  $Z^* = 3.2$  of Ni arises primarily from O  $p$  and metal  $3d$  states with contributions of 5.5 and 1.8, respectively, confirming once again the role of the metal (Mn)  $3d$  states. In comparison, the antisymmetric charge of 2.1 for Nb in  $LiNbO_3$  is mostly contributed by oxygen  $p$  states. Importantly, Nb being in  $d^0$  state does not exhibit the interesting effects of magnetic nature as observed for LNMO. Referring to Table- 7.2 and comparing with Table-VI in Ref.[23] we make the interesting observation that upon changing the magnetic ordering from FM to FiM in  $La_2NiMnO_6$ , the behavior to the  $Z^*$  matrix becomes more akin to  $LiNbO_3$ , with nearly symmetric off-diagonal components of  $Z^*$  at oxygen sites and nearly similar antisymmetric off-diagonal components of  $Z^*$  between Ni and Mn (in case  $LiNbO_3$  they are identical between two Nb ions in the unit cell due to symmetry). Presence of large off-diagonal elements of  $Z^*$  have been also observed for relaxor  $PbMg_{1/3}Nb_{2/3}O_3$  [24], but like  $LiNbO_3$  it also does not show the interesting effects of magnetic nature.

While the symmetry of the structure allows antisymmetric Born charge in LNMO, its magnitude depends on the energies of the  $d$  orbitals and hence on the type of magnetic ordering. Being motivated by this finding, we determined the Born effective charges of another insulating double perovskite, namely,  $Sr_2CrOsO_6$  [25], which also has a rhombohedral symmetry in certain temperature range. Though, we observe antisymmetric off-diagonal Born effective charges at O  $s$  site, driven by the symmetry of the rhombohedral phase, its magnitude is found to be much smaller ( $\approx 0.3$ ). The observed case in LNMO is therefore a rare event where the geometry, chemistry, and magnetism work hand-in-hand to produce such a spectacular effect.

## 7.8 Summary and outlook

We carried out first-principles density functional calculations to examine the electronic and magnetic structure of  $\text{La}_2\text{NiMnO}_6$ , in particular, to understand the origin of the dielectric anomaly reported recently. We could correctly reproduce the ferromagnetic insulating behavior of the compound, the ferromagnetism being governed by the superexchange interaction. Our study further showed the presence of soft IR-active phonon modes exhibiting strong coupling with spin, which explains the observed dielectric anomaly. The fact that the jump in the dielectric constant at  $H = 0$  T, occurs at a temperature  $T_{\text{jump}}$  below  $T_c$  happens because close to  $T_c$  the magnetic moment is not fully developed due to thermal fluctuation while at a lower temperature the moment gets fully developed and makes the effect of coupling to phonon degrees of freedom appreciable enough to observe the jump in the dielectric constant. This is corroborated by the fact that  $T_{\text{jump}}$  becomes closer to  $T_c$  upon application of a magnetic field, which helps overcome the thermal fluctuation and enhance the magnetization. Note that the superexchange driven B-site magnetism based dielectric anomaly discussed here is complementary to the mechanism of the low-temperature dielectric anomaly discussed for  $\text{EuTiO}_3$  [26], which is A-site based weak magnetism driven. Additionally, we have provided a first-principles theoretical evidence for a magnetism-dependent electrostructural coupling in LNMO: it exhibits an anomalously large antisymmetric component of the BEC matrix that depends sensitively on the magnetic order. Fundamental understanding developed here in terms of aspects of symmetry and electronic structure responsible for the fascinating properties of LNMO should stimulate further efforts in designing new materials exhibiting magnetism-dependent electrostructural coupling. This would lead to changes in the intensity of the IR spectra upon application of magnetic field as well as rotation of the plane of vibration of Ni upon shining a plane polarized IR radiation, with respect to the plane of polarization of the incident IR radiation.

# References

- [1] S. VanHouten, Phys. Lett. **2**, 215 (1962).
- [2] B.T. Matthias, R.M. Bozorth, J.H. VanVleck, Phys. Rev. Lett. **7**, 160 (1961).
- [3] P.K. Baltzer, H.W. Lehmann, M. Robbins, Phys. Rev. Lett. **15**, 493 (1965).
- [4] T. Kimura, S. Kawamoto, I. Yamada, M. Azuma, M. Takano, Y. Tokura, Phys. Rev. B **67**, 180401 (2003).
- [5] M.A. Subramanian, A.P. Ramirez, W.J. Marshall, Phys. Rev. Lett. **82**, 1558 (1999).
- [6] A. Wold, R.J. Arnott, J.B. Goodenough, J. Appl. Phys. **29**, 387 (1958).
- [7] J.B. Goodenough, A. Wold, R.J. Arnott, N. Menyuk, Phys. Rev. **124**, 373 (1961).
- [8] N.Y. Vasanthacharya, P. Ganguly, J.B. Goodenough, C.N.R. Rao, J. Phys. C **17**, 2745 (1984).
- [9] R.I. Dass, J.-Q. Yan, J.B. Goodenough, Phys. Rev. B **68**, 064415 (2003).
- [10] N. S. Rogado, J. Li, A.W. Sleight, and M. A. Subramanian, Adv. Mater. **17**, 2225 (2005).
- [11] C. L. Bull, D. Gleeson, and K. S. Knight, J. Phys. Condens. Matter **15**, 4927 (2003).
- [12] P. Ghosez and X. Gonze, J. Phys.: Condens. Matter **12**, 9179 (2000).
- [13] K. Asai et al., J. Phys. Soc. Jpn. **47**, 1054 (1978).
- [14] M. Sonobe and K. Asai, J. Phys. Soc. Jpn. **61**, 4193 (1992).
- [15] M. C. Sanchez et al., Phys. Rev. B **65**, 144409 (2002).
- [16] K. I. Kugel and D. I. Khomskii, Sov. Phys. Usp. **25**, 231 (1982).
- [17] C. J. Fennie and K. M. Rabe, Phys. Rev. B **72**, 214123 (2005).
- [18] M. Born and K. Huang, *Dynamical Theory of Crystal Lattices* (Oxford University Press, Oxford, 1968).

- 
- [19] D. J. Singh and Chul Hong Park, Phys. Rev. Lett. **100**, 087601 (2008).
- [20] Ph. Ghosez, J.-P. Michenaud, and X. Gonze, Phys. Rev. B **58**, 6224 (1998).
- [21] Alessio Filippetti and Nicola A. Hill, Phys. Rev. B **65**, 195120 (2002).
- [22] S. Massidda, M. Posternak, A. Baldereschi, and R. Resta, Phys. Rev. Lett. **82**, 430 (1999).
- [23] M. Veithen and Ph. Ghosez, Phys. Rev. B **65**, 214302 (2002).
- [24] N. Choudhury, R. E. Cohen, and E. J. Walter, Comput. Mater. Sci. **37**, 152 (2006).
- [25] H. Das, M. De-Raychaudhury, and T. Saha-Dasgupta, Appl. Phys. Lett. **92**, 201912 (2008).
- [26] C. J. Fennie and K. M. Rabe, Phys. Rev. Lett. **97**, 267602 (2006).

# Chapter 8

## Conclusion

The interplay between charge, orbital and spin degrees of freedom in transition metal oxides manifests the wide range of properties reported in literature. Understanding this complex interplay is a great challenge for modern condensed matter physics. In this thesis, we have picked up few transition metal oxides and studied their properties using Density functional theory (DFT) as well as first principles derived model Hamiltonian approach combined with many body techniques like, quantum Monte Carlo (QMC) method, dynamical mean field theory (DMFT) and exact diagonalization (ED). The main findings are listed below.

**Chapter-3** The underlying magnetic structure of the spin-gapped system  $\text{CuTe}_2\text{O}_5$  were investigated using first-principles electronic structure calculations based on the NMTO-downfolding technique. The proposed spin model was solved by quantum Monte Carlo method.

*The main findings are:*

1. The strongest Cu-Cu interaction in  $\text{CuTe}_2\text{O}_5$  is the one between fourth nearest neighbor mediated by two O-Te-O bridges ( $J_4$ ) followed by the interaction mediated by a single O-Te-O bridge ( $J_6$ ). This is in contrast to the fact that  $J_6$  was found in Ref.[Phys. Rev. B **74**, 174421 (2006))] employing the extended Hückel tight-binding (EHTB) study to be the strongest interaction. We also obtained that the Cu-Cu interaction within the structural dimer unit ( $J_1$ ) is rather weak as opposed to the findings of the EHTB study, though both ours and the EHTB study found the structural dimer interaction not to be the leading interaction. The underlying spin model for  $\text{CuTe}_2\text{O}_5$  derived out of our calculations is therefore different from that suggested in Ref.[Phys. Rev. B **74**, 174421 (2006)]].
2. The computed magnetic susceptibility for the proposed model by performing quantum Monte Carlo (QMC) simulations (stochastic series expansion) showed good agreement with the experimental observations.
3. In view of the fact that the magnetic susceptibility is often found to be an insensitive quantity to the details of the magnetic structure, we also calculated temperature

and magnetic-field dependent magnetization as well as the specific heat as a function of temperature. These results need to be tested in terms of further experimental investigations to resolve the underlying microscopic model for  $\text{CuTe}_2\text{O}_5$  completely.

**Chapter-4:** Our attempt was to reveal the origin of the contrasting properties of  $\text{La}_2\text{CuO}_4$  in  $T'$  phase compared to  $T$  phase. It was experimentally reported that while  $\text{La}_2\text{CuO}_4$  in the  $T$  structure is strongly insulating, the same in  $T'$  structure appears to be conducting with a difference in resistivity of orders of magnitude. Our first clue of investigation was the difference in their crystal structure, which is described as the change in position of the apical oxygen to a position below or above the planar oxygens of  $\text{CuO}_2$  plane. We used dynamical mean field theory (DMFT) together with density functional theory within LDA approximation, to incorporate the correlated nature of the electrons.

*The main findings are:*

1. Our study showed that the change in position of the out-of-plane oxygen between  $T$  and  $T'$  structures, resulting into significant changes in the one-particle electronic structure.
2. These differences in the one-particle electronic structure translates into insulating solution in case of  $T$  structure and correlated metallic situation in case of  $T'$  structure upon incorporation of correlation effect.

**Chapter-5** The unusually high ferromagnetic (FM) transition temperature in the double perovskite system  $\text{Sr}_2\text{FeMoO}_6$  was explained in terms of a kinetic-energy driven mechanism that recently proposed a destabilization trend of the FM phase as one doped the system with electrons through model calculations. There were two restrictions in the model calculations: (i) the calculations were carried out in two dimension, (ii) only single band were considered. However these restrictions are not strictly true for real systems. We therefore checked this scenario in  $\text{La}^{3+}$  ion doped SFMO system, that mimic electron doping into the system, using first-principles calculations which take into account all the structural and chemical aspects correctly, combined with the with exact diagonalization of Fe-Mo Hamiltonian constructed in a first-principles Wannier-function basis.

*The main findings are:*

1. Our calculation showed destabilization of the FM phase with the increase of electron doping and a transition to a kinetic-energy driven antiferromagnetic phase in the La-rich region, in agreement with the results obtained on the basis of previous model calculations.

2. We found that the delicate balance between FM and antiferromagnetic (AFM), is governed by the extent of hybridization between the localized transition metal (TM) site (Fe in this case) and delocalized TM site (Mo in this case).

**Chapter-6** In the first part of this chapter, employing first principles density functional calculations, together with solution of the low-energy, model Hamiltonian constructed in a first principles manner, we explored the origin of magnetism and  $T_c$  trend in Cr-based double perovskite series,  $\text{Sr}_2\text{CrB}'\text{O}_6$  ( $\text{B}'=\text{W}/\text{Re}/\text{Os}$ ).

*The main findings are:*

1. From the observed dehybridization effect between  $\text{Cr-}t_{2g}$  and  $\text{B}'\text{-}t_{2g}$  states together with the increasing trend of the spin splitting at the  $\text{B}'$  site we concluded that there is a growing intrinsic moment that develops at  $\text{B}'$  site.
2. Therefore we proposed that to understand the magnetism in this series one needs to include the superexchange (SE) between the moment at Cr site and the intrinsic moment at  $\text{B}'$  site together with double exchange.
3. By solving the low-energy model Hamiltonian constructed in a first principles manner with exact diagonalization method we reproduced correct trend of  $T_c$  in this series.

In the second part of this chapter we investigated the magneto optical (MO) effects in this double perovskite series.

*The main findings are:*

1. Our study showed a large Kerr rotation of about  $-2^\circ$  to  $-2.5^\circ$  in  $\text{Sr}_2\text{CrWO}_6$  and  $\text{Sr}_2\text{CrReO}_6$  and a moderately large Faraday rotation of about  $-0.25 \times 10^6$  deg/cm in insulating  $\text{Sr}_2\text{CrOsO}_6$ , justifying their applicability for industrial use as read heads.

**Chapter-7** Another double perovskite system  $\text{La}_2\text{NiMnO}_6$ , was studied in this chapter. The motivation of this study was twofold: (a) to explain the room temperature semiconducting ferromagnetic behavior of the system, (b) to explore the origin of the magnetic field induced dielectric anomaly observed experimentally near the ferromagnetic transition temperature.

*The main findings are:*

1. Our calculations correctly reproduced the ferromagnetic semiconducting nature of the system and the theoretically calculated ferromagnetic transition temperature ( $T_c$ ) is quite comparable with the experimentally determined one.

2. Our study revealed the existence of very soft infrared active  $\Gamma$ -point phonons that couple strongly with spins at the Ni and Mn sites through modification of the superexchange interaction. We concluded that these modes are the origin for the observed dielectric anomaly in  $\text{La}_2\text{NiMnO}_6$ .
3. We found a magnetism-dependent electrostructural coupling in this compound through the investigation of our calculated Born effective charges.